Textile reinforced mortar to masonry bond under static and fatigue loading

A Thesis Submitted to The University of Nottingham
for the Degree of Doctor of Philosophy

Kuanysh Makashev

September 2021

Abstract

There is a growing interest in strengthening existing masonry buildings and structures due to their continuous structural deterioration, which is accelerated by the effect of adverse environmental actions, e.g., earthquakes, high-speed winds, heavy rainfalls and the continuous increase of traffic loads. Textile Reinforced Mortars (TRM) have been proven to provide several advantages over more traditional strengthening approaches; they are applicable in low temperatures, provide fire resistance, and are low cost. TRM, that belong to the more general family of Fabric Reinforced Cementitious Matrices (FRCM) - involve high strength fibre textile materials impregnated in inorganic cement or lime-based mortars.

As in every externally bonded strengthening technique, one of the key parameters controlling the effectiveness of TRM is the bond between the strengthening material and the substrate. Over the past fifteen years, the mechanics of TRM to masonry bond have been investigated experimentally, analytically, and numerically for the case of quasi-static loading. However, experiments demonstrate a large variabilty vis-a-vis the anticipated bond strength. Conversely, the case of fatigue loading has not garnered much attention. Experiments conducted on FRP strengthened concrete specimens have demonstrated the detrimental effect of fatigue on the corresponding interfacial properties. With the objective of further investigating the effect of bond and contribute to the state-of-the-art in interface properties, this Thesis provides results from an experimental investigation on the TRM to masonry bond strength under monotonic and cyclic loading conditions.

At the first stage, the textile reinforcement tensile properties were determined by carrying out tensile tests on bare textiles. Next, the bond behaviour between TRM and masonry substrate under quasi-static loading was extensively investigated. The investigated parameters were the bond length, the textile-fibre material and the epoxy resin coating. Finally, for the first time, a series of single-lap shear tests under fatigue loading has been conducted on textile fibre TRM bonded to masonry, considering various bond lengths and load ranges.

The experimental results establish that TRM and masonry bond behaviour depends on textile materials used and the anchorage lengths. Furthermore, this work highlights the beneficial effect of the epoxy-resin coating compared to the uncoated counterpart specimens; it increases the fibre textiles' tensile properties, improves the bonding conditions, and alters the failure mode of carbon and glass fibre-textile material. The results of bond behaviour under low cycle fatigue loading tests showed that the load range considerably affects the fatigue life of TRM strengthened components resulting in significantly lower strengths when compared to the quasi-static case.

Acknowledgements

Writing a doctoral thesis is a long individual journey, which can not be realised without the help, support and advice of a number of individuals. First and foremost. I want to express my gratitude to my supervisor Dr Savvas Triantafyllou for his advice, guidance, and encouragement during the three years of this research. His contribution was crucial and enabled me to understand the needs of research, plan my work, and achieve the objectives in an environment of collaboration and friendly debate.

I would like also to thank Dr. Georgia Thermou for her support and assistance in the last year of my PhD study. Her scientific knowledge, lab experience, positive thinking, and personal characters helped me in my PhD. I also deeply thank Dr. Walid Tizani for his assistance during my PhD study.

I would like to acknowledge the financial support of the Center for International Programs (CIP) in Kazakhstan for providing me with the chance to complete my PhD studies.

I would also like to thank my colleagues, Dr. Florentia Kariou and Dr. André Vieira, for their endless help and support was so important for me to overcome the challenges of the experimental works in the lab. I would like also to greatly acknowledge the contribution of the lab manager Mr. Tom Buss and Mr. Jason Greaves at Wolfson Laboratory, the L2 Lab manager Mr. Mike Langford, the L2 chief technician Mr. Nigel Rook, the technicians Mr. Ali Palmer, Mr. Bal Loyla and Mr. Gary Davies for their assistance to achieve the experimental work.

I feel grateful to my family, mother, brother, and sister, who always believed in me and supported me to fulfil my dreams. Even though they were far away, they always felt next to me by supporting me in difficult times.

I am deeply grateful to my sweetheart wife Saule, my lovely daughter Tomiris, and my son Tamerlan for being close to me all the time. Their sincere feelings, love, patience, and continuous encouragement motivated me to achieve my goals.

Contents

Abstract i

Acknowledgements ii

Contents vii

List of Tables ix

List of Figures xiii

Chapter 1 Introduction 1

1.1 Background and motivation 1

1.2 Project scope 5

1.3 Aims and objectives 5

1.4 Methodology 6

1.5 Research outputs 7

1.6 Report layout 8

Chapter 2 Literature Review 10

2.1 Introduction 10

2.2 Strengthening using composite materials. 11

2.2.1 Textile fibre materials. 12

2.2.2 Inorganic matrix 16
2.3 TRM bond tests under static loading 17
2.3.1 Tests conducted on glass fibre textile reinforced mortars 20
2.3.2 Tests conducted on carbon fibre textile reinforced mortars 22
2.3.3 Tests conducted on basalt fibre textile reinforced mortars 23
2.3.4 Comparative studies on the effect of the textile material. 24
2.3.5 The effect of coating of the textile material 26
2.4 A critical reflection on the results of quasi static bond tests. 27
2.5 Bond behaviour under fatigue loading 33
2.5.1 Fiber reinforced polymers 34
2.5.2 Textile reinforced mortars 35
2.6 Analytical modelling of the TRM to masonry bond 36
2.7 Numerical modelling for masonry structures 41
2.7.1 Discretization approaches 41
2.7.2 Constitutive modelling 43
2.8 Numerical simulation of interface mechanics 47
2.8.1 Interface modelling by the cohesive surface approach 47
2.8.2 Contact pressure-overclosure relationships 48
2.8.3 Tangential behaviour - Coulomb friction model 50
2.8.4 Bond test FE modelling 52
2.9 Chapter summary 53

Chapter 3 Material characterisation 56

3.1 Introduction 56
3.2 Clay bricks 56
3.3 Mortars 58
3.3.1 Mortar mix 58
3.3.2 Mechanical properties of the mortars 58
3.4 Textile fibre materials 59
3.4.1 Tensile tests on dry textiles. 61
3.4.2 Comparisons with published test results 64

3.5 Concluding Remarks. 68

Chapter 4 TRM to masonry bond under static loading 70

4.1 Introduction 70

4.2 Experimental Programme 71

4.2.1 Test Specimens and experimental parameters 71

4.2.2 Specimen preparation 72

4.2.3 Shear bond test setup. 73

4.2.4 Experimental Results 75

4.2.5 Failure modes. 78

4.3 Discussion 81

4.3.1 The effect of the bond length 81

4.3.2 The effect of in house coating 82

4.3.3 The effect of the textile fibre material 85

4.4 Comparison to the literature 87

4.4.1 Analytical modelling 90

4.5 Concluding Remarks. 98

Chapter 5 Masonry to TRM bond under fatigue loading 100

5.1 Introduction 100

5.2 Experimental program. 101

5.2.1 Test specimens and experimental setup 101

5.2.2 Fatigue testing loading envelopes 105

5.3 Experimental results from the quasi static bond tests 106

5.4 Fatigue testing experimental results 110

5.4.1 Fatigue failure modes 123

5.5 Discussion 135

5.5.1 Response Stages 135

5.5.2 The effect of the loading range. 138

5.5.3 The effect of the bond length 142

5.5.4 Global slip. 144

5.6 Concluding Remarks. 151

Chapter 6 Finite element modelling **153**

6.1 Introduction 153

6.2 Bond test modelling 153

6.2.1 Geometry and type of elements 154

6.2.2 Application of the cohesive modelling approach on the masonry to TRM bond behaviour 155

6.2.3 Finite element analysis results and discussion 156

6.2.4 The effect of the bond length: numerical vs experimental results . 166

6.2.5 Effect of the textile material 169

6.2.6 Effect of mesh size of strengthening mortar 170

6.3 TRM coupon test modelling 174

6.3.1 Materials definition 176

6.3.2 Finite element analysis results 177

6.4 Modelling of masonry wall specimens 177

6.4.1 Description of the model 177

6.4.2 Finite element analysis results and discussion 183

6.5 Concluding Remarks 190

Chapter 7 Conclusions and Future Outlook **191**

7.1 Main Contributions 191

7.2 Conclusions on the experimental work conducted 192

7.3 Limitations and Suggestions for Further Improvements 194

Bibliography **196**

Chapter A Summary of experimental results available in the literature **205**

Chapter B List of Abbreviations **210**

List of Tables

2.1 Textile mesh sizes typically used in the literature 13

2.2 Tensile tests on single roving and grid strip (Carozzi & Poggi 2015) 14

3.1 Results of compression tests on bricks 57

3.2 Mortar properties 59

3.3 Textile fibre materials parameters 60

3.4 Tensile properties of the fibre-textile materials 67

4.1 Wall Specimens 74

4.2 Bond test results: Average values of peak loads and peak stresses Failure modes according to Fig. 2.5 77

4.3 Material parameters employed in the analytical mode. The calibrated parameters are highlighted in grey color. 98

5.1 Specimen details 102

5.2 Average test result for monotonic quasi-static tests. 109

5.3 Results from quasi-static tests: Comparisons between the 100 kN and 25 kN actuators 109

5.4 Loading envelopes per specimen 110

5.5 Fatigue tests result of basalt textile in case of 60% of P_{max} 117

5.6 Fatigue tests result of basalt textile in case of 70% of P_{max} 118

5.7 Fatigue tests result of basalt textile in case of 80% of P_{max} 119

5.8 Fatigue tests result of heavy coated carbon textile in case of 60% of P_{max} . . 120

5.9 Fatigue tests result of heavy coated carbon textile in case of 70% of P_{max} . . 121

5.10 Fatigue tests result of heavy coated carbon textile in case of 80% of P_{max} . 122

5.11 Response stages versus number of cycles (carbon specimens) 135

5.12 Response stages versus number of cycles (basalt specimens) 137

6.1 Interaction property masonry wall to strengthening mortar 156

6.2 The variation on the interaction property between strengthening mortar and textile 166

6.3 Experimental and simulated result compare bond test 169

6.4 Tensile test result on fibre-textile materials 175

6.5 Wall specimens: Comparison between experimental and simulated failure modes 184

6.6 Textile properties of the FE models 186

A.1 Tensile tests on bare fibre textiles 206

A.2 FRCM to masonry bond tests 207

A.2 FRCM to masonry bond tests 208

A.2 FRCM to masonry bond tests 209

List of Figures

1.1 Licensed vehicles by type since 1909. The graph is originally created from data available in (Department for Transport Statistics UK 2016) 2

1.4 Methodology flowchart 7

2.1 Textile reinforced mortar (TRM) 12

2.2 Typical grid configuration 14

2.5 Failure modes (De Felice et al. 2018) 17

2.7 Schematic representation of the fabric sections depending on the impregnation treatment 27

2.8 Exploitation ratios per textile fibre material from the experimental data provided in Table A.2 30

2.9 Glass fibre textiles: Average maximum load per unit width from the bond tests provided in Table A.2 31

2.10 Carbon fibre textiles: Average maximum load per unit width from the bond tests provided in Table A.2 32

2.11 Basalt fibre textiles: Average maximum load per unit width from the bond tests provided in Table A.2 32

2.13 Diagrams, describing equations and fracture energy functions of (a) local law A; (b) local law B; (c) local law C; and (d) local law D. (Barducci et al. 2020) 39

2.14 Scheme of the TRM system at the basis of the developed model Grande et al. (2018) 40

2.16 Simplified micro-modelling Lourenço & Rots (1997) 44

2.17 Yield criteria in the meridional plane Drucker-Prager (SIMULIA, 2016) . . . 44

2.18 Schematic of hardening and flow for the linear model in the p–t plane (SIMULIA, 2016) 45

2.19 Yield surface and flow rule of CDP model (deviatoric plane) 47

2.20 Flow rule of CDP model (meridian plane) 48

2.23 Linear damage evolution Smith (2012) 51

2.24 Frictional behavior Smith (2012) 51

3.1 Typical stress–strain curve for bricks under quasi-static compression 57

3.3 Property of cement based mortar compare to the current study (current study result highlighted with red) 59

4.1 Overview of test specimens (all dimensions in mm) 71

4.2 Preparation of the masonry wallettes 71

4.11 Variation of the ultimate load as a function of the bond length 81

4.12 Exploitation ratio 83

4.16 Glass fiber textile reinforced mortars: Average maximum load per unit width in shear bond tests(number before brackets represent bond lengths, mesh size in brackets) 87

4.17 Basalt fiber textile reinforced mortars: Average maximum load per unit width in shear bond tests(number before brackets represent bond lengths, mesh size in brackets) 88

4.18 Carbon fiber textile reinforced mortars: Average maximum load per unit width in shear bond tests(number before brackets represent bond lengths, mesh size in brackets) 89

4.19 Schematic of the TRM system at the basis of the analytical model presented in Grande et al. (2018). 92

4.20 Stress equilibrium and deformation of infinitesimal section 92

4.21 Debonding stages 93

5.1 Variation of bond lengths 103

5.34 Curves P_{max}-N_s and fitting line in case of carbon FRP from Carloni et al. (2012) 142

5.36 Bond length against maximum applied load (average) in static case 144

6.2 Loading of specimen 156

6.25 Maximum applied load against bond length test result versus model glass coated and uncoated 167

6.26 Maximum applied load against bond length test result versus model Carbon light coated and uncoated 168

6.27 Maximum applied load against bond length test result versus model Carbon heavy coated and uncoated 168

6.28 Maximum applied load against bond length test result versus model coated basalt 168

6.29 Maximum load P_{max} FEM per material. The case of L_b=250mm is considered170

6.38 Experimental setup and geometry of the TRM coupon Raoof & Bournas (2017) 175

6.39 FE model- Loading of the coupon sample 176

6.40 FE model mesh of the coupon sample 177

6.45 Wall specimen: Boundary conditions 182

6.48 Maximum principal stress S_G3 a) TRM b) Masonry wall 185

6.49 Maximum principal stress S_G7 a) TRM b) Masonry wall 185

6.50 Maximum principal stress S_B3 a) TRM b) Masonry wall 186

6.51 Maximum principal stress S_B7 a) TRM b) Masonry wall 187

6.52 Maximum principal stress S_G3_(co) a) TRM b) Masonry wall 187

6.53 Maximum principal stress S_G7_(co) a) TRM b) Masonry wall 188

6.54 Maximum principal stress S_C1 a) TRM b) Masonry wall 188

6.55 Maximum principal stress S_C1_(co) a) TRM b) Masonry wall 189

1 Introduction

1.1 Background and motivation

Structural strengthening is an active and highly innovative field of engineering research. The need for such a research direction stems from an unquestionable fact; a significant portion of buildings and bridges currently in operation has long exceeded its, initially designed for, life span.

With regards to the UK's building stock, nearly 60% of the UK's residential buildings were built before 1960 according to the Department for Communities and Local Government (2012). With regards to infrastructure, masonry bridges are an essential part of the transport infrastructure both in the UK and worldwide. In Europe, their operational and economic value is undoubted since they sum up to 40% of the total European bridge stock (Page 1994). In the UK, masonry bridges still constitute a large portion of the total bridge stock in the waterway, railway, and road networks (Hughes 1996). Overall, 64% of those bridges are over 100 years old (Bell 2004). Although they have been built to meet the design requirements of their corresponding era, they are now required to serve the demands of modern traffic.

Over the last 100 years, the number of vehicles on the road has been rapidly increasing, along with their average speed and weight. The total number of licensed vehicles in the UK has increased from 143,000 in 1909 to 38,682,700 in 2019 according to the Department of Transport Department for Transport Statistics UK (2016), see also, Fig.1.1. Furthermore, the miles travelled by vehicles in total in the UK has increased from 28.9 billion miles in 1949 to 356.5 billion miles in 2015 as shown in

Fig.1.2a (Department for Transport Statistics UK 2016). Although the absolute number of vehicles and miles travelled from heavy goods vans is low when compared to other types, the maximum load for permitted lorry increased significantly from 12 tonnes in 1904 to 44 tonnes in 1996 (Ryall 2008). Such an increase, both in the mileage and in the total lorry subjects the structures to cyclic loading envelopes of higher frequency and of increased intensity rendering fatigue damage a plausible scenario.

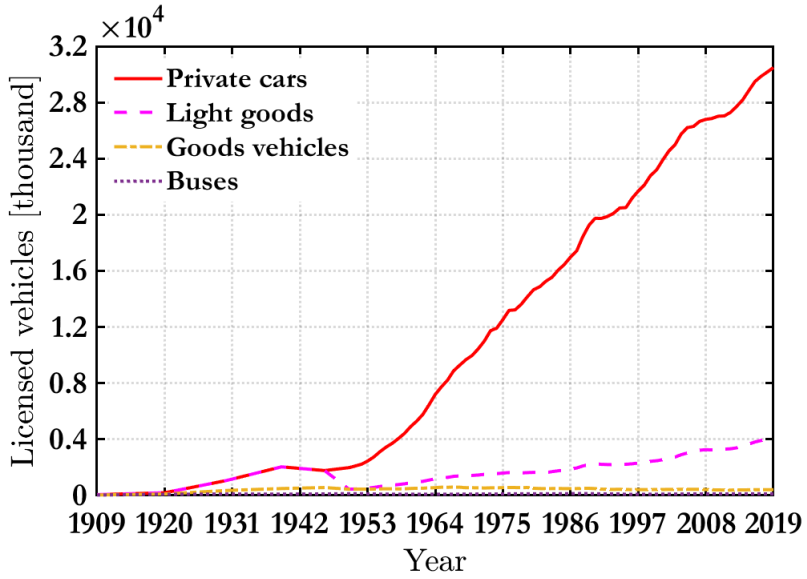

Figure 1.1: Licensed vehicles by type since 1909. The graph is originally created from data available in (Department for Transport Statistics UK 2016)

Not only are ageing structures asked to sustain increased loads due to rising operational demands, they also need to withstand the adverse effects of an ever-changing and dynamic environment due to, e.g., earthquakes, floods, and wildfires. Recent events such as the 2017 Central Italy earthquakes (Mazzoni et al. 2018) and the 2020 Samos–Izmir earthquake (Nuhoğlu et al. 2021) have resulted in a significant number of collapsed or damaged masonry structures. Coburn et al. (1992) reported that more than 1100 fatal earthquakes resulted in 1.53 million deaths during the last century. A total of 75% of the fatalities were caused by building collapses; out of these 65% were due to the collapse of masonry buildings. Augenti & Parisi (2010) reported that buildings of significant cultural and historical importance suffered damages due to their construction characteristics or to inadequate seismic strengthening provisions. Typical cases of the impact of flooding on masonry bridges are the Ballynameen Bridge over the river Faughn near Cladys, Northern Ireland shown in Fig. 1.3a, (Solan et al. 2019) and the collapse of the Trigno river bridge, Italy shown in Fig. 1.3b (Zampieri

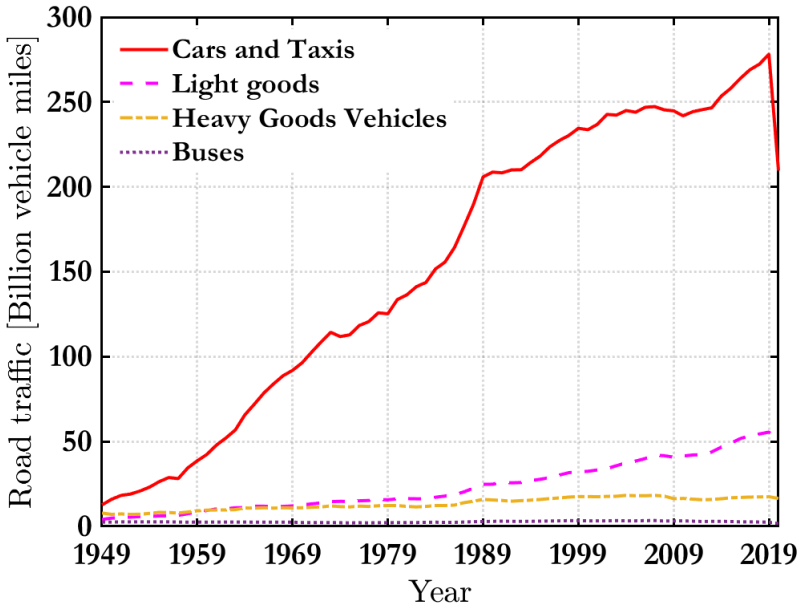

(a)

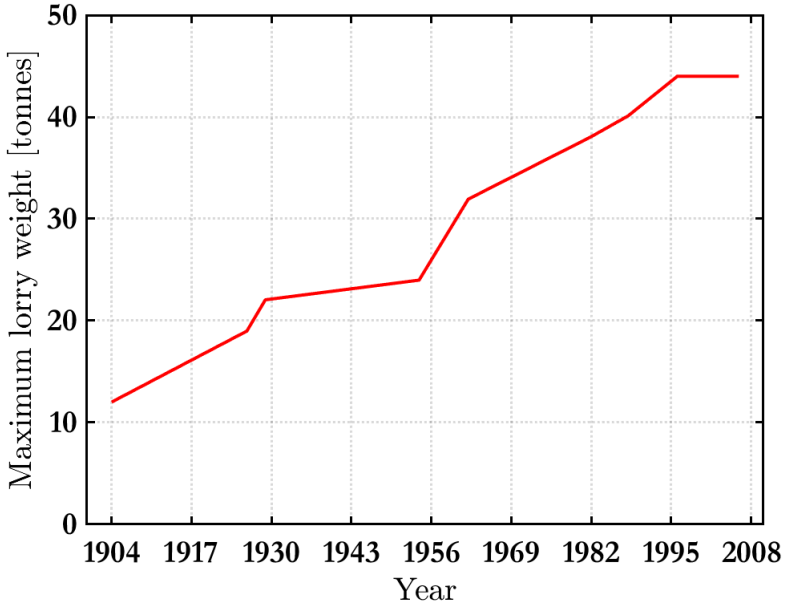

(b)

Figure 1.2: a) Vehicle miles by vehicle type in Great Britain since 1949. The graph is generated from data available in (Department for Transport UK 2016) b) Variation of heavy vehicle load with time (Ryall 2008)

et al. 2017).

(a)

(b)

Figure 1.3: a)failure of an arch bridge (Ballynameen Bridge) over the River Faughn near Cladys, Northern Ireland Solan et al. (2019) b) Collapse of the Trigno river bridge (Italy) flooding event Zampieri et al. (2017)

The data listed above clearly indicate the need for detailed research on the deterioration of masonry buildings and structures. Furthermore, the requirement for providing innovative solutions vis-à-vis towards the strengthening of unreinforced masonry structures is clearly identified (Triantafillou 1998). An additional advantage of structural strengthening that has been highlighted in the literature is the possibility of minimising the effects of terrorist attacks that may lead to the collapse of buildings, bridges, and infrastructure (Wu et al. 2009).

Textile reinforced mortar (TRM) composites have emerged as a promising alternative to the fibre reinforced polymers (FRP) in case of strengthening existing UM structures (Tetta et al. 2015, Elsanadedy et al. 2013, Ismail & Ingham 2016, Askouni & Papanicolaou 2017). TRM comprises a high-strength fibre textile embedded in an inorganic matrix. The effectiveness of the strengthening method naturally crucially relies on the bond between the TRM and the substrate. Poor bond conditions inevitably lead

to the under-utilization of the textile fibre material, which is the expensive constituent of the composite material (Kouris & Triantafillou 2018, Leone et al. 2017, Ombres et al. 2018, Carozzi et al. 2017, Askouni & Papanicolaou 2017).

1.2 Project scope

Considering the aforementioned, this project investigates the bond behaviour between textile reinforced mortar and masonry substrate under static and low cycle fatigue conditions. Typically, the strengthening of unreinforced masonry structures increases their robustness and prolongs their operation life due to enahncement of the mechanical properties of the virgin material and the redistribution of the stresses from the substrate (strengthened element) to the strengthening solution (Kim & Heffernan 2008). However, the effectiveness of the externally strengthened composite material largely depends on the bond between the externally bonded grids and the existing substrate. Debonding may lead to premature failure and, thus, to a low degree of exploitation of the strengthening system.

To this end, a significant number of experimental and numerical investigations have been conducted to examine the mechanics governing the textile-reinforced mortars to masonry bond under static loading conditions. However, more work is needed to investigate additional parameters, such as the influence of in-house coating and properties of the mortar matrix. Furthermore, the majority of research conducted focuses on quasi-static cases; the case of low cycle fatigue loading has not been investigated. This research will endeavour to address this gap in current knowledge.

1.3 Aims and objectives

The overarching aim of this research is to quantify and assess the bond behaviour between TRM and masonry wallets under static and fatigue loading conditions. To achieve this, the following research objectives are identified:

(i). Conduct an extensive literature review to analyse the current state-of-the-art regarding bond behaviour between TRM and masonry interface, textile materials,

and mortar matrix used;

(ii). Experimentally investigate the bond between TRM and masonry in case of quasi-static conditions by examining the effect of various parameters such as the type of the textile fibre material, the bond length, and the application of epoxy resin coating on the bond;

(iii). Experimentally investigate the performance of TRM masonry bond under fatigue loading conditions and examine the effect of various parameters such as the bond length, the load range, and the type of textile material employed;

(iv). Develop appropriate numerical models for simulating the bond mechanisms between TRM and masonry and finally

(v). Use the key findings regarding the TRM to masonry bond to simulate TRM strengthened elements under out-of-plane bending loading conditions.

1.4 Methodology

To achieve these research objectives, this project is built upon the following methodological steps, also shown in Fig. 1.4. The first step is a review of the existing knowledge relevant to this research topic. The review provides insight into the physical phenomenon of the bond between TRM and masonry. Based on the literature review, the investigated parameters of the experimental campaign were chosen and the test setup and specimen configurations were designed. The fatigue loading test setup and specimen configurations were chosen based on the conclusions drawn from the literature review and the experience gained from the quasi-static tests.

The experimental campaign was supplemented by a numerical simulation campaign with the objective of identifying appropriate simulation strategies of increased accuracy. The Abaqus FE software was used to build, run and post-process the numerical models.

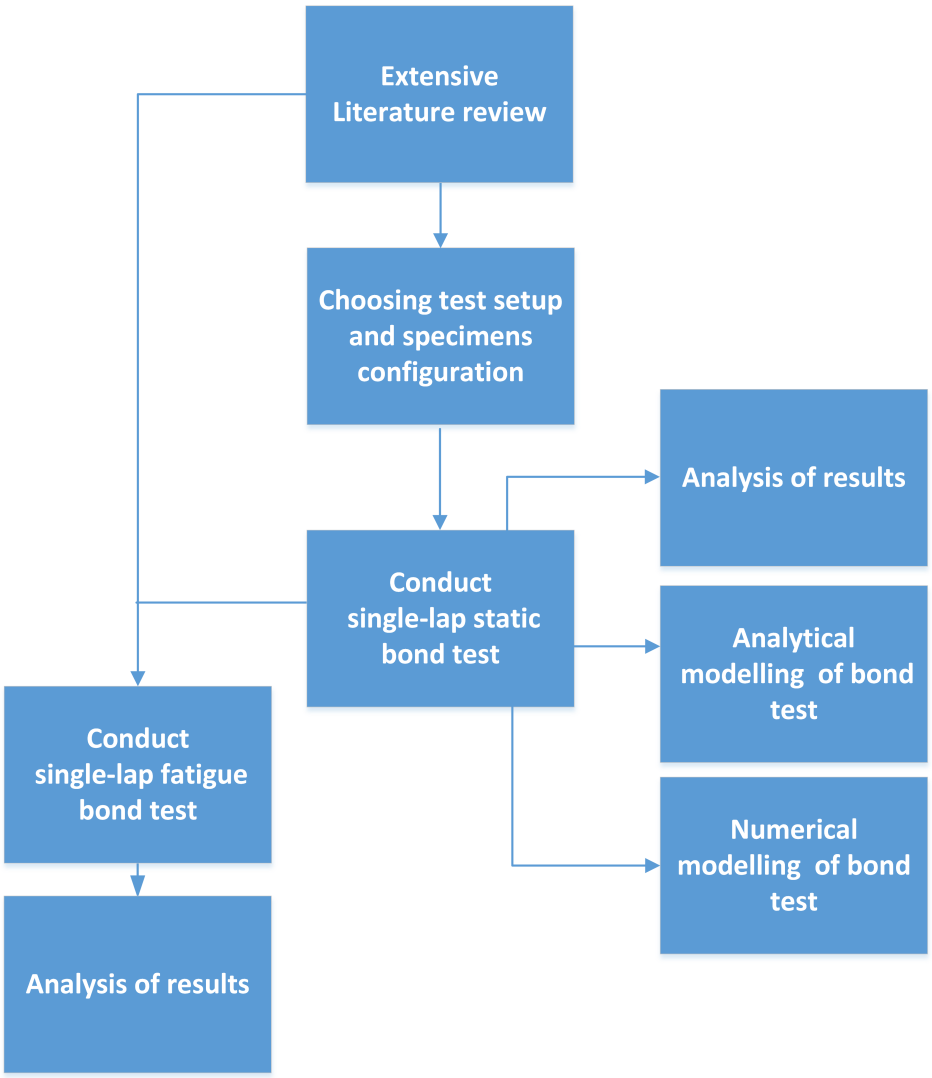

Figure 1.4: Methodology flowchart

1.5 Research outputs

The key outcomes of this research have been disseminated through the following routes

Proceedings in international Conferences

(i). Kuanysh Makashev, Savvas P. Triantafyllou, Georgia E. Thermou and Walid Tizani "Basalt textile reinforced mortar to masonry bond under static and fatigue loading: An experimental investigation", 74th RILEM Annual Week and 40th Cement and Concrete Science Conference, Sheffield 31 08 – 04 09, 2020.

(ii). Kuanysh Makashev, Savvas P. Triantafyllou, Walid Tizani, and Dionysis Bournas

"An experimental investigation on the TRM to masonry bond under fatigue loading", 10th International Conference on FRP Composites in Civil Engineering (CICE 2020), Istanbul 1-3 July 2020.

Presentations in International Conferences

(i). Kuanysh Makashev and Savvas Triantafyllou "TRM to masonry bond strength: The effect of the textile fibre material", Engineering Mechanics Institute Conference 2019 (EMI2019), Lyon France.

Journal publications (under preparation) Furthermore, the following manuscripts are currently under preparation to be submitted for peer review

(i). Kuanysh Makashev, Savvas P. Triantafyllou, Georgia E. Thermou, Walid Tizani "An experimental investigation on the TRM to masonry bond strength"

(ii). Kuanysh Makashev, Savvas P. Triantafyllou, Georgia E. Thermou, Walid Tizani "Coated carbon textile reinforced mortar to masonry bond under fatigue loading: An experimental investigation",

1.6 Report layout

This thesis is organised as follows. In Chapter 2, a thorough literature review is presented on textile reinforced mortars with a particular focus on the mechanics of bond and the experimental state-of-the-art vis-à-vis bond under quasi-static and fatigue loading conditions. The mechanical properties of the materials used in this work are presented in Chapter 3. In Chapter 4, the experimental campaign undertaken to investigate bond under quasi-static loading conditions is presented and discussed. The experimental campaign undertaken to investigate the bond under fatigue loading conditions is discussed in Chapter 5. The numerical simulation strategy established to simulate the TRM to masonry bond is presented in Chapter 6. Furthermore, the identified bond mechanical properties are used to simulate TRM strengthened masonry elements under out-of-plane bending conditions. Finally, Chapter 7 summarises the findings and highlights the conclusions from the research. The contribution of the

research to knowledge is outlined, limitations are recognised, and recommendations for future research are provided.

2 Literature Review

2.1 Introduction

Unreinforced masonry structures (URM) constitute a significant portion of the existing building stock worldwide (Papanicolaou et al. 2011); most notably, they involve structures of extreme cultural and historical importance. Interventions in the form of structural strengthening are necessary to mitigate the adverse effects of ageing and also increase their bearing capacity vis-à-vis natural and man-made hazards (Bernat et al. 2013).

To this point, a large number of techniques has been proposed for the strengthening of URM structures, e.g. surface treatment, shotcrete or ferrocement overlays, Fibre reinforced polymers (FRP), Textile reinforced mortars (TRM), and grout or epoxy resin injections (Papanicolaou et al. 2011, Shabdin et al. 2018). FRP and TRM in particular have emerged as highly efficient and low footprint strengthening solutions; they both harness the advantages of high strength and high stiffness fibre materials leading to composites of favourable strength to weight ratios when compared to conventional strengthening techniques.

In this Chapter, the concept of TRM as a composite material is described. The TRM to masonry bond performance is covered with a particular focus on the experimental investigations that have been undertaken to shed light to the mechanics of the bond. To this end, a detailed presentation of the available experimental studies on the following topics is included: (a) the bond behaviour between TRM and masonry substrate under static and cyclic conditions and (b) the textile fibre materials

used. Finally, aspects of analytical bond models are briefly discussed to facilitate the discussion in the next Chapters.

2.2 Strengthening using composite materials

During the past decades, the development of strengthening techniques utilising advanced composite materials has received considerable attention both from an academic and an industrial standpoint, see, e.g. in, Kouris & Triantafillou (2018) for a thorough review on the subject.

Fibre-Reinforced Polymers (FRPs) constitute a composite material typically used to strengthen existing structures. FRPs consist of high-strength fabrics, e.g., aramid, glass, basalt, or carbon embedded within a polymer matrix (Ku et al. 2011). To this point, a significant number of research endeavours have examined the performance of masonry structures strengthened with FRP, see, e.g. Triantafillou (1998), Stratford et al. (2004), Foraboschi (2004), Tan & Patoary (2004), Krevaikas & Triantafillou (2005), Bertolesi et al. (2020). The main advantages of the FRP strengthening technique can be summarised in the following, i.e.

(i). good corrosion resistance;

(ii). efficient use of material for the seismic strengthening structures due to their high strength-to-mass and stiffness-to-mass ratios;

(iii). imperceptible repair, extremely important for historic buildings;

(iv). easily adaptable to a particular strengthening application;

Despite their advantages, a number of drawbacks have also been identified in the literature, see, e.g., Tetta et al. (2015). These mainly pertain to the features of the epoxy resin used to bond the polymer matrix and the fibres. In particular, FRPs demonstrate a rapid decrease of their mechanical properties in high temperatures, are associated with a high cost of the epoxy resin and are not applicable in wet surfaces and at low temperatures (Bertolesi, Milani & Poggi 2016). Most importantly, FRPs pose a health hazard to construction workers causing skin irritation and inflammation in case of poor ventilation (Papanicolaou et al. 2008).

Over the past 15 years, the textile reinforced mortar (TRM) (Fig. 2.1) has been proposed as an alternative solution in structural strengthening with several applications in masonry structures, see, e.g., Papanicolaou et al. (2008), Garmendia et al. (2014). The TRM technique is a sub-class of the FRCM (fabric reinforced cementitious matrix) or TRC (textile reinforced concrete) (Kong et al. 2017) techniques. To this point, the TRM has been used as a strengthening technique for existing structures, see, e.g., Tetta et al. (2015), Elsanadedy et al. (2013), Ismail & Ingham (2016) and Askouni & Papanicolaou (2017) for the case of concrete and unreinforced masonry structures, respectively.

Similar to the FRP, the TRM comprises a textile fibre mesh (e.g., glass, carbon, or basalt) which is however impregnated within an inorganic, typically cement based, matrix; limestone matrices are also employed. As a result, health hazards stemming from organic resins are mitigated. Furthermore, the TRM can be applied in wet surfaces and has been recently shown to perform optimally even at high temperatures (Tetta & Bournas 2016, Raoof & Bournas 2017).

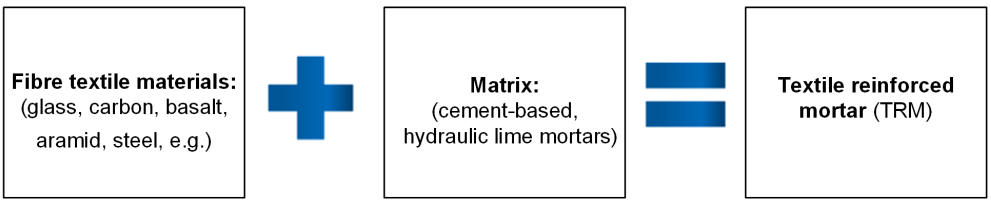

Figure 2.1: Textile reinforced mortar (TRM)

2.2.1 Textile fibre materials

Textile fibres play a vital role in the TRM strengthening system. The fibres are typically made of glass, carbon, basalt, aramid, polypropylene (PP), polyparaphenyle benzobisoxazole (PBO), or steel, see, e.g. Triantafillou (2016).

The mesh rovings of the textile may be arranged in two orthogonal directions (Fig. 2.2), namely the warp and weft directions. However, configurations utilising rovings in more than two directions are also available, see, e.g. Giaretton et al. (2018). Research has demonstrated that the fibre textile mechanical properties are improved by impregnating the textile in epoxy resin as discussed in Leone et al. (2017), Donnini et al. (2016). Although coating is typically made from epoxy resin or epoxy vinyl ester

resin, bitumen is also being used.

The mesh size of the textile varies significantly as shown in Table 2.1. For instance, the mesh sizes employed for glass fibre textiles are typically in the range between 10x10 mm to 15x15 mm. The mesh size of carbon textile are usually in the range of 9.4x9.4 mm to 30x30 mm. The basalt textile mesh that has been employed in most studies is equal to 25x25 mm.

Table 2.1: Textile mesh sizes typically used in the literature

Mesh size (mm)	Material	Source
15.7x10.1	glass	Alecci et. al (2016)
12x12	glass	Raoof et. al (2017)
12x12	glass	Leone et. al (2017)
15x15	glass	
33x33	glass	
66x66	glass	
99x99	glass	
12x12	glass	
15x15	glass	Carozzi et. al (2017)
7.6x7.6	glass	
10x12.5	glass	
15x10.1	glass	
25x25	glass	
30x30	carbon	
10x10	carbon	
30x30	carbon	
10x10	carbon	
17.5x17.5	carbon	Padalu et. al (2018)
9.4x9.4	carbon	
20x20	carbon	
10x10	carbon	
10x10	carbon	Ombres et. al (2019)
10x10	carbon	
6x6	carbon	Alecci et. al (2016)
10x10	carbon	Raoof et. al (2017)
10x20	carbon	Carozzi et. al (2015)
12x12	carbon	
12x12	carbon	
17x12	carbon	
17x12	carbon	Al-Salloum et. al (2012)
10x10	carbon	
10x10	carbon	
25x25	basalt	
25x25	basalt	Padalu et. al (2018)
50x50	basalt	Raoof et. al (2017)
25x25	basalt	

The textile mechanical properties are characterised via tensile coupon tests. Ac-

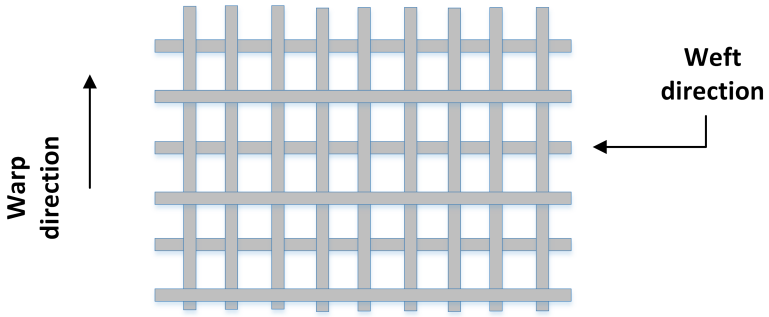

Figure 2.2: Typical grid configuration

cording to the literature, there is no specific standard for the material characterisation of textile fibre materials. To this point, two main types of tensile tests have been utilised, i.e. tensile tests on a single textile roving (SR) (Carozzi & Poggi 2015) and tensile tests on a textile mesh consisting of several rovings (Ombres et al. 2018).

Carozzi & Poggi (2015) conducted tensile tests on both single rovings and textile meshes according to EN ISO 10618/2005. The experimental results compare two test variants, namely single and multiple roving, are summarised in Table 2.2. The experimental result demonstrates a satisfactory comparison between single and grid rovings. Only PBO textile fibres demonstrated a higher variability in average maximum stress between single (3900 MPa) and multiple rovings (3397 MPa). The authors hypothesized that the different values of the ultimate strength are due to the non-uniform distribution of stresses in the four yarns.

Table 2.2: Tensile tests on single roving and grid strip (Carozzi & Poggi 2015)

Material	Tensile tests	Average failure stress (MPa)	CoV (%)
PBO-1 fiber	Roving	3900	3.2
PBO-1 fiber	Grid strip of width 4 cm (4 rovings)	3397	7.3
Glass fiber	Yarn in the warp direction	1233	2.7
Glass fiber	Grid strip of width 5 cm (3 yarns in the warp direction)	1121	1.3
Carbon fiber	Roving	1944	14.9
Carbon fiber	Grid strip of width 4 cm (4 rovings in the warp direction)	1913	10.4

Table A.1 in Appendix A summarises the main experimental results that have been reported in the literature from tensile tests conducted on textiles. It becomes evident that the geometrical layout of the specimens employed varies significantly. As also shown, the length of textile coupons ranges from 135mm to 330mm, whereas the

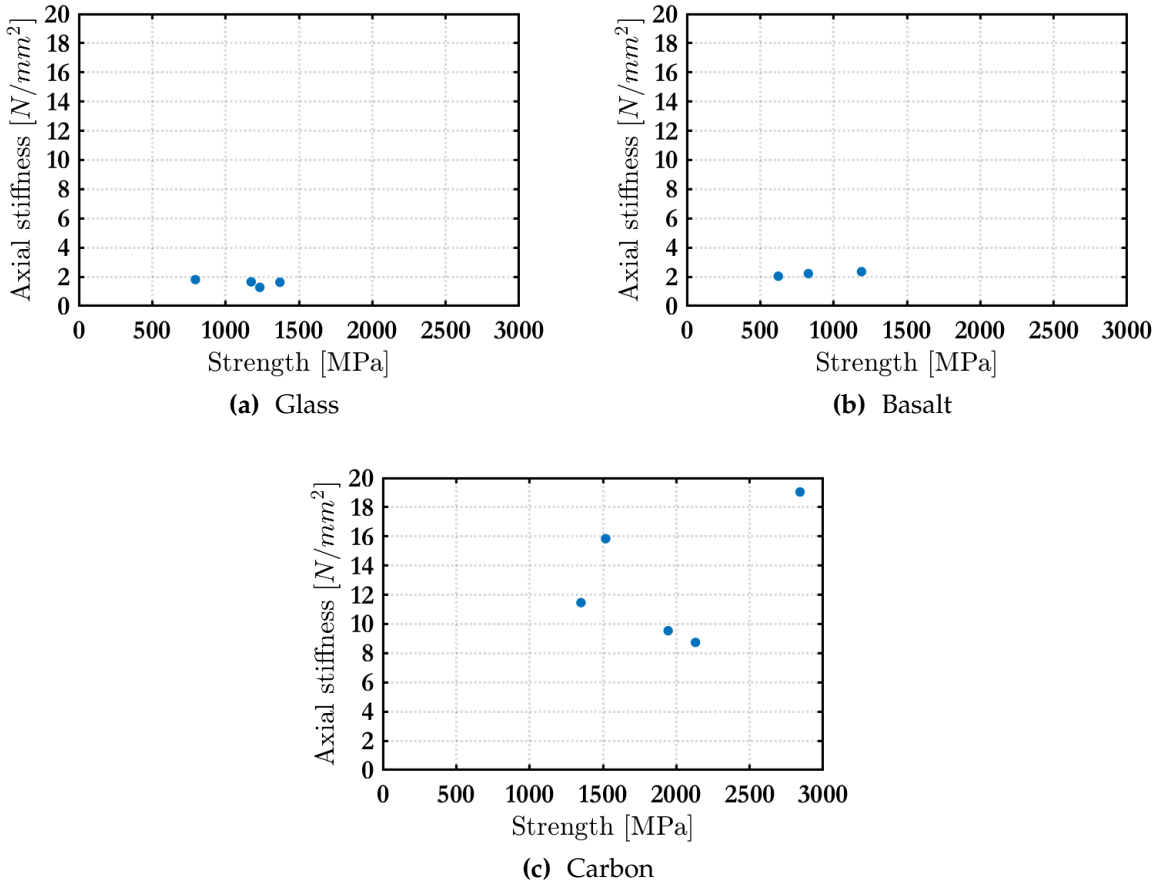

(a) Glass **(b)** Basalt

(c) Carbon

Figure 2.3: Axial stiffness versus strength based on the test results summarised in Table A.1

width of specimens lies in a range of 25 mm to 50 mm. In terms of instrumentation, the displacement in all tests was recorded using either LVDTs or extensometers. In all cases, to improve the gripping of the fabrics to the testing machine, two aluminium plates were bonded by an epoxy resin to the end of the bare fibers.

The axial stiffness of the textile material (also provided in Table A.1) is typically used as a means of comparing the mechanical properties of textiles with varying mesh sizes.

The axial stiffness of the each textile is evaluated as:

$$K_t = t_f \cdot E_f, \tag{2.1}$$

where (t_f) is the nominal thickness and (E_f) is the Young's modulus.

The nominal thickness (t_f) was estimated based on the equivalent smeared distribution of fibres and is defined as the ratio of the textile weight (per unit area) to the

density as shown in Eq. 2.2

$$t_f = \frac{\omega}{\rho}, \tag{2.2}$$

where (ω) is the weight of the textile and (rho) is the density of the fibre-textile.

In Fig. 2.3 the axial stiffness of the textile fibre materials provided in Table A.1 is plotted against the corresponding strength in three commonly used textile materials, namely glass, basalt, and carbon. The plots clearly demonstrate the sparsity of the measured strength in all cases of the materials examined. As expected, the carbon fibre textile material demonstrates the highest values of axial stiffness and strength. It is of interest to note that the corresponding measures for the glass and basalt fibre textile materials are practically identical, Fig. 2.3a, Fig. 2.3b.

2.2.2 Inorganic matrix

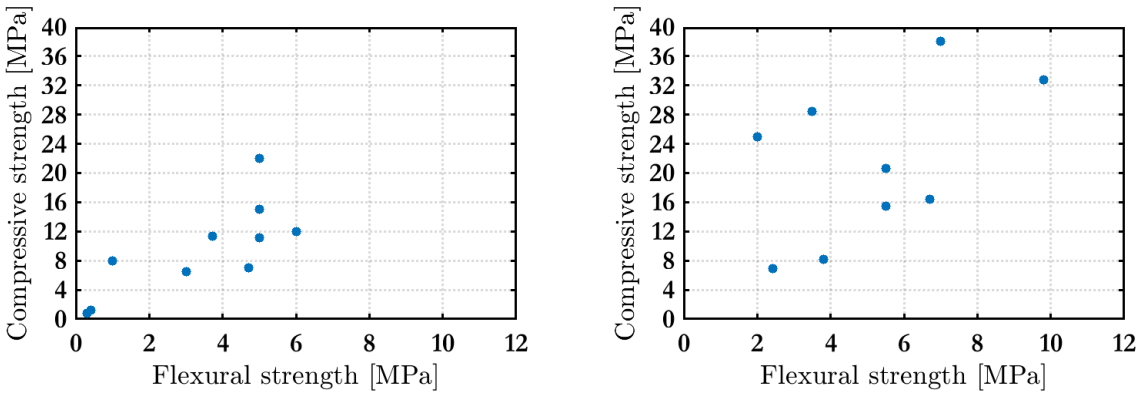

(a) Lime based mortar **(b)** Cement based mortar

Figure 2.4: a) Property of lime based mortar b) Property of cement based mortar

Textiles are usually bonded to the structural elements by lime, cement, or geopolymer mortars with thicknesses typical of a plaster layer. Compared to the FRP, the inorganic matrices do not provide the same adhesive property because the inorganic mortar cannot fully penetrate between the fibres filaments. This is because the dimension of the cement grain is too large in contrast to the mesh size of textiles. In Fig. 2.4a the relation between the compressive and the flexural strength is shown for the case of lime-based mortars. Similarly, Fig. 2.4b shows the compressive and flexural strength of cement-based mortars that were used as a matrix in TRM applications retrieved from the literature. It is noticeable on the graphs that cement-based mortars

demonstrates higher compressive and flexural strength compared to lime-based mortars. On average however the flexural strength ranges between 2 and 6 MPa in both types of mortars.

2.3 TRM bond tests under static loading

As in every strengthening solution, a key parameter in the effectiveness of the TRM is the bond between the composite material and the existing structure. This interfacial property has been often found to be the weak link in TRM strengthening, see, e.g. Carozzi et al. (2016), resulting in the under-utilisation of the textile fibre material, which is the most expensive part of that rehabilitation technology (Kouris & Triantafillou 2018).

According to the Recommendation of RILEM Technical Committee 296250-CSM (De Felice et al. 2018) there are six failure modes vis-à-vis the bond between TRM and masonry as shown in Fig. 2.5: (A) cohesive debonding in the masonry; (B) debonding at the matrix-to-substrate; (C) debonding at the textile-to-matrix interface; (D) sliding off the textile within the matrix; and (E1/E2) tensile rupture of the textile (meaning partial or complete rupture of one or more fibre yarns).

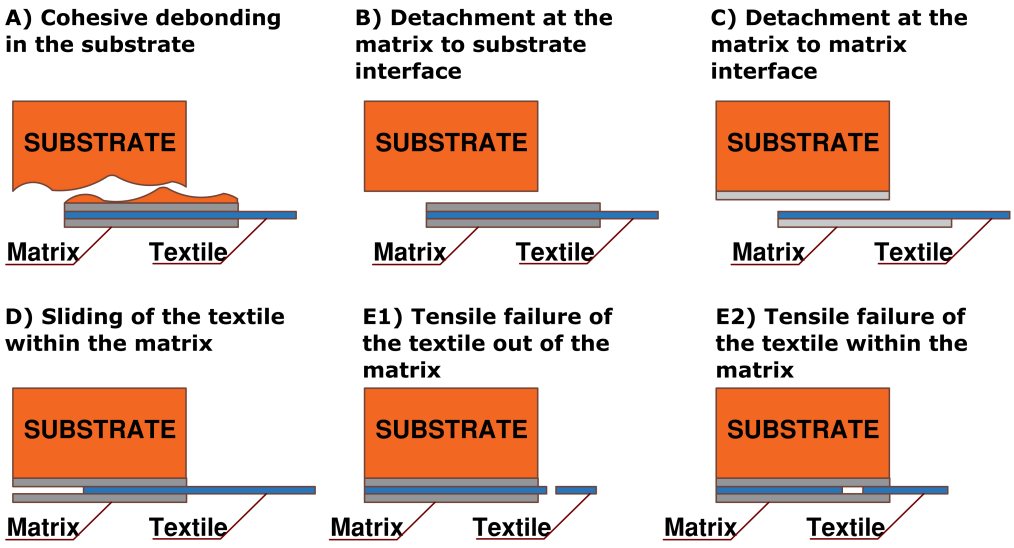

Figure 2.5: Failure modes (De Felice et al. 2018)

Bond tests are used to characterise the shear bond performance of TRM to masonry. To this end, a significant number of experimental and analytical investigations

have been performed to examine the mechanics governing the TRM to masonry interface, see, e.g., Carozzi & Poggi (2015), Ghiassi et al. (2016), Dalalbashi et al. (2018), Leone et al. (2017). Consistent with experiments performed in polymer based composites, two test setups have been primarily utilised, i.e., single- and double-lap tests. In common the single-lap test setup is more widely utilised in the literature as this test is easier to conduct compared to the double-lap see, e.g., Leone et al. (2017), Lignola et al. (2017) Fig. 2.6. Mostly this is related to the specimens preparations, the double-lap test sample must have an ideal symmetry of TRM to masonry bond from both sides. Sneed et al. (2015) compared between single-and double-lap shear tests on reinforced concrete specimens strengthened with PBO-TRM. According to their findings, the idealised load responses of single- and double-lap shear tests are similar until the peak load is reached. However, in the double-lab test, debonding did not occur symmetrically at the same time on both sides, which resulted in slightly decreased values of the maximum load compared to the similar values of the single-lap test configuration. Given this, the authors further concluded that the double lap test setup is not valid to describe the post-peak response of the bonded composite (especially the global slip) unless simultaneous debonding occurs and perfect symmetry is maintained. However, the drawbacks of the single lap test setup as pointed out in extensive experimental campaigns, on glass, carbon and basalt textile materials which were conducted across numbers of European laboratories is the bond test results are significantly affected by the equipment used in the laboratory practices e.g., Leone et al. (2017), Lignola et al. (2017), Carozzi et al. (2017).

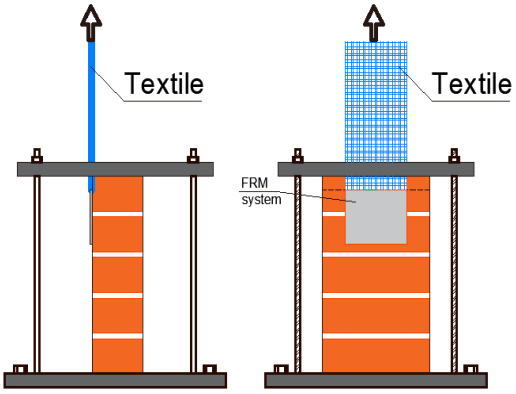

(a)

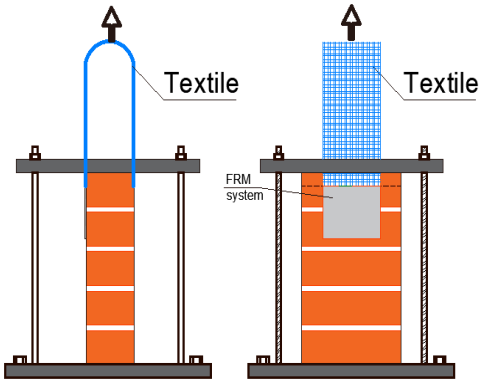

(b)

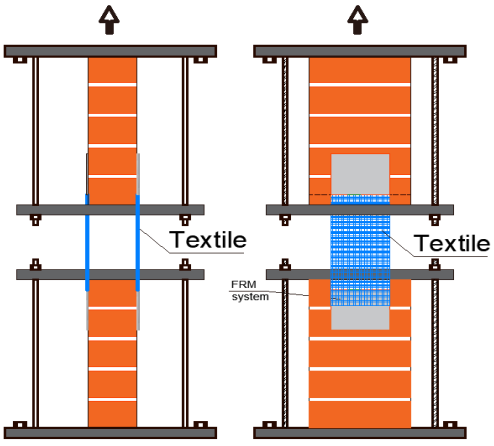

(c)

Figure 2.6: Bond test setup used: (a) single test set-up; (b) double test set-up; and (c) double-lap test set-up

2.3.1 Tests conducted on glass fibre textile reinforced mortars

The most widely utilised textile material for the TRM strengthening system is glass. Giaretton et al. (2018) considered the case of three directional glass fibres, namely vertical (principal)—V, horizontal—H, diagonal—D to investigate the TRM to masonry bond . The anchorage length and width was 200 mm and 50 mm, respectively. The maximum load observed from the tests were 0.915 KN (COV 24%) for the V and H–glass direction and 0.851 KN in the N direction. The failure mode observed in all cases was textile rapture. Maroudas & Papanicolaou (2017) examined the bond behaviour between the masonry and TRM strengthening with alkali-resistant (AR) glass fibre textile. A single-lap test setup was used and the bond length varied from 50 mm to 200 mm. In general, the failure mode observed was slippage of the fibres at the textile to matrix interface in all specimens. The reported failure mode of the highest bond length (250 mm) was slippage and fibre rupture. The maximum applied load was found to increase by increasing the bond length up to 200 mm and then remain constant. Hence, the effective bond length was determined to be 200 mm.

Carozzi et al. (2014) investigated the bond behaviour between masonry and glass TRM for three bond lengths, namely 50 mm, 100 mm, and 150 mm. They used a push-pull double-lap test setup. Two mortar types were used, i.e. cement and lime-based. In the case of cement mortar, the failure mode observed in the shorter bond length was slippage of the textile out of the matrix. Conversely textile rupture occurred for the longer bond length. Increasing the bond length was accompanied by increasing maximum load and the effective bond length was determined to be 150 mm. For the case of the lime based mortar, debonding occurred at the 100 mm bond length and textile rupture at the 150 mm bond length, similar to the cement based mortar.

A thorough study with regards to the glass fabric cementitious matrix to masonry bond mechanism was conducted by Leone et al. (2017). The authors conducted an experimental program involving 11 glass textiles that were tested using both double and single lap shear test setups. Three of the glass textile were coated with epoxy vinyl-ester resin. The textiles used had different mesh sizes, weight per area, and Young's modulus as shown in Table 2.3. The masonry walls comprised five bricks joined with a mortar width of 10 mm, 260 mm bond length was used in the experimental cam-

Table 2.3: Bond test results from(Leone et al. 2017). failure mode notation corresponds to the defintions provided Fig. 2.5

FRCM type	Bond length, width (mm)	Mesh size (mm)	L_{max} (KN)	Slip at peak (mm)	Failure mode
A	265Lx100w	15x15	1.19(25)*	0.75(22)*	D-E1-E2
B-33	260Lx100w	33x33 (coated)	4.7(23)*	0.31(39)*	A-E2
B-66	240Lx140w	66x66 (coated)	14.7(16)*	4.34(20)*	A-D
B-99	120Lx30w	99x99 (coated)	7.4(15)*	0.96(59)*	-
C	260Lx60w	12x12	2.8(8)*	0.70(37)*	D
D-1	260Lx100w	15x15	1.1(14)*	0.01(25)*	E1
D-2	260Lx40w	7.6x7.6	0.6(16)*	0.44(57)*	D
E	260Lx75w	n/a	2.1(7)*	2.17(19)*	E1-D
F	260Lx40w	10x12.5	1.5(8)*	1.27(17)*	D
G	260Lx100w	15.7x10.1	3.0(9)*	4.58(29)*	E2-D
H	260Lx125	25x25	1.9(28)*	1.19(62)*	E1-D

*Coefficient of variation [%]

paign, and the width of the textile varied from 30 mm to 140 mm. Furthermore, ten different types of mortar were used. As clearly shown from the results (Table 2.3), the maximum applied load greatly varied with the properties of the textile material employed in each case. The highest recorded value was for the case of FRCM impregnated with epoxy-vinyl ester resin of a 33 x 33 mm mesh size and a bond length of 240 mm width of 140 mm. The maximum applied load was equal to 14.7 kN (University of Perugia) and 16.4 kN (University of Triest). The failure mode observed was textile debonding at the University of Perugia and slippage and debonding at the University of Triest. The lowest value recorded corresponded to the uncoated glass specimen with a mesh size of 7.6 x 7.6 mm at a bond length of 260 mm and width of 40 mm. This was equal to 0.6 kN, with the corresponding failure mode being textile slippage within the matrix.

The results of this study clearly demonstrated the high variability of the bond performance and failure mechanisms of glass TRM materials with different geometrical and mechanical properties. It further demonstrated that the high variability persists even for the case of similar textiles tested in different laboratories, see, e.g., A, E, H at Table 2.3. This is a clear indication on the necessity for conducting furhter experimental testing to identify and understand the mechanics of the bond.

2.3.2 Tests conducted on carbon fibre textile reinforced mortars

Ombres et al. (2018) have investigated the bond between masonry and a carbon textile reinforced mortar. The authors conducted a series of direct shear tests with a single layer of the carbon TRM varying the bond length of 150 mm, 200 mm, 250 mm,and 300 mm. An uncoated carbon textile with a mesh size of 10 mm in both directions was used. The mass density and equivalent thicknesses are 168 g/m^2 and 0.047 mm. Brick masonry walls comprised a set of six clay bricks with the dimension of 250x120x55 mm stacked together. Four LVDTs used to measure displacement. The first two LVDTs were placed on the bonded front side of the brick wall to the measured displacement of the aluminium T-shaped plate fixed on the carbon textile at the end of the bonded area. The remaining two LVDTs were used to measure the displacements of the masonry units in correspondence to the loaded end. The failure of the tested samples was textile slippage within the matrix for all tested models. The failure occurred out of the textile-to-matrix interface, while the mortar matrix was not affected in the failure mode. According to the authors, the bond length affected the failure mode. Particular specimens with the shortest bond length of 150 mm had substantial fibre-to-matrix slippage at the loaded end. Samples with the highest bond length 300 mm the large fibres/matrix slip observed after crack development in the midspan. The bond length of 200 mm and 250 mm had a combined failure mode. The matrix interface persisted fully bonded to the masonry walls in all tested specimens.

D'Ambrisi et al. (2013) used a double-lap bond test to investigate the bond between masonry to carbon FRCM material. The investigated parameters were the bond length, namely 110 mm, 230 mm, and 350 mm. The failure mode detected was cracking of the mortar matrix followed by the slippage of the textile. According to the authors, the effective anchorage length was equal to 110 mm; increasing the bond length up to 350 mm did not increase the maximum load.

Carozzi et al. (2017) investigated the response of carbon fibre textile on a single-lap test setup using different textile mesh sizes and a constant bond length of 260 mm. Various failure modes were observed; slippage of the textile within the matrix and textile rupture were the most common. In some cases, debonding at the matrix-textile interface and cracking of the external layer of mortar were also noted. The

data collected in this study provides a better understanding of the bond behaviour of carbon TRM materials with masonry structures. However, the different failure modes that occurred among specimens of the same group in most cases (C-FRCM_1, C-FRCM_2, C-FRCM_3, and C-FRCM_4) demonstrate the need for further investigation experimental work to establish standard procedure between carbon TRM and masonry substrate.

2.3.3 Tests conducted on basalt fibre textile reinforced mortars

With regards to the bond behavior of basalt FRCM, Lignola et al. (2017) presented an extensive experimental campaign, which was conducted across 10 European laboratories. The campaign comprised a series of single-lap direct-shear tests. Four different types of FRCM system were used. The basalt textiles had a yarn spacing of 6 mm, and 25 mm. The textile weight varied from 220 g/m^2 to 350 g/m^2. The bond length in all cases was equal to 260 mm, and the width was in the range of 50 mm to 125 mm. The test results has a high scatter with regards to the slip at a maximum applied load (COV higher than 50 %). Similar trends were observed in the corresponding strengths. This further supported the argument raised by Leone et al. (2017) that even for the same typology of test setup and specimen layout, the bond test results are significantly affected by the equipment used the laboratory practices. However, from the data collected Lignola et al. (2017) were able to assert that when the bond is good, i.e., when the peak stress of bonded fibres is similar to the peak stress of the composite in tension and hence the failure mode is fibre rupture, the scattering tends to decrease. Conversely, when the failure mode shifts to fibre slippage, the scatter increases.

Barducci et al. (2020) also investigated the bond performance of basalt TRM to masonry using both single- and double-lap shear tests with the objective of examining the effect of the matrix strength on the bond strength. For that purpose they considered the following types of mortar, i.e.,

(i). Commercial lime mortar matrix (MK);

(ii). Cement mortar matrix mixed in the laboratory (MC);

(iii). Lime mortar matrix mixed in the laboratory (ML);

(iv). Cement-lime mortar matrix mixed in the laboratory (MCL).

A constant anchorage length used was across all specimens equal to 220 mm. The textile width was 95 mm. Two main failure modes were observed depending on the test setup. In particular, fibre rupture out of the matrix was observed in all single-lap tests. Conversely, textile slippage was observed in all double-lap tests with the exception of double-lap specimens strengthened with the MK mortar. In this latter case, the specimens failed due to textile rupture. The authors concluded that the better bond performance showed by commercial lime mortar, i.e., the highest load values with the lowest COV.. Contrary to the worst result represented by cement-lime mortar matrix-based FRCM, i.e., lowest load values and consistent COV.

2.3.4 Comparative studies on the effect of the textile material

Ascione et al. (2015) investigated the bond behaviour between TRM and masonry units when strengthened with four textile types, namely basalt-steel, carbon, glass-aramid, and steel textiles impregnated in two mortar matrices such as fibre-reinforced pozzolan cement mortar and a mineral-natural hydraulic lime. Moreover, three variants of substrates, such as modern clay bricks, historic clay bricks, and tuff units, were used in this study. The bond length in all shear bond tests was 200 mm. Different failure modes were observed in each textile material. Specimens with basalt textile fibres failed due to textile rupture out of the matrix. Carbon textile failed due to the slippage of the textile, whereas glass-aramid due to rupture within the bonded length. Debonding of the mortar matrix occurred in the case of cement-based mortar strengthening with steel textile mesh. In the case of lime-based mortar, debonding occurred in the textile to matrix interface.

De Felice et al. (2014) investigated the bond behaviour between masonry and TRM in the case of several textile materials, namely carbon (CTRM), steel-reinforced grout (SRG), and basalt (BTRM). Both single and double lap tests were performed. The bond length in the study varied in a range of 55 to 440 mm and the bond width from 40 mm to 100 mm. The total TRM thickness was 6–7 mm. The failure mode of the basalt textile material shifted from debonding at the substrate mortar interface in the shortest bond length to textile slippage within the matrix at the longest bond length.

Inevitably, the increase of the bond length did not result in significantly improving the maximum load. Different failure modes depending on the bond length were also observed in the case of CTRM. The shortest 55 mm and 110 mm bond length failed due to sliding of the fibres within the matrix. Conversely, the longest bond length, 220 mm, resulted in debonding at the fiber-matrix interface. The medium bond length of 165 mm gave rise in a combined failure mode i.e., debonding and sliding the fibres within the matrix. Therefore, the effective bond length, in this case, was higher than 165 mm. The SRG strengthening specimens failed due to debonding at the substrate to matrix interface. Thus, the effective bond length in SRG was found to be 220 mm, which is higher than carbon textile material.

Alecci et al. (2016) experimentally investigated the bond behaviour of cement-matrix-based composites (CMCBC) reinforced with three different textiles, namely carbon, polybenzoxazole (PBO), and glass using the double-shear test setup. Three bond lengths were considered, i.e., 150 mm, 200 mm, and 250 mm. According to the test result, increasing the bond length did not influence the maximum load in carbon and PBO textile materials. Therefore, the effective bond length was determined as to be equal to or less than 150 mm. On the contrary, the specimens strengthened with glass textile demonstrated an effective bond length between 150 mm and 200 mm. It is interesting to note that even though the carbon textile materials attained the maximum load amongst all materials, the exploitation ratio (stress from textile coupon test divided to stress from bond test) lay in the range from 56% to 58%. On the other hand, the glass textile had the lowest maximum load and the highest exploitation ratio from 94% to 98%. The authors concluded that, in all of the three composites, the debonding phenomena occur at the fiber-matrix interface, after tensile cracks in the matrix and fiber-matrix slip happen.

Carozzi & Poggi (2015) also conducted a thorough comparative study on the bond performance of different textile fibre materials, i.e., glass, carbon,PBO, glass PBO (PBO-G) using a push-pull double-lap test setup. In the glass fibre textile material applied, the increased bond length resulted in increasing the maximum applied load and the effective bond length equal to 150 mm. The failure mode was manifested as textile slippage in 50 mm and 100 mm bond length and shifted to textile rapture when the bond length increased to 150 mm. The proposed failure mode of specimen

strengthening with carbon textile was slippage between the mesh to matrix interface. The maximum load did not influence the bond length in the case of carbon FRCM. Moreover, the bond length was not influenced by increasing bond length in terms of PBO composite, and the failure mode identified as a progressive failure of the rovings. When the hybrid textile combination used, glass and PBO resulted in the lowest maximum applied load compared to bare PBO. Furthermore, the failure mode stated was the rupture of glass textile followed by partial rupture of PBO textile.

2.3.5 The effect of coating of the textile material

The application of epoxy resin coating on the textile fibre material has been found to increase the rigidity of the textile and eliminate the slippage among the filaments. Consequently, the contact contact between the matrix and the fibres has been found to considerably improve, see, e.g., (Donnini et al. 2016, Kariou et al. 2018).

Donnini et al. (2016) examined the effect of coating on the bond of carbon textile reinforced mortars to masonry. Varying pre-impregnation strategies were considered, namely: dry fabric (Dry), light impregnation (L), medium impregnation (M), and high impregnation (H) as shown in Fig. 2.7. Furthermore, the layer of the quartz sand applied to the textile after the coating impregnated in the three-level light (L), medium (M), and high (H). The bond length used in the experimental campaign was equal to 150 mm. The mesh size of the textile was 20 x 20 mm. The weight of the dry textile was 180 g/m^2. The application of light, medium, and high coating increased the weight by 36 %, 82%, and 205%, respectively. In addition, the application of light, medium, and high quartz sand layers increased the weight of the dry carbon by 390 %, 455 %, and 1000%, respectively. In total, 70 samples (with a dimension of 410 x 60 x 10 mm) were tested, for the tensile test using a clevis grip system, as described in Annex A of AC434, and 21 double-lap shear tests were performed (3 identical samples were used per variant). The failure mode for most samples was slippage fibres of the matrix. This was not the case for the high impregnation of the epoxy resin and epoxy resin with sand was slippage and failure of the matrix out of the bonded area. The authors concluded that the utilisation of the epoxy resin has the potential to significantly improve the mechanical performance of the FRCM strengthening system. However, coating of the textile may negatively affect the ease

of applying the FRCM.

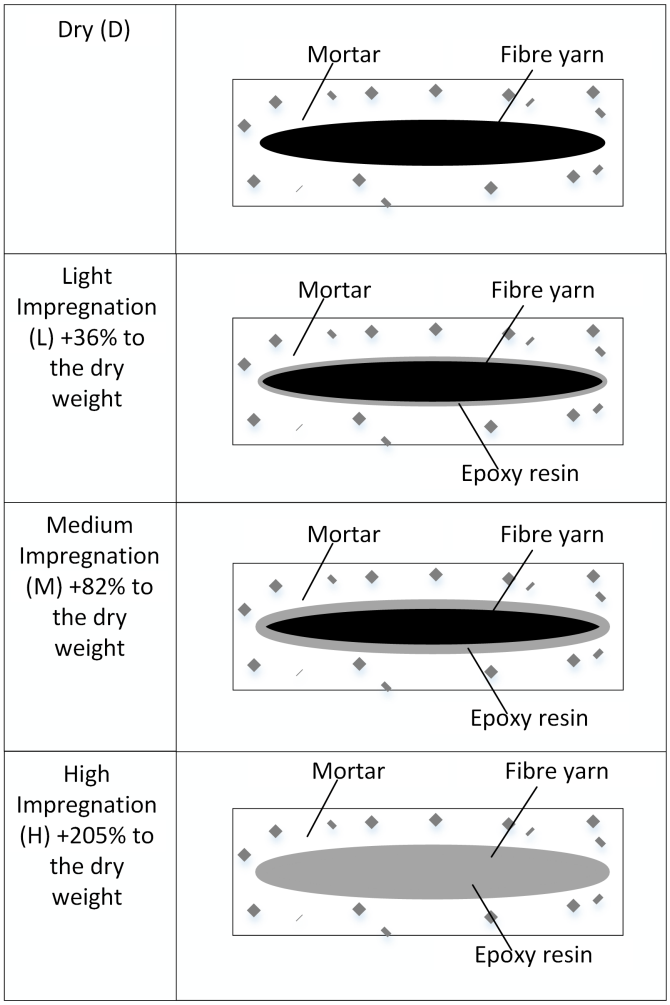

Figure 2.7: Schematic representation of the fabric sections depending on the impregnation treatment

2.4 A critical reflection on the results of quasi static bond tests

Based on the literature review, the three primary parameters, such as textile materials, mortar matrix, and adhesion between TRM and masonry elements, significantly affected the bond between TRM and masonry substrate.

An appropriate exploitation ratio (tensile coupon test result to bond test result) was obtained in basalt textile materials (80%) in most studies Fig. 2.8 (Maroudas & Papanicolaou 2017, Leone et al. 2017, Alecci et al. 2016). Therefore the basalt textile is most suitable to work with lime-based mortar, which is compatible with strength-

ening cultural heritage buildings. On the other hand, in literature, the bond between TRM and in house coated glass textile was not investigated, despite the fact it has a good case of strengthening masonry structures (Kariou et al. 2018). Carbon textile reinforced mortar (CTRM), in most cases, has a lower exploitation ratio compare to the basalt and glass textile Fig. 2.8. On the other hand, CTRM has the highest bond strength. Therefore, carbon textile can be more suitable for strengthening masonry bridges where structures subjected the high load. Based on the literature, the main limitation of basalt textile reinforced mortar (BTRM) is the mesh size of the textile; in most cases, it is 25x25 mm or more Table 2.1.

Taking into account that textile materials have a different equivalent thickness de Felice et al. (2020) suggested that more useful to compare TRM system to load per unit width corresponding to bond (f_b) failure. In Fig. 2.9 the average maximum load per unit width in shear bond tests for the case of glass TRM is shown.

As seen from the bar chart, the results demonstrate a significant variability. It points out that the further developments among single and double-lap test setup due to different accuracy in the misalignment of all the rovings concerning the loading direction demonstrate the need for further experimental work to establish a standard procedure between glass FRCM and masonry substrate. Moreover, the different failure modes occurred among specimens of the same group in some cases (e.g., group A, E, H) (Leone et al. 2017).

The Fig. 2.10 shows the direct comparison between de Felice et al. (2020), Donnini et al. (2016), Ombres et al. (2018),D'Ambrisi et al. (2013), Alecci et al. (2016) in case of carbon textile, where f_b maximum applied load in direct bond test divided by unit width. In the case of, the number after the names represents the bond lengths of the tested specimens.

As mentioned above, Donnini et al. (2016) (Fig. 2.10) experimentally investigated the carbon fibres with different coating levels. This is indicative that the coating of the textile could considerably enhance the bond property of bare textile. The result shows that the light impregnation improves the bond property by 9.4 %, whereas medium and high epoxy resin coating by 76% and 75%, respectively. The quartz sand impregnation on fabric after coating also shows a positive result, i.e., 36%, 55% and 117% for the light (LS), medium (MS) and high(HS) impregnation. In addition to different

types of coating on carbon fibre textile, Donnini et al. (2016) reported that only a single bond length of 150 mm was used. A failure mode of slippage of the textile within the mortar combined with textile rupture was observed. Therefore, additional studies on the in-house epoxy resin coated composite need to be conducted using different bond lengths, textile materials, levels of impregnation to provide further results in terms of failure mode and effective bond length.

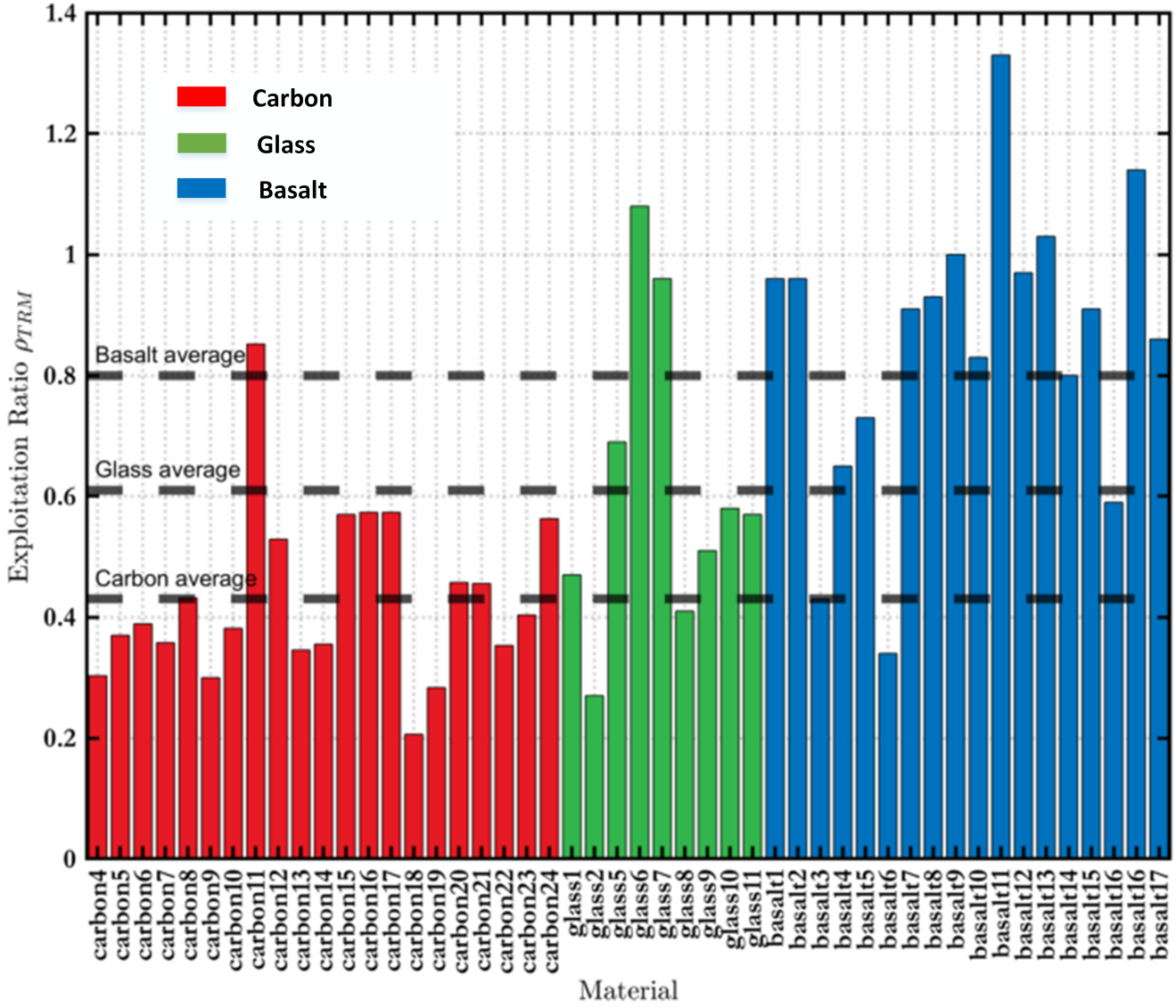

Figure 2.8: Exploitation ratios per textile fibre material from the experimental data provided in Table A.2

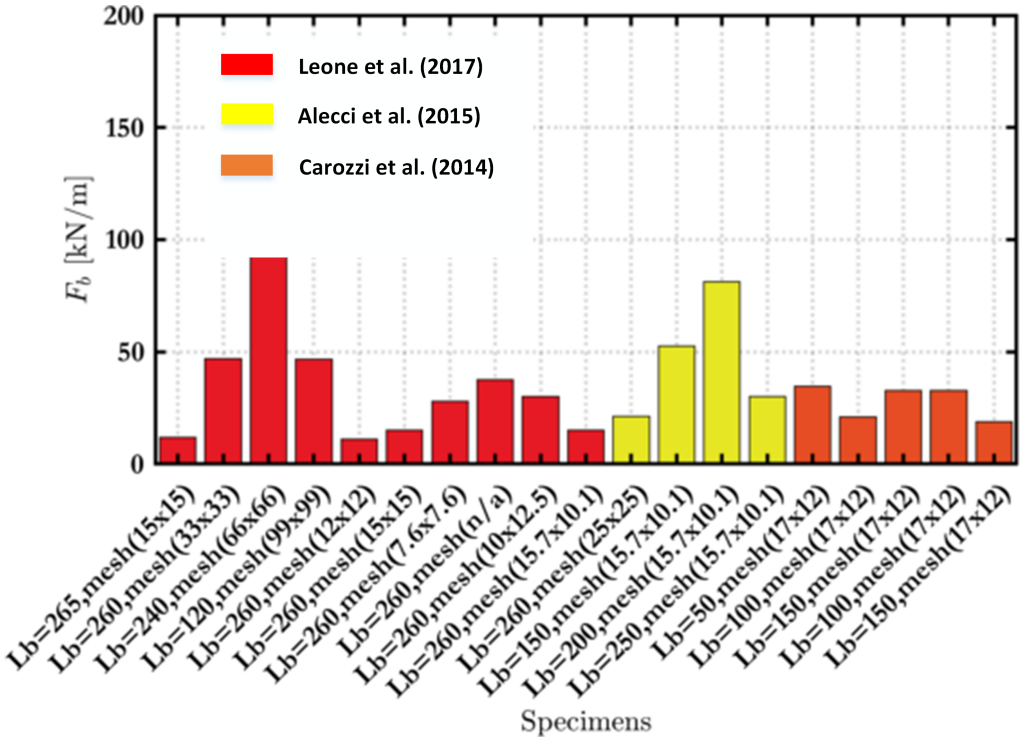

Figure 2.9: Glass fibre textiles: Average maximum load per unit width from the bond tests provided in Table A.2

The bond between carbon textile reinforced mortar was investigated in several studies Ascione et al. (2015), D'Ambrisi et al. (2013), Alecci et al. (2016), Donnini et al. (2016), De Santis et al. (2018), Ombres et al. (2018). According to the studies, the common failure modes are slippage of the textile. However, different failure patterns appear, such as textile rupture see Carozzi et al. (2017) where, in some cases, the textile rupture occurred. It is interesting to note that the exploitation ratio in common in range between 40% to 60 % Alecci et al. (2016) or lower Carozzi et al. (2017). The carbon textile property can be improved significantly by applying an in-house epoxy resin coating. At this point, the effect on epoxy resin treatment of carbon textile by different coating only reported in Donnini et al. (2016). However, the bond length effect has not investigated; only 150 mm used. A failure mode of slippage of the textile within the mortar combined with a textile rupture observed. Therefore, in future research, the effect of the epoxy resin treatment, bond length, and the different mortar needs to be conducted to determine the failure mode's effective bond length and the mortar fitting.

The bond behaviour between masonry and basalt textile reinforced mortar was investigated in several studies De Felice et al. (2014), Lignola et al. (2017), Barducci

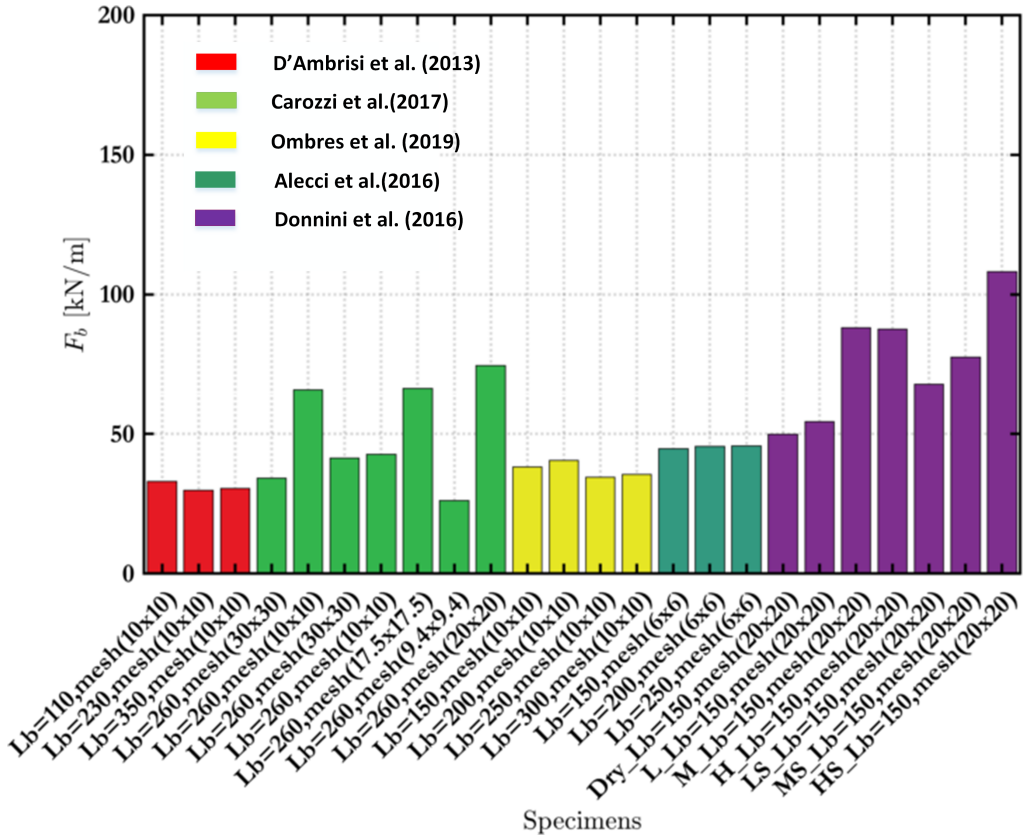

Figure 2.10: Carbon fibre textiles: Average maximum load per unit width from the bond tests provided in Table A.2

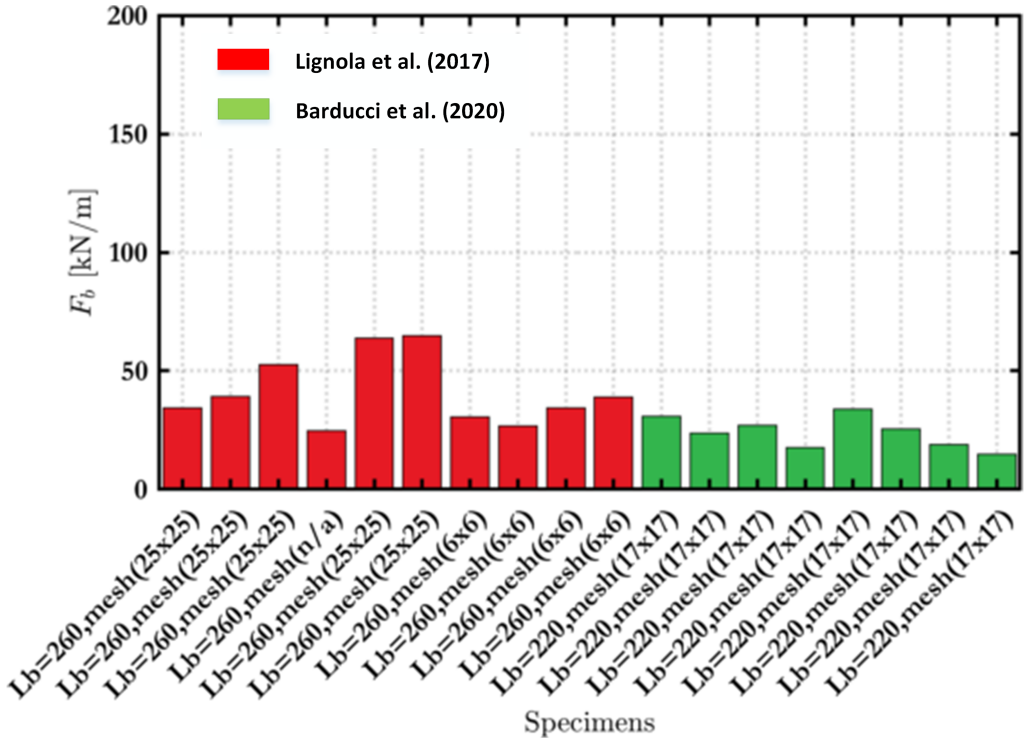

Figure 2.11: Basalt fibre textiles: Average maximum load per unit width from the bond tests provided in Table A.2

et al. (2020) Fig. 2.11. According De Felice et al. (2014)) the failure mode of basalt textile was inconsistent and depending on the anchorage length. However, the effective bond length was not derived. Lignola et al. (2017) conducted extensive experimental work with different types of basalt textile using a constant bond length equal to 260 mm. Barducci et al. (2020) performed an extensive experimental investigation on different types of strengthening mortar matrix using the bond length equal to 220 mm and both single- and double-lap shear tests setup. Therefore, more studies are required on basalt textile to TRM bond behaviour to investigate the bond length influence to provide different results regarding failure mode and effective bond length.

2.5 Bond behaviour under fatigue loading

Fatigue is a type of failure that occurs in materials subjected to dynamic and cyclic stresses (Ahsan 2014). In general, in literature, three common forms of fatigue is recognized: high cycle fatigue (HCF), low cycle fatigue (LCF) and thermal-mechanical fatigue (TMF). If the P_{max} in a load cycle is less than 50% of the static failure load, the test is assumed to be performed under high-cycle fatigue conditions. On the other hand, if P_{max} is greater than 50% of the static failure load, the test is performed under low-cycle fatigue conditions (Carloni et al. 2012). If temperature changes result in considerable thermal expansion and contraction and thus significant strain excursions are assumed to be TMF conditions (Campbell 2015).

In general, in fatigue loading conditions, failure occurs due to fatigue at stress levels much lower than the yield strength of material for a static case. Minor flaws or cracks are present internally or externally on the body. At these flaws, the level of stress is very high due to stress concentration. As a result, cracks can grow at these flaws under the cyclic loadings due to plastic deformations, even if applied normal stresses are lower than the elastic limit. The undamaged structure cannot withstand the applied load when the crack length becomes large due to the reduced stress resisting area. Consequently, this causes a very rapid crack growth resulting in a sudden failure of the structure (Naik et al. 1993).

Contrary to the case of static loading, the TRM to masonry bond under cyclic or fatigue loading has not received much attention to this point. Indeed, the majority of

the, very recent, investigations have primarily focused on the FRP or TRM to concrete bond under fatigue loading conditions. However, as already indicated in Chapter 1, the assessment of the fatigue life is of particular importance when considering strengthening applications of critical infrastructure such as masonry bridges.

2.5.1 Fiber reinforced polymers

Carloni et al. (2012) performed single-lap bond tests to investigate the fatigue bond behaviour between concrete substrate and FRP. The FRP composite comprised continuous unidirectional carbon fiber sheets in a two-part thermosetting epoxy matrix. The anchorage length was equal to 152 mm. Before the fatigue tests, the four specimens were tested under static load up to the failure, to determine P_{crit}. The P_{crit} was determined as the mean value of the load of four tests. Then the fatigue test was performed. The load ranges of the fatigue test chosen of 60%, 70% and 80% of the average value of the quasi-static test result. Fatigue cycling performed in load control at 1 Hz. Their results indicated a significant decrease in the interfacial bond stiffness during the fatigue tests. The high-stress fatigue life (80%) dominated by crack initiation, whereas lowering load range (60%) by crack propagation.

Zheng et al. (2015) also investigated the FRP to concrete bond under fatigue loading. However, in their study they opted for a double-lap test setup. Furthermore, they examined the effect of temperature and humidity variations on the bond strength. The specimens were strengthened with a carbon fiber laminate (CFL). The experimental study was carried out at three fatigue load levels, namely 60%, 70%, and 80%. Three specimens were tested under static loading conditions to determine P_{crit}. The specimens were first subjected to pre-treatment in an environmental chamber in a simulated environment with constant temperature and relative humidity (RH) (60 C, 95%). The authors concluded that the hygrothermal environment adversely affects the bond behaviour between FRP and concrete interface; the fatigue life after treatment is significantly shorter than that of the untreated specimens. In a higher P_{crit} level, namely 80%, the maximum decrease of fatigue life observed by 76.9%. The P_{crit} value is highly affected by the number of cycles to failure. The failure mode was FRP debonding, which is occurred in the substrate of concrete.

2.5.2 Textile reinforced mortars

The previous researchers in their works of the TRM fatigue behaviours mainly focused on the strengthening perspective and general effectiveness of the TRM strengthening technique. Aljazaeri & Myers (2017) investigation of the strengthening Reinforced Concrete (RC) beams under fatigue life went through the 2000000 cycles and then subjected beams monotonic post fatigue loading.

To improve the comprehension of TRM composite materials service life under cyclic loading, investigated with attention on fatigue tests that represent the seismic activity. Mesticou et al. (2017) have studied the fatigue performance of the TRM tensile coupons reinforced with two types of fibres glass mesh size of 3 x 5 mm and carbons (7 x 7 mm and 4 x 4 mm). Each sample subjected to 100 cycles of fatigue life under 60 % and 80 % of the maximum load. The authors concluded that the stiffness during the loading cycles increases with increased fatigue load. Mesh have not high effect on the fatigue life. The monotonic test shows the elastic performance in the global and macroscopic performances, which are not affected by cyclic loading, under such experiments where the bond performance of the TRM strengthening system, not the primary case. The authors concluded understanding the bond failure mechanism of the TRM and masonry surfaces under fatigue load quite complicated.

D'Antino et al. (2015) have investigated the bond behaviour of FRCM composites and concrete substrate under fatigue and post fatigue behaviour. In this case, the single-lap direct-shear test set-up used. The fatigue load protocol was determined to investigate the effects of different frequencies and different load ranges. The concrete blocks used were 125 mm deep, 125 mm wide, and 375 mm long. The bonded length and width were 330 mm and 60 mm. Three different frequency rates used in the experimental tests, namely 1 Hz, 3 Hz, and 5 Hz. In addition, three different load ranges were used, namely 20–50%, 35–65%, and 20–65% (D'Antino et al. 2015). The failure type of the specimens under fatigue load is different from the quasi-static monotonic loading. In particular, the specimens subjected to the fatigue load failed due to the rupture of some fibers filaments within the bonded length. On the other hand, the fibre rapture in the quasi-static monotonic condition was subjected only to limited numbers of specimens observed in previous work.

Calabrese et al. (2020) investigated the effect of PBO fibre-reinforced cementitious matrix FRCM composites externally bonded on the concrete prism under fatigue loading. The concrete prisms had nominal dimensions equal to 150x150 mm cross-section and 500 mm length. The P^f_{min} and P^f_{max} in fatigue cycles were equal to 25% and 50% of the average peak load of the quasi-static monotonic tests, respectively. The specimens subjected to the fatigue load failed due to matrix-fiber debonding and eventual rupture of the fibers at the strip loaded ends. The authors concluded that the failure mode observed is debonding at the matrix-fibre interface, highlighting the importance of matrix to fibre bond properly.

Researchers concluded that the FRCM system has excellent fatigue behaviour. Notable that all researchers highlighted the need to investigate further the fatigue performance of substrate (RC or UM) strengthened with various modified FRCM reinforcement ratios needs to be conducted. Bond behaviour between TRM and substrate is an important aspect in strengthening configurations, and further investigation needed to investigate the bond performance.

2.6 Analytical modelling of the TRM to masonry bond

According to the literature, several local bond-slip analytical models exist that simulate the TRM (or FRP) to masonry interface properties, e.g., Yuan et al. (2004, 2012), D'Antino et al. (2014), Grande et al. (2018), Bertolesi, Milani & Poggi (2016), Bertolesi et al. (2014), Milani et al. (2021). Two models are often utilised, i.e., the bilinear model and an exponential model.

According to the researchers, the bilinear model represents the adherence bond of FRP strengthening with good approximation. The exponential model has better coverage of the real behaviour of the strengthening due to the softening branch given the viscosity of the cement matrix (Ombres et al. 2018). According to the bilinear model, the bond-slip law is linear until the bond shear stress reaches the peak stress τ_f, at where the s_f is the corresponding slip value Fig. 2.12a. The development of the micro-cracks is causing the linear decreasing of the bond shear stress with the interfacial slip producing the interfacial softening. The shear stress is diminished to zero when the slip is higher than s_0, signalling that the shear fracture (or debonding

or macro cracking) of a local bond element. As in the bilinear model, the residual stress after debonding lacks the friction and aggregate interlock over the debonded length of the joint is negligible.

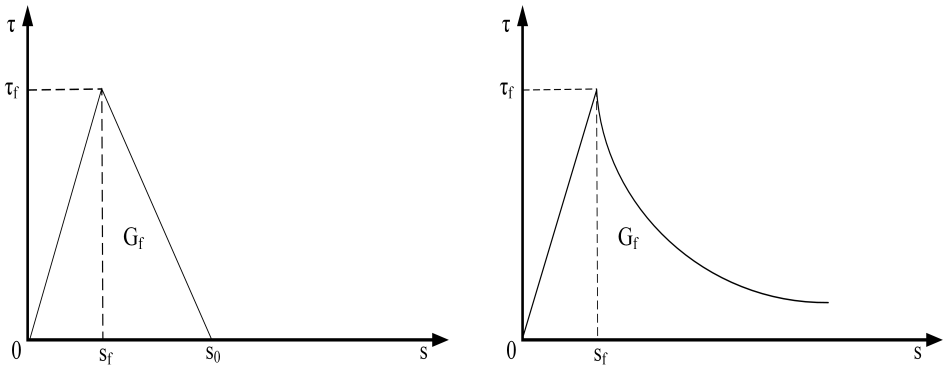

Figure 2.12: Local bond slip models: (a) bilinear; and (b) exponential (Ombres et al. 2018)

The differences in the exponential model, after the linear relationship between the shear stress and interface slip up to the peak values τ_f and slip value s_f the bond-slip low decreasing gradually.

The mathematical expression of the bilinear bond slip relation is:

$$f(s) = \begin{cases} \frac{\tau_f}{s_f} s & \text{when } 0 \leq s \leq s_f \\ \frac{\tau_f}{s_0 - s_f}(s_0 - s) & \text{when } s_f < s \leq s_0 \\ 0 & \text{when } s > s_0 \end{cases} \tag{2.3}$$

whereas for the exponential model it is:

$$f(s) = \begin{cases} \frac{\tau_f}{s_f} s & \text{when } 0 \leq s \leq s_f \\ \tau_f e \frac{-\tau_f}{k}(s - s_f) & \text{when } s > s_f \end{cases} \tag{2.4}$$

Parameter k represents the fracture energy of the softening branch of the law that is:

$$k = \int_{s_f}^{+\infty} f(s) ds \tag{2.5}$$

The parameter s_0 can be determined assuming $G_{f.BILINEAR} = G_{f.EXPONENTIAL}$ (Yuan et al. 2012) and the values of $G_{f.BILINEAR}$ $G_{f.EXPONENTIAL}$, the interfacial frac-

ture energy values of the considered model, are expressed as:

$$G_{f.BILINEAR} = \frac{1}{2} s_0 \tau_f \tag{2.6}$$

$$G_{f.EXPONENTIAL} = \frac{1}{2} s_f \tau_f + k \tag{2.7}$$

Consequently:

$$s_0 = \frac{2k}{\tau_f} + s_f \tag{2.8}$$

Barducci et al. (2020) represents four linear local bond-slip lows Fig. 2.13. In all cases, the initial linear branch is linear up to the peak shear stress. However, the post-peak behaviours are varying, namely, linear descending Fig. 2.13, brittle Fig. 2.13), and plastic Fig. 2.13. Moreover, both null and finite residual shear stress Fig. 2.13 addressed for the linear descending case.

Razavizadeh et al. (2014) proposed the simple three linear model bond-slip low to investigate the bond behaviour of SRG-strengthened masonry units. The following equation can mathematically define the modal:

$$\begin{cases} \tau = \tau \frac{s}{s_0} & if \quad 0 \leqslant s \leqslant s_o \\ \tau = \tau_m (\tau_m - \tau_r (\frac{s - s_0}{s_1 - s_0}) & if \quad s_0 < s \leq s_1 \\ \tau = \tau_r & if \quad s_1 < s \leq s_u \\ \tau = 0 & if \quad s > s_u \end{cases} \tag{2.9}$$

where s_m is the bond strength, s_r is the residual bond stress, s_0 is the slip corresponding to s_m, s_1 is the slip at the end of the softening branch where the cohesion is lost, and only friction resists and s_u is the ultimate slip. These parameters calibrated next with the experimental results (Razavizadeh et al. 2014).

Grande et al. (2018) Proposed the bond model where the bond behaviour between masonry and TRM layer is mainly governing by the interface between textile and mortar matrix. The scheme illustrated in Fig. 2.14 and can be summarised as follows:

(i). the support and the lower mortar layer are assumed rigid;

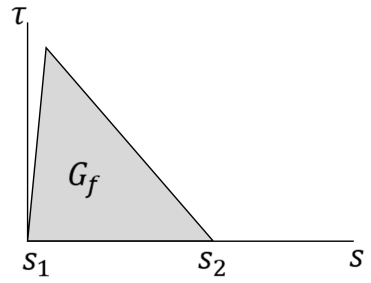

$$\tau[s(x)] = \begin{cases} \dfrac{\tau_1 s(x)}{s_1} & 0 \le s(x) \le s_1 \\ \dfrac{\tau_1}{s_2 - s_1}\left(s_2 - s(x)\right) & s_1 < s(x) \le s_2 \\ 0 & s(x) > s_2 \end{cases}$$

$$G_f = \frac{\tau_1 s_2}{2}$$

(a)

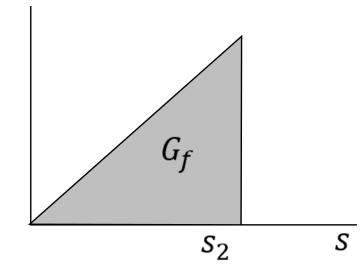

$$\tau[s(x)] = \begin{cases} \dfrac{\tau_1}{s_1} s(x) & 0 \le s(x) \le s_2 \\ 0 & s(x) > s_2 \end{cases}$$

$$G_f = \frac{\tau_1 s_2}{2}$$

(b)

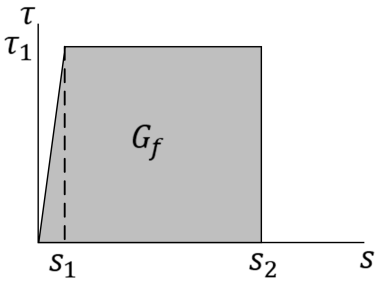

$$\tau[s(x)] = \begin{cases} \dfrac{\tau_1}{s_1} s(x) & 0 \le s(x) \le s_1 \\ \tau_1 & s_1 < s(x) \le s_2 \\ 0 & s(x) > s_2 \end{cases}$$

$$G_f = \tau_1 (s_2 \frac{s_1}{2}$$

(c)

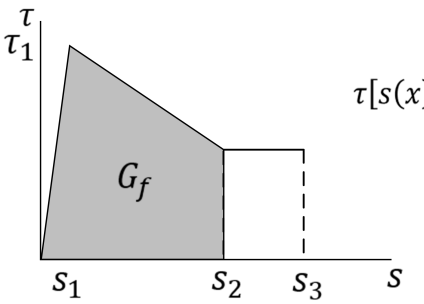

$$\tau[s(x)] = \begin{cases} \dfrac{\tau_1}{s_1} s(x) & 0 \le s(x) \le s_1 \\ \dfrac{\tau_1 - \tau_2}{s_1 - s_2}\left(s(x) - s_2\right) + \tau_2 & s_1 < s(x) \le s_2 \\ \tau_2 & s(x) > s_2 \end{cases}$$

$$G_f = \frac{\tau_2 (s_2 - s_1)}{2} + \frac{\tau_1 s_2}{2}$$

(d)

Figure 2.13: Diagrams, describing equations and fracture energy functions of (a) local law A; (b) local law B; (c) local law C; and (d) local law D. (Barducci et al. 2020)

(ii). the (lower and upper) mortar/reinforcement interfaces are modelled as zero-thickness elements with only shear deformability;

(iii). the upper mortar layer and the reinforcement are assumed deformable only axially.

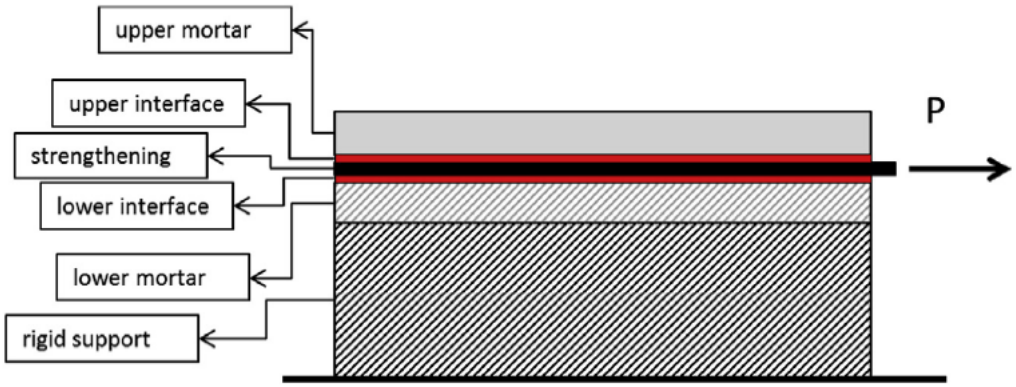

Figure 2.14: Scheme of the TRM system at the basis of the developed model Grande et al. (2018)

According to the model provided the four main stages can characterise the behaviour of the TRM system and can be written as follows:

(i). DP0–undamaged state;

(ii). DP1–damage involving only the interfaces (de-bonding);

(iii). DP2–damage involving only the upper mortar (cracking);

(iv). DP3–damage involving both the interfaces and the upper mortar (de-bonding/cracking).

The response of the specimens identified by three steps denoted as part 1, 2, and 3. When the bond length is long enough, debonding occurred at both upper and lower interfaces. Part 1 (0<x< L-a-b) is governed by 2.10

$$\begin{cases} \frac{d^2 s_1^i}{dx^2} - K_1(s_1^i + s_1^e = 0 \\ (\frac{d^2 s_1^i}{dx^2} - \frac{d^2 s_1^e}{dx^2}) + K_2 s_1^e = 0 \end{cases} \tag{2.10}$$

where the Part 2 governed by (L-a-b< x<L-b)

$$\begin{cases} \frac{d^2 s_1^i}{dx^2} - K_1 s_1^e = 0 \\ (\frac{d^2 s_1^i}{dx^2} - \frac{d^2 s_1^e}{dx^2}) + K_2 s_1^e = 0 \end{cases} \tag{2.11}$$

finally Part 3 L-b< x< L

$$\begin{cases} \frac{d^2 s_3^i}{=} 0 \\ \frac{d^2 s_3^i}{dx^2} - \frac{d^2 s_3^e}{dx^2} = 0 \end{cases} \tag{2.12}$$

The differential equation system listed above has an analytical solution that depends on the twelve constant integration defined by introducing suitable boundary condition. Which expressed as:

$$\begin{aligned} \sigma_{P1}(0) &= 0 \\ \sigma_{c1}^e(0) &= 0 \qquad\qquad \sigma_{c3}^e(0) = 0 \\ \sigma_{c1}^e(L-a-b) &= \sigma_{c2}^e(L-a-b) \\ \sigma_{p1}^e(L-a-b) &= \sigma_{p2}^e(L-a-b) \\ \sigma_{c2}^e(L-b) &= \sigma_{c3}^e(L-b) \\ \sigma_{p2}^e(L-b) &= \sigma_{p3}^e(L-b) \\ s_1^i(L-a-b) &= s_2^i(L-a-b) \quad s_1^e(L-a-b) = s_2^e(L-a-b) \\ s_2^i(L-b) &= s_3^i(L-b) \qquad s_2^e(L-b) = s_3^e(L-b) \\ s_1^i(L-a-b) &= s_1 \end{aligned} \tag{2.13}$$

The analytical solution listed above is suitable for predicting the bond behaviour between masonry and TRM in case of debonding. The same model successfully used by Wang et al. (2020).

2.7 Numerical modelling for masonry structures

2.7.1 Discretization approaches

Numerical simulation of unreinforced masonry is an arduous task. The material is composite, consisting of masonry units and mortar joints (see, Fig. 2.15a) each with an involved constitutive response. In the case of masonry components strengthened with externally bonded layers, e.g., FRP or TRM, one has to also consider the nonlinear response of the strengthening material and the bond at the interface of the constituents.

Furthermore, the anisotropy and dimension of the involved units, the material properties of units and mortar, the arrangement of bed and head joints, and the quality of workmanship should be considered. To this end, the Finite Element Method (FEM) has evolved to a level of maturity that enables an accurate and relatively effective simulation.

According to the literature, two main FEM approaches are identified vis-à-vis the simulation of masonry structures, i.e., the heterogeneous and homogeneous approach. The heterogeneous approach considered the masonry and the mortar joints as separate elements. Conversely, in the homogeneous approach masonry is considered as a uniform composite material with homogenised material properties based on a homogenisation law, e.g., the rule of mixtures. The homogeneous approach has been traditionally used to model masonry structures due to its computational advantages in terms of simulation speed; however the heterogeneous method is considered to be more exact as one can resolve interaction phenomena at the meso-scale (Ahmad et al. 2014). It is of interest to note that depending on the intended level of resolution, the heterogeneous approach can be further characterised as detailed or simplified. These modelling strategies are schematically depicted in Fig. 2.15.

The detailed micro-modelling approach shown in Fig. 2.15b provides the most accurate resolution of the component's response. In this approach, the mortar joints and the masonry units are represented by continuum elements, such as quadrilateral plane stress elements or 3D hexahedral elements. Hence, the actual material properties of the mortar and stone (brick) unit, namely Poisson's ratio, Young's modulus, and the corresponding inelastic characteristics, can be utilised in this approach. As expected however, this approach becomes computationally intensive. To alleviate this while harnessing the benefits of fine resolution, the approach of simplified micro meddling was established (Fig. 2.15c), see, e.g., in Shing et al. (1992), Berto et al. (2004), Milani (2008), Stavridis & Shing (2010), La Mendola et al. (2014).

In this case, the mortar joints are modelled by interface elements, while continuum elements are used to model the masonry units as shown in Fig. 2.16. The size of the masonry units is increased up to half of the bed and top joints.

Finally, the macro-model shown in Fig. 2.15d is based on the homogenisation of the material properties of the masonry and the mortar joint (Bertolesi, Milani &

Lourenço 2016). Typically, this approach is employed only when computational speed is of the utmost importance, e.g., to analyse the response of an entire structure. This method is appropriate when the large structures considered. However, as masonry is not a homogeneous material, this method can not accurately resolve the local behaviour of masonry structures, .e.g, crack evolution.

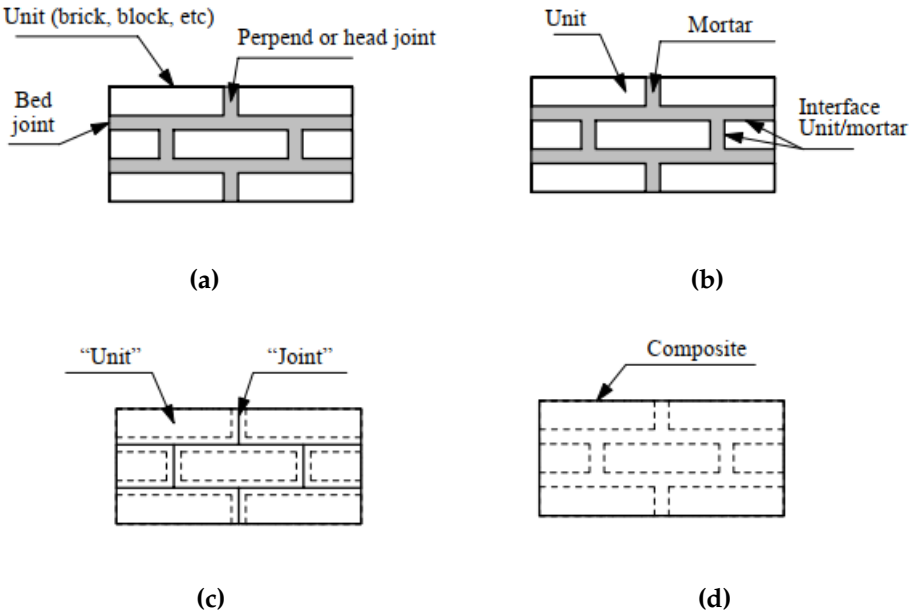

Figure 2.15: Modelling strategies for masonry structures Lourenço (1997): (a) masonry sample; (b) detailed micro-modelling; (c) simplified micro-modelling; (d) macromodeling

2.7.2 Constitutive modelling

Several constitutive models have been proposed in the literature within either a micro- or macro-modelling approach. For a thorough review the reader may consider Lourénço et al. (1997), Milani et al. (2006), D'Altri et al. (2019). In this work, two constitutive models, i.e., the concrete damage plastiticy model and the Drucker-Prager plasticity model are examined as they are readily available in the commercial finite element software Abaqus, and they have been found to provide accurate results as further discussed in Chapter 6.

Drucker–Prager plasticity model The Drucker and Prager (DP) plasticity model was proposed by Drucker & Prager (1952). The yield surface of the model is provided by

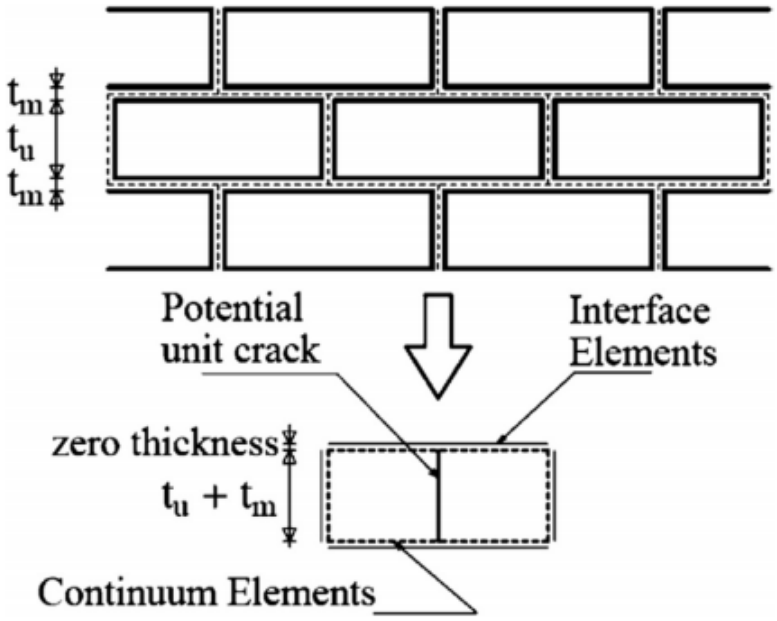

Figure 2.16: Simplified micro-modelling Lourenço & Rots (1997)

Eq. (2.14) and graphically depicted in Fig. 2.17

$$F = t - ptan\beta - d = 0 \tag{2.14}$$

where t is a stress measure defined in Eq. (2.15), p is the hydrostatic or volumetric stress tensor defined in Eq. (2.16), q is the Von Mises criterion equivalent stress defined in Eq. (2.17), d is the cohesion of the material Eq. (2.19), β is the friction angle of the material Fig. 2.17, r is the third invariant of the deviatoric stress Eq. (2.18), and K is the ratio of the yield stress in triaxial tension to the yield stress in triaxial compression (usually $0.778 \leqslant K \leqslant 1.0$).

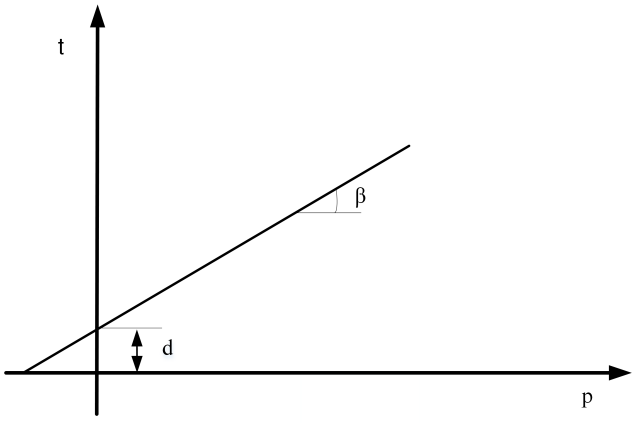

Figure 2.17: Yield criteria in the meridional plane Drucker-Prager (SIMULIA, 2016)

$$t = \frac{1}{2}q\left[1 + \frac{1}{K} - (1 - \frac{1}{K})(\frac{r}{q})^3\right] \tag{2.15}$$

$$p = \frac{I_1}{3} = \frac{\sigma_{11}\sigma_{22}\sigma_{33}}{3} \tag{2.16}$$

$$q = \sqrt{3J_2} \tag{2.17}$$

$$r = J_3 = \frac{1}{3}\left[(\sigma_{11} + \sigma_{22} + \sigma_{33})^3 - (\sigma_{11} + \sigma_{22} + \sigma_{33})^2(\sigma_{11} + \sigma_{22} + \sigma_{33}) + \frac{2}{9}(\sigma_{11} + \sigma_{22} + \sigma_{33})^3\right] \tag{2.18}$$

$$d = (\frac{1}{K} + \frac{1}{3}tan\beta)\sigma_t \tag{2.19}$$

The flow potential (G) used in this model is given in Eq. (2.20), where the geometric scheme is given in Fig. 2.18

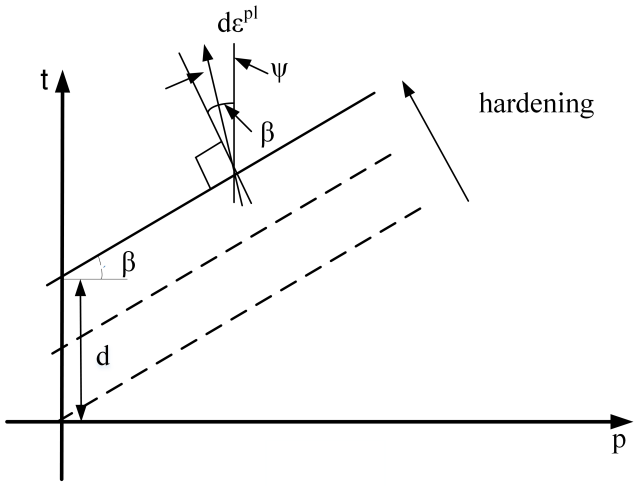

Figure 2.18: Schematic of hardening and flow for the linear model in the p–t plane (SIMULIA, 2016)

$$G = t - ptan\psi \tag{2.20}$$

where:

(i). (ψ) dilation angle in the p–t plane

(ii). (p) hydrostatic or volumetric stress tensor

The flow potential G and yield surface F depend on t. Hence, G is associated with the deviatoric plane. In other words, the dilation angle (ψ) and the material function angle (β) may vary. Therefore the model will be not associated with the p-t plane.

In case of the materials such as concrete or masonry, the linear Drucker-Prager model is typically used without the association of the flow in the p-t plane. In this model, the G is determined to be normal to the yield surface in the deviatoric Π plane, but there is a dilation angle (ψ) to the t-axis, which is ψ ¡ β Fig. 2.18. For simplicity, the ψ set to equal β and K=1.

Concrete Damage Plasticity (CD) Although the concrete damage plasticity (CDP) model has been developed by Lubliner et al. (1989) and later extended by the seminal work of Lee & Fenves (1998) to simulate the nonlinear cyclic response of concrete, it may has been extensively used for the case of masonry, see, e.g., Resta et al. (2013), Bolhassani et al. (2015), Minga et al. (2018), Bhosale & Desai (2019). The CDP is developed on the basis of two main failure mechanism, i.e., cracking in tension and crashing in compression. Hence, it allows tracking of the tension and compression damage from micro to macro cracking separately. In Fig. 2.21, the the tensile (Fig. 2.21a) and compressive (Fig. 2.21b) envelopes of the stress-strain response are shown. The uniaxial tensile response is linear until the failure σ_{t0}. At the peak point, cracks initiate, accompanied by stress-strain softening behaviour. The compression graph is linear until the yield stress σ_{c0}. The yield surface of CDP model in the deviatoric stress plan is not a circle to allow for different yield triaxial tension and compression stresses (Fig. 2.19). This noncircular yield surface is governed by the shape parameter K_c. Physically, parameter K_c is interpreted as a ratio of the second stress invariant for tension and compression at same hydrostatic stress. This ratio must satisfy the condition $0.5 \leqslant K_c \leqslant 1$ to ensure the convexity of the surface.In the CDP model, potential plastic flow under a three-dimensional state of stress is defined using two input parameters. These two parameters are dilation angle (ψ) and flow potential eccentricity (ϵ). A geometrical interpretation of ψ and ϵ are shown in Fig. 2.20. The plastic regime contains stress hardening, followed by strain-softening after reaching the ultimate stress σ_{cu}.

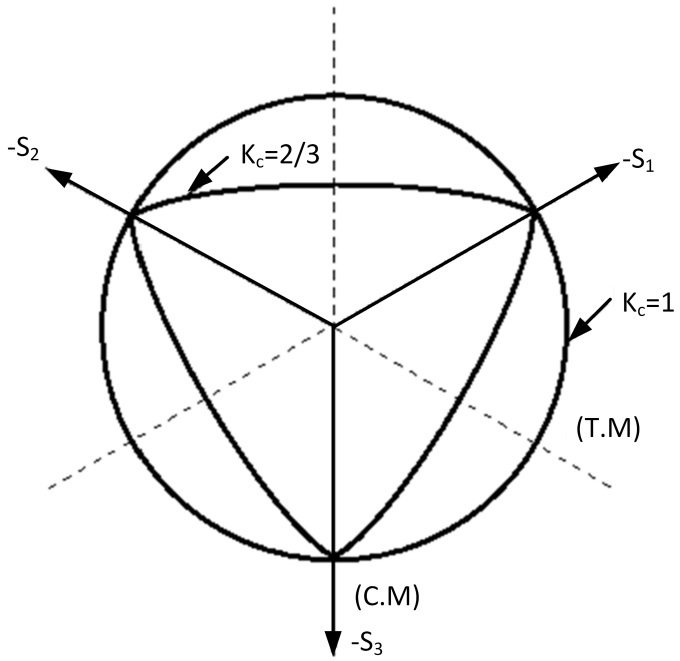

Figure 2.19: Yield surface and flow rule of CDP model (deviatoric plane)

2.8 Numerical simulation of interface mechanics

2.8.1 Interface modelling by the cohesive surface approach

In general, cohesive modelling is used to account for the physics developing at the interface between bonded materials. These physics can be described on the basis of three main methods, i.e, (1) uniaxial stress-based, (2) continuum-based, and (3) traction–separation constitutive models. Continuum based modelling can be used when the adhesive material has a finite thickness and the traction-separation based modelling where the intermediate glue material is thin and considered of null thickness. The traction-separation-based modelling involves a model of the initial loading, damage initiation, and damage propagation, which leads to failure of the bonded interface. The traction–separation constitutive models can also be used when the glue is very thin and may be considered a zero-thickness material for practical purpose. Before the damage, the cohesive behaviour follows a linear traction–separation law and progressive degradation of the bond stiffness leads to bond failure.

$$max\left(\frac{t_n}{t^0}, \frac{t_s}{t_s^0}, \frac{t_t}{t_t^o}\right) = 1 \tag{2.21}$$

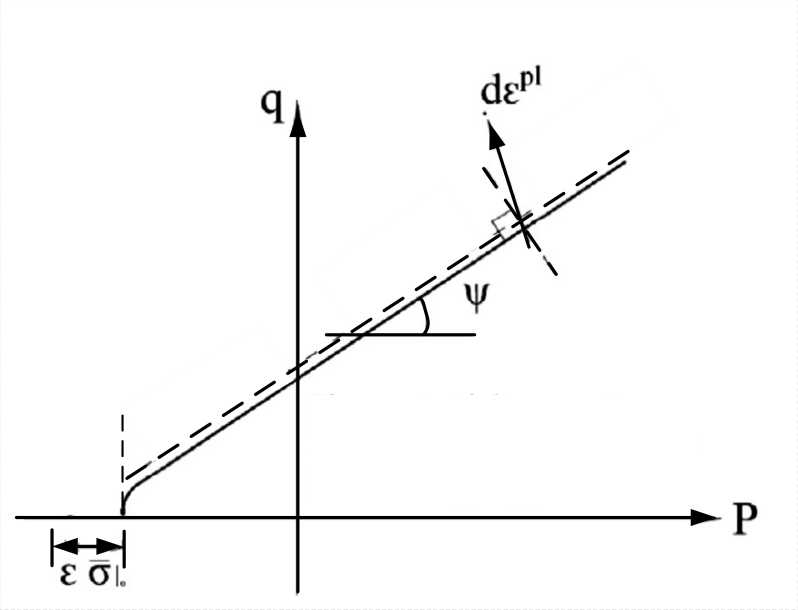

Figure 2.20: Flow rule of CDP model (meridian plane)

The Fig. 2.22 represents the typical traction separation behaviour. The elastic part, the traction vector consist of three components the normal t_n and two shear components t_s, t_t. When the maximum nominal stress ratio reaches the value of 1 Eq 2.21 the damage initiates. Also, in this model δ_n^0, δ_s^0 and δ_t^0 represent the corresponding initial separation caused by pure normal, in plane and out-of-plane shear stresses, respectively.

The linear damage evolution in Abaqus software can de define using the effective displacement at complete failure δ_m^f, relative to the effective separation at the initiation of damage δ_m^0 or the energy dissipated due to failure G^c. The Fig. 2.23 represents linear damage evolution. The G^c is equal to the fracture energy.

2.8.2 Contact pressure-overclosure relationships

The softened contact relationship in which the contact pressure is a linear function of the clearance between the surfaces used as a surface-based contact. Softened contact used to model a soft, thin layer on one or both contact surfaces. It can also be used for numerical reasons as they make resolving the contact condition easier.

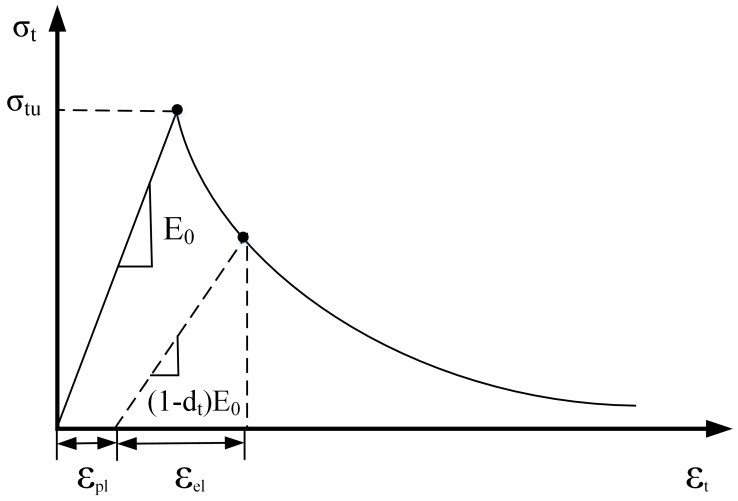

(a) Tension

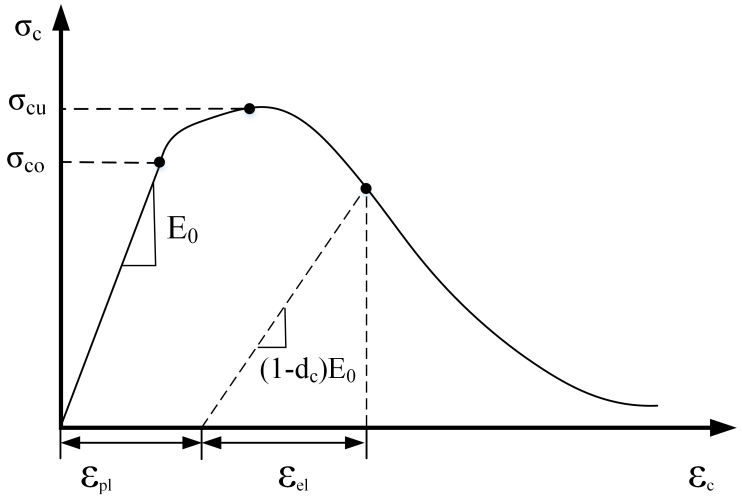

(b) Compression

Figure 2.21: Response of concrete to uniaxial loading. Figure adapted from the Abaqus theory manual Smith (2012) (a) Tension (b) Compression

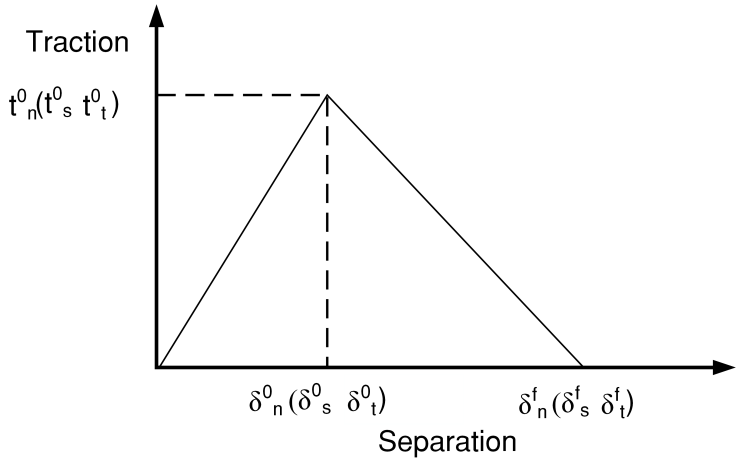

(a)

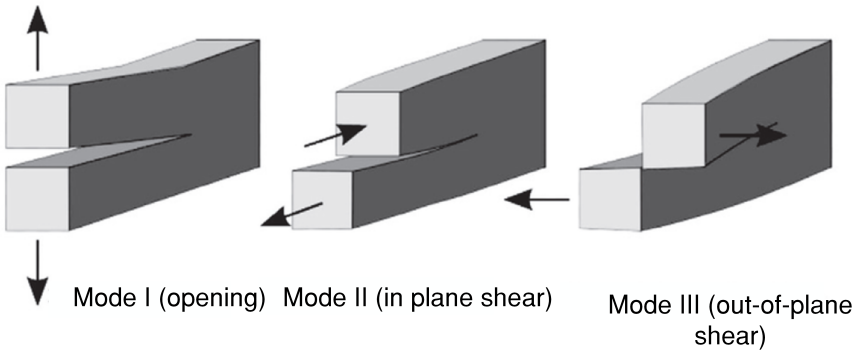

(b)

Figure 2.22: Typical traction–separation behaviour Smith (2012) (a) Traction-separation response (b) Fracture modes

2.8.3 Tangential behaviour - Coulomb friction model

The Coulomb friction model describes two contacting surfaces where the model characterises the friction behaviour utilise the coefficient of friction. General two contacting surfaces can carry on the stress up to the maximum value where the sliding starts. In particular, it determines the critical shear stress (τ_{crit}) where the slippage is starts determined by Eq. 2.22.

$$\tau_{crit} = \mu\rho \tag{2.22}$$

Where (μ) is the friction coefficient and (ρ) the contact pressure between the two surfaces.

The optimal behaviour of the Coulomb friction model represents in Fig. 2.24

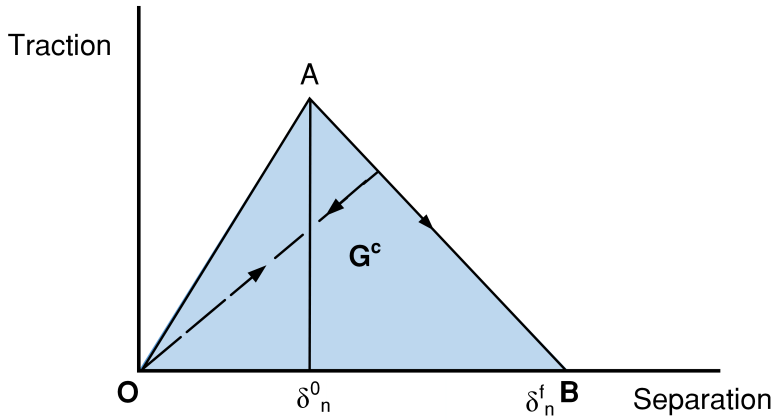

Figure 2.23: Linear damage evolution Smith (2012)

(solid line).

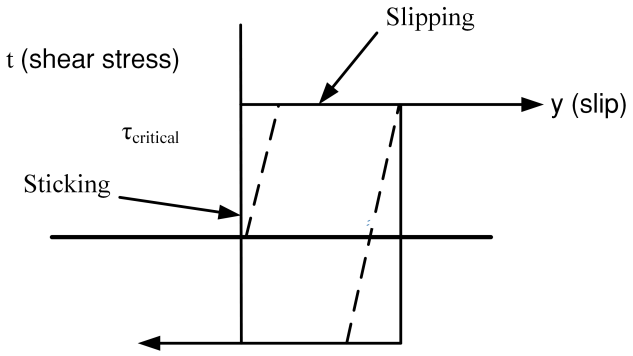

Figure 2.24: Frictional behavior Smith (2012)

There was zero relative slip of the surfaces when they bonded (the shear stresses are below (τ_{crit}). After the critical shear reached, the surfaces begin moving infinitely. In general, even when applying a small amount of shear stress, there is a finite sliding between contacts. The dotted line on the Fig. 2.24, represents the realistic behaviour of the Coulomb model. The finite value of the sticking stiffness: penalty method defined automatically by Abaqus/Standard. The penalty method permits elastic sliding of surfaces when they should have stuck. The automatic value of elastic slip (γ_i) is determined by Eq. 2.23

$$\gamma_i = l_i F_f \tag{2.23}$$

where (F_f) is the slip tolerance equal to 0.005 (default value) and (l_i) is the characteristic contact surface length.

2.8.4 Bond test FE modelling

FE modelling of the bond behaviour has been proven an efficient tool for for understanding the influential parameters on the bond response and the changes in failure modes. To this end, several researchers, see, e.g., DeHoff et al. (1995), Jendele & Cervenka (2006), Lu et al. (2005), Li et al. (2015) and more recently Milani et al. (2020, 2021) have developed numerical models to simulate the bond using the finite element method.

Razavizadeh et al. (2014) developed a fine resolution finite element model using the DIANA FE software (DIANA FEA 2017) to simulate the bond in SRG strengthened masonry walls. Eight-noded plane stress elements were used for the brick and the grout (labelled as CQ16M). The steel was modelled using two-node truss elements (labelled as L2TRU). Two sets of six node zero-thickness interface elements (labelled as CL12I) were used to connect the brick–mortar (BM) and for the steel–mortar (SM) interfaces. The constraints and loading conditions were according to actual test applications.

Carozzi et al. (2014) investigated the behaviour of glass fibers reinforced cementitious matrix and masonry (single bricks) using three different bond lengths of 50, 100 and 150mm and masonry pillars of 300mm bond length on a push-pull double-lap test setup. The finite element modelling of push-pull double-lap tests was performed by fully 3D finite element approach, based on sequential quadratic programming. It used a 3D model with 8-noded rigid and infinitely resistant 8-noded elements. Glass fibre grid modelled through non-linear truss elements are interacting with the mortar matrix by non-linear tangential stresses. The model represents good agreement with the actual tests.

Li et al. (2015) studied the bond behaviour of FRP-concrete bonded joints under static and dynamic loadings, using the K&C concrete damage model in LSDYNA FE software. The dilation of concrete influences the simulation results. A high dilation angle increases the confinement of concrete, thus leading to higher loading capacity.

Wang et al. (2020) developed a 2D FE model to examine the bond between TRM and masonry using the Abaqus 6.14 software Smith (2012). In this work, the main constituents, namely the textile, the mortar matrix and the masonry wall, were modelled

by linear elastic 8-node quadrilateral plane-stress elements. The elements were connected via zero-thickness cohesive elements where local bond-slip constitutive laws (with linear elastic behaviour until debonding failure) was used.

Bertolesi, Milani & Lourenço (2016) investigated bond behaviour between curved masonry pillar and carbon FRP composite material. The authors used single-lap shear tests and different curvature radii (1500 and 3000 mm), and the position in reinforcement (intrados and extrados) is studied. The numerical model used is a 2D plane, a micro-modelling (heterogeneous) approach, where the constituent materials (masonry units, mortar joints and FRP reinforcement) were modelled separately. Abaqus commercial software was used to perform modelling. The proposed FE numerical models require only the mechanical properties of the constituent materials used, obtained from conventional laboratory tests. The authors concluded that the result of FE modelling fitted well with experimental observations.

A common denominator in all the aforementioned approaches is that a 2D finite element formulation is opted for in conjunction with a cohesive element (zero-thickness) approach to account for the constitutive response of the interface. Clearly, a 2D implementation is computationally efficient when compared to a full 3D description of the domain. However, a 2D implementation implies that the stress distribution across the width of the textile is uniform. This may not be the case, especially when trying to reproduce actual experimental results. A 3D implementation would allow for arbitrary defects to be introduced in the specimen, hence giving rise, if put within a statistical analysis framework, to a more realistic representation of the actual response.

2.9 Chapter summary

According to the literature review, TRM can significantly enhance the mechanical properties of UM structures and hence have the potential of being widely used in the construction industry. However, there is no consensus on the corresponding manufacturing processes, i.e. type of textile materials, textile coating, and mortar matrix. There is an open field for research in terms of bond behaviour between masonry and TRM. Failure patterns in debonding the UM to TRM is a critical concern as if it

compiles various failure modes depending on the textile and mortar matrix. To this end, a significant number of experiments were conducted to examine the mechanics governing the textile-reinforced mortars to masonry bond under static loading conditions. However, many questions still need to be examined, namely the influence of the mortar matrix on bond behaviour, in-house coating of textiles, and textile materials. On the other hand, despite the number of investigations done in a static case, the debonding process between UM and TRM under low cycle fatigue load became an issue due to limited information. The materials utilized to manufacture TRM could be divided into two parts, i.e., inorganic mortar matrixes and textile fibre materials. The design of TRM provided several fundamental principles, namely durability, increasing porosity diminishing, enhancement in microstructure and inhomogeneity. Also, materials and the preparation procedure have a considerable influence on TRM parameters. The high cost of textile is the main part of the TRM and cost approximately 35 % (Furtado et al. 2020). The percentage amount could vary in a wide range due to the price of the textile materials, where glass cost less and carbon the most. However, the textile material could be appropriately chosen when applied as a strengthening solution. Otherwise, it could result in less technical characteristics of the material than expected. The mortar matrix for the TRM is divided into cement-based and lime-based mortar, where the lime mortar is used mainly for strengthening historical buildings. In contrast, cement-based mortar is better for structures where high strength is needed. Based on the literature survey, the following points can be highlighted:

(i). Single-lap test setup preferable to investigate the TRM to masonry bond behaviour, due to failure in case of the double-lab test setup did not occur symmetrically at the same time on both sides, which resulted in slightly decreased values of the maximum load compared to the similar values of the single-lap test configuration. Moreover, the double lap test setup is not valid to describe the post-peak response of the bonded composite (especially the global slip) unless simultaneous debonding occurs and perfect symmetry is maintained.

(ii). According to the literature review, it is observed that the high variability of the bond performance and failure mechanisms of masonry to TRM. It further demonstrated that the high variability persists even for the case of similar tex-

tiles tested in different laboratories, see, e.g., Lignola et al. (2017), Leone et al. (2017), Carozzi et al. (2017) demonstrate the need for further experimental work to establish standard procedure between TRM and masonry substrate.

(iii). Research on the bond between in-house coated textile reinforced mortar and masonry is very scarce. The only available study is that of Donnini et al. (2016) which was built on only one set of bond lengths (150mm) and one textile material (carbon) where the specimens were demonstrated a good bond performance after epoxy resin treatment. Thus the bond behaviour of epoxy resin coated textile with various bond lengths, and textile materials need to be evaluated.

(iv). Despite the number of investigations done in a static case, the debonding process between UM and TRM under low cycle fatigue load became an issue due to the limited amount of information.

(v). A common denominator in most approaches is that a 2D finite element formulation is chosen in conjunction with a cohesive element (zero-thickness) approach to account for the constitutive response of the interface. A 2D implementation is computationally efficient when compared to a full 3D description of the domain. However, a 2D implementation implies that the stress distribution across the width of the textile is uniform. This may not be the case, especially when trying to reproduce actual experimental results. A 3D implementation would allow for arbitrary defects to be introduced in the specimen hence giving rise, if put within a statistical analysis framework, to a more realistic representation of the actual response.

3

Material characterisation

3.1 Introduction

In this Chapter, the experimental results of the material characterisation campaign conducted within the remit of this research are presented and discussed. This pertains to all the constituent materials employed in this study, i.e., the bricks, the mortars, and the textiles. The material properties of the epoxy resin used for coating are also provided. The brick material properties where identified by compressive tests. The joint and strengthening mortar properties were identified by a set of compressive and tensile tests. Finally, a set of tensile tests on dry textile fibres was performed to identify the pertinent features, namely, the ultimate tensile stress, the ultimate tensile strain, and the modulus of elasticity.

3.2 Clay bricks

The bricks used in this study were clay bricks typically available in the UK market, with nominal dimensions of 215 x 102.5 x 65 mm. To determine their compressive strength and Young's modulus, five bricks were tested under static compressive loading according to BS EN 1015-11 (EN 1999).

The specimens were cleaned with the brush to remove any superfluous materials and dust. The compressive tests were performed in a 3000 KN universal testing machine (Denison). The specimens were centrally positioned between two 30 mm thick steel plates; the load was applied along the longitudinal direction of the brick.

The displacements were monitored via two potentiometers placed on the two sides of the bricks. The compressive strength was calculated according to Eq. (3.1)

$$f_b = \frac{P_b^{max}}{A} \tag{3.1}$$

where P_b^{max} is the maximum applied load and A (mm^2) is the loaded area. The Young's modulus (E_b) was calculated as the slope of the linear branch of the stress-strain curve recorded during the test.

A typical stress-strain plot is shown in Fig. 3.1. The stress-strain curve remains linear (elastic behaviour) to about one-third of the ultimate strength of the brick. The behaviour, subsequently, becomes non-linear until the maximum stress. Failure at post-peak loading is unstable and the collapse of bricks occurred suddenly. The maximum compressive load, the maximum compressive strength, and the Young's modulus are presented in Table 3.1.

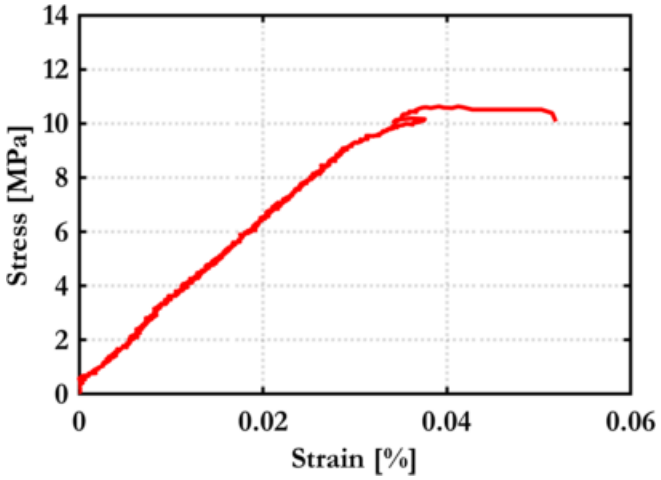

Figure 3.1: Typical stress–strain curve for bricks under quasi-static compression

Table 3.1: Results of compression tests on bricks

Specimen	P_b^{max} [kN]	f_b [MPa]	E_b [MPa]
B1	70	11.2	6.5
B2	78	12.4	27
B3	72	11.6	25
B4	97	15.5	46
B5	67	10.7	30
Mean	78(11.9*/0.15**)	12.5(1.91*/0.15**)	32(14*/0.44**)

*Standard deviation/ **Coefficient of Variation

3.3 Mortars

3.3.1 Mortar mix

The mortars used to build the masonry wallettes joints (joint mortar) and the TRM layers (strengthening mortar) were cement based. For the joint mortar, a 1:4 cement to sand mix was used for all specimens. The corresponding water to mortar ratio was established after trial mixes to achieve the proper workability. This value was approximately equal to 0.25 in all specimens.

The inorganic mortar that was used for the strengthening was a dry binder comprising cement and polymers at a ratio 8:1 by weight. The preparation of the mortar mixture was carried out using water to cementitious material ratio equal to 0.23 by weight.

3.3.2 Mechanical properties of the mortars

The flexural and compressive strength for the joint and strengthening mortars were determined via prism tests according to EN 1015-11 EN (1999). For each case, nine prisms were tested in three point bending bending, as shown in Fig. 3.2. The compressive strength was established with uniaxial compression tests conducted on the splitted parts of the flexural prisms. The resulting tensile and compressive strengths for the joint and strengthening mortar are shown in Table 3.2.

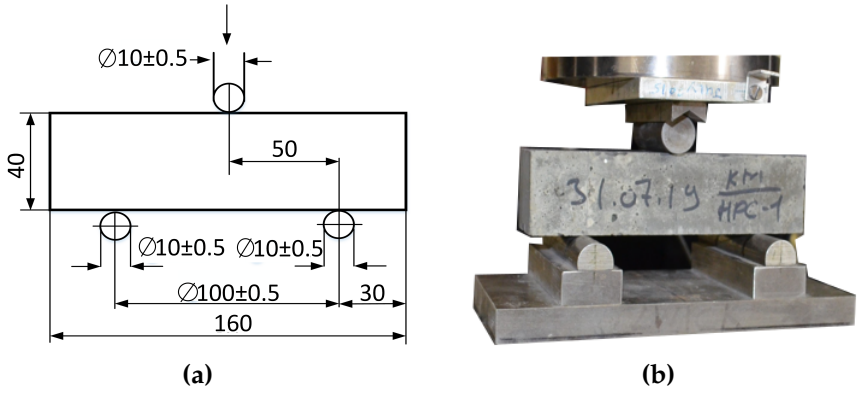

Figure 3.2: Mortar test setup (a) Specimen geometry (all dimensions in mm), (b) Actual test setup

Table 3.2: Mortar properties

Mortar	Tensile strength [MPa]	Compressive strength [MPa]
	Bond test	
Joint	1.85 (0.50*/0.26**)	7.82 (0.36*/0.04**)
Strengthening	4.95 (0.17*/0.03**)	28.90 (0.17*/0.02**)
	Fatigue test	
Joint	2.01 (0.26*/0.13**)	7.58 (0.55*/0.07**)
Strengthening	5.13 (0.57*/0.11**)	32.34 (1.43*/0.04**)

* Standard deviation/ ** Coefficient of Variation

In Fig. 3.3 values of the compressive strength versus flexural strength of cement-based mortars typically used in the literature are plotted and compared against the corresponding values used in this study. Overall, the compressive strength is in the range of 6.9 to 38 MPa and the flexural strength of 2 to 9.8 MPa. In general, the compressive strength recorced in this research is 35% higher than the mean strength of the available tests. However, the tensile (flexural) strength is marginally higher by 3.6%. Based on the findings of Barducci et al. (2020), this could hint that the mortar strength employed in this study is not a decisive factor on the bond strength when compared to the bond test results reviewed in Chapter 2.

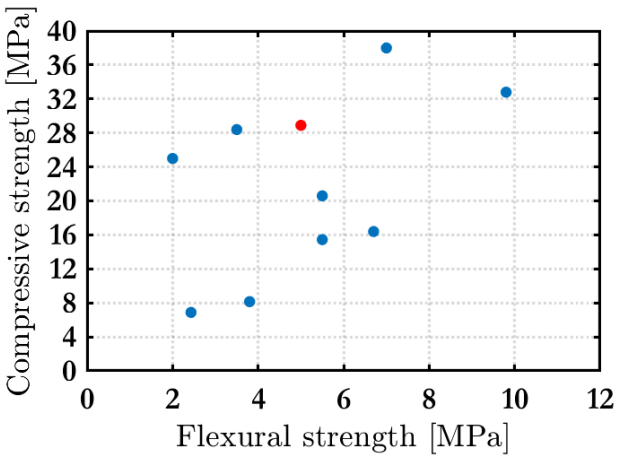

Figure 3.3: Property of cement based mortar compare to the current study (current study result highlighted with red)

3.4 Textile fibre materials

Four textile fibre materials were used in this research, i.e., glass, basalt, heavy-weight carbon, and light-weight carbon; the corresponding mesh sizes are shown in Fig. 3.4.

The basalt textile fibre material used was a commercially coated material with 10 % of a bituminous binder.

The textile materials properties i.e., the weight (W), the nominal thickness (t_f), the tensile strength (f_f^t), and the Young's modulus (E_f), as provided in the manufacturer datasheets, are presented in Table 3.3. The nominal thickness (t_f) was calculated using Eq. (2.2). The axial stiffness(K_t) is calculated as the nominal thickness to Young's modulus product according to Eq. (2.1).

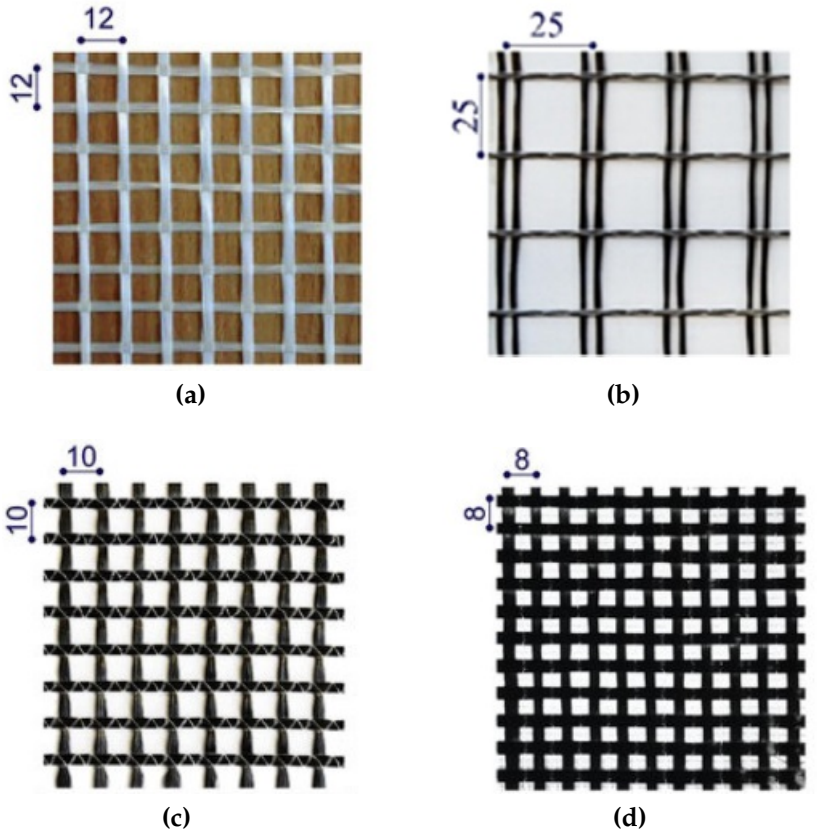

Figure 3.4: Textile fibre mesh sizes (a) glass textile, 220 g/m^2 (b) basalt textile, 220 g/m^2 (c) heavy carbon textile, 348 g/m^2 (d) light carbon textile, 220 g/m^2

Table 3.3: Textile fibre materials parameters

Material [/]	W [g/m^2]	t_f [mm]	f_f^t [MPa]	E_f [GPa]	K_t [N/mm^2]
Glass	220	0.044	1351	74	3.3
Basalt	220	0.037	1400	89	3.26
Carbon (heavy)	348	0.097	3800	225	21.83
Carbon (light)	220	0.062	4800	225	13.95

To investigate the effect of coating of the heavy-weight carbon, light-weight carbon, and glass fibre textiles were coated in-house using an epoxy resin with a 2:1

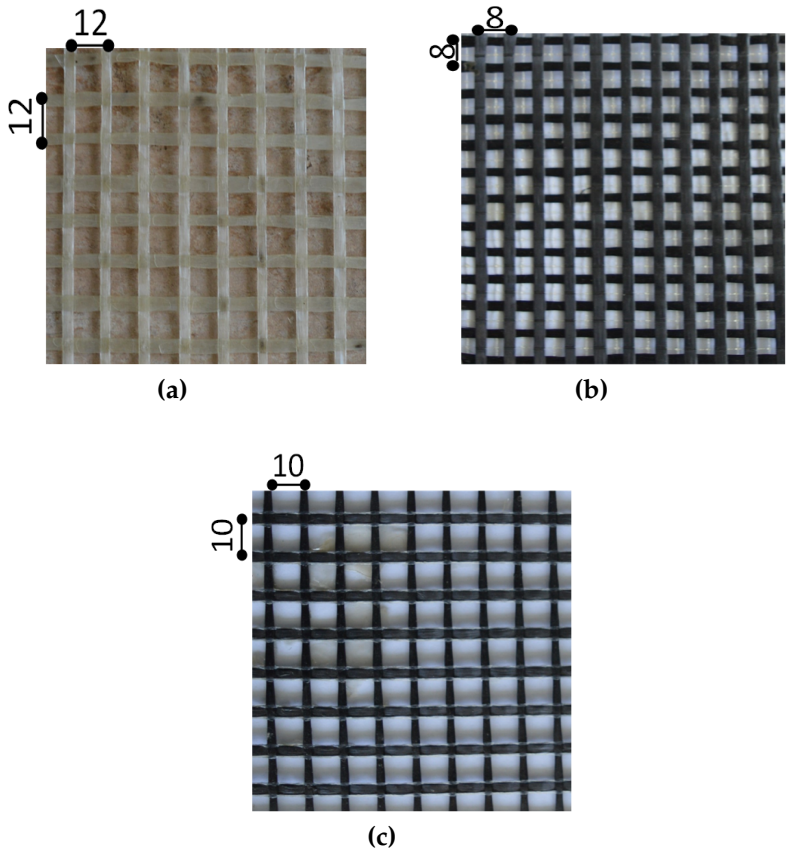

Figure 3.5: Coated textiles (a) glass coated textile 300 g/m^2 (b) light carbon textile 331 g/m^2 (c) heavy carbon textile 413 g/m^2

mix ratio by weight. It is essential to note that in all cases, the mesh size and the corresponding application procedure ensured that the roving spacings were not filled/covered by resin. Typical snapshots of the coated textiles are shown in Fig. 3.5. According to the corresponding data sheet, the epoxy resin elastic modulus and tensile strengths were 1.8 GPa and 37 MPa, respectively. The weights of each textile material after coating are provided in Fig. 3.5.

3.4.1 Tensile tests on dry textiles

A series of tensile tests on a single layer of fibre textile material were conducted to determine the textile tensile properties in the direction of loading as per the ASTM D5034 specifications (ASTM 2011). Tests were performed for all seven types of textile fibre materials used in this study, i.e., glass, coated glass, light carbon, coated light carbon, heavy carbon, coated heavy carbon, and basalt.

In all cases, the free length of the specimen was 250 mm, and the width was

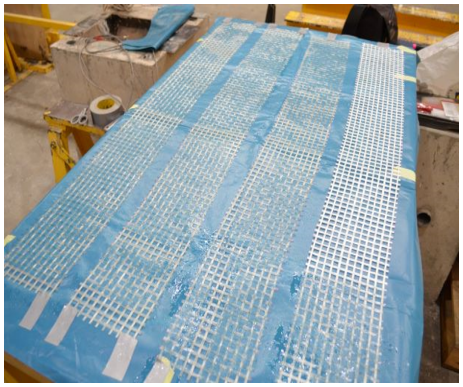

(a) Step1

(b) Step2

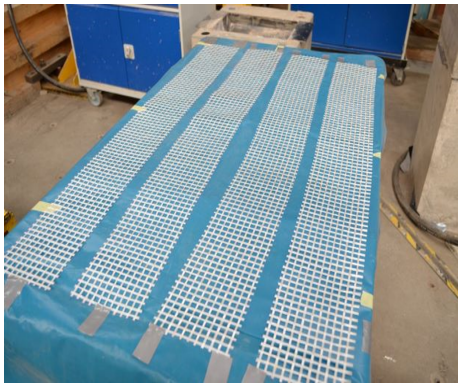

(c) Step3

Figure 3.6: Epoxy resin application steps.

80 mm. Three identical specimens were tested per case to reduce variability. The naming convention adopted is X_Y, where X corresponds to the textile fibre material (Ch-heavy carbon, Cl-light carbon, G- glass, B-basalt) and Y corresponds to the test specimen a,b and c. The suffix 'co' is appended when the textile fibre material coated with epoxy resin. All samples were cut in the wrap direction of the textile rolls.

The coating of the textile fibre material was performed according to the following procedure:

(i). The textile was cut in strips with nominal dimensions W =120 mm and L =1000 mm (Fig. 3.6a);

(ii). The textile was placed flat onto a work-bench, taped to prevent slip and painted using a roller with a foam nozzle (Fig. 3.6b);

(iii). The coated textile was left on the table for 2 days to allow the resin to cure before being used for TRM strengthening (Fig. 3.6c).

The tests were performed using displacement control at a rate of 0.02 mm/sec in a Zwick universal testing machine fitted with a 200kN load cell. The elongation was measured using two LVDTs with a 15 mm stroke and a 0.01 mm sensitivity Fig. 3.7.

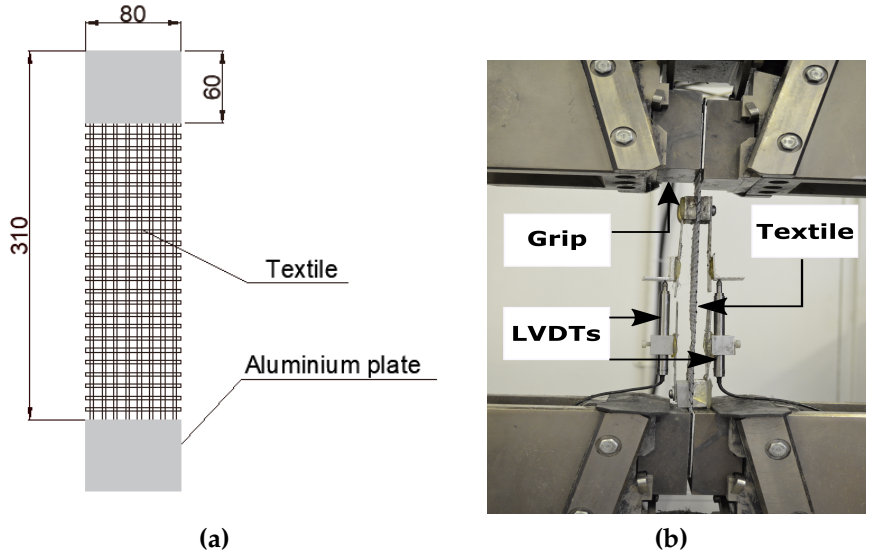

Figure 3.7: Test setup (a) Geometry of textile coupon (all dimensions in mm), (b) Actual test setup

The failure mode in all specimens was textile rupture in the central region as shown in Fig. 3.8. The corresponding stress strain curves are shown in Fig. 3.9. The tensile stress was calculated according to Eq. (3.2)

$$\sigma^t = \frac{\text{Load}}{t_f \cdot n_r \cdot d_m} \tag{3.2}$$

where σ^t is the tensile stress, n_r is the number of rovings of the sample and d_m is the mesh size. The nominal thickness t_f is provided in Table 3.3.

The resulting mean values of the fibre textile ultimate tensile stress f_f^t, the corresponding strain ε_f^u, and the modulus of elasticity E_f are shown in Table 3.4. The modulus of elasticity (E_f) was calculated by dividing the ultimate tensile stress (f_f^t) to the corresponding ultimate tensile strain (ε_f^u) because the behaviour of the textile is linear up to failure. These significantly diverge from the maufacturer values shown in Table 3.3 but are in good agreement with the tensile tests conducted by Raoof et al. (2017) on the similar textile meshes.

The coated heavy carbon fibre textile used have the highest ultimate tensile stress and modulus of elasticity, as shown in Table 3.4. The epoxy resin coating was ben-

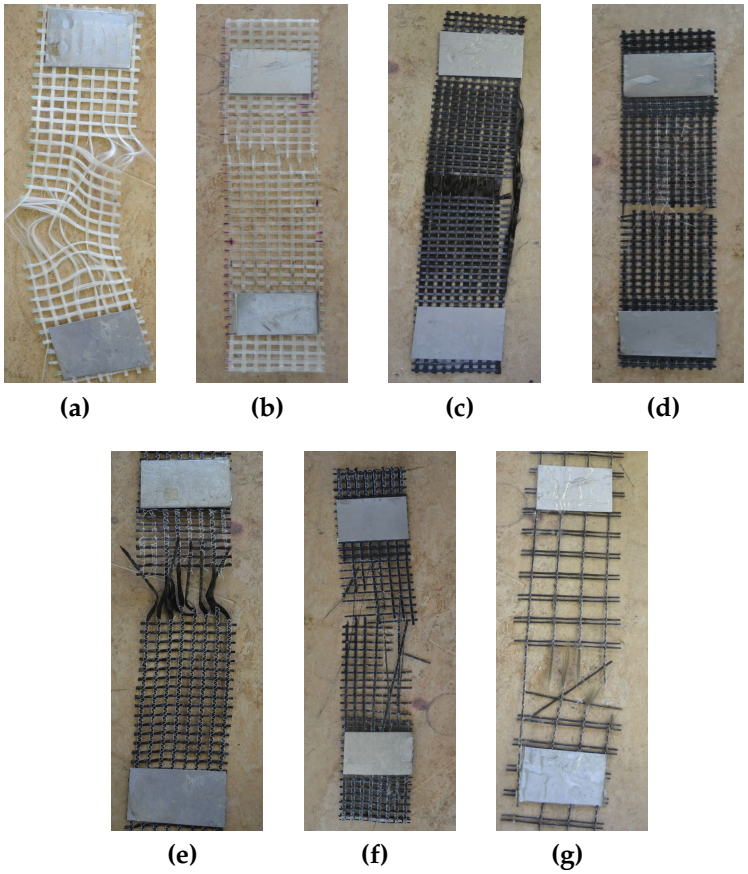

Figure 3.8: Textile tensile tests failure modes (a) glass (b) coated glass (c) light carbon (d) light carbon coated (e) heavy carbon (f) heavy carbon coated (g) basalt

eficial for both coated carbon textiles resulting in higher ultimate tensile stress and modulus of elasticity than the uncoated ones (see Table 3.4). The glass fibre textile demonstrated the lowest mechanical properties. The epoxy resin was also beneficial on the coated glass textile, demonstrating increased, ultimate tensile stress and modulus of elasticity than the uncoated glass fibre textile. In addition, coated glass and coated basalt fibre textiles resulted in close response in terms of ultimate tensile stress and modulus of elasticity.

3.4.2 Comparisons with published test results

In this Section, the results obtained from the textile material characterisation procedure are compared to results already published in the literature. The experimental outcomes are compared in terms of the strength of the textile f_f^t and the textile fibre geometry to assess the repeatability of the results obtained by different laboratories and the influence of different test methodologies.

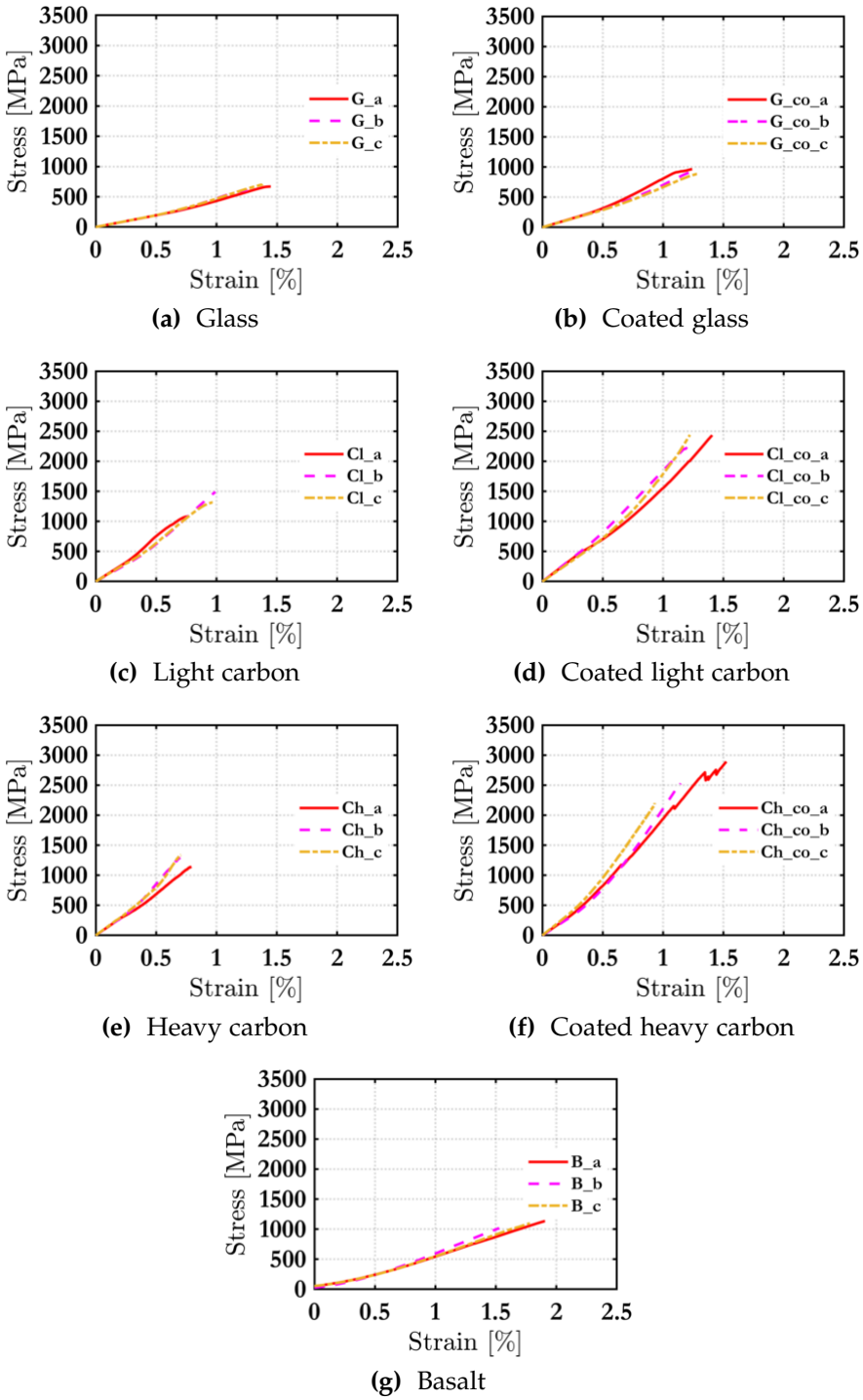

(a) Glass **(b)** Coated glass

(c) Light carbon **(d)** Coated light carbon

(e) Heavy carbon **(f)** Coated heavy carbon

(g) Basalt

Figure 3.9: Textile tensile tests stress strain curves

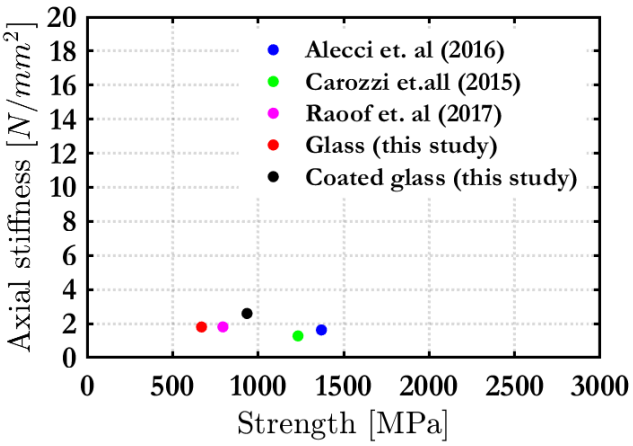

(a) Glass

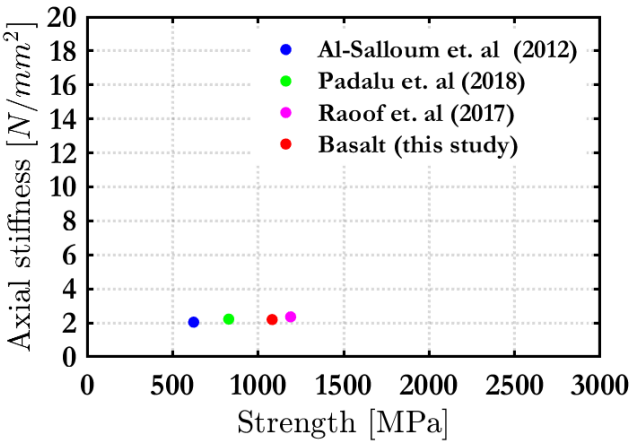

(b) Basalt

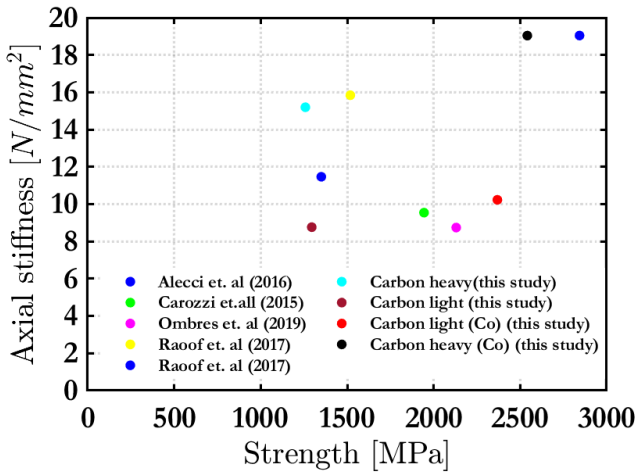

(c) Carbon

Figure 3.10: Comparison of the stress versus axial stiffness between published and current study

Table 3.4: Tensile properties of the fibre-textile materials

Textile	f_f^t [MPa]	ε_f^u [%]	E_f [GPa]
Glass	669	0.75	47
	(19.5)* (0.05)**	(0.05)* (0.07)**	(2.54)* (0.05)**
Glass coated	935	1.26	70
	(45)* (0.05)**	(0.02)* (0.02)**	(5.56)* (0.08)**
Carbon (light)	1295	0.90 (0.12)	140
	(205)* (0.15)**	* (0.14)**	(5.68)* (0.08)**
Carbon (light)	2368	1.27	170
coated	(117)* (0.04)**	(0.11)* (0.09)**	(10)* (0.06)**
Carbon (heavy)	1258	0.73	160
	(103)* (0.08)**	(0.05)* (0.07)**	(17)* (0.10)**
Carbon (heavy)	2541		196
coated	(347)* (0.13)**	1.20 (0.30)* (0.25)**	(9.5)* (0.06)**
Basalt	1082	2.22	59
	(59)* (0.05)**	(0.33)* (0.15)**	(3.21)* (0.05)**

*Standard deviation, **Coefficient of variation

Raoof et al. (2017) used a glass fibre textile with an identical mesh size to the one used in this study. The ultimate tensile stress obtained was 794 MPa, which is comparable to the strength established via the tests conducted in this work; however, the dimension of the coupon was different of 60 mm long and 50 mm width. Carozzi & Poggi (2015) performed tensile test on single rovings and obtained a higher stress value of 1233 MPa. The rovings were cut from a textile with a mesh size of 19 mm x 15.5 mm.

Carozzi et al. (2014) performed a tensile test on a single roving of a styrene butadiene rubber (SBR) glass cut from a textile of a 17 mm x 12 mm mesh size. The ultimate tensile stress obtained was 1144 MPa. The response is comparable to that of the epoxy resin coated textile used in this study, where 935 MPa ultimate tensile stress was observed. Finally, Alecci et al. (2016) used a glass textile of different mesh size (15.7 x 10.1mm) and a 0.023 mm nominal thickness and obtained an ultimate tensile stress and modulus of elasticity equal to 1370 MPa and 70.8 GPa, respectively.

Fig. 3.10a shows that the current study results are consistently lower than the others even though the axial stiffness is comparable. Although the results are comparable with Raoof et al. (2017) the mean of the other tests is more representable of the anticipated strength of the glass fibre material. It is worth noting that all researchers improve the gripping of the fabrics to the testing machine, by epoxy resin bonded two

aluminium plates to the end of the dry fibers.

With regards to the basalt textile fibre material, Al-Salloum et al. (2012), Padalu et al. (2018), Raoof et al. (2017) conducted tensile on a textile with a similar mesh size and corresponding axial stiffness. The comparison is shown in Fig. 3.10b. Clearly, the results obtained from all studies are scattered. In particular, Al-Salloum et al. (2012) recorded a ultimate tensile stress 623 MPa whereas Padalu et al. (2018) 828 MPa Fig. 3.10b. Raoof et al. (2017) recorded a tensile strength of 1190 MPa that is closer to the results obtained in this study. Overall, the tensile strength recorded in our experiments is 20% higher from the mean value of the tests available. This shows the importance of standardising the tensile coupon tests since all listed above researchers had a different textile coupon dimension.

Finally, in the case of the carbon fibre textile Alecci et al. (2016), Carozzi & Poggi (2015), Ombres et al. (2018) used a similar geometry mesh size (10 x 10 mm) but different nominal thickness (0.047 mm). The resulting tensile strengths were equal to 1350, 1944, and 2130 MPa, respectively as shown in Fig. 3.10c. The increased variability in this cases highlights the fact that both the mesh size and the nominal thickness contribute to the textile strength. The comparisons are shown in Fig. 3.10c.

3.5 Concluding Remarks

In this chapter, the experimental test results of clay brick, strengthening mortar and textile were presented. The main conclusions drawn for the experiments are summarised below:

(i). This chapter presents all the pertinent mechanical properties for the materials used to conduct experimental work on masonry to TRM bond test. The variability observed in the published mechanical properties of textile fibre materials, also when compared to values provided from the manufacturers, clearly highlights the requirement for performing coupon material testing.

(ii). The in-house epoxy resin coated textile has a positive effect on the maximum tensile strength of the textile. The coated glass had a tensile strength that was 151% higher compared to its uncoated counterpart. The corresponding increase

for the case of the light and heavy carbon textiles was 82% and 101%, respectively.

4

TRM to masonry bond under static loading

4.1 Introduction

As stated in Chapter 2 the most extensively investigated textile fibre materials for the TRM is glass, carbon and basalt. However, these three types of textile fibre materials are quite rare compared to a single experimental campaign. Furthermore, the comparison of in-house coated glass and carbon textile fibre materials is limited in the literature. This chapter presents the experimental results of the quasi-static single-lap bond tests that were conducted in this research. The main purpose of this experimental campaign was to investigate the bond at the TRM/masonry substrate interface considering the following key investigated parameters, i.e., (a) the textile fibre material, i.e., light and heavy carbon glass, basalt textiles (b) the bond length L_b (100, 150, 200, and 250 mm) and (c) the epoxy resin coating. The Chapter explains in detail the specimen preparation, i.e., the wall manufacturing, the specimen assemblage, and the coating of the textiles with epoxy resin where applicable. The data used to visualise the specimen behaviour during the tests enabled the identification of the failure mode for each type of test to identify the failure mechanism. The results demonstrate that the uncoated glass fibre textiles result in the lowest values of the peak loads regardless of the bond length. Furthermore, the experimental results highlight the beneficial effect of the epoxy resin coating that practically doubles the bond strength of the TRM.

4.2 Experimental Programme

4.2.1 Test Specimens and experimental parameters

In total, 84 specimens were manufactured, strengthened and subjected to single-lap shear tests. The specimens details are presented in (Fig. 4.1). Each masonry wallette comprised five bricks irrespective of the bond length Fig. 4.2.

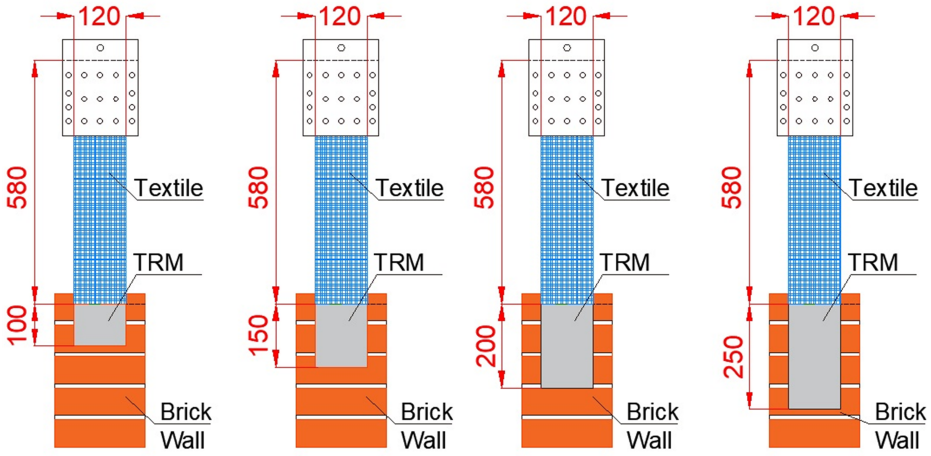

Figure 4.1: Overview of test specimens (all dimensions in mm)

Figure 4.2: Preparation of the masonry wallettes

Typical clay bricks, available in the UK market, were used with nominal dimensions 215 x 102.5 x 65 mm. A 1:4 cement to sand ratio mortar was used for the

joint mortar mix. The amount of water was defined by trial mixes until the desired workability was achieved and was equal to 0.25. The property of mortar joint and strengthening mortar are discussed in the previous chapter.

4.2.2 Specimen preparation

The walletes were strengthened with a single TRM layer one week after construction. The overall length of the textile was L_t =1000 mm; the free length of the textile was L_f =400 mm in all cases. All specimens were tested one month after construction. The application of the TRM layer was performed according to the following procedure Fig. 4.3:

(i). Air pressure was used to remove dust from the masonry wall surface (Fig. 4.3a);

(ii). The wall was slightly dampened and a first layer of mortar was applied at the entire surface of the wall (Fig. 4.3b);

(iii). The textile layer was applied and impregnated into the previously applied mortar using hand pressure (Fig. 4.3c);

(iv). A final layer of mortar was applied to completely cover the textile (Fig. 4.3d).

It is of interest to note that the the application of the TRM layer was performed with the wallette positioned vertically to better emulate the actual, on site, application practice. Hence, the TRM layer thickness was not a controlled but rather a targeted parameter. Measurements of the thickness prior to testing showed that the targetted value of 6 mm was achieved within a 5% margin.

The procedure was completed while the mortar was fresh to achieve optimum adhesion of the TRM layer. The final strengthened configuration is shown in Fig. 4.3c. An unbonded margin of 25 mm was considered in all specimens to minimise the impact of edge effects, i.e., avoid stress concentrations (de Felice et al. 2016, De Felice et al. 2018) (see, also, Fig. 4.4a).

The specimens with their corresponding parameters are shown in Table Table 4.1. The naming convention adopted is X_Y, where X corresponds to the textile fibre material (Ch-heavy carbon, CL-light carbon, G- glass, B-basalt) and Y corresponds to the

(a) Step 1

(b) Step 2

(c) Step 3

(d) Step 4

Figure 4.3: TRM layer application steps

bonded length. The suffix 'co' is appended when the textile fibre material coated with epoxy resin. The total number of TRM configurations tested was 28. A varying number of identical specimens was tested per configuration, as also shown in Table 4.1.

4.2.3 Shear bond test setup

The walletes were clamped to the strong floor using a steel reaction frame as shown in Fig. 4.4. The steel frame comprised two steel plates connected with four threaded stainless steel rods. The textile fibre material was attached to the actuator through

Table 4.1: Wall Specimens

Specimen	Bond length [mm]	Number of specimens	Textile fibre	In-house coating
G_100	100	4	Glass	No
G_150	150	4	Glass	No
G_200	200	5	Glass	No
G_250	250	4	Glass	No
G_100_(Co)	100	5	Glass	Yes
G_150_(Co)	150	4	Glass	Yes
G_200_(Co)	200	3	Glass	Yes
G_250_(Co)	250	3	Glass	Yes
Cl_100	100	3	Light carbon	No
Cl_150	150	4	Light carbon	No
Cl_200	200	4	Light carbon	No
Cl_250	250	3	Light carbon	No
Cl_100_(Co)	100	4	Light carbon	Yes
Cl_150_(Co)	150	3	Light carbon	Yes
Cl_200_(Co)	200	3	Light carbon	Yes
Cl_250_(Co)	250	3	Light carbon	Yes
Ch_100	100	3	Heavy carbon	No
Ch_150	150	4	Heavy carbon	No
Ch_200	200	4	Heavy carbon	No
Ch_250	250	3	Heavy carbon	No
Ch_100_(Co)	100	3	Heavy carbon	Yes
Ch_150_(Co)	150	3	Heavy carbon	Yes
Ch_200_(Co)	200	3	Heavy carbon	Yes
Ch_250_(Co)	250	4	Heavy carbon	Yes
B_100	100	5	Basalt	No
B_150	150	4	Basalt	No
B_200	200	4	Basalt	No
B_250	250	4	Basalt	No

steel plates; these were connected together via a set of seventeen bolts. Rubber plates were installed at the plate/ textile interface to increase friction and prevent damage to the textile. All bolts were fastened using a torque wrench.

Two LVDTs with a 20 mm stroke and a 0.05 mm sensitivity were used to measure the relative displacements between the TRM and the brick substrate. Displacements were also captured with digital image correlation (DIC) (Dantec), see, also, Fig. 4.5; the TRM surface was painted white to facilitate the DIC measurements.

The load was applied using a servo-hydraulic actuator fitted with a load cell with a maximum capacity of 100 KN at a displacement rate of 0.003 mm/s, i.e., 0.18 mm/ min which is typical for TRM to masonry bond tests (see, e.g., De Santis &

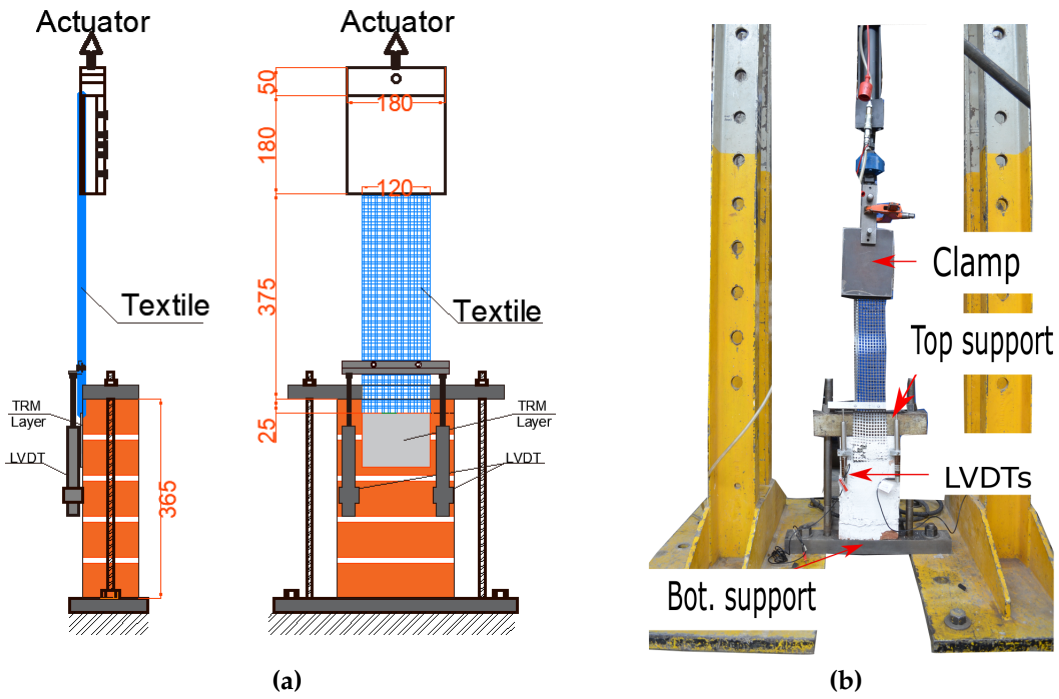

Figure 4.4: Test setup (a) test setup details (all dimensions in mm), (b) actual test setup

de Felice 2015) and ensures quasi-static conditions. Data was collected, synchronised and recorded using a fully-computerised data acquisition system at a frequency of 4 Hz.

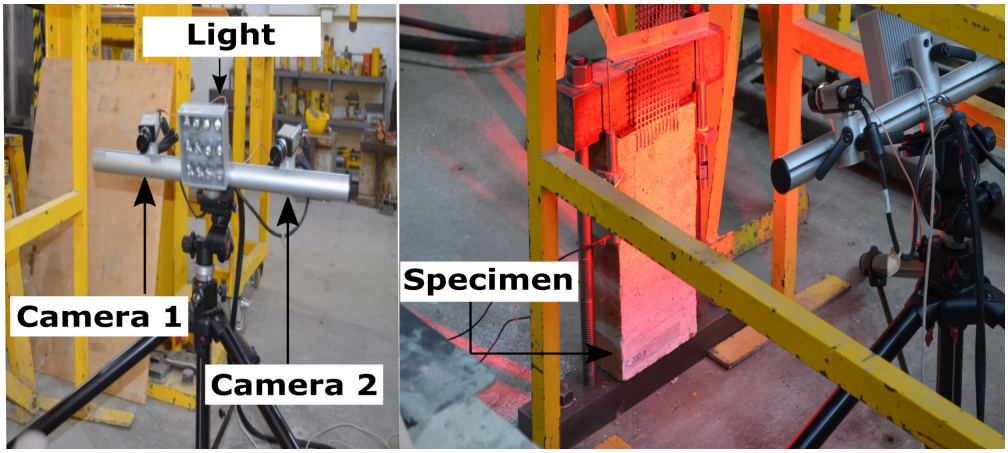

Figure 4.5: Test setup

4.2.4 Experimental Results

The force-slip paths for all specimens are shown in Fig. 4.6. For each group of identical specimens, the force-slip paths were derived by averaging the results of the three specimens that resulted in the lowest coefficient of variation; the failure mode

was examined and was found identical for each group.

The force-slip paths shown in Figs. 4.6c and 4.6e for the uncoated light and heavy carbon specimens, respectively, demonstrate an increasing linear branch up to a maximum load followed by a gradual reduction until the experiment is stopped. However, the response of the coated light and heavy carbon specimens, shown in Figs. 4.6d and 4.6f, respectively, are characterised by a sudden drop after the maximum load.

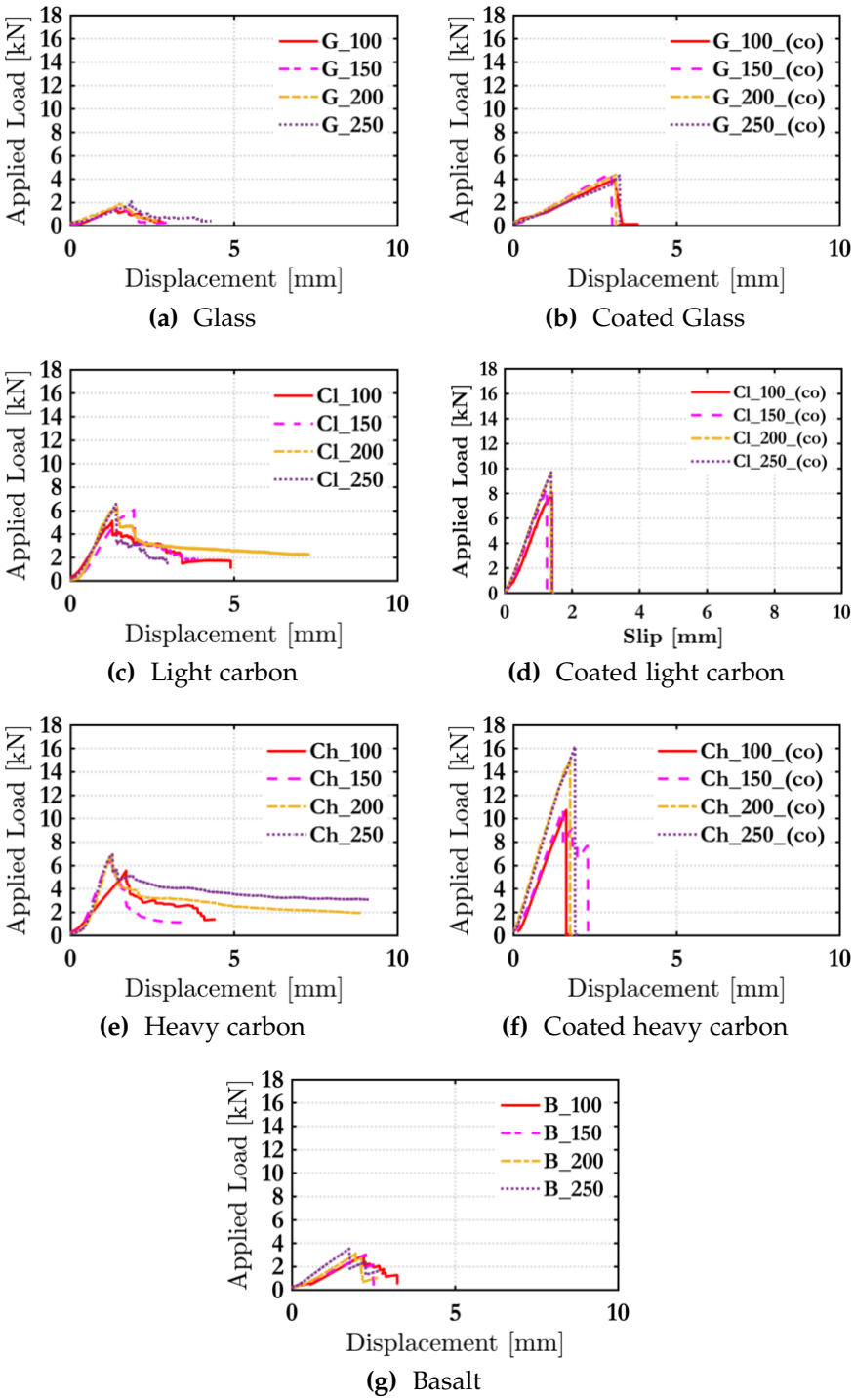

(a) Glass **(b)** Coated Glass

(c) Light carbon **(d)** Coated light carbon

(e) Heavy carbon **(f)** Coated heavy carbon

(g) Basalt

Figure 4.6: Bond tests results

The maximum loads P_{max}, the maximum stresses at the textile f^b_{max}, and the corresponding failure modes are summarised in Table 4.2 for all specimens. The maximum stress was evaluated using Eq. (2.22).

In terms of maximum load, the highest value was recorded for the case of coated heavy carbon Ch_250_(Co) at a bond length of 250 mm ($P_{max} = 16.11$ kN). The lowest value was 1.52 kN recorded in the uncoated glass specimen G_100 at a bond length of 100 mm.

Table 4.2: Bond test results: Average values of peak loads and peak stresses Failure modes according to Fig. 2.5

Specimen	Peak Load			Peak Stress			Failure
-	Mean [kN]	St.Dev [kN]	CoV -	Mean [MPa]	St.Dev [MPa]	CoV -	mode
G_100	1.52	0.15	0.10	262	26	0.10	D
G_150	1.82	0.25	0.14	313	43	0.14	D
G_200	1.89	0.30	0.16	325	52	0.16	D
G_250	2.05	0.40	0.20	352	69	0.20	D
G_100_(Co)	3.94	0.43	0.14	678	89	0.14	E1
G_150_(Co)	4.50	0.52	0.12	775	90	0.12	E1
G_200_(Co)	4.38	0.59	0.13	754	101	0.13	E1
G_250_(Co)	4.32	0.53	0.12	742	92	0.12	E1
Cl_100	5.44	0.33	0.08	731	55	0.08	D
Cl_150	6.07	0.20	0.03	815	27	0.03	D
Cl_200	6.32	0.23	0.04	849	30	0.04	D
Cl_250	6.57	0.47	0.07	883	63	0.07	D
Cl_100_(Co)	8.04	0.66	0.08	1080	89	0.08	C
Cl_150_(Co)	8.44	0.16	0.02	1133	21	0.02	C
Cl_200_(Co)	9.61	0.83	0.09	1292	112	0.09	C
Cl_250_(Co)	9.71	0.38	0.04	1304	51	0.04	C
Ch_100	5.53	0.72	0.13	475	62	0.13	D
Ch_150	6.01	0.74	0.01	548	8	0.01	D
Ch_200	6.60	0.54	0.08	567	46	0.08	D
Ch_250	6.65	0.51	0.08	571	44	0.08	D
Ch_100_(Co)	10.73	0.71	0.07	922	61	0.07	C
Ch_150_(Co)	10.77	0.59	0.05	925	51	0.05	C
Ch_200_(Co)	15.06	1.03	0.07	1293	89	0.07	C
Ch_250_(Co)	16.11	0.59	0.04	1384	50	0.04	C
B_100	2.96	0.32	0.13	637	83	0.13	E1
B_150	3.01	0.39	0.13	650	85	0.13	E1
B_200	3.16	0.12	0.04	682	25	0.04	E1
B_250	3.55	0.54	0.15	766	117	0.15	E1

D-sliding off the textile within the matrix;
E1-tensile rupture of the textile;
C-debonding at the textile-to-matrix interface;

4.2.5 Failure modes

The failure modes observed for the different bond lengths are shown in Figs. 4.7- 4.10 for the glass, light carbon, heavy carbon, and basalt textile fibre specimens, respectively.

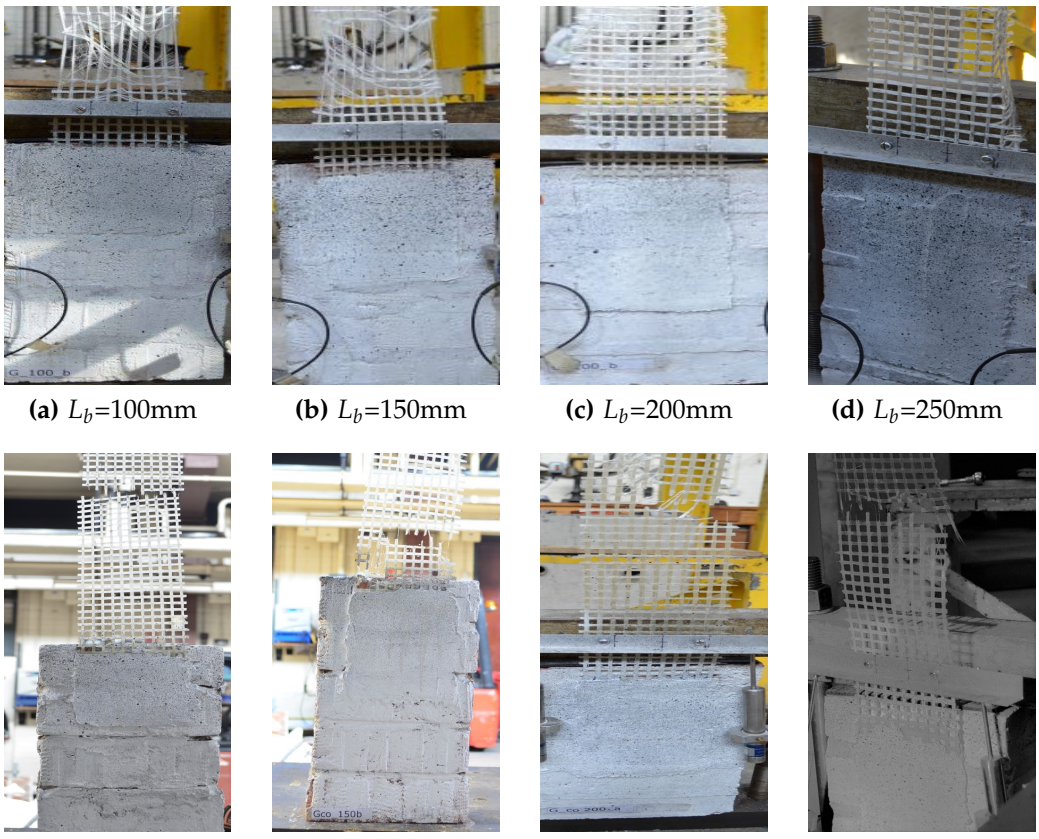

(a) L_b=100mm **(b)** L_b=150mm **(c)** L_b=200mm **(d)** L_b=250mm

(e) L_b=100mm **(f)** L_b=150mm **(g)** L_b=200mm **(h)** L_b=250mm

Figure 4.7: Typical failure modes of specimens strengthened with glass textile (a)-(d) uncoated and (e)-(h) coated glass fibre textiles.

Textile slippage occurred in all non-coated glass specimens and in all non-coated carbon specimens (both light and heavy). All the specimens strengthened with dry carbons fibre-textile material failed due to slippage of the carbon fibres at the textile-matrix interface. At the early stage of loading, hairline cracks initiated from the left towards to the right at the edge of the bonded region, which was followed by slippage of the textile through the mortar as presented in Fig. 4.8 a-b, and Fig. 4.9 a-b.

In all coated carbon specimens, either heavy or light, the failure mode observed was detachment at the matrix to matrix interface. When the load was close to the maximum load, the cracks were formed at the edge of the bonded region. This was followed by a gradual tensile failure of the mortar layer which resulted in complete

(a) L_b=100mm **(b)** L_b=150mm **(c)** L_b=200mm **(d)** L_b=250mm

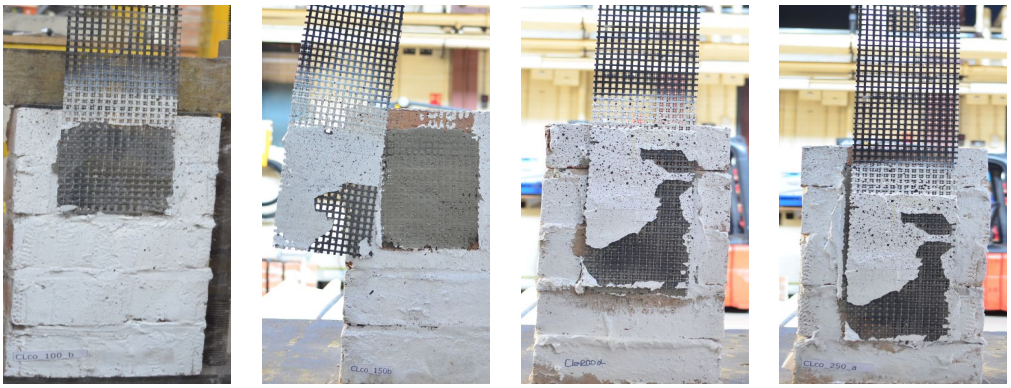

(e) L_b=100mm **(f)** L_b=150mm **(g)** L_b=200mm **(h)** L_b=250mm

Figure 4.8: Typical failure modes of specimens strengthened with light carbon textile (a)-(d) uncoated and (e)-(h) coated light carbon fibre textiles.

detachment of the textile from the mortar matrix as shown in Fig. 4.8 c-h, and Fig. 4.9 c-h. The effective bond length is larger than 250 mm for the case of both coated carbon textile fibre specimens where failure was manifested by detachment at the matrix to matrix interface. This is indicative of the fact that the strengthening mortar employed in this experimental campaign would not enable the textile to develop its tensile strength.

The failure mode observed in all basalt and coated glass specimens were textile rupture when the maximum load was attained (see Fig. 4.7 c-h and Fig. 4.10). In case of coated glass specimens with a bond length of 100 and 150 mm the cracks hairline formed when the maximum load was almost attained at the edge of the bonded area. Whereas the longest reinforcement of 200 and 250 mm, cracks appear initiated an early stage of loading at the edge of the TRM. In basalt textile specimens the hairline cracks were formed during the linear part of the load displacement curve at the border of the TRM material (see Fig. 4.6g). For the all anchorage lengths rupture of the textile

(a) L_b=100mm **(b)** L_b=150mm **(c)** L_b=200mm **(d)** L_b=250mm

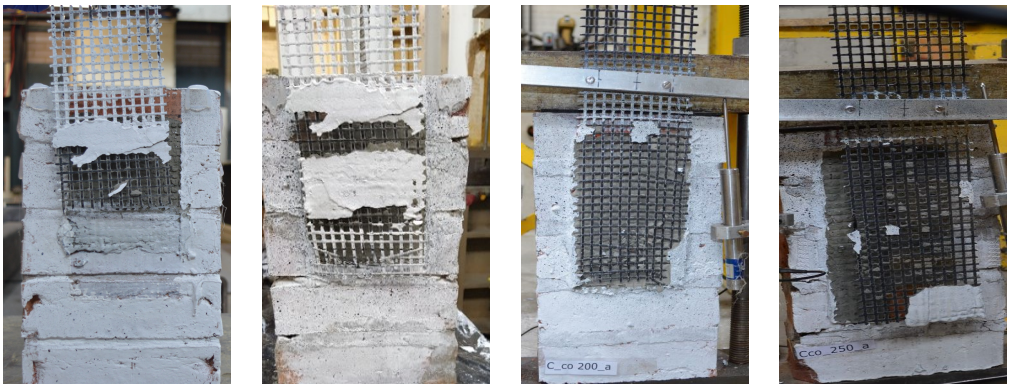

(e) L_b=100mm **(f)** L_b=150mm **(g)** L_b=200mm **(h)** L_b=250mm

Figure 4.9: Typical failure modes of specimens strengthened with heavy carbon textile (a)-(d) uncoated and (e)-(h) coated heavy carbon fibre textiles.

(a) L_b=100mm **(b)** L_b=150mm **(c)** L_b=200mm **(d)** L_b=250mm

Figure 4.10: Typical failure modes of specimens strengthened with basalt fibre textiles.

was observed adjacent to the bonded area as presented in Fig. 4.10

4.3 Discussion

4.3.1 The effect of the bond length

Increasing values of the bond length resulted in increasing values of the maximum attained load P_{max}. The variation of the average P_{max} in all materials for increasing values of the bond length is shown in Fig. 4.11. In all cases a linear trend is observed, with the exception of the coated heavy carbon fibre textile strengthened specimens. It is interesting to note that the main growing of the average P_{max} is observed in 150 mm bond length compared to 100 mm in case of uncoated glass and both uncoated carbons. The further increasing bond length resulting negligible rising of average P_{max}. In-house coated glass and manufactured coated basalt demonstrated practically same average P_{max} in case of all bond lengths.

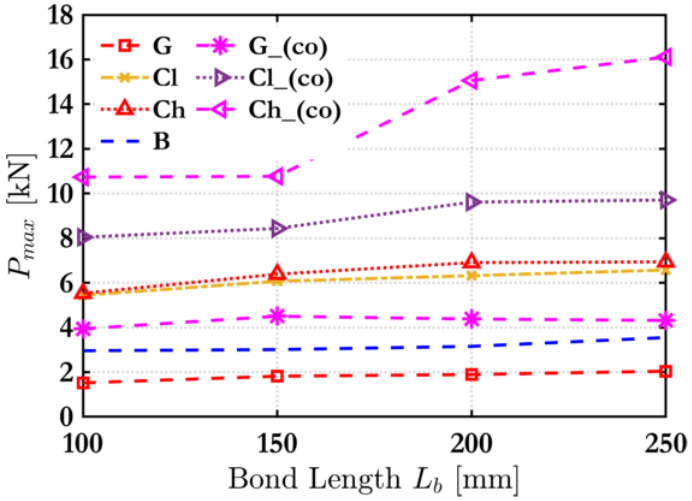

Figure 4.11: Variation of the ultimate load as a function of the bond length

With the exception of the coated heavy carbon textile fibre specimens, after a certain bond length the maximum load tends to stabilise (Fig. 4.11); this bond length corresponds to the effective bond length, L_{eff}. The effective bond length is in the range of 150-200 mm for the uncoated heavy and light and above 250 mm for the coated light carbon specimens.

The effective bond length seems to be larger than 250 mm for the case of the heavy coated carbon textile fibre specimens where failure was manifested by detachment at the matrix to matrix interface. This is indicative of the fact that the strengthening mortar employed in this experimental campaign did not enable the textile to develop

its tensile strength.

The coated heavy carbon specimens failure mode was textile debonding (in all bond lengths). However, the debonding mechanism is varying from the bond length. In the case of Ch_100_ (Co), the failure occurred sharply. The Ch_150_ (Co) failure starts with crack initiation in around 90% of the peak load and then moves to debonding of the textile. In the case of 200 mm and 250 mm bond length, the debonding starts at the same load level as the peak load in 100 and 150 mm, then the debonding stops, and the load starts to grow until the complete detachment.

The specimens that failed with slippage of the fibres within the matrix, i.e., uncoated glass, heavy and light carbon, demonstrated residual strengths that are associated with the friction forces developed at the fibre to mortar interface. The force is practically constant for the case of glass and light carbon fibre textiles and overall increases linearly with the bond length for the case of the heavy carbon fibre textile. The latter observation is consistent with the results reported in Raoof et al. (2016) where a similar textile fibre material was utilised. However, our results demonstrate that the residual strength greatly depends also on the fibre to mortar interface properties; in this case fibre pull-out tests can provide valuable insight (Dalalbashi et al. 2018).

Even though the observed failure mode in all basalt specimens was a textile rupture, the recorded P_{max} for L_b= 250 mm 12% increased with respect to the L_b =200 mm. However, in a former case, the failure mode was manifested by partial rupture textile, which hints at a misalignment of the applied load and attributed to uncertainties introduced by the test setup.

4.3.2 The effect of in house coating

The distribution of P_{max} for each material is shown in Fig. 4.14 for the case of L_b= 100, 150, 200 and 250 mm. The uncoated light and heavy textile fibre specimens practically attained the same maximum load; this agrees with the observed failure mode, i.e., textile slippage in both cases. Hence, the textile to matrix interface properties seem to largely depend on the smoothness of the roving surface rather than the geometry of the textile mesh.

The exploitation ratio, defined as

$$\rho_{TRM} = f^b_{max} \Big/ f^u_f \tag{4.1}$$

where f^b_{max} is the fibre textile ultimate tensile stress, f^u_f is the maximum stress at bond test result.

is plotted versus the bond length for each textile fibre material in Fig. 4.12.

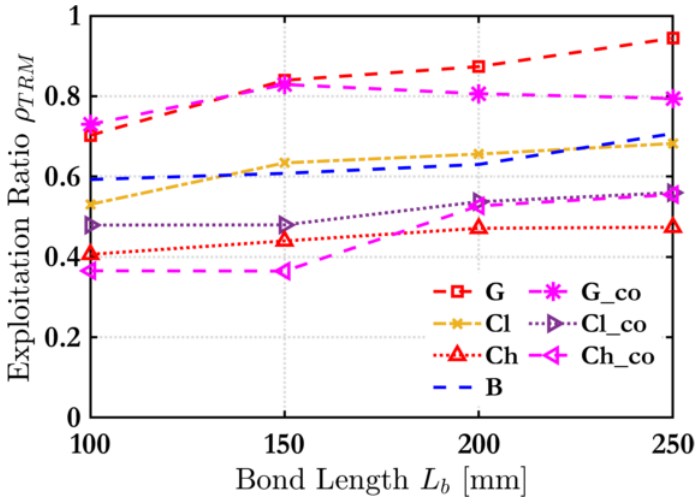

Figure 4.12: Exploitation ratio

Since the light carbon fibre textile has a lower nominal thickness (Table 3.4), a 1.5 times higher exploitation ratio is achieved in the case of the light carbon textile fibre material as shown in Fig. 4.12.

All coated specimens demonstrated increased values of P_{max} compared to the corresponding uncoated ones. In particular, the maximum load recorded for the 250 mm coated heavy carbon specimen increased by 142% compared to the uncoated one. The increase for the 250 mm coated light carbon fibre textile was 48%. Since in both cases the failure mode was identical, i.e., detachment at the textile to fibre interface, the difference in the effect of coating is attributed to the coarser mesh of the heavy carbon textile that allows for a better utilisation of the textile to mortar interlocking mechanism. However, it is of interest to note that the coated light and heavy carbon fibre textiles demonstrate practically identical exploitation ratios as shown in Fig. 4.12 hence rendering the light carbon fibre textile a more viable strengthening solution. In the case of glass textile, the increase was 158%, 147%, 131% and 110% for the 100, 150, 200 and 250 mm bond lengths Fig. 4.13.

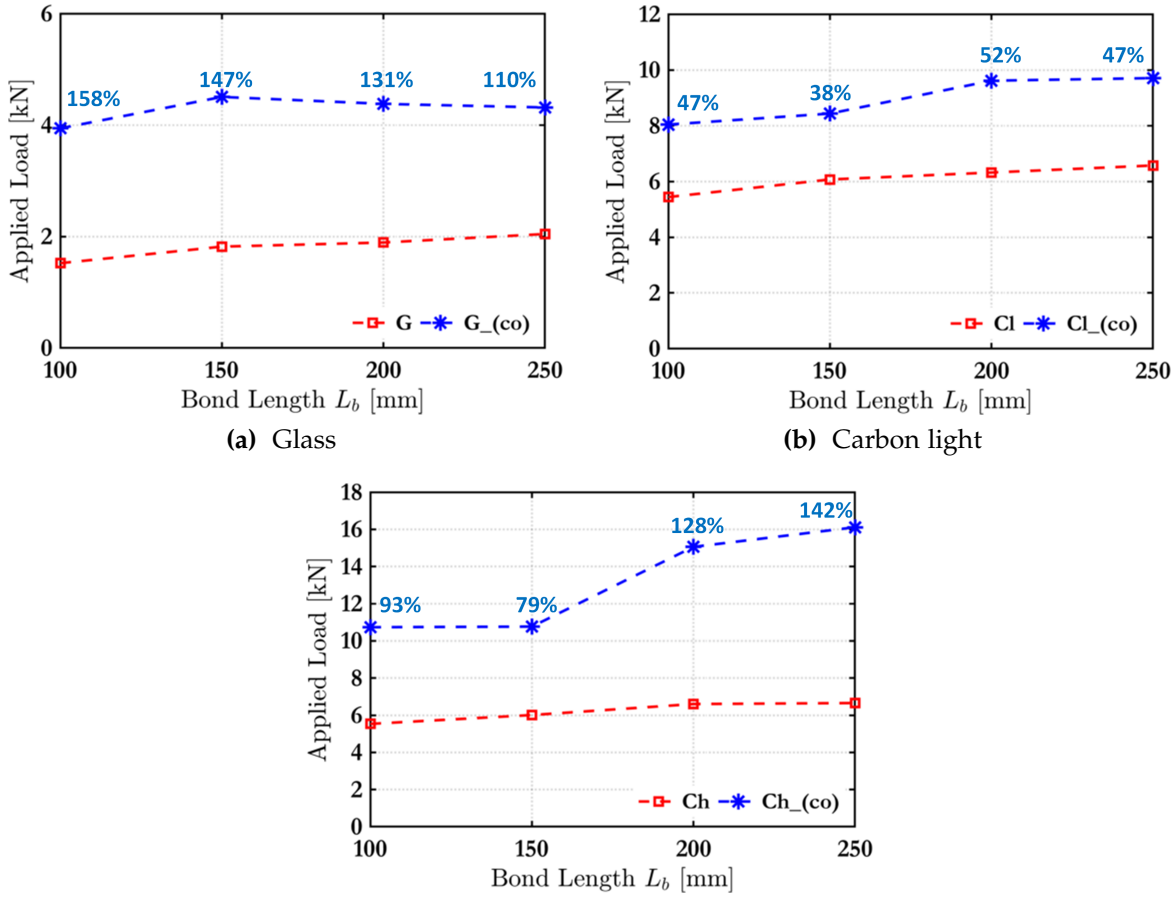

(a) Glass **(b)** Carbon light

(c) Carbon heavy

Figure 4.13: The effect of in house coating

The beneficial effect of the coating is two-fold. On the one hand, it increases the rigidity of the flexible mesh hence facilitating its application. In addition, it enhances the fibre to matrix stress transfer mechanism by bonding the inner and outer filaments of the rovings, also increasing the surface roughness of the latter. As a result, the distribution of stresses in the textile becomes more uniform, and the fibres are better utilised in carrying tensile forces. This is further reflected in Fig. 4.12 where all coated specimens demonstrate increased exploitation ratios compared to their uncoated counterparts. This becomes particularly evident when observing the failure modes of the specimens, which shifted from textile slippage to detachment at the matrix to matrix interface.

To investigate this hypothesis, P_{max} is plotted against the axial stiffness of the textile for the uncoated and the coated specimens in Figs. 4.15a and 4.15b, respectively. In each figure, 4 lines are plotted each corresponding to a particular bond length. The axial stiffness of the each textile is evaluated by Eq. 2.1 where t_f is the nominal

thickness shown in Table 3.4 and E_f is the Young's modulus determined from the tensile tests as shown in Table 3.4.

In the uncoated specimens, the effect of the axial stiffness is practically negligible. Furthermore, the spread between the lines corresponding to the different bond lengths is marginal. This clearly agrees well with the observed failure mode, i.e., textile slippage; the interface mechanism between the textile and the mortar dictates the response.

Conversely, in the case of the coated specimens (Fig. 4.15b), the increased axial stiffness is shown to magnify the effect of the bond length on P_{max} as manifested by the distance between the lines corresponding to identical bonded lengths. This further highlights the beneficial effect of the textile stiffness on enabling the uniform distribution of stresses within the matrix. Furthermore, for the same L_b, the maximum load increases with increasing axial stiffness, contrary to the uncoated specimens. This indicates that coating enhances the matrix to fibre interlocking mechanism by providing texture to the textile surface.

The aforementioned become particularly evident in the specimens strengthened with glass and carbon fibre textiles (either light or heavy). In the former case, the failure mode shifted from local slippage of the fibres to textile rupture. In the latter, the failure mode shifted from textile slippage to detachment at the matrix to matrix interface.

A minor downside of the full utilisation of the textile strength is that it results in reduced post-failure deformability. Furthermore, all coated specimens demonstrated null residual strengths as opposed to the uncoated specimens.

4.3.3 The effect of the textile fibre material

The type of the textile fibre material significantly affected the measured response. The distribution of P_{max} for each material considered is shown in Fig. 4.14 for the case of L_b= 100, 150, 200 and 250 mm. In Fig. 4.15, the recorded P_{max} are plotted against the axial stiffness of the fibre textile $K_t = t_f \cdot E_f$. The lowest values of P_{max} were recorded for the specimens strengthened with glass fibre textiles that have the lowest axial stiffness. Conversely, the specimens coated with heavy carbon textile fibre materials,

i.e., those bearing the highest axial stiffness resulted in the highest values of P_{max}. This is again attributed to the beneficial effect of the textile stiffness on enabling the uniform distribution of stresses within the matrix.

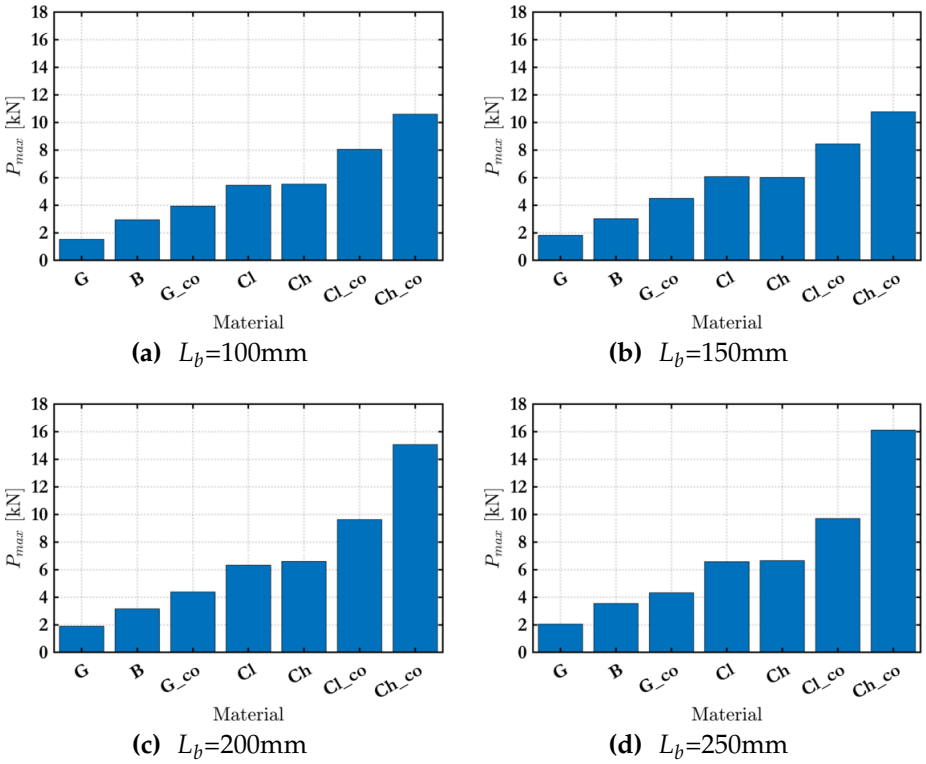

(a) L_b=100mm **(b)** L_b=150mm

(c) L_b=200mm **(d)** L_b=250mm

Figure 4.14: Maximum load P_{max} per material.

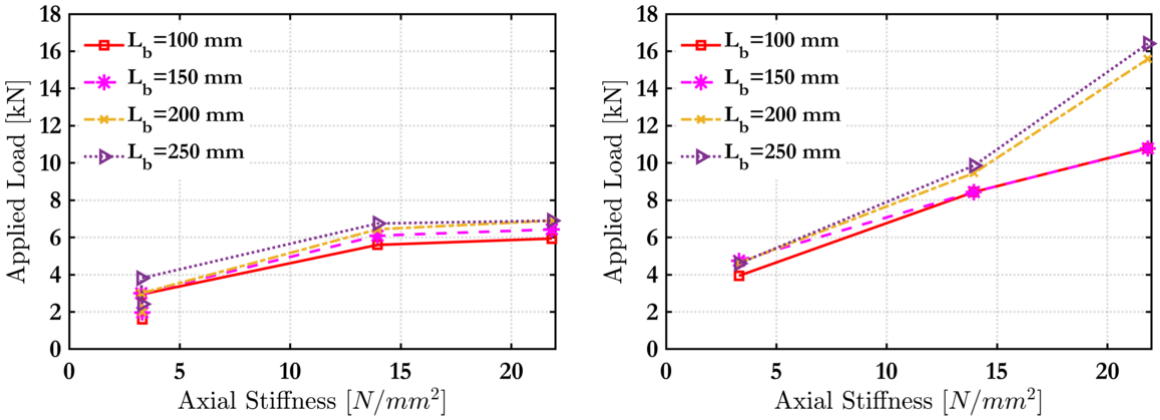

(a) Uncoated textiles **(b)** Coated textiles

Figure 4.15: Maximum load against the axial stiffness of the textile

It is of interest to note that even though the uncoated glass and the basalt textile fibre materials have practically the same axial stiffness, their corresponding maximum loads are not identical. In particular, the basalt textile fibre results in higher loads, despite the fact that its mesh is coarser. This is attributed to the different surface

properties of the glass and basalt rovings that in the former case impose a lower friction factor and hence facilitate slippage of the fibres within the mortar matrix. This hypothesis is further supported by the difference in the observed failure modes, i.e., textile rupture in the case of basalt versus textile sliding in the case of glass.

With the exception of coated glass, the exploitation ratios vary linearly with the bond length. The bilinear trend in the case of coated glass is attributed to the Even though the carbon textile fibre materials result in higher values of P_{max}, their corresponding exploitation ratios are lower than the glass textile.

4.4 Comparison to the literature

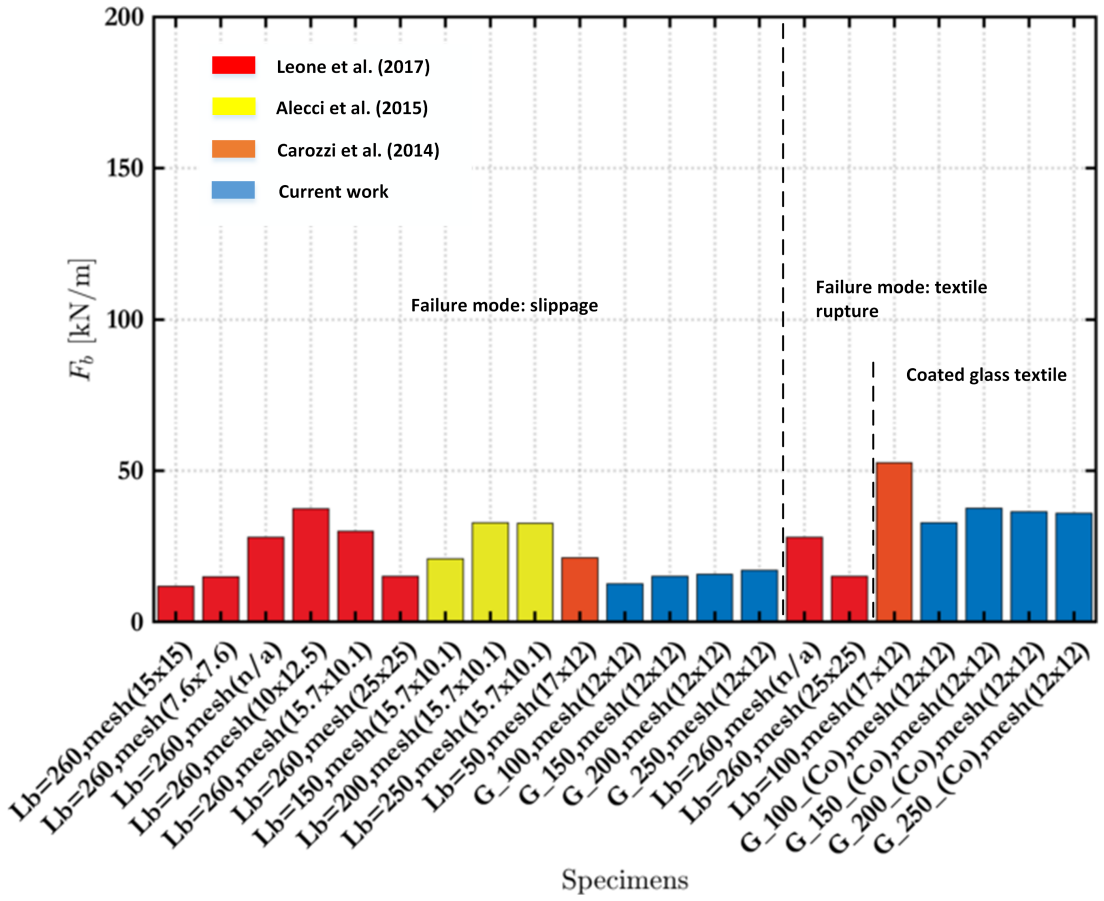

Figure 4.16: Glass fiber textile reinforced mortars: Average maximum load per unit width in shear bond tests(number before brackets represent bond lengths, mesh size in brackets)

Taking into account that textile materials have a different equivalent thickness de Felice et al. (2020) suggested that the load corresponding to tensile (f_t) or bond (f_b) failure normalized to the textile width, is a more representative metric of the TRM system response. In Figs. 4.16, 4.17, and 4.18, a direct comparison is attempted

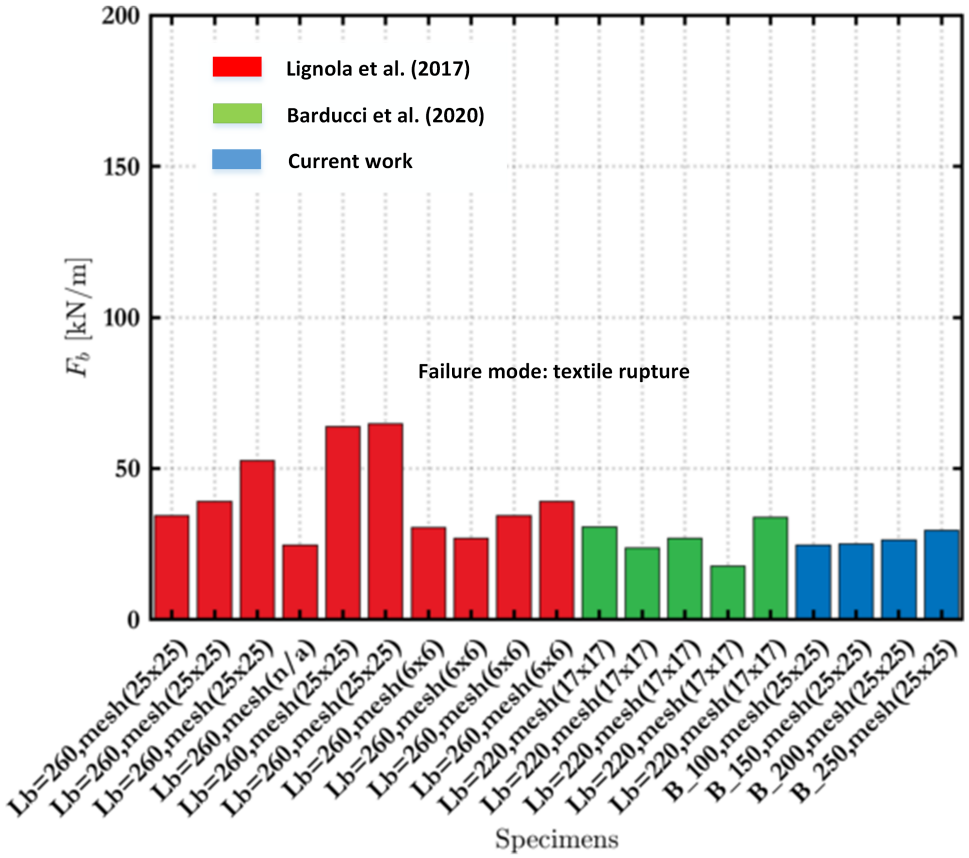

Figure 4.17: Basalt fiber textile reinforced mortars: Average maximum load per unit width in shear bond tests(number before brackets represent bond lengths, mesh size in brackets)

between the results obtained in this work and results available in the literature, i.e., from Carozzi et al. (2014), Leone et al. (2017), Lignola et al. (2017), Barducci et al. (2020), de Felice et al. (2020), De Felice et al. (2014), Ombres et al. (2018) as already discussed in Chapter 2.

With regards to the glass fibre textile specimens and the comparisons shown in Fig. 4.16, the following key observations are made. In Carozzi et al. (2014), a glass textile fibre material coated with styrene-butadiene rubber (SBR) of a 17x12 mm mesh size was used. The load per unit width obtained was 30 kN/m and 34 kN/m for the 100 mm and 150 mm bond lengths, respectively. The response is similar to that of the epoxy resin coated glass textile used in this study, i.e., 32 kN/m and 37 kN/m for the same bond lengths. In, Leone et al. (2017) three different glass fibre textiles were used with a 15x15 mm, 7.6x7.6 mm, and 25x25 mm mesh size respectively. The load per unit widths retrieved from Leone et al. (2017) were 11 kN/m, 15 kN/m, and 15.2 kN/m, respectively. These are similar normalised loads obtained in this research for the G_100, G_150, G_ 200, G_250 12.6 kN/m, 15.1 kN/m, 15.7 kN/m and 17.04 kN/m.

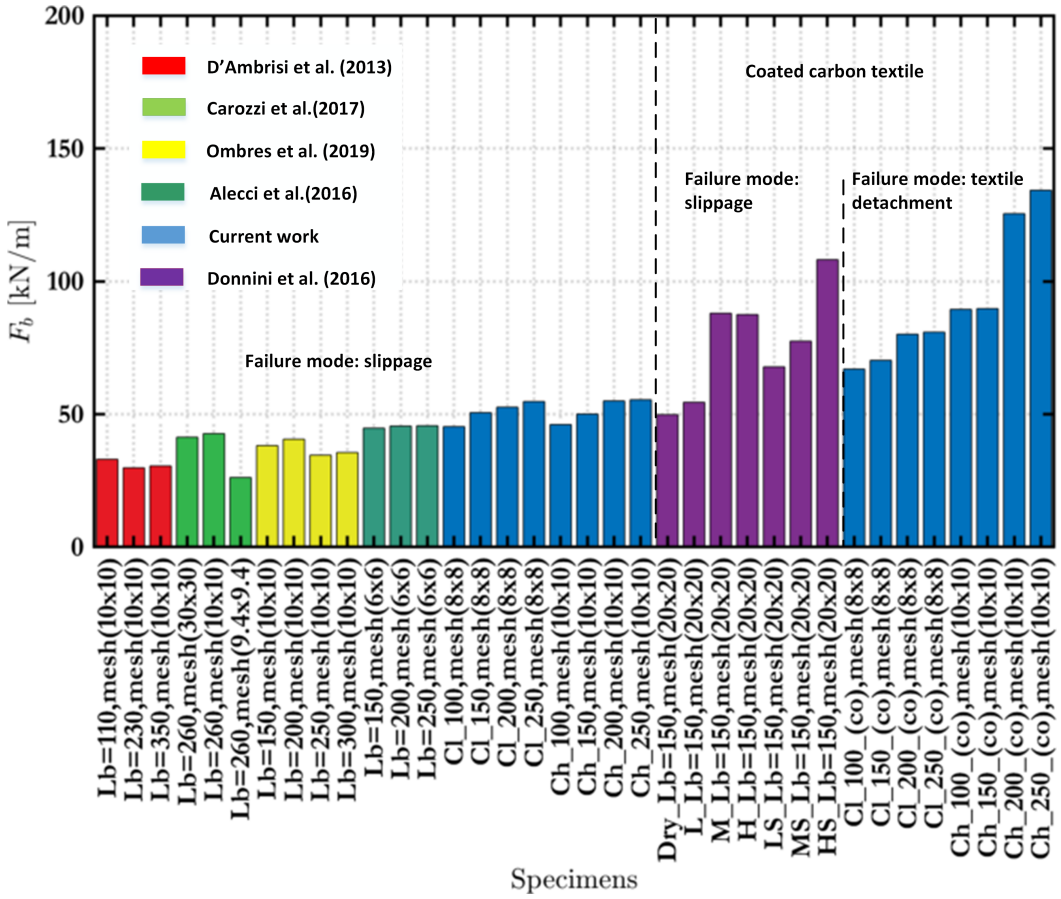

Figure 4.18: Carbon fiber textile reinforced mortars: Average maximum load per unit width in shear bond tests(number before brackets represent bond lengths, mesh size in brackets)

Lignola et al. (2017) used basalt of 25x25 mm, and 6x6 mm mesh size and higher young's modulus of 107 GPa. Load per unit width was 34.4 kN/m and 39 kN/m for 25x25 mm and 30.5 kN/m, 26.8 kN/m and 34.4 kN/m in 6x6 mm the anchorage length was equal to 260 mm in all cases.

Barducci et al. (2020) used basalt textile of 17x17 mm and several mortar matrixes. It is interesting to note that the result varies depending on the mortar used. For instance, commercially available mortar represents the best result 30.7 kN/m cement-based 23.7 kN/m and lime-based 26.9 kN/m. In the present study, the highest result shows specimens with 250 mm bond length 29.5 kN/m whereas the lowest 100mm 24.5 kN/m. The effect of the bond length did not investigate in the studies listed above.

de Felice et al. (2020) used carbon fibre-textile of the lower thickness of 0.047 mm compared with this study, and similar mesh size (10x10mm) and reinforced with fibre-reinforced cement, polymers. This resulted in slightly higher load per unit width,

equal to 63 kN/m concerning the current work. On the other hand, C4 specimens of practically the same mesh size of 9.4x9.4 mm and higher thickness of 0.061 mm and reinforced the same mortar demonstrate practically two times lower load per unit width of 36 kN/m. It interesting to note that the tests were carried out in different laboratories. This demonstrates that the mechanical characteristics of textile and mortar matrix may affect the bond test result, and the shear bond tests are sensitive to implementation, which changed from laboratory to laboratory. The current work result close to the highest result of de Felice et al. (2020) and equal to 55.4 kN/m.

In common, according to the Fig. 4.18 the current work results in good agreement with the De Felice et al. (2014), Ombres et al. (2018) where the same mesh size used.

The Fig. 4.18 demonstrates the load per width obtained in the experimental studies from Table A.2. Donnini et al. (2016) used carbon textile of mesh size in both directions (20x20 mm), compared to this study and constant bond length of 150 mm. The carbon fibres were in-house coated with different levels of epoxy resin impregnating, namely: dry fabric (Dry), light impregnation (L), medium impregnation (M), and high impregnation (H). Moreover, the effectiveness of quartz sand impregnation on fabric after coating was investigated with three levels of treatment such as light (LS), medium (MS) and high (HS). The increase between dry and medium impregnating was 76%. The response is similar to that of the epoxy resin coated textile used in this study, where 79% improvement compares to the dry textile was observed in the equivalent bond length 150 mm.

4.4.1 Analytical modelling

As highlight in literature behaviour of TRM strengthened masonry elements is primarily governed by the textile to mortar matrix interface, as the interface between the mortar matrix and the substrate is usually stronger when compared to the former(Grande et al. 2018, Wang et al. 2020). Therefore, a simple modelling strategy that assumes that the upper layer of the mortar matrix and the masonry substrate are rigid and fully coupled (no relative slip) is used in this study. Therefore, a simple modelling strategy that assumes that the upper layer of the mortar matrix and the masonry substrate are rigid and fully coupled (zero relative slip) is used in this study.

The nonlinearity of the strategy is only reflect on nonlinear behaviour at the interface between the textile and the top and bottom layer of the mortar matrices Fig. 4.19).

In this section, the bond-slip analytical model presented in Grande et al. (2018) is used in view of the experimental results derived in this work. The analytical model is derived on the basis of the following assumptions, i.e.,

(i). The support and the lower mortar layer (Fig. 4.19) are assumed rigid;

(ii). the (lower and upper) mortar/reinforcement interfaces are modelled as zero-thickness elements with only shear deformability;

(iii). the upper mortar layer and the reinforcement are assumed deformable only axially.

According to the hypotheses listed above, the deformation of an infinitesimal section is schematically represented in Fig. 4.20. Where the displacement of the textile (U_t) is equal to the lower interface slip (S_1), and the displacement of the top layer of the mortar matrix (U_m) is equal to the lower interface slip (S_1) minus the upper interface slip (S_1^e). There are, the normal stresses at the top layer of the mortar matrix (σ_m) and in the textile (σ_t),t-TRM thickness.

Furthermore, the following constitutive law is assumed between the textile interface and the lower mortar layer

$$\tau^i = \begin{cases} G^i s^i & \text{if } s^i \leq s_1 \\ 0 & \text{if otherwise} \end{cases}, \tag{4.2}$$

where τ^i is the shear stress at the interface, s^i is the slip at the interface, G^i is the shear modulus and s_1 is the slip threshold value.

In Grande et al. (2018), the model is derived on the basis of appropriate equilibrium and compatibility conditions to describe the following set of individual states

(i). DP0–undamaged state;

(ii). DP1–damage involving only the interfaces (debonding);

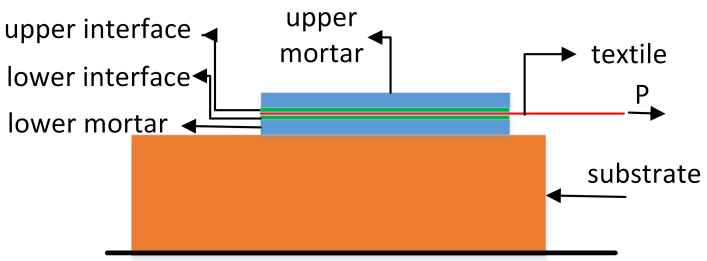

Figure 4.19: Schematic of the TRM system at the basis of the analytical model presented in Grande et al. (2018).

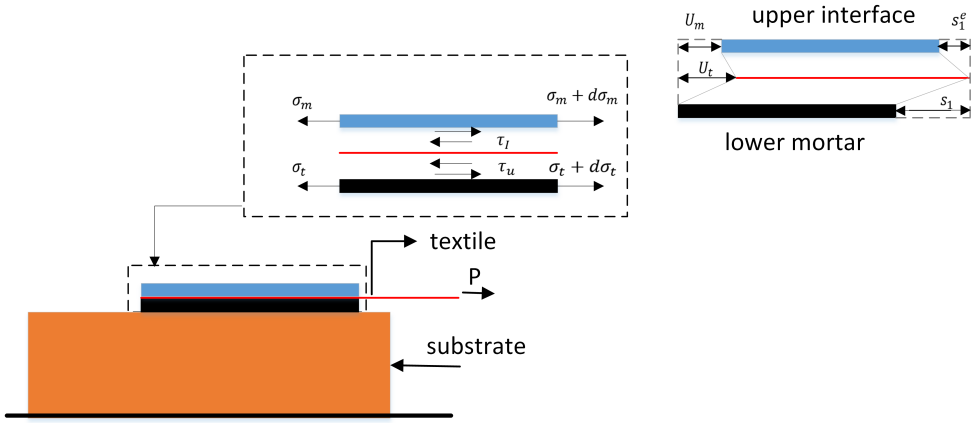

Figure 4.20: Stress equilibrium and deformation of infinitesimal section

(iii). DP2–damage involving only the upper mortar (cracking);

(iv). DP3–damage involving both the interfaces and the upper mortar (de-bonding/cracking).

Since in our experiments the failure modes observed were textile slippage in the uncoated and detachment and textile breakage in coated specimens, the only relevant states are DP0 and DP1; we consider that the matrix cracking observed at the coated specimens had only a minor effect in the observed response.

Considering the case of a specimen subjected to a controlled displacement with a maximum value δ_{max}, the governing equations describing the response of the specimen at DP1 are defined on the basis of three steps. At the end of the first step the lower interface is assumed to attain its shear strength at the loaded end of the specimen. At the end of the second step, the upper mortar to textile interface is assumed to have reached its shear strength. At this point, the lower interface is assumed to be debonded for a length a. At the end of the final step, the global slip has assumed the value δ_{max} and the upper interface has debonded for a length b Fig. 4.21. Hence, during the entire process the specimen is assumed to be slit in parts depending on

the values of the debonding lengths a and b.

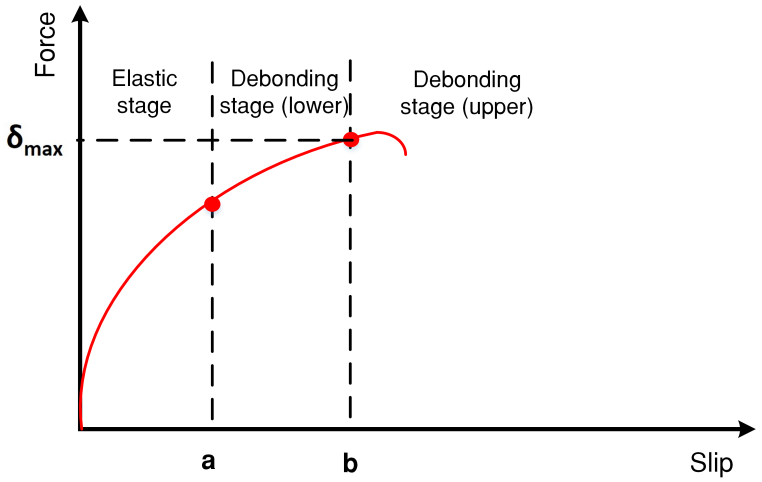

Figure 4.21: Debonding stages

Based on the aforementioned, the governing equations for the three sub-domains of the specimen are defined according to Eqs. (2.5)-(2.7) below.

In particular, Part "1" ($0 < x < L - a - b$) is governed by

$$\begin{cases} \frac{d^2 s_1^i}{dx^2} - K_1(s_1^i + s_1^e) = 0 \\ (\frac{d^2 s_1^i}{dx^2} - \frac{d^2 s_1^e}{dx^2}) + K_2 s_1^e = 0 \end{cases}, \tag{4.3}$$

where s_1^i is the slip of the lower interface at Part "1", s_1^e is the slip of the upper interface at Part "1" and $K_1 = G^i/t_f E_f$, $K_2 = G^i/t_c E_c$ are material constants; t_c and E_c are the thickness of the upper mortar layer and the mortar Young's modulus, respectively.

Furthermore, Part "2" ($L - a - b < x < L - b$) is governed by

$$\begin{cases} \frac{d^2 s_1^i}{dx^2} - K_1 s_1^e = 0 \\ (\frac{d^2 s_1^i}{dx^2} - \frac{d^2 s_1^e}{dx^2}) + K_2 s_1^e = 0 \end{cases} \tag{4.4}$$

and finally Part 3 (L-b< x< L) is governed by

$$\begin{cases} \frac{d^2 s_3^i}{dx^2} = 0 \\ \frac{d^2 s_3^i}{dx^2} - \frac{d^2 s_3^e}{dx^2} = 0 \end{cases} \tag{4.5}$$

Eqs. (4.3)-(4.5) can be solved considering also appropriate boundary and continuity conditions. Furhter information along with a thorough discussion on the ap-

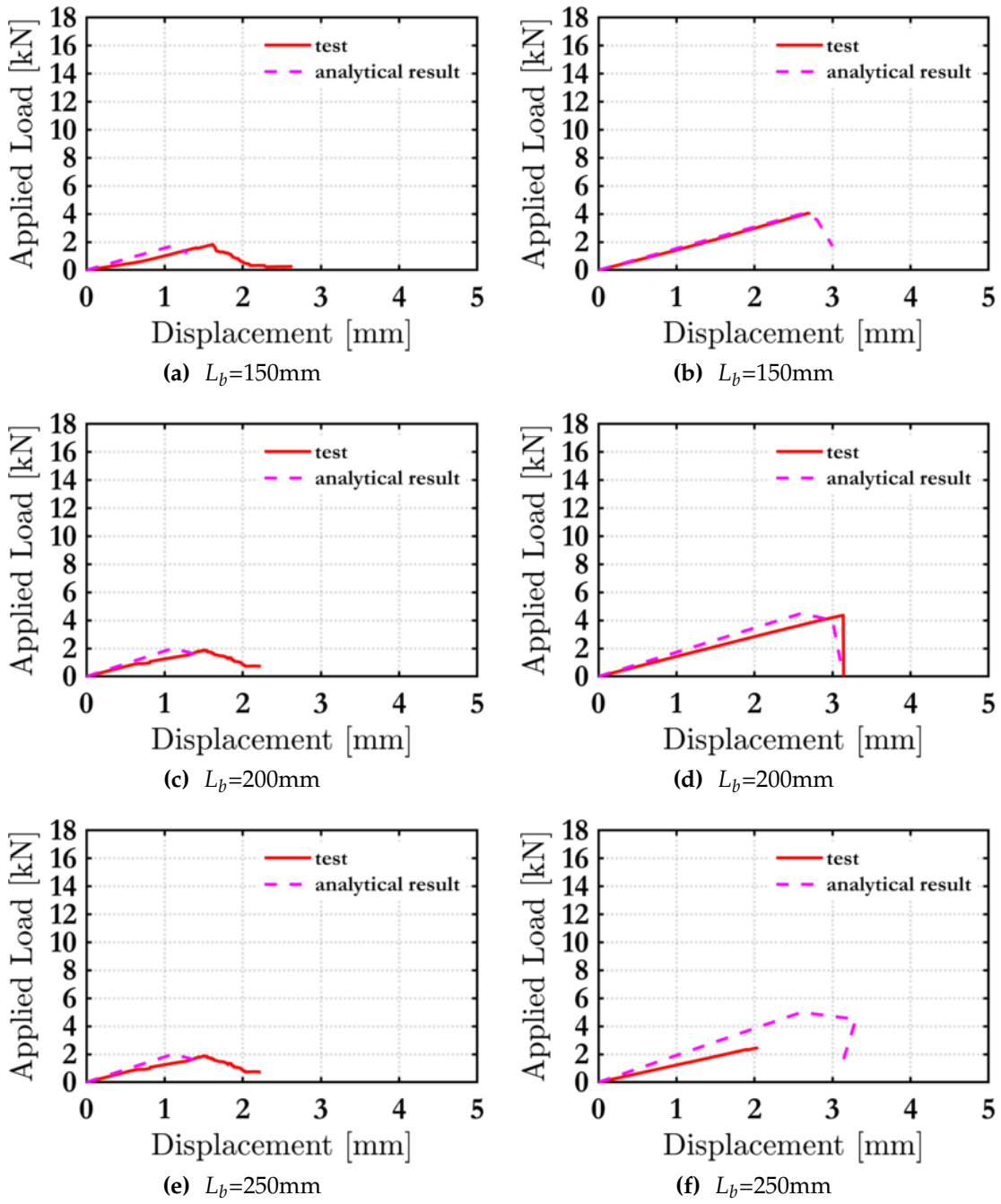

(a) L_b=150mm **(b)** L_b=150mm

(c) L_b=200mm **(d)** L_b=200mm

(e) L_b=250mm **(f)** L_b=250mm

Figure 4.22: Comparison of results of analytical models with experimental results glass and glass coated

plication of the model can be retrieved in Grande et al. (2018), see, also, Wang et al. (2020).

Indeed, the analytical model used in this study is considered only one failure mode as detachment of the textile fibre materials from the matrix and linear law with zero residual strength. The main purpose to usage of this model is to implement simple modelling strategy to capture the maximum values of load (δ_{max}) the slip (s_1) corresponding to δ_{max} in the independence of failure modes. This hypothesis is

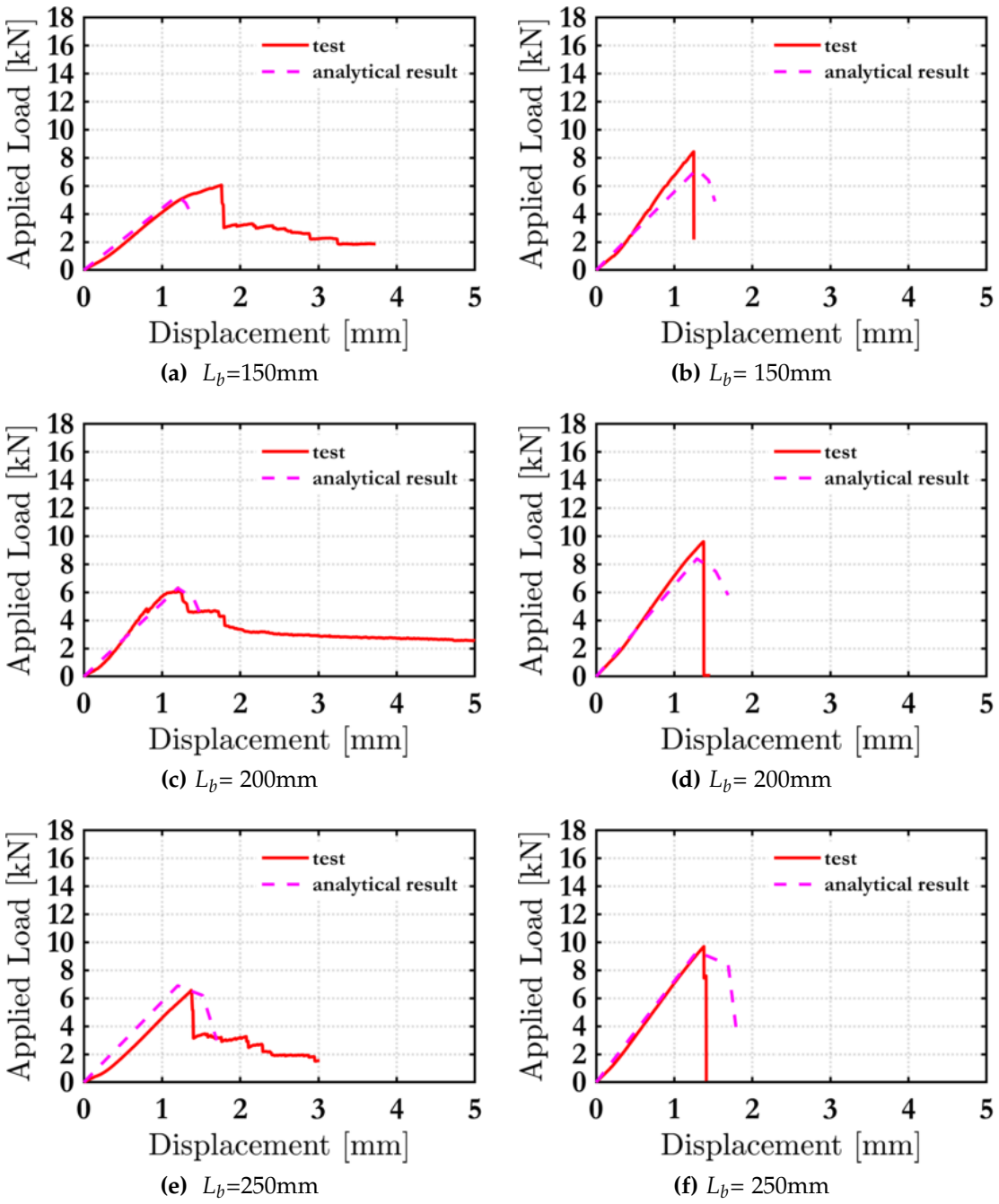

(a) L_b=150mm **(b)** L_b= 150mm

(c) L_b= 200mm **(d)** L_b= 200mm

(e) L_b=250mm **(f)** L_b= 250mm

Figure 4.23: Comparison of results of analytical models with experimental results carbon light and carbon light coated

supported by the result achieved.

The experimental data obtained in this experimental campaign compared with analytical model. The parameters used for the modelling are presented in Table 4.3. The comparison between, test results and analytical modelling of the load-slip response are shown in Fig. 4.22. The value of s_1 (the slip value corresponding to maximum load) at first was chosen from the result from bond test (average of s_1 between all bond lengths) then calibrated with shear strength of the interface τ_i until the result

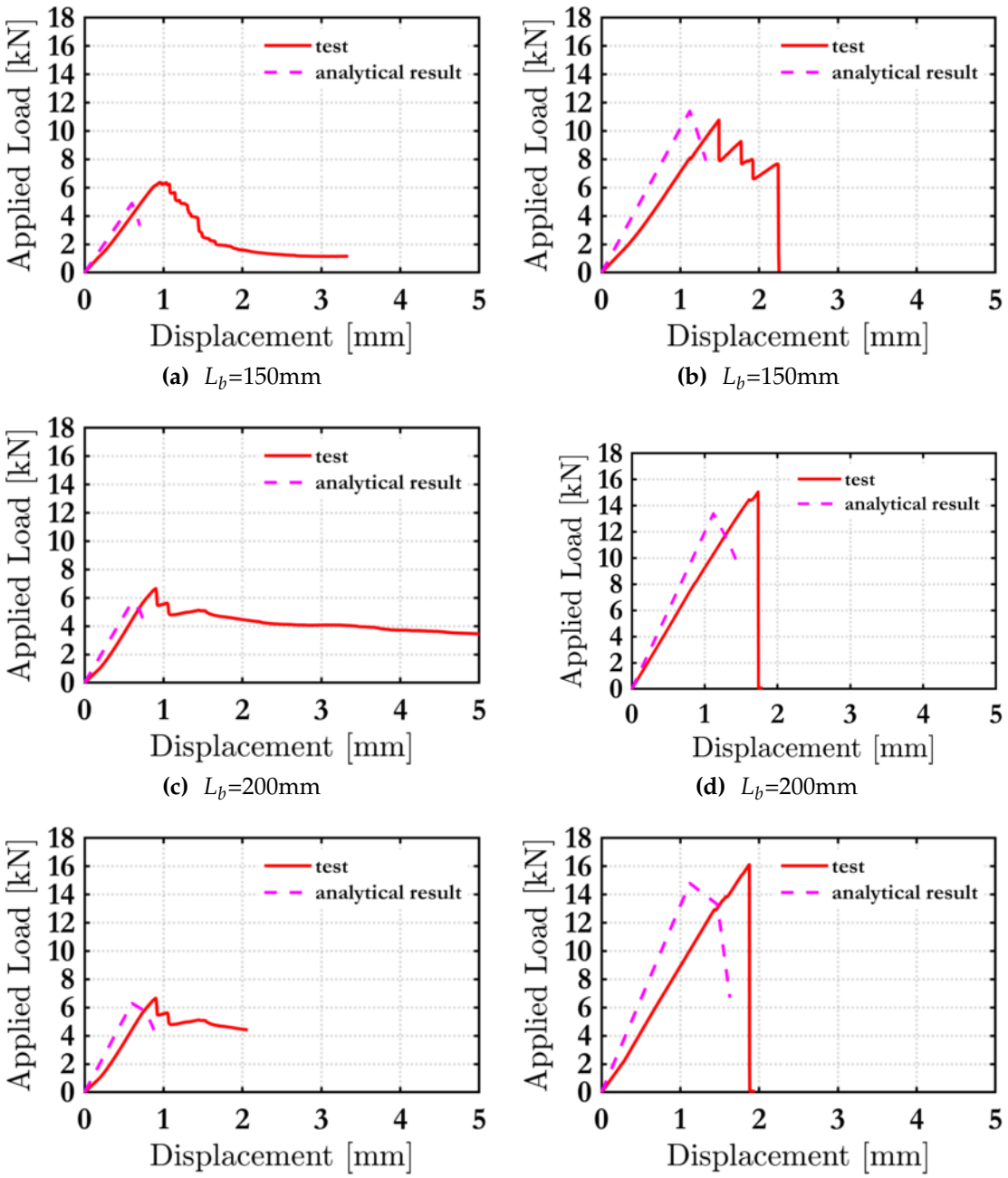

(a) L_b=150mm **(b)** L_b=150mm

(c) L_b=200mm **(d)** L_b=200mm

(e) L_b=250mm **(f)** L_b=250mm

Figure 4.24: Comparison of results of analytical models with experimental results carbon heavy and carbon heavy coated

is converged with test values. It should be noted that for the simplifications the s_1 value was constant in all bond lengths used. test result. The analytical result obtained from the model have a reasonable fitting with result from a real tests.

Even though the uncoated carbons textile materials parameters are slightly different, both demonstrate the same strength at the interface. The interface behaviour is crucial for the stress transfer between the matrix and the textile yarn. The adhesive property of the inorganic matrix is not as strong as in the FRP system. Furthermore,

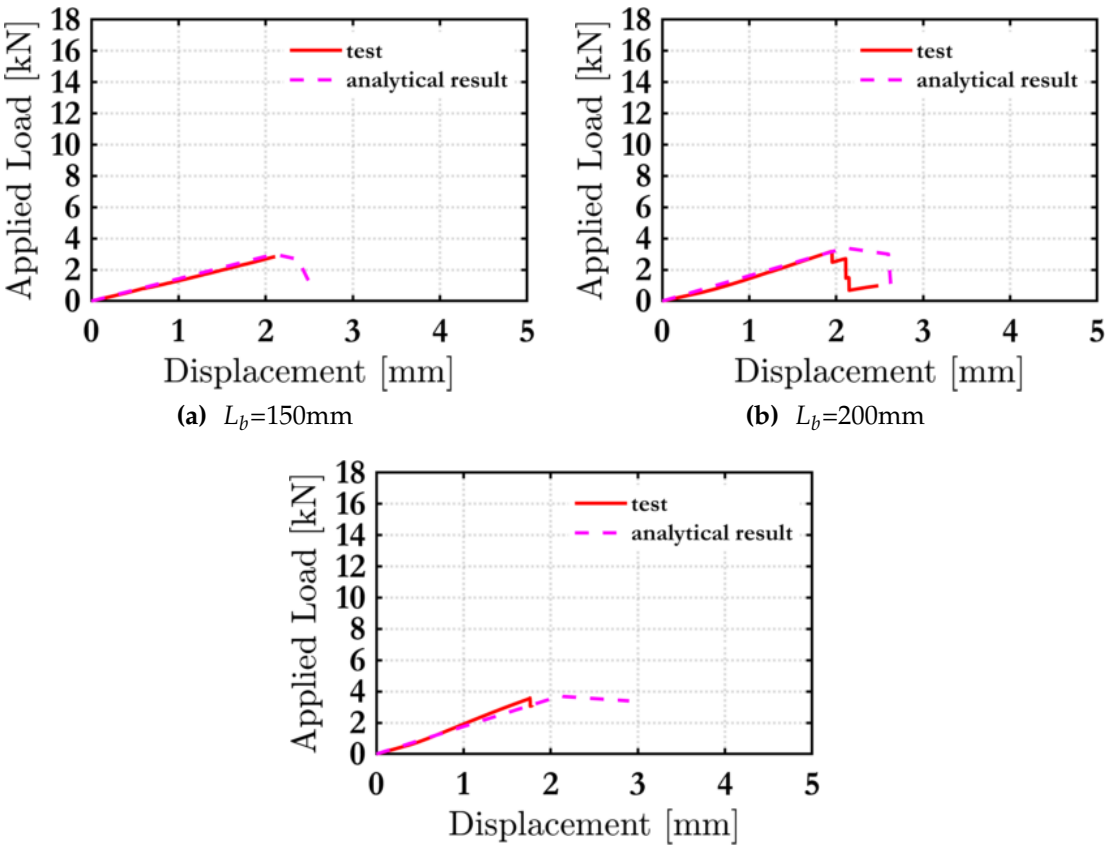

(a) L_b=150mm **(b)** L_b=200mm

(c) L_b=250mm

Figure 4.25: Comparison of results of analytical models with experimental results basalt

the cement grain is too large to penetrate the fiber yarns fully. These irregular penetrations lead to different inner and outer bond characteristics. The mesh size of the textile is different, and it can be assumed that the property of the textile may vary. The mortar penetrations in the large textile mesh can be worse than the smaller mesh size. Thus, it can lead to the equalisation of the strength at the interface between two uncoated carbons. Moreover, both textile represents the same failure mode slippage, which means that the failure mechanism is the same and the interface strength value can be close.

According to the result, the coated specimens demonstrate increasing interface strength is due to the after impregnation the textile becomes a rigid thin fabric and the slippage between filaments can be reduced. Moreover, the stress distribution is more uniform when the textile is coated, which is leads to more filaments taking parts in load carrying function.

As a result, the coating has increased the bonding in matrix and fibres interface and the resulting influence on both the peak load and the slip to the maximum applied

Table 4.3: Material parameters employed in the analytical mode. The calibrated parameters are highlighted in grey color.

Material	E_f	E_c**	t	t_f	τ_i	s_1
[-]	[GPa]	[MPa/GPa]	[mm]	[mm]	[MPa]	[mm]
Carbon (light)	140	15000/15*	4	0.062	0.35	1.2
Carbon (light) coated	170	15000/15*	4	0.062	0.50	1.4
Carbon (heavy)	160	15000/15*	4	0.097	0.35	0.9
Carbon (heavy) coated	196	15000/15*	4	0.097	0.7	1.5
Glass	47	15000/15*	4	0.044	0.10	1.1
Glass coated	196	15000/15*	4	0.044	0.10	2.6
Basalt	59	15000/15*	4	0.037	0.10	2.1

*Data reported in the data sheet

load. (see for example Donnini et al. (2016))

The model could reasonably capture the (δ_{max}) the slip (s_1) corresponding to δ_{max} in all four types of textile materials either coated or non-coated. However future work is recured to investigate the post peak responses of bond between TRM and masonry (residual strength) experimentally and analytically.

4.5 Concluding Remarks

An extensive experimental campaign was conducted to investigate the TRM to masonry bond strength considering as key investigated parameters the bond length, the textile fibre material, the effect of epoxy resin coating, and the strength of the mortar matrix. The main conclusions drawn for the experiments are summarised below:

(i). By increasing the bond length, the bond capacity increases bi-linearly for all materials examined. After a certain bond length, i.e., the effective bond length L_{eff}, the bond capacity marginally increases. With the exception of the coated carbon fibre textile fibre materials (heavy and light), the bond length was found to be L_{eff} =150 mm in all specimens.

(ii). In the high strength in-house coated carbon textile fibres, the mortar strength could not accommodate their increased tensile capacity and the specimens failed in detachment even at L_b= 250mm. Therefore the effective length is higher than 250 mm.

(iii). The in-house epoxy resin coating positively effected on the maximum load capacity in all bond lengths. The coated glass, light and heavy carbon. demonstrated increased values of P_{max} by 110%, 42%, and 132%, respectively when compared to their uncoated counterparts (250 mm bond length case).

(iv). The maximum loads recorded were found to increase with increasing values of the textile axial stiffness in an non-proportional manner.

(v). The values of P_{max} recorded for the industrially coated basalt textile fibre material were higher than the uncoated glass despite the fact that their axial stiffness is practically similar. Hence, in this case the bond relies primarily on the the fibre to mortar interface properties and hence highlights the importance of fibre pull out tests to further quantify the response.

(vi). The most positive effect of epoxy resin coating is observed in the case of heavy carbon and glass where the mesh size is 10 mm and 12 mm respectively. Whereas the light carbon with a mesh size of 8 mm does not provide the same maximum load increasing as glass and heavy carbon.

(vii). The bond behaviour as observed in analytical model is not only depend on the mechanical and geometrical properties of the textile and mortar matrix, but also the threshold value of slip (s_1) and the coefficient of shear stress at the interface (τ_i) at the interface between the textile and mortar matrix.

5

Masonry to TRM bond under fatigue loading

5.1 Introduction

The experimental campaign undertaken to investigate the TRM to masonry bond under fatigue loading is presented in this Chapter. As discussed in Chapter 2, the case of TRM to masonry bond under quasi-static conditions has been extensively investigated in the literature both from an experimental and an analytical/computational standpoint. Conversely, the case of low cycle fatigue has only very recently began to receive attention.

In this Chapter, the experimental campaign undertaken to investigate the bond behaviour between the TRM material and the masonry substrate under low cycle fatigue loading is presented, using different bond lengths and fibre-textile materials and epoxy-resin coating.

As was mentioned in chapter 2, If the maximum load in a load P^f_{max} cycle, is less than 50% of the quasi-static failure load, the test is to be performed under high-cycle fatigue conditions. High-cycle fatigue typically entails millions of cycles before the complete failure of the specimen (time-consuming test). On the other hand, if the maximum load P^f_{max} is greater than 50% of the quasi-static failure load, the test is to be performed under low-cycle fatigue conditions. The investigation in this work is confined to the low cycle fatigue as this experimental study attempts to investigate the influence of different P^f_{max} and compare between two textile materials and compare it

with available in literature data on FRP to concrete bond under fatigue load subjected to low-cycle fatigue loads applications.

According to Chapter 4, the basalt textile represents a proper exploitation ratio and has an undamaged strengthening area. The second stage was to investigate the influence of the loading regime on the in-house coated heavy carbon textile since this material showed better performance in the case of the maximum applied load. An increasing the bond lengths in specimens strengthening with basalt textile did no significant change the P_{max}. On the other hand, the increasing bond lengths in the case of the heavy-coated carbon displayed the increased P_{max}. Therefore, bond lengths also were chosen as a parameter, namely 150 mm, 200 mm and 250 mm. To thoroughly investigate the potential effect of low cycle fatigue loading, three load ranges was chosen (60%, 70% and 80%), which were also suggested in the literature see, e.g. Carloni et al. (2012), Zheng et al. (2015). The 100 kN actuator could not give the upper and lower limits expected. It can be due to the load range is too small for the 100 kN actuator. Therefore the actuator was changed to 25 kN, where the upper and lower load range was as expected. Next, to confirm that the actuator change would not influence the quasi-static test result, a series of single lap monotonic tests was conducted on a 25 kN actuator. In this research, a total of 54 specimens were tested under fatigue loading. The investigated parameters were the bond length, the loading range, and the textile fibre material. The experimental program is thoroughly described in the following sections, and the results are presented and discussed. The main conclusion is drawn based on the experimental results and discussion.

5.2 Experimental program

5.2.1 Test specimens and experimental setup

A single lap shear test experimental set-up was employed similar to the quasi-static case to facilitate comparisons between the two loading envelopes. The dimensions of the specimens, which were similar to the ones tested under quasi-static conditions (see also Chapter 4) are shown in Fig. 5.1 for the sake of completeness. Three different values of the bonded lengths of the textile were considered, i.e., 150 mm, 200 mm, and

250 mm as also shown in Fig. 5.1.

Table 5.1: Specimen details

Specimen	Type of fabrics	Bond length	Type of load	P_{max} (%)	Number of specimens
B_150_s	Basalt	150	static	-	4
B_200_s	Basalt	200	static	-	4
B_250_s	Basalt	250	static	-	4
B_150_c60	Basalt	150	fatigue	60	3
B_200_c60	Basalt	200	fatigue	60	3
B_250_c60	Basalt	250	fatigue	60	3
B_150_c70	Basalt	150	fatigue	70	3
B_200_c70	Basalt	200	fatigue	70	3
B_250_c70	Basalt	250	fatigue	70	3
B_150_c80	Basalt	150	fatigue	80	3
B_200_c80	Basalt	200	fatigue	80	3
B_250_c80	Basalt	250	fatigue	80	3
Ch_150_(Co)_s	heavy carbon	150	static	-	4
Ch_200_(Co)_s	heavy carbon	200	static	-	4
Ch_250_(Co)_s	heavy carbon	250	static	-	4
Ch_150_(Co)_c60	heavy carbon	150	fatigue	60	3
Ch_200_(Co)_c60	heavy carbon	200	fatigue	60	3
Ch_250_(Co)_c60	heavy carbon	250	fatigue	60	3
Ch_150_(Co)_c70	heavy carbon	150	fatigue	70	3
Ch_200_(Co)_c70	heavy carbon	200	fatigue	70	3
Ch_250_(Co)_c70	heavy carbon	250	fatigue	70	3
Ch_150_(Co)_c80	heavy carbon	150	fatigue	80	3
Ch_200_(Co)_c80	heavy carbon	200	fatigue	80	3
Ch_250_(Co)_c80	heavy carbon	250	fatigue	80	3

The specimens were masonry wallets comprising five clay bricks with individual dimensions of 215 x 102.5 x 65 mm. The joint thickness was 10 mm in all cases. The total height of each wallette was 365 mm. The bonded area had a width equal to 120 mm. The bonded area was positioned at a 25 mm distance from the wallet edges to prevent any undesirable edge effects. The thickness of the TRM layer was approximately 6 mm.

All samples were strengthened with a single TRM layer. The preparation of the specimens was performed according to the following steps. First, the TRM border lines were marked on the specimen (Fig. 5.2a). Then dust removed from the surface with air pressure and the wallette surface was slightly damped with water. The first layer of the cement-based mortar applied to the prepared surface (Fig. 5.2b) then textile attached and pressed to allow mortar to penetrate throughout fabric mesh

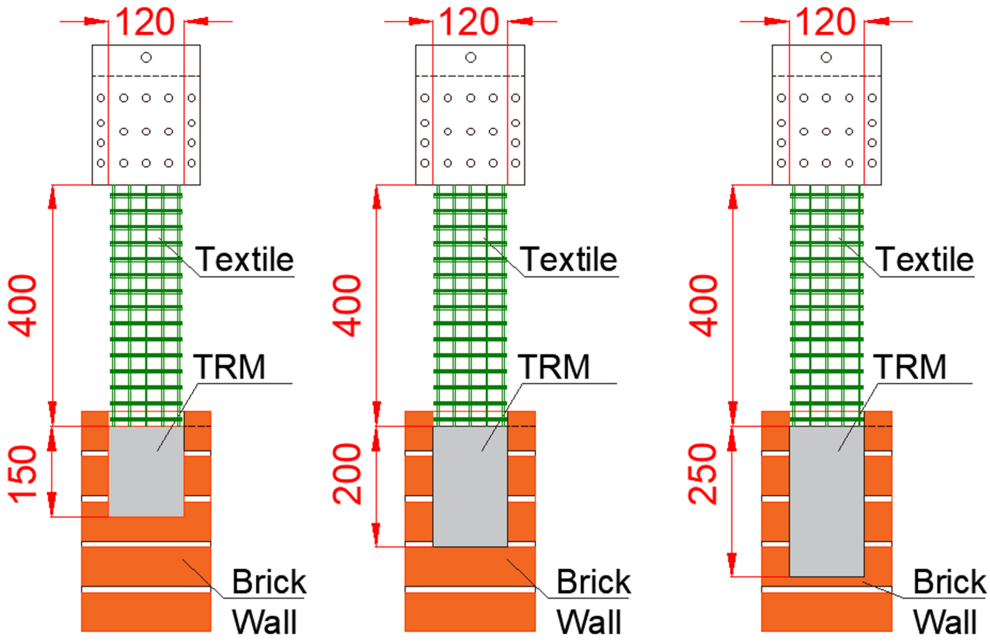

Figure 5.1: Variation of bond lengths

(Fig. 5.2c). A final textile layer was applied to completely cover the textile (Fig. 5.2d).

The specimen was fixed between two rigid steel plates with dimensions of 60 x 60 x 500 mm. The two plates were connected through 4 steel rods to ensure that the wallet would not move upwards during load application. The bottom plate was fixed with two steel plates on the strong floor Fig. 5.3b.

The free length of the textile was 400 mm in all specimens. The textile was connected to the actuator using two steel plates. Rubber pads were used at the textile to steel interface to improve grip and avoid damage to the textile. The naming convention used for the specimens is X_V1_Y_V2 where X corresponds to the textile fibre material, i.e., B for basalt and Ch for heavy carbon, and V1 corresponds to the bonded length. Furthermore, Y corresponds to the loading condition, i.e., 's'-static' and 'c'-cyclic, and V2 denotes the maximum applied load P^{f}_{max}. Finally, the suffix 'Co' denotes the application of in-house coating Table 5.1.

Two linear variable differential transducers (LVDTs) with a maximum stroke of 15mm were directly attached on the wallette. Two similar LVDTs were used to measure the relative displacement of the textile to the wall Fig. 5.3. The load-slip response was recorded with a fully computerised data accusation system at a constant rate of 4 Hz.

(a) Step1

(b) Step2

(c) Step3

(d) Step4

Figure 5.2: TRM layer application steps

It should be noted that after several attempts conducted with the 100 kN actuator, it was clearly seen that the load range expected was too far from the actual upper and lower limits, mainly higher, and this was leading to the premature failure of the specimens. Then the same attempt was made with the 25 kN actuator, where the upper and lower load range were accurate. Then to confirm that the actuator's change would not influence the quasi-static test results, a series of the single lap monotonic test was conducted on the 25 kN actuator. Comparing these results to the results alredy discussed in Chapter 4, it was concluded that the change of the actuator did not have any influence.

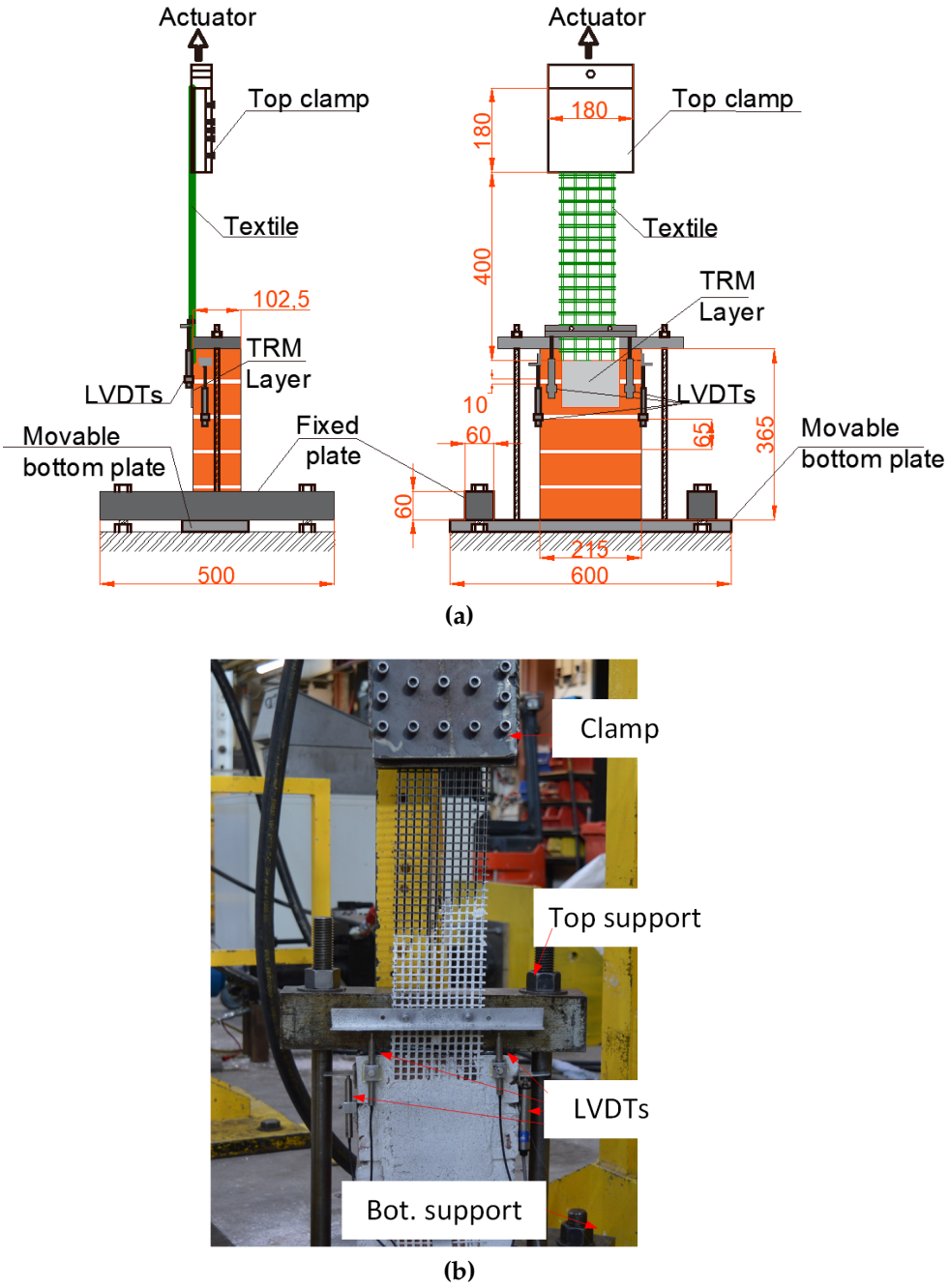

Figure 5.3: (a) Test setup dimensions (all dimensions in mm), (b) Actual test setup

5.2.2 Fatigue testing loading envelopes

The upper and lower bounds of the cyclic envelop were established with respect to the failure load derived from the quasi-static test for each configuration.

As discussed in Section 2.5.1 the fatigue test was carried out within a range of a maximum (P^f_{max}) and a minimum (P^f_{min}) load value. According to the literature when the P^f_{max} is less than 50% of the maximum load from the quasi-static tests, the test cor-

responds to high-cycle fatigue conditions. Conversely, when P^f_{max} is higher than 50% of the maximum load the test corresponds to low-cycle fatigue conditions (Carloni et al. 2012). A typical low-cycle fatigue envelope are considered in this experimental work(Carloni et al. 2012, Zheng et al. 2015). The upper boundary of the load envelope was defined as $P_{upper} = 0.6P_{max}$, $P_{upper} = 0.7P_{max}$ and $P_{upper} = 0.8P_{max}$; the lower boundary of the loading envelope was defined as $P_{lower} = 0.15P_{max}$. The load P^f_{max} is the average value of the maximum loads recorded under quasi-static conditions see, e.g, (Carloni et al. 2012, Zheng et al. 2015).

It is of interest to note that according to typical fatigue testing procedures, all specimens were pre-loaded up to the mean value of the cyclic load range (D'Antino et al. 2015). No damage was observed in all specimens during this preloading stage. The mean value was calculated according to the following equation

$$P_{meanA} = (P^f_{max} + P^f_{min})/2 \tag{5.1}$$

where the amplitude values were calculated as:

$$P_{amplitude} = (P^f_{max} - P^f_{min})/2 \tag{5.2}$$

All fatigue tests were conducted in load control at a rate of 1Hz. Data were recorded with a fully computerized acquisition system at a constat rate of 4Hz.

5.3 Experimental results from the quasi static bond tests

The identified key parameters of the experimental results, i.e., the maximum load of each specimen, the average maximum load, and the observed failure modes, are summarised in Table 5.2. Four identical specimens were used for each bond test configuration. The resulting force-displacement plots are shown in Fig. 5.4 for the specimens strengthened with basalt textile and Fig. 5.5 for the specimens strengthened with coated carbon. As expected, in all cases the load increases linearly until failure (Fig. 5.4, Fig. 5.5).

In the basalt textile material specimens, the failure mode was textile fracture out

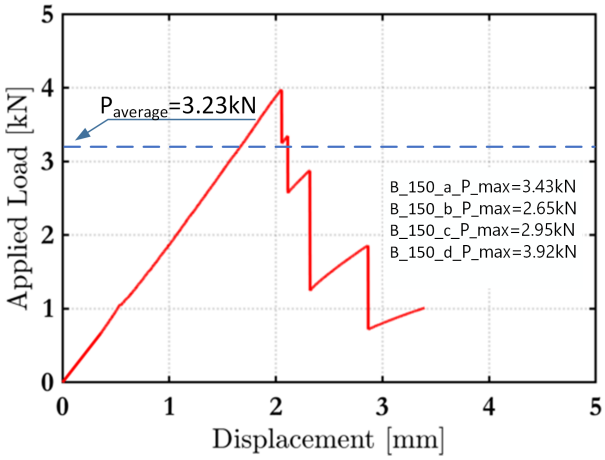

(a) L_b=150mm

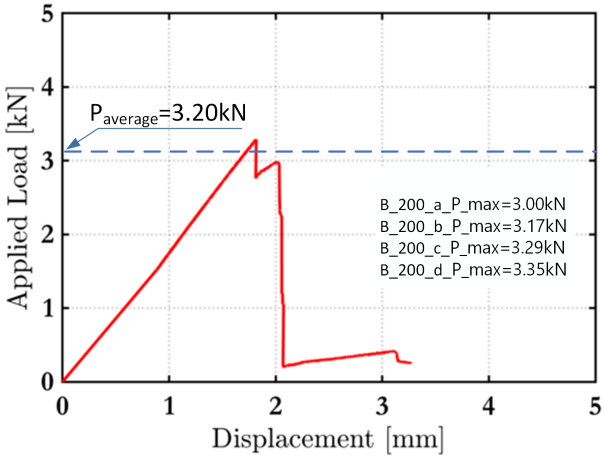

(b) L_b=200mm

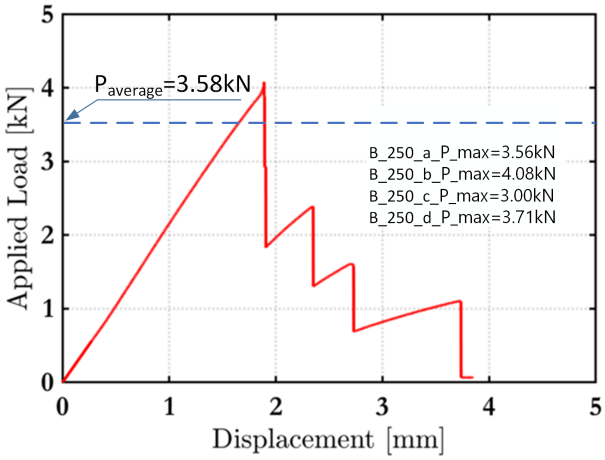

(c) L_b=250mm

Figure 5.4: Typical applied load–global slip response for monotonic quasi-static tests for various bond lengths in case of basalt textile (25kN actuator): (a) 150mm, (b) 200mm and (c) 250mm

of the matrix in all cases; this indicated that full bond conditions were achieved even at the 150 mm bond length in the basalt textile material. As a result, the average values of the attained maximum loads for all bond lengths were very close, see also,

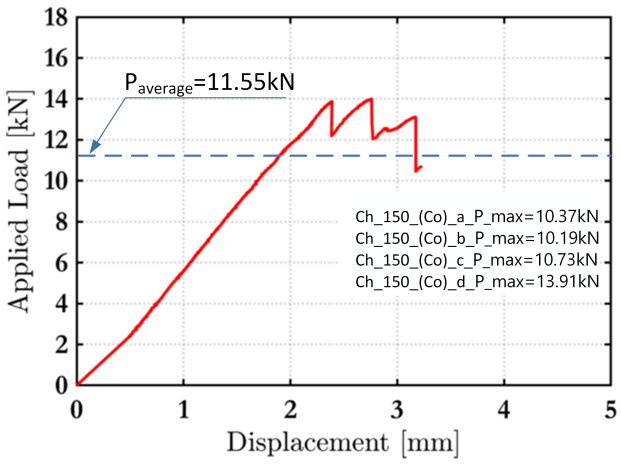

(a) L_b= 150mm

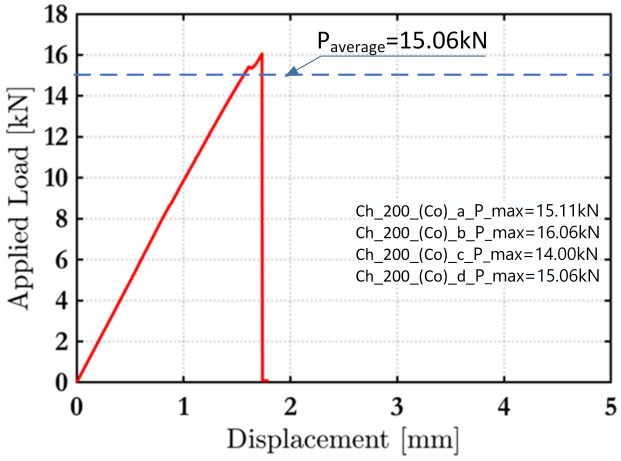

(b) L_b=200mm

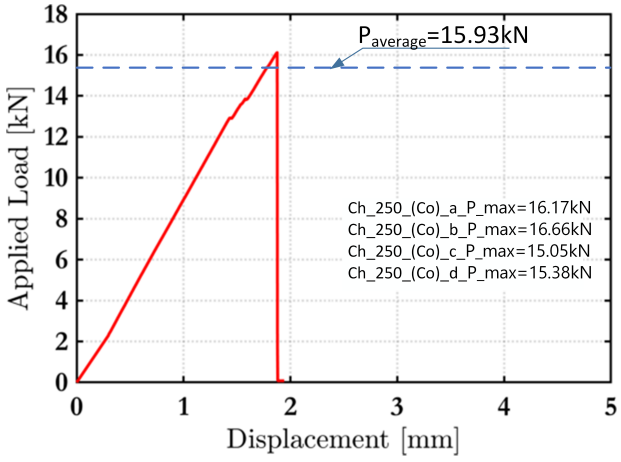

(c) L_b=250mm

Figure 5.5: Typical applied load–global slip response for monotonic quasi-static tests for various bond lengths in case of heavy coated carbon textile(25kN actuator): (a) 150mm, (b) 200mm and (c) 250mm

Fig. 5.4.

In the case of the coated heavy carbon textile material, the failure mode was

detachment at the matrix to substrate interface in all cases. The corresponding maximum loads were hence linearly increasing as a function of the bond length as shown in Fig. 5.36, the maximum load increasing maximum applied load with increasing the bond lengths. Thus, in this case the mortar matrix would not provide the required level of bond even at the 250 mm bond length.

Table 5.2: Average test result for monotonic quasi-static tests.

Specimen bond length	Test result by specimen [kN]				Average [kN]	Failure mode
	a	b	c	d		
B_150	3.43	2.65	2.95	3.92	3.23 (0.55)* (0.17)**	E1
B_200	3	3.17	3.29	3.35	3.2 (0.15)* (0.05)**	E1
B_250	3.56	4.08	3	3.71	3.58 (0.45)* (0.12)**	E1
Ch_150_(Co)	10.37	10.19	10.73	13.91	11.55 (1.42)* (0.12)**	C
Ch_200_(Co)	15.11	16.06	14.00	15.08	15.06 (0.72)* (0.04)**	C
Ch_250_(Co)	16.17	16.66	15.5	15.38	15.93 (0.52)* (0.04)**	C

**Standard deviation
**Coefficient of variation
E1-Tensile failure of the textile out of the matrix
C-Detachment at matrix to substrate interface

Table 5.3: Results from quasi-static tests: Comparisons between the 100 kN and 25 kN actuators

Actuator Capacity [kN]	Specimen	Maximum Load (average) [kN]	Deflection at maximum load [mm]	Failure Mode
100	B_150	3.01(0.39)*(0.13)**	2.24(0.14)*(0.06)**	E1
	B_200	3.16(0.12)*(0.04)**	1.93(0.11)*(0.07)**	E1
	B_250	3.55(0.54)*(0.15)**	1.75(0.08)*(0.04)**	E1
	Ch_150_(Co)	10.77(0.59)*(0.05)**	1.48(0.13)*(0.06)**	C
	Ch_200_(Co)	15.06(1.03)*(0.07)**	1.73(0.14)*(0.08)**	C
	Ch_250_(Co)	16.11(0.59)*(0.04)**	1.88(0.11)*(0.06)**	C
25	B_150	3.23(0.55)*(0.17)**	2.13(0.10)*(0.04)**	E1
	B_200	3.2(0.15)*(0.05)**	1.87(0.06)*(0.03)**	E1
	B_250	3.58(0.45)*(0.12)**	1.815(0.65)*(0.04)**	E1
	Ch_150_(Co)	11.55(1.42)*(0.12)**	1.935(0.15)*(0.09)**	C
	Ch_200_(Co)	15.06(0.72)*(0.04)**	1.78(0.05)*(0.02)**	C
	Ch_250_(Co)	15.93(0.52)*(0.04)**	1.96(0.08)*(0.04)**	C

**Standard deviation
**Coefficient of variation
E1-Tensile failure of the textile out of the matrix
C-Detachment at matrix to substrate interface

The experimental results in all cases are in good agreement to the results presented in Chapter 4; the latter were retrieved using a 100kN actuator. This verified the hypothesis that the experimental results derived in Chapter 4 provide a robust

and accurate data-set to compare against the results of the fatigue testing campaign Table 5.3.

5.4 Fatigue testing experimental results

In total, 54 direct shear tests were performed under load control. The load was linearly varying in the range $\begin{bmatrix} P_{min} & \lambda P_{max} \end{bmatrix}$ at a frequency of 1Hz until failure; P_{max} denotes the quasi-static maximum load (average value over four tests) shown in Table 5.2 and λ is the loading factor, i.e., $\lambda \in (0.6, 0.7, 0.8)$. In all cases, the minimum applied load was $P_{min} = 0.15 P_{max}$. The loading protocol bounds for each case are shown in Table 5.4.

Table 5.4: Loading envelopes per specimen

Specimen [-]	P_{min} [kN]	$0.6P_{max}$ [kN]	$0.7P_{max}$ [kN]	$0.8P_{max}$ [kN]	Frequency [Hz]
B_150	0.48	1.93	2.26	2.58	1
B_200	0.48	1.92	2.24	2.56	
B_250	0.54	2.15	2.50	2.86	
Ch_150_(Co)	1.73	6.93	8.08	9.24	
Ch_200_(Co)	2.26	9.03	10.54	12.05	
Ch_250_(Co)	2.40	9.55	11.15	12.74	

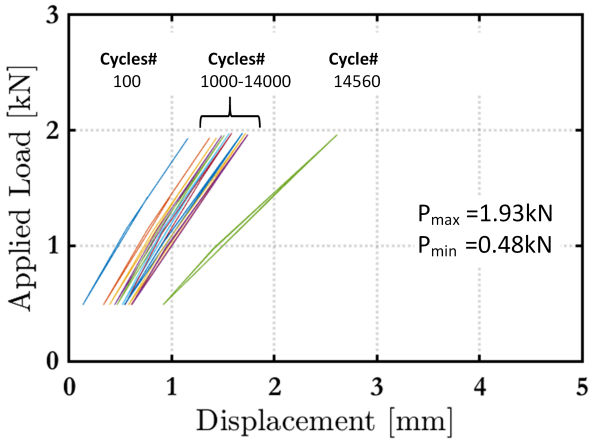

(a) L_b=150mm

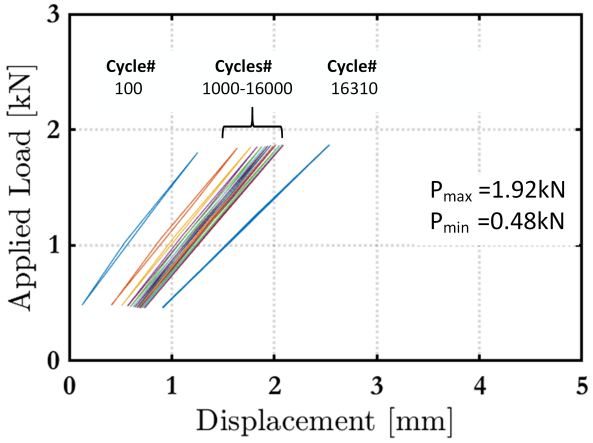

(b) L_b=200mm

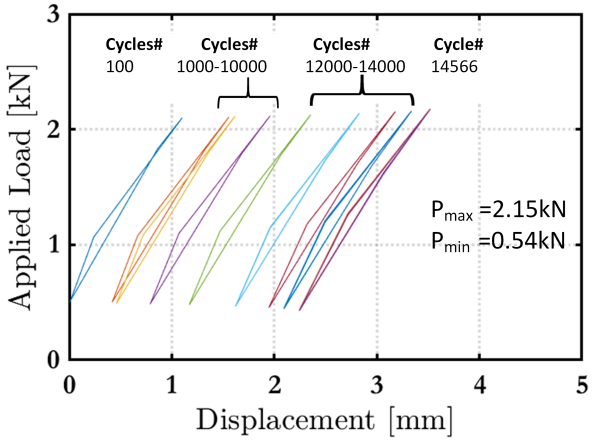

(c) L_b=250mm

Figure 5.6: Fatigue test load global slip plots for $P_{max} = 0.6P_{max}$ basalt textile : (a) 150mm, (b) 200mm, and (c) 250mm bond length

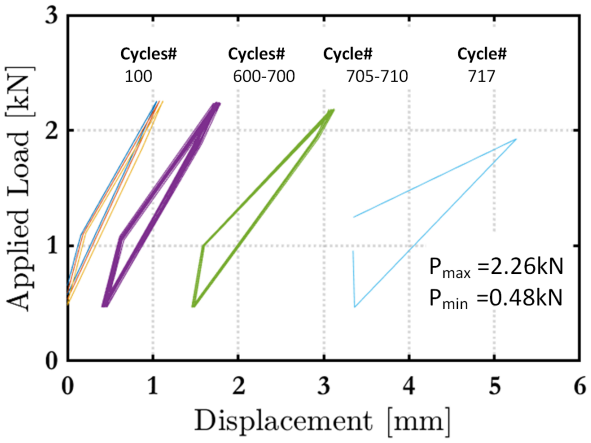

(a) L_b=150mm

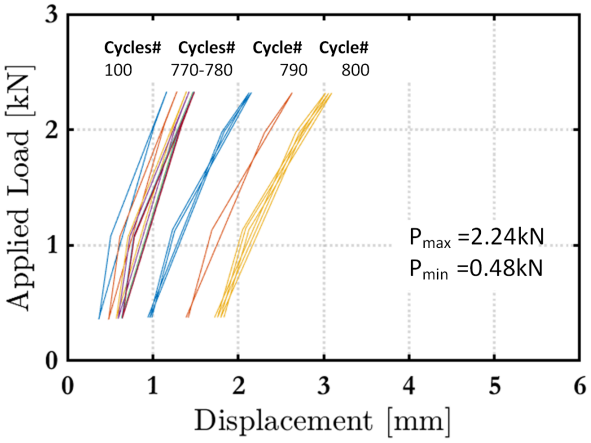

(b) L_b=200mm

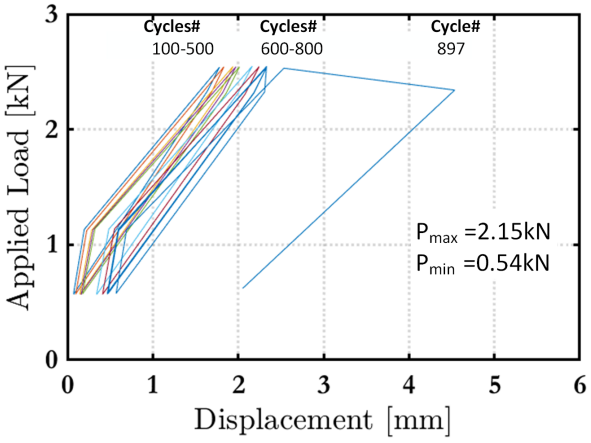

(c) L_b=250mm

Figure 5.7: Fatigue test load global slip plots for $P_{max} = 0.7P_{max}$ basalt textile: (a) 150mm, (b) 200mm, and (c) 250mm bond length

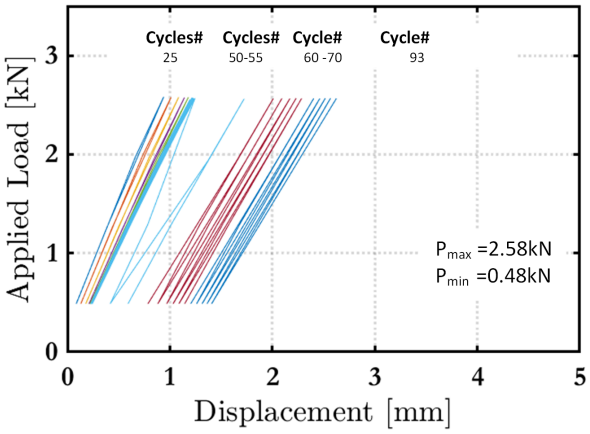

(a) L_b=150mm

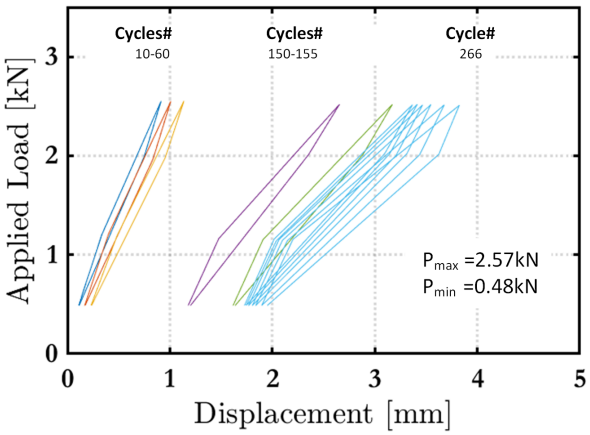

(b) L_b=200mm

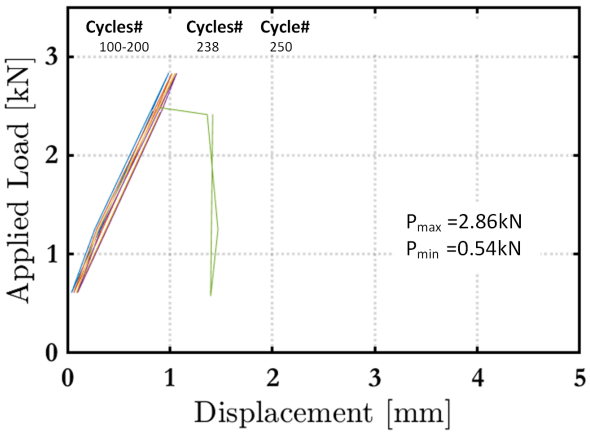

(c) L_b=250mm

Figure 5.8: Fatigue test load global slip plots for$P_{max} = 0.8P_{max}$ basalt textile: (a) 150mm, (b) 200mm, and (c) 250mm bond length

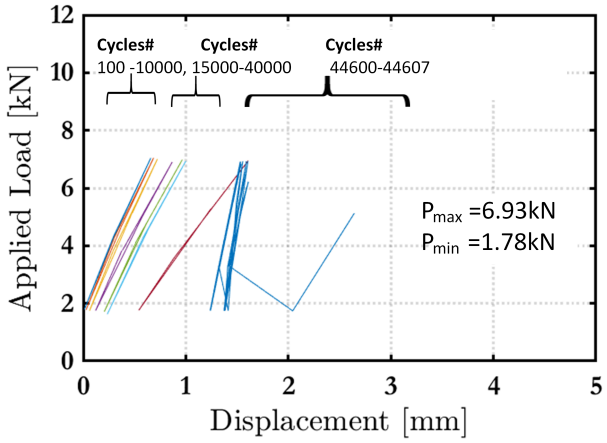

(a) L_b=150mm

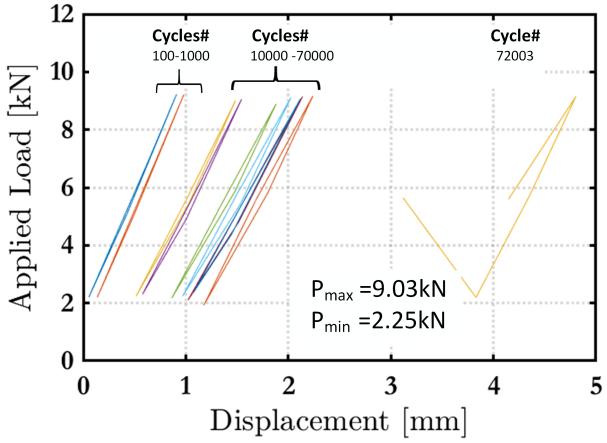

(b) L_b=200mm

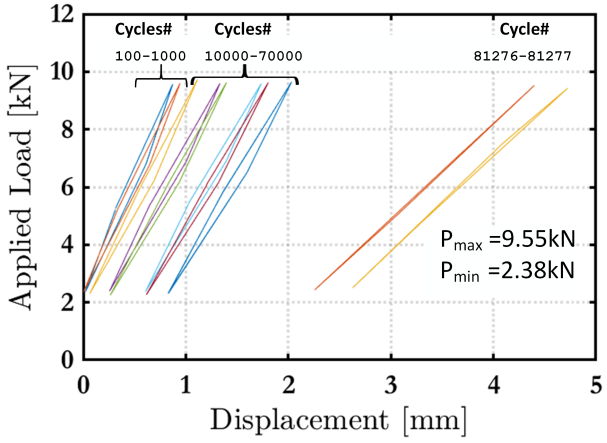

(c) L_b=250mm

Figure 5.9: Fatigue test load global slip plots for $P_{max} = 0.6P_{max}$ coated carbon textile: (a) 150mm, (b) 200mm, and (c) 250mm bond length

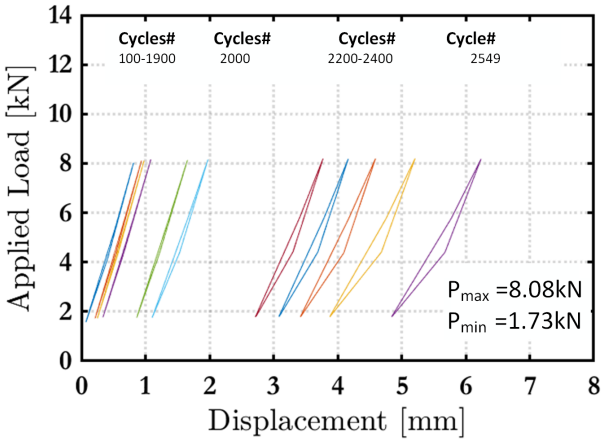

(a) L_b=150mm

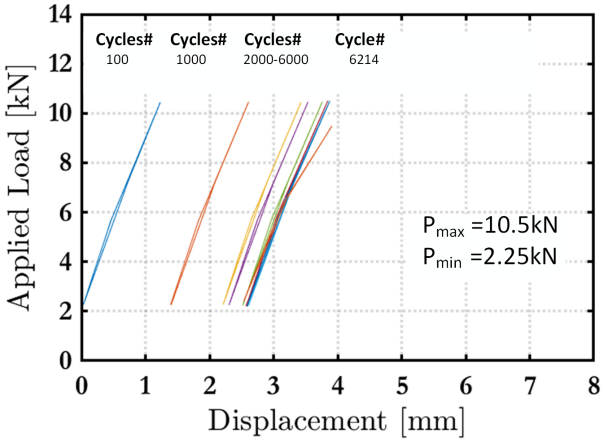

(b) L_b=200mm

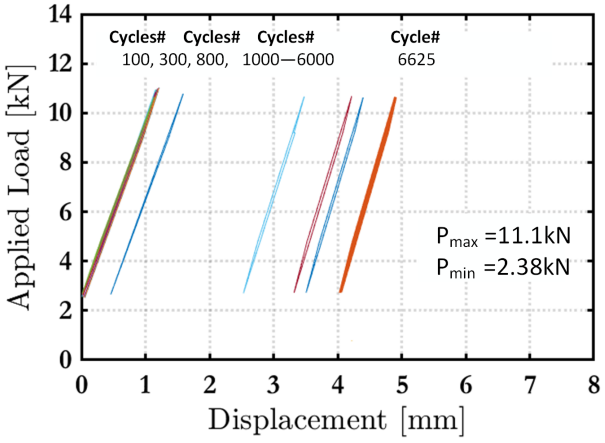

(c) L_b=250mm

Figure 5.10: Fatigue test load global slip plots for $P_{max} = 0.7P_{max}$ coated carbon textile: (a) 150mm, (b) 200mm, and (c) 250mm bond length

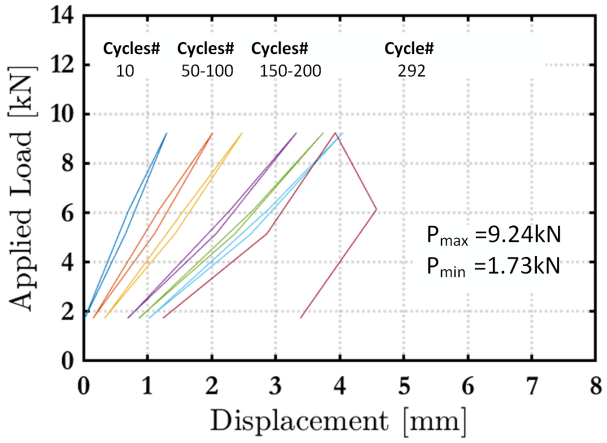

(a) L_b=150mm

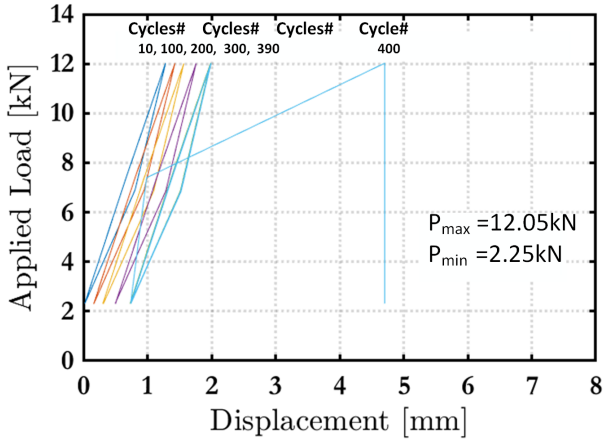

(b) L_b=200mm

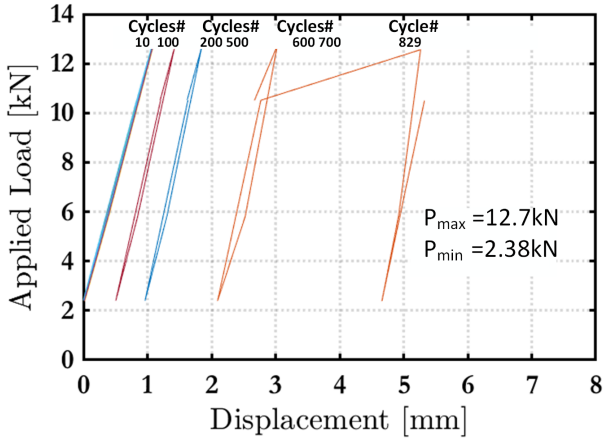

(c) L_b=250mm

Figure 5.11: Fatigue test load global slip plots for $P_{max} = 0.8P_{max}$ coated carbon textile: (a) 150mm, (b) 200mm, and (c) 250mm bond length

Table 5.5: Fatigue tests result of basalt textile in case of 60% of P_{max}

Specimens	P_{max} [kN]	P_{min} [kN]	P_{max} [%]	P_{min} [%}	Ns	Failure mode
B_150_a	1.97	0.49	61.07	15.13	14523	D
B_150_b	1.92	0.50	59.48	15.48	15606	D
B_150_c	1.94	0.46	60.07	14.9	14497	D
average	1.94	0.48	60	14.11	14875	-
-	0.02*	0.01*	0.6*	0.58*	517*	-
-	0.01**	0.03**	0.01**	0.03**	0.034**	-
B_200_a	1.93	0.49	60.44	15.28	16307	D
B_200_b	1.87	0.50	58.35	15.50	14794	D
B_200_c	1.96	0.45	60.20	13.28	15980	D
average	1.92	0.48	59.6	14.68	15693	-
-	0.03*	0.02*	0.93*	0.99*	649*	-
-	0.01**	0.04**	0.01**	0.06**	0.041**	-
B_250_a	2.13	0.50	59.56	14.05	16382	D
B_250_b	2.15	0.55	60.00	15.33	15226	D
B_250_c	2.14	0.52	59.71	14.50	14272	D
average	2.04	0.52	59.75	14.5	15293	-
-	0.12*	0.02*	0.18*	0.53*	862*	-
-	0.06**	0.03**	0.003**	0.03**	0.056**	-
*St.d, **CoV.						

Table 5.6: Fatigue tests result of basalt textile in case of 70% of P_{max}

Specimens	P_{max} [kN]	P_{min} [kN]	P_{max} [%]	P_{min} [%}	Ns	Failure mode
B_150_a	2.27	0.47	70.22	14.54	717	D
B_150_b	2.17	0.46	67.13	14.23	834	D
B_150_c	2.26	0.48	69.91	14.85	768	D
average	2.23	0.47	69.01	14.54	773	-
-	0.04*	0.01*	1.39*	0.25*	47.89*	-
-	0.02**	0.02**	0.02**	0.02**	0.06**	-
B_200_a	2.23	0.47	69.60	14.67	795	D
B_200_b	2.22	0.47	69.91	14.67	682	D
B_200_c	2.24	0.48	69.91	14.98	800	D
average	2.24	0.47	69.81	14.77	759	-
-	0.01*	0.00*	0.25*	0.15*	57.91*	-
-	0.00**	0.01**	0.00**	0.01**	0.07**	-
B_250_a	2.48	0.48	69.18	13.39	655	D
B_250_b	2.50	0.54	69.74	15.06	748	D
B_250_c	2.33	0.52	70.57	14.78	902	D
average	2.50	0.52	69.83	14.41	768	-
-	0.02*	0.03*	0.57*	0.73*	101.85*	-
-	0.01**	0.05**	0.01**	0.05**	0.13**	-
*St.d, **CoV.						

Table 5.7: Fatigue tests result of basalt textile in case of 80% of P_{max}

Specimens	P_{max} [kN]	P_{min} [kN]	P_{max} [%]	P_{min} [%}	Ns	Failure mode
B_150_a	2.52	0.44	77.95	15	70	D
B_150_b	2.58	0.48	79.81	15	93	D
B_150_c	2.59	0.54	80.12	15	87	D
average	2.56	0.49	0.79	15.15	83	-
-	0.03*	0.03*	0.95*	1.10*	9.90*	-
-	0.01**	0.07**	0.01**	1.1**	0.07**	-
B_200_a	2.59	0.54	80.83	16.8	266	D
B_200_b	2.54	0.44	79.27	13.73	193	D
B_200_c	2.58	0.45	80	14.35	208	D
average	2.57	0.43	80.21	14.98	222	-
-	0.021*	0.04*	0.67*	1.34*	31.47*	-
-	0.00**	0.09**	0.00**	0.09**	0.14**	-
B_250_a	2.90	0.55	80.89	15.34	250	D
B_250_b	2.82	0.52	81.45	14.50	325	D
B_250_c	2.79	0.54	77.82	15.06	357	D
average	2.87	0.53	80.05	14.96	310	-
-	0.05*	0.01*	1.59*	0.34*	45*	-
-	0.01**	0.02**	0.01**	0.02**	0.15**	-
*St.d, **CoV.						

Table 5.8: Fatigue tests result of heavy coated carbon textile in case of 60% of P_{max}

Specimens	P_{max} [kN]	P_{min} [kN]	P_{max} [%]	P_{min} [%}	Ns	Failure mode
Ch_150_(Co)_a	7.02	1.68	60.75	14.54	34984	D
Ch_150_(Co)_b	6.96	1.70	60.23	14.71	51445	D
Ch_150_(Co)_c	6.96	1.76	60.23	15.23	44607	D
average	6.98	1.71	60.41	14.83	43679	-
-	0.03*	0.03*	0.24*	0.29*	6751.98*	-
-	0.00**	0.02**	0.00**	0.02**	0.15**	-
Ch_200_(Co)_a	9.05	2.24	60.08	14.87	74759	D
Ch_200_(Co)_b	9.03	2.21	59.95	14.70	64294	D
Ch_200_(Co)_c	9.1	2.25	60.41	14.94	72006	D
average	9.06	2.23	60.15	14.84	70353	-
-	0.03*	0.01*	0.20*	0.10*	4429.32*	-
-	0.00**	0.01**	0.00**	0.01**	0.06**	-
Ch_250_(Co)_a	9.49	2.40	59.57	15.10	94821	D
Ch_250_(Co)_b	9.42	2.31	59.13	14.50	65100	D
Ch_250_(Co)_c	9.63	2.33	60.45	14.63	81277	D
average	9.51	2.35	59.72	14.74	80399	-
-	0.09*	0.04*	0.55*	0.26*	12149.11*	-
-	0.01**	0.02**	0.01**	0.02**	0.15**	-
*St.d, **CoV.						

Table 5.9: Fatigue tests result of heavy coated carbon textile in case of 70% of P_{max}

Specimens	P_{max} [kN]	P_{min} [kN]	P_{max} [%]	P_{min} [%}	Ns	Failure mode
Ch_150_(Co)_a	8.06	1.71	69.76	14.82	2337	D
Ch_150_(Co)_b	8.17	1.76	70.70	15.22	3061	D
Ch_150_(Co)_c	8.07	1.75	69.81	15.14	2549	D
average	8.10	6.98	70.09	15.06	2649	-
-	0.05*	0.03*	0.43*	0.17*	303.91*	-
-	0.01**	0.00**	0.01**	0.01**	0.11**	-
Ch_200_(Co)_a	10.28	2.25	68.22	14.92	4667	D
Ch_200_(Co)_b	10.46	2.21	69.47	14.70	5002	D
Ch_200_(Co)_c	10.50	2.21	69.73	14.70	6214	D
average	10.41	2.23	69.14	14.77	5294	-
-	0.10*	0.02*	0.66*	0.10*	664.64*	-
-	0.01**	0.01**	0.01**	0.01**	0.13**	-
Ch_250_(Co)_a	11.11	2.40	69.71	15.10	6828	D
Ch_250_(Co)_b	11.00	2.53	69.06	15.88	4898	D
Ch_250_(Co)_c	11.06	2.36	69.46	14.78	6625	D
average	11.06	2.43	69.41	15.25	6117	-
-	0.04*	0.07*	0.27*	0.46*	865.94*	-
-	0.00**	0.03**	0.00**	0.03**	0.14**	-
*St.d, **CoV.						

Table 5.10: Fatigue tests result of heavy coated carbon textile in case of 80% of P_{max}

Specimens	P_{max} [kN]	P_{min} [kN]	P_{max} [%]	P_{min} [%}	Ns	Failure mode
Ch_150_(Co)_a	9.22	1.73	79.75	14.96	210	C
Ch_150_(Co)_b	9.23	1.73	79.87	15.00	292	D
Ch_150_(Co)_c	9.21	1.73	79.70	14.96	321	D
average	9.22	1.73	79.78	6.98	274	-
-	0.01*	0.00*	0.07*	0.03*	47.01*	-
-	0.00**	0.00**	0.00**	0.00**	0.17**	-
Ch_200_(Co)_a	12.16	2.24	80.73	14.90	313	D
Ch_200_(Co)_b	12.21	2.25	81.05	14.96	463	D
Ch_200_(Co)_c	12.03	2.32	79.86	15.37	400	D
average	12.13	2.27	80.55	15.08	392	-
-	0.08*	0.03*	0.50*	0.21*	61.50*	-
-	0.01**	0.01**	0.01**	0.01**	0.16**	-
Ch_250_(Co)_a	12.56	2.39	78.87	14.98	672	C
Ch_250_(Co)_b	12.83	2.32	80.51	14.54	900	C
Ch_250_(Co)_c	12.69	2.39	79.66	14.97	915	D
average	12.69	2.36	79.68	14.83	829	-
-	0.11*	0.03*	0.67*	0.21*	111.18*	-
-	0.01**	0.01**	0.01**	0.01**	0.13**	-
*St.d, **CoV.						

The average load-slip response plots of the basalt and coated carbon textiles specimens are shown in Figs. 5.6-5.8 (basalt) and Figs 5.9-5.11 (carbon) for the case of $\lambda = 60\%$, $\lambda = 70\%$, and $\lambda = 80\%$, respectively. In these plots, snapshots of the cyclic response are provided for brevity. In all cases, the final cycle prior to failure is also shown. Contrary to the quasi-static tests, the failure mechanism initiates with cracks in the mortar matrix followed by slippage of the fibres.

The experimental results are also summarized in Table 5.5-Table 5.7 in terms of the corresponding numbers of cycles up to the failure, the actual (measured) upper and lower values of the applied load, and the observed failure modes. It is worth mentioning that the coefficient of variation was, in all cases, less than 10%. Overall, the fatigue tests results indicates that the number of cycles dramatically increases if

the fatigue-load range decreases. The average reported maximum numbers of cycles up to failure in case of 60% of maximum load were 80399 and 15293 for coated heavy carbon and basalt, respectively and 829 and 310 of $\lambda = 80\%$ (in case of 250 mm bond length). Due to the sensitivity of the testing actuator, the actual applied upper and lower load varied in each specimen and, therefore, slightly different from the nominal load values.

5.4.1 Fatigue failure modes

In the following, the failure modes obseved in the fatigue tests are discussed. To facilitate the discussion, these are grouped in terms of loading factor, i.e., 60%, 70%, and 80%.

5.4.1.1 The case of λ =60%

Overall, the failure mechanism of basalt textile comprises 3 distinct stages, i.e.,

(i). Loading from cycle 1 to approximately 15000. During this stage the specimen sustains the applied load although at increasing displacements.

(ii). textile slippage initiation (the second part which occurs right before the failure)

(iii). failure

This 3-stage description directly corresponds to the ratchetting patterns shown in Fig. 5.6. Ratcheting in this case corresponds to micro-cracks developing at the mortar that facilitate micro-slippage of the textile; when the micro-cracks merge into visible cracks, the displacement increases considerably.

It is important to note that as these cracks do not evolve symmetrically, symmetry is lost in the test resulting in a non-uniform stress distribution on the textile. Hence, the textile fractures only partially as shown in Figs. 5.12-5.26. The average number of cycles before failure appears to be quite close, namely 14875, 15693 and 15293 for the 150 mm ,200 mm, and 250 mm bond length, respectively in the case of basalt textile (Table 5.5). It is noteworthy that the coefficient of variation is around 5%. The following three main steps describe the failure mechanism of the basalt specimens:

The failure mechanism of carbon coated specimens subjected to the 60 % of maximum load differs from that observed in the basalt specimens and comprises four stages, i.e.,

(i). cracks initiate at the mortar (usually in range of 500-1000 cycles (60% of P_{max})

(ii). cracks propagate (the longest parts where the slippage increases gradually)

(iii). matrix detachment

(iv). failure

(a) Loading (cycle 1)

(b) Textile slippage initiation (cycle 14870)

(c) Failure: slippage off the textile within the matrix (cycle 14875)

Figure 5.12: Evolution of damage with increasing number of cycles basalt textile $P_{max} = 0.6P_{max}$:L_b=150mm

(a) Loading cycle 1

(b) Textile slippage initiation cycle 15685

(c) Failure: slippage off the textile within the matrix cycle 15693

Figure 5.13: Evolution of damage with increasing number of cycles basalt textile $P_{max} = 0.6P_{max}$:L_b=200mm

(a) Loading cycle 1

(b) Textile slippage initiation cycle 15284

(c) Failure: slippage off the textile within the matrix cycle 15293

Figure 5.14: Evolution of damage with increasing number of cycles basalt textile $P_{max} = 0.6P_{max}$:L_b=250mm

(a) Crack initiation at the matrix cycle 723

(b) Crack propagation at the matrix cycle 15000

(c) Initiation of matrix detachment cycle 40252

(d) Failure: slippage off the textile within the matrix cycle 43679

Figure 5.15: Evolution of damage with increasing number of cycles carbon coated $P_{max} = 0.6P_{max}$:L_b=150mm

(a) Crack initiation at the matrix cycle 800

(b) Crack propagation at the matrix cycle 20000

(c) Initiation of matrix detachment cycle 51431

(d) Failure: slippage off the textile within the matrix cycle 70353

Figure 5.16: Evolution of damage with increasing number of cycles carbon coated $P_{max} = 0.6P_{max}$:L_b=200mm

(a) Crack initiation at the matrix cycle 845

(b) Crack propagation at the matrix cycle 26666

(c) Initiation of matrix detachment cycle 58431

(d) Failure: slippage off the textile within the matrix cycle 80399

Figure 5.17: Evolution of damage with increasing number of cycles carbon coated $P_{max} = 0.6P_{max}$:L_b=250mm

The failure mechanism begins with small cracks in the mortar matrix at the top edge of the bonded surface. Cracking evolved gradually and led to fibre slippage within the matrix. In common specimens with coated carbon, the first visible cracks appear in a range from 500 to 1000 cycles in case of 60% of maximum load. Then the cracks propagate in slow speed up to the following steps, where the matrix detachments occurred at the top of the samples, which is develop and lead to the sudden failure when the specimen is no longer able to carry the prescribed load.

5.4.1.2 The case of λ =70%

For the case of the basalt textile specimens, the maximum number of cycles achieved before failure appears to be similar, i.e., 773, 759, and 768, in case of 150 mm, 200 mm, and 250mm, respectively (see also the low CoV reported in Table 5.6). Contrary to the quasi-static tests, the failure mechanism initiates with cracks in the mortar matrix followed by slippage of the fibres. However, the observed slippage along the width of the mortar was not uniform, eventually leading to a non-uniform distribution of stress on the textile at high cycles. As a result, all specimens failed due to a gradual rupture of the textile near the TRM; the failure mechanism of at the 70% case has the same traits as that of 60% specimens.

The specimens strengthened with coated carbon also demonstrated a similar failure mode to those tested at 60% of the maximum load. However, the fatigue life

is relatively shorter. For example, the first visible cracks appear in the cycle range between 100 to 300, which is two times faster than in the 60% load range. In contrast to the lower load range, the failure of the specimens followed after the matrix detachment starts.

(a) Loading cycle 1

(b) Textile slippage initiation cycle 769

(c) Failure: slippage off the textile within the matrix cycle 773

Figure 5.18: Evolution of damage with increasing number of cycles basalt textile $P_{max} = 0.7P_{max}$:L_b=150mm

(a) Loading cycle 1

(b) Textile slippage initiation cycle 756

(c) Failure: slippage off the textile within the matrix cycle 759

Figure 5.19: Evolution of damage with increasing number of cycles basalt textile $P_{max} = 0.7P_{max}$:L_b=200mm

(a) Loading cycle 1

(b) Textile slippage initiation cycle 763

(c) Failure: slippage off the textile within the matrix cycle 768

Figure 5.20: Evolution of damage with increasing number of cycles basalt textile $P_{max} = 0.7P_{max}$:L_b=250mm

(a) Crack initiation at the matrix cycle 180

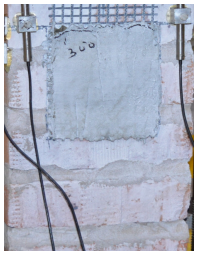

(b) Crack propagation at the matrix 700

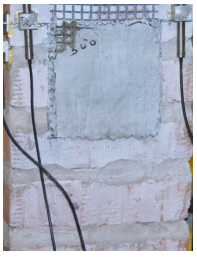

(c) Initiation of matrix detachment cycle 2017

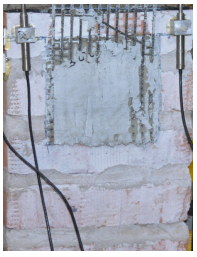

(d) Failure: slippage off the textile within the matrix cycle 2649

Figure 5.21: Evolution of damage with increasing number of cycles carbon coated $P_{max} = 0.7P_{max}$:L_b=150mm

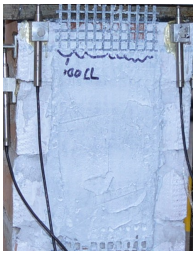

(a) Crack initiation at the matrix cycle 204

(b) Crack propagation at the matrix cycle 700

(c) Initiation of matrix detachment cycle 3222

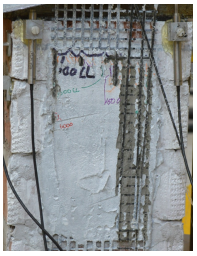

(d) Failure: slippage off the textile within the matrix cycle 5294

Figure 5.22: Evolution of damage with increasing number of cycles carbon coated $P_{max} = 0.7P_{max}$:L_b=200mm

(a) Crack initiation at the matrix cycle 214

(b) Crack propagation at the matrix cycle 1033

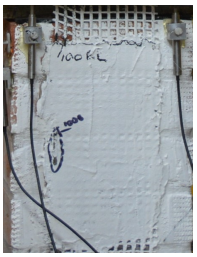

(c) Initiation of matrix detachment cycle 4000

(d) Failure: slippage off the textile within the matrix cycle 6117

Figure 5.23: Evolution of damage with increasing number of cycles carbon coated $P_{max} = 0.7P_{max}$:L_b=250mm

It is interesting to note that the TRM fatigue behaviour to masonry bond has a pretty similar stage described by Pino et al. (2017). The first stage, steady and gradual increasing damage accompanied by the numbers of cracks appearance and then the local FRCM debonding occurs at crack locations surface, which is similar to the first and second stage 60% and 70% of the load range coated carbon. In the second stage, as the author reported, the concrete cracks are propagating at a more gradual rate and finally, the brittle fracture occurred in the steel followed by sudden FRCM delamination.

5.4.1.3 The case of λ =80%

For the case of the basalt textile specimens, the average number of cycles is varying from bond lengths, i.e., 83, 222, and 310 for the 150 mm, 200 mm, and 250 mm bond lengths, respectively Table 5.7. The failure mechanism was initiated with small cracks in the mortar matrix at the top edge of the bonded surface; cracking gradually evolved and led to fibre slippage Fig. 5.24b. This is manifested in the load-displacement plot through a gradual degradation of the unloading and reloading stiffness. It is interesting to note that although the cracks were initially uniformly distributed in the matrix, a preferential direction was soon established that eventually led to a non-uniform distribution of stresses on the textile. The failure mechanism of at the 80% case has the same steps as that of 60% and 70% specimens. A typical cyclic load-displacement response under 80% of the maximum load shown in Fig. 5.8 for the case of the 200mm bond length. All results are summarised in Table 5.7.

The failure mode of carbon coated specimens, exposed to the highest load level in this test series varied from the two listed below. At the beginning of the test, the first visible cracks appeared in the 50-100 cycles range, i.e., ten times quicker than the 60% case Fig. 5.28b. The matrix detachment step, which repeated in both 60 and 70 % load ranges, was neglected Fig. 5.28c. For all specimens, the crack propagation step indicated the approaching of the sample failure Fig. 5.28d. All test results are summarised in Table 5.10. The main fatigue life steps can be listed in following:

(i). loading

(ii). first cracks initiation (usually in range of 50- 100 cycles)

(iii). cracks propagation

(iv). failure

(a) Loading cycle 1

(b) Textile slippage initiation cycle 81.5

(c) Failure: slippage off the textile within the matrix cycle 83.5

Figure 5.24: Evolution of damage with increasing number of cycles basalt textile $P_{max} = 0.8P_{max}$:L_b=150mm

(a) Loading cycle 1

(b) Textile slippage initiation cycle 221

(c) Failure: slippage off the textile within the matrix cycle 222

Figure 5.25: Evolution of damage with increasing number of cycles basalt textile $P_{max} = 0.8P_{max}$:L_b=200mm

(a) Loading cycle 1

(b) Textile slippage initiation cycle 308

(c) Failure: slippage off the textile within the matrix cycle 310

Figure 5.26: Evolution of damage with increasing number of cycles basalt textile $P_{max} = 0.8P_{max}$:L_b=250mm

(a) Loading cycle 1

(b) Cracks initiation cycle 50

(c) Cracks propagation cycle 154

(d) Failure: slippage off the textile within the matrix cycle 274

Figure 5.27: Evolution of damage with increasing number of cycles carbon coated $P_{max} = 0.8P_{max}$:L_b=150mm

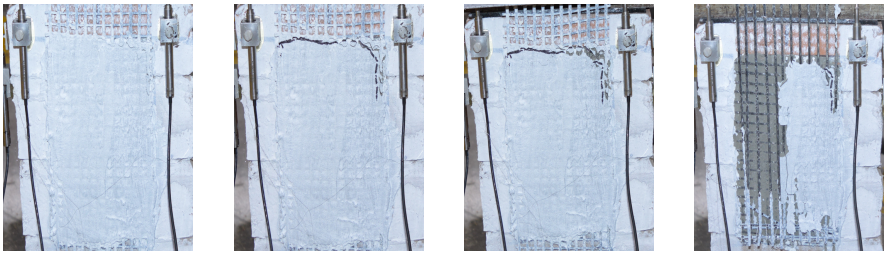

(a) Loading cycle 1

(b) Cracks initiation cycle 78

(c) Cracks propagation cycle 220

(d) Failure: slippage off the textile within the matrix cycle 392

Figure 5.28: Evolution of damage with increasing number of cycles carbon coated $P_{max} = 0.8P_{max}$:L_b=200mm

(a) Loading cycle 1

(b) Cracks initiation cycle 50

(c) Cracks propagation cycle 340

(d) Failure: slippage off the textile within the matrix cycle 829

Figure 5.29: Evolution of damage with increasing number of cycles carbon coated $P_{max} = 0.8P_{max}$:L_b=250mm

It should be noted the failure mode represents the variability from the slippage to matrix detachment with is close to the result of the quasi-static case Table 5.10.

As mention previously, the quasi-static test was carried out in a displacement control while the fatigue test at force control. In the monotonic test, the displacement and the evolution of failure could be controlled. The fatigue test applied in force control. Therefore when the specimens could not resist the prescribed load, the failure occurred suddenly. In this case, the differences between the failure mode of fatigue and monotonic loading could be due to different test control mechanisms.

5.5 Discussion

5.5.1 Response Stages

In the case of the carbon coated specimens, the observed failure modes are characterized by four distinct stages (see, also, Fig. 5.31a and Table 5.11). At the first stage, uniformly distributed cracks initiate at the mortar, near the top bond surface (Fig. 5.30a I). The occurrence of multiple cracks in the matrix identifies the beginning of stage two (Fig. 5.30a II).

In most cases, a smooth evolution of cracks was observed from stages one to two (Fig. 5.31a I, II); phase one and two can be assumed as a good matrix-to-textile bond. The detachment of the mortar matrix signposts the beginning of the third stage and the transition point between stages 2 and 3 identified by increasing displacement values (Fig. 5.31a III).

Table 5.11: Response stages versus number of cycles (carbon specimens)

Bond length	Stage 1 [N_s]	Stage 2 [N_s]	Stage 3 [N_s]	Stage 4 [N_s]
		$P_{max}60\%$		
150	723	15000	40252	43679
200	800	20000	51431	70353
250	845	26666	58431	80399
		$P_{max}70\%$		
150	180	700	2017	2649
200	204	700	3222	5294
250	214	1033	4000	6117
		$P_{max}80\%$		
150	70	154	226	274
200	78	220	356	392
250	89	340	583	829

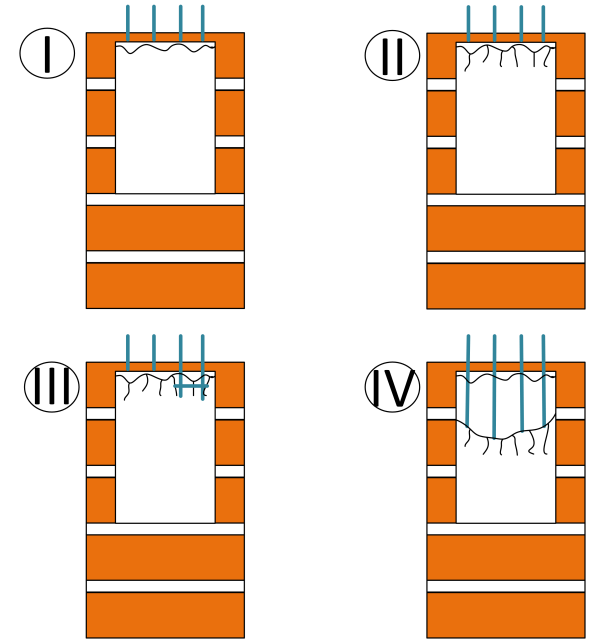

(a) Coated carbon

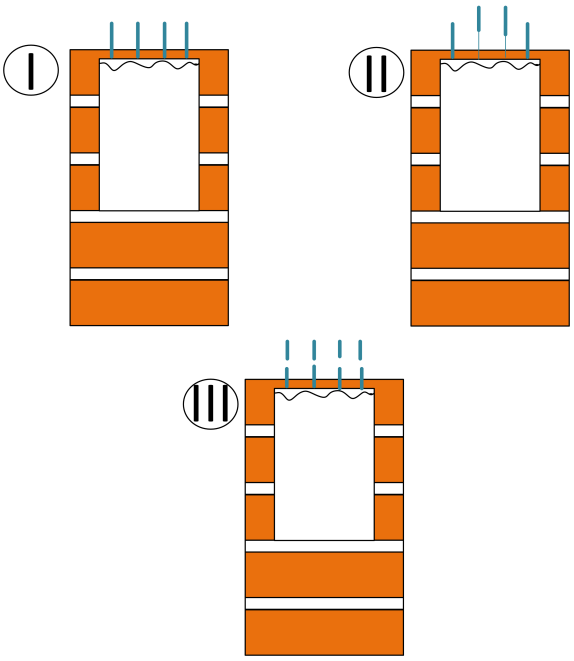

(b) Basalt

Figure 5.30: TRM to masonry bond under fatigue loading: failure modes

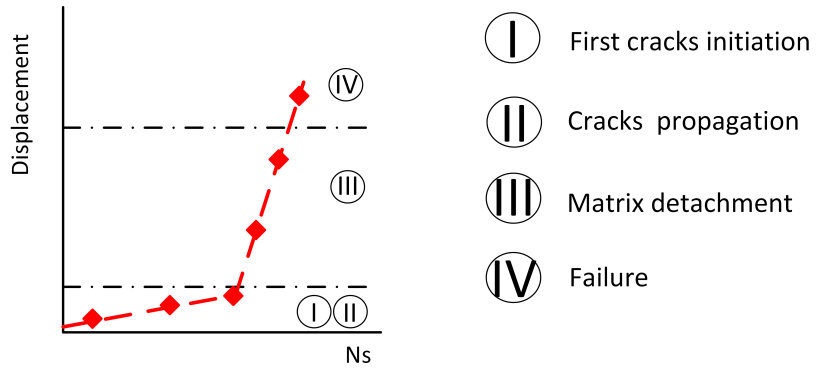

(a) Coated carbon

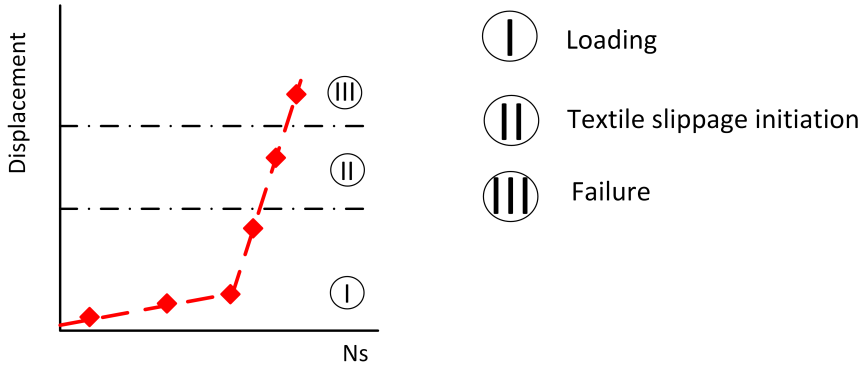

(b) Basalt

Figure 5.31: TRM to masonry bond fatigue response stages

Table 5.12: Response stages versus number of cycles (basalt specimens)

Bond length	Stage 1 [N_s]	Stage 2 [N_s]	Stage 3 [N_s]
		P_{max}60%	
150	1	14870	14875
200	1	15685	15693
250	1	15284	15293
		P_{max}70%	
150	1	769	773
200	1	756	759
250	1	763	768
		P_{max}80%	
150	1	81.5	83.5
200	1	221.33	222.33
250	1	308	310

The third phase can be assumed as a brittle bond behaviour between textile to mortar (Fig. 5.30a III). The fourth stage corresponds to the the failure of the specimens

when the samples are no longer able to carry the imposed load Fig. 5.30a. Table 5.11 shows in detail the average N_s of each stage up to the failure cycle with regards to three bond lengths (150, 200 and 250 and three load ranges (% 60,% 70 and % 80 of P_{max}).

In the case of the basalt textile, three steps are typically identified (see, also Fig. 5.31b Table 5.12). In the case of the basalt textile, stage one shows the loading of the specimen (Fig. 5.30b I). Stage one represents the safe part in fatigue life, which is represented by increasing the displacement value (Fig. 5.31b I). Stage 2 represents the textile slippage initiation, which is just before stage three, where failure occurs (Fig. 5.30b II,III). Generally, the development of the cracks is due to the matrix is cyclically damaged by friction between the fibres and matrix. The formation of the cracks may widely change depending on the property of textile fibres used. Moreover, the time remaining from stage one to two depends on the upper loading envelope, i.e. 60% 70% and 80% and bond lengths.The number of cycles representing each step are shown in Table 5.12.

5.5.2 The effect of the loading range

As anticipated, the lowest loading factor, i.e., λ =60% results in the most extended fatigue life compared to λ =70% and λ =80%. At λ =60%, the slope of the loading-unloading branch of the force-displacement plots gradually decreases for both the basalt and the heavy carbon textile fibre material, as shown in Fig. 5.6 and Fig. 5.9, respectively. This is indicative of the progressive loss in the stiffness of the interfacial bond between TRM and masonry substrate.

The key outcomes of the fatigue testing campaign, namely the actual (as applied) upper and lower values of the load, along with the numbers of cycles up to the failure (fatigue life) and failure modes, are summarized in Tables 5.5-5.7 for the basalt textile and Tables 5.8 -5.10 for the coated heavy carbon textile, respectively. Based on the result obtained from the tests the curve between load range P_{max} and the average number cycles up to the failure N_s are presented in Fig. 5.32, Fig. 5.33 for each bond lengths. The X- axis in these figures corresponds to P_{max} and the Y-axis to the number of cycles up to failure.

With regards to these figures, it can be deduced that the fatigue life is significantly affected by the load range. The lower the uppoer bound of the applied load, the more cycles were required up to the failure.The higher P_{max} ($\lambda = 70\%$ and $\lambda = 80\%$) represent rapid cracks accumulations which is lead to promptly failure of the specimens. This theory is supported by Table 5.12 and Table 5.11 where fatigue life steps occurred more rapidly in specimens of higher see e.g., $\lambda = 70\%$ than in $\lambda = 60\%$ in case of both tested materials. The variation of the number of cycles with respect to the load factor is shown in the semi-log plots presented in Figs 5.32 5.33 for L_b= 150 mm, 200 mm and 250 mm, respectively. It is of interest to note that the trend is practically linear. The linear relationship exists between P_{max} and the logarithmic value of fatigue life (N_s).

TRM to masonry bond test under fatigue loading conditions is difficult to run due to time spend on one test. At least three samples are required (to reduce variability) for each case. With the objective of reducing the required number of testing, and via a regression analysis on the results obtained in this experimental campaign, Eqs. (5.3) and (5.4) are suggested to infer the the required number of cycles until failure for the $\lambda = 60\%$ and $\lambda = 80\%$ factors, respectively, using as a reference the results of experiments on $\lambda = 70\%$, i.e.,

$$^{0.6}N_s = \frac{100}{8}^{0.7} N_s \tag{5.3}$$

and

$$^{0.8}N_s = \frac{100}{8^{0.7}} N_s, \tag{5.4}$$

where $^{0.6}N_s$, $^{0.7}N_s$ and $^{0.8}N_s$ are the number of cycles until failure fpr $\lambda = 60\%$, ($\lambda = 70\%$, and $\lambda = 80\%$, respectively and the coefficient 0.08 was determined via a least square fit. It is worth noting that this coefficient was defined and fitted both textile materials tested and all bond lengths (Figs 5.32-5.33). However, more tests are needed involving various textile materials and bond lengths to confirm this theory.

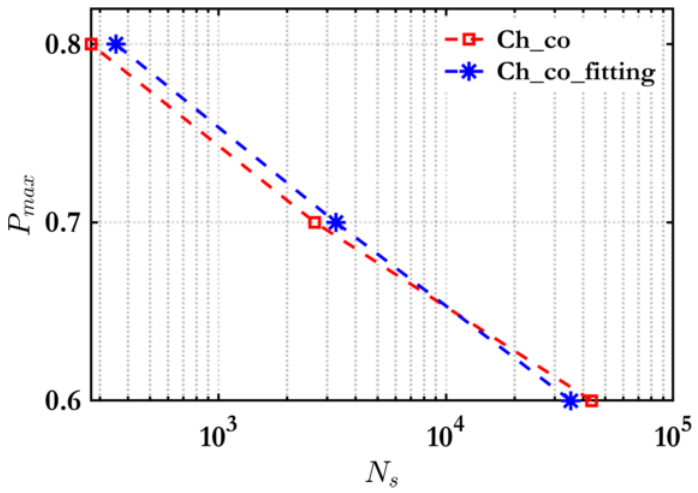

(a) L_b=150mm

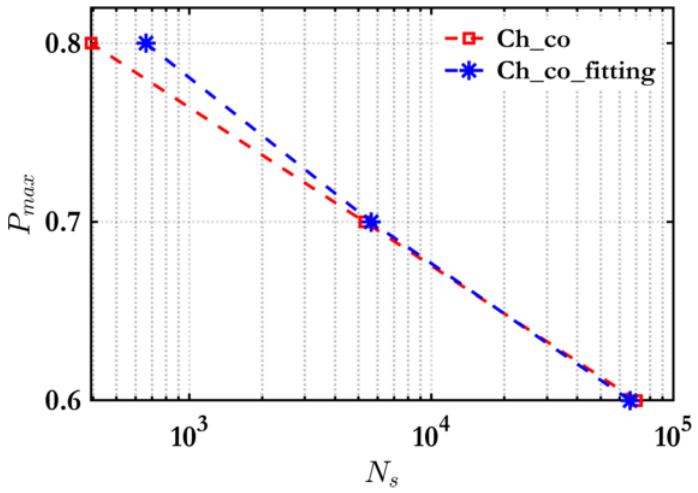

(b) L_b=200mm

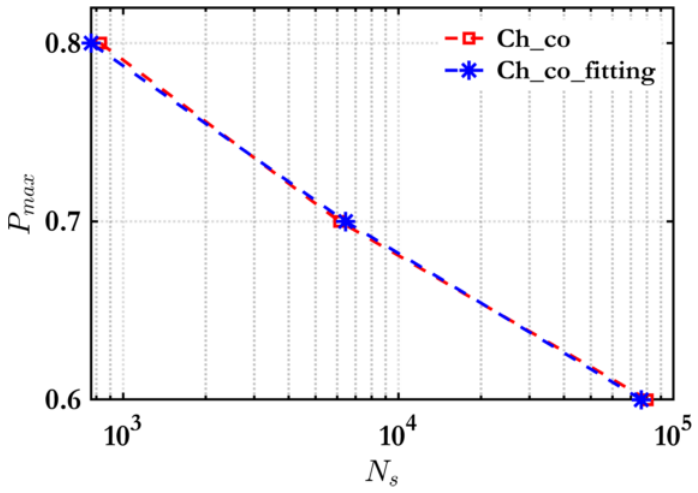

(c) L_b=250mm

Figure 5.32: Curves P_{max}-N_s in case of coated carbon textile

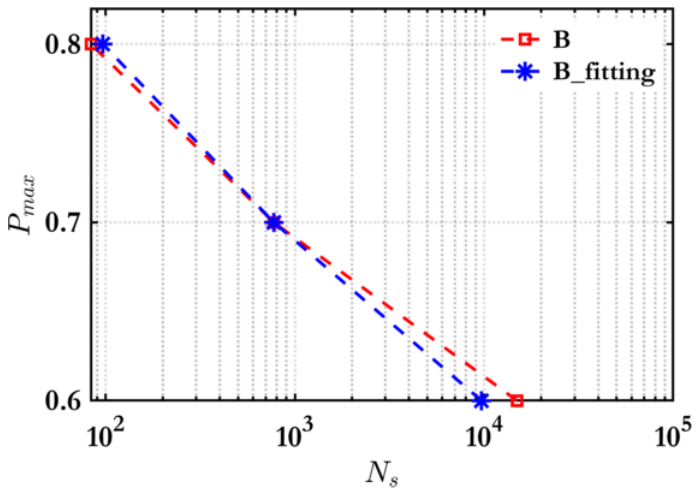

(a) L_b=150mm

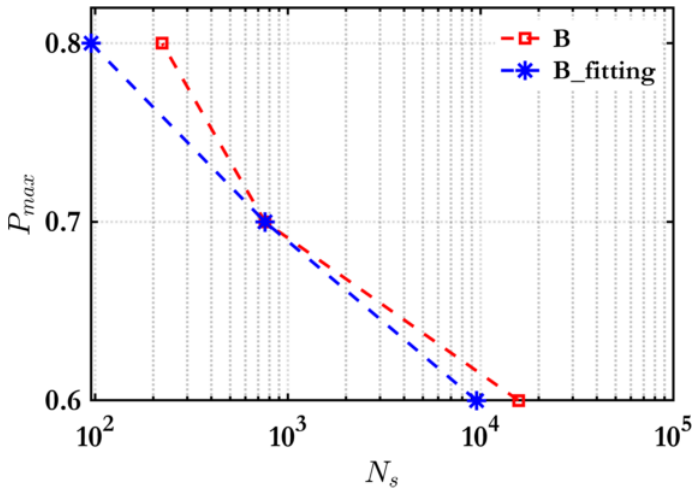

(b) L_b=200mm

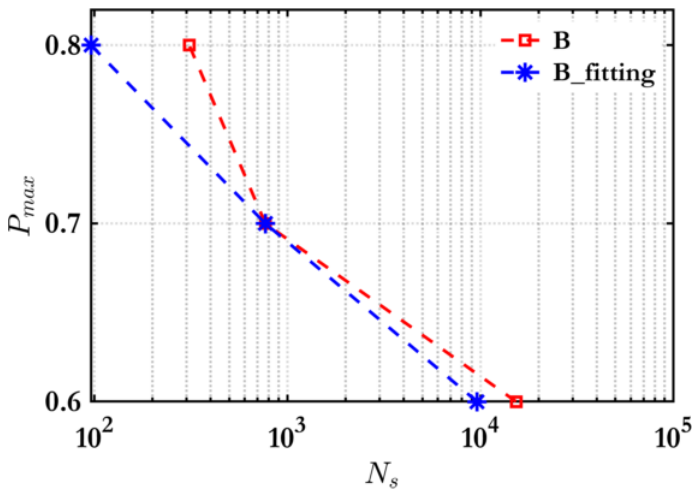

(c) L_b=250mm

Figure 5.33: Curves P_{max}-N_s in case of basalt textile

It is of interest to note that the fitting equation based on the test result of $\lambda = 70\%$

can also be used in the case of specimens strengthened with FRP. For this purpose, in Fig. 5.34 the resulting fitting line is compared against the experimental results presented in Carloni et al. (2012).

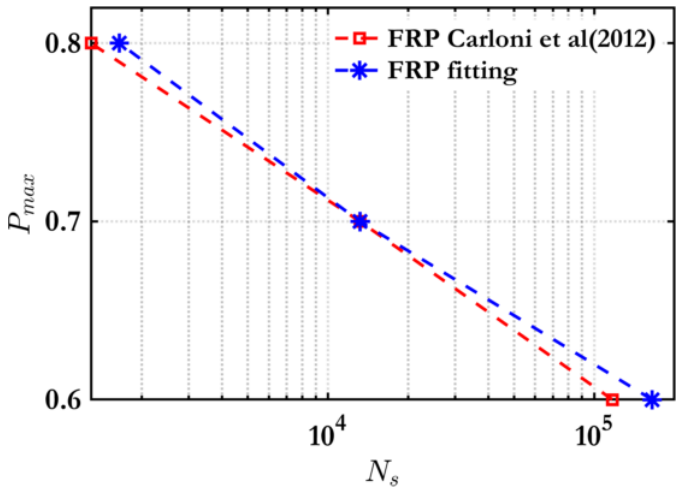

Figure 5.34: Curves P_{max}-N_s and fitting line in case of carbon FRP from Carloni et al. (2012)

5.5.3 The effect of the bond length

The effect of three different bond lengths among the three load ranges under fatigue load is investigated in the present study. Fig. 5.35 presents the bond lengths against maximum numbers of cycles up to failure for three load ranges concerning two textile materials. It is observed that as the bond length increases, the maximum number of cycles up to failure increases accordingly in the coated carbon. It is interesting to note that the graphs of $P_{max} = 0.6P_{max}$ and $P_{max} = 0.7P_{max}$ have a similar pattern as in the static case, the same bond length Fig. 5.36 for both tests textile materials.

The maximum level of load range ($\lambda = 80\%$) represents a more linear trend in both textiles comparing the behaviour of three bond lengths at lower load amplitude (15–60%) of coated carbon specimens. It can be noted that the average number of cycles up to the failure increased by 61 % and 84% regarding 200 mm and 250 mm bond lengths, respectively. It is interesting to note that the values are approximately two times higher compare with the quasi-static test. Where increases were by 30% and 38% concerning 200 mm and 250 mm bond lengths, this trend remains in a higher-amplitude range (70%-15%) and the increase almost three-time greater and comprise 99 and 130% in comparison to monotonic tests. This trend is partly continued in the highest load range (80%-15%), increasing by 42% and 202% of 200 mm and 250 mm

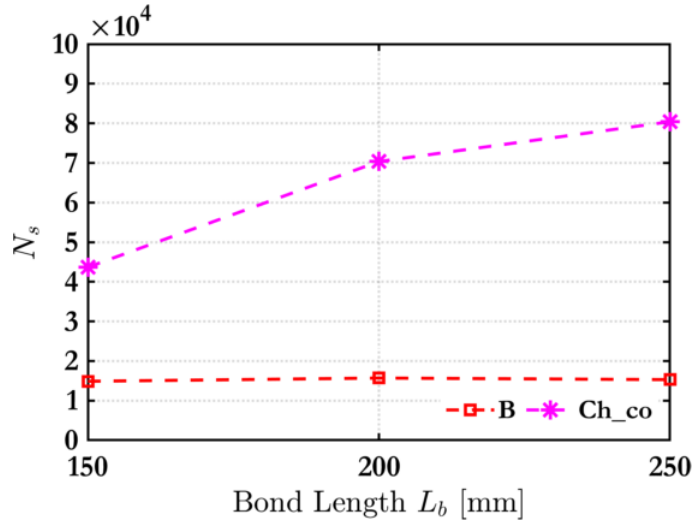

(a) $P_{max} = 0.6P_{max}$

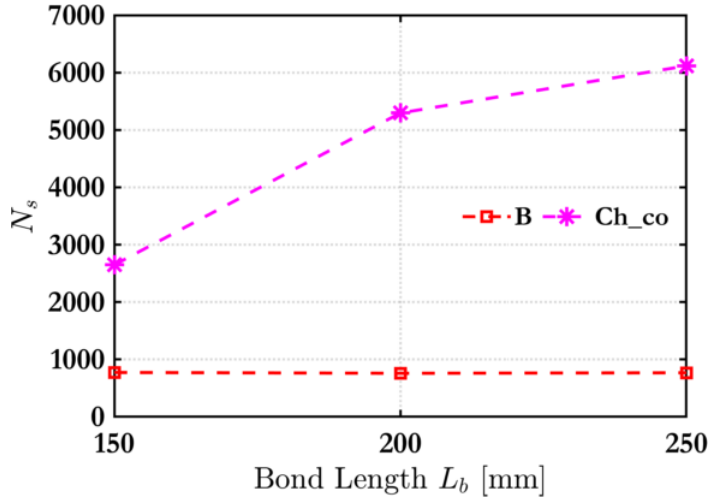

(b) $P_{max} = 0.7P_{max}$

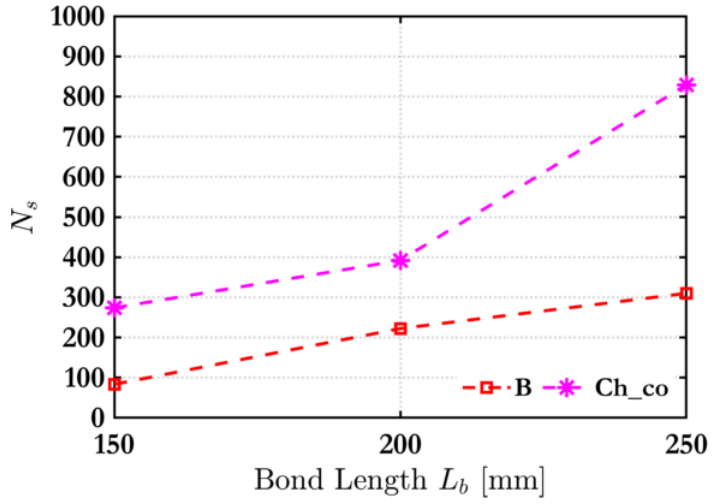

(c) $P_{max} = 0.8P_{max}$

Figure 5.35: Bond lengths against maximum numbers of cycles until failure: (a) 150mm, (b) 200mm and (c) 250mm

bond lengths, respectively.

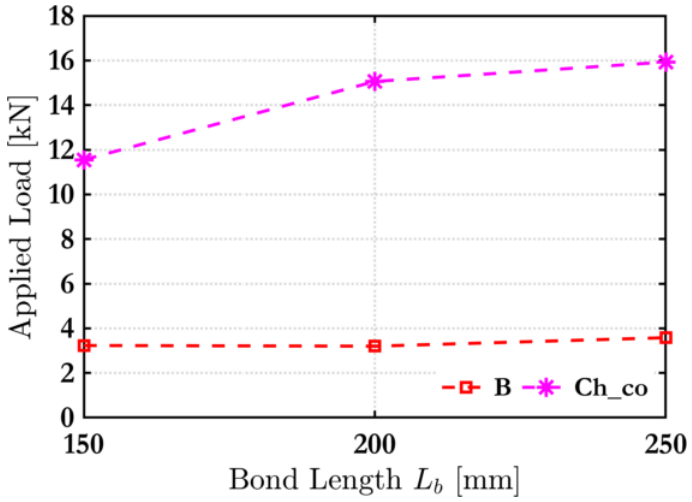

Figure 5.36: Bond length against maximum applied load (average) in static case

This tendency remains in the case of basalt textile. Again the similar quasi-static test trend represents with regards to $\lambda = 60\%$ and $\lambda = 70\%$. In contrast, $\lambda = 80\%$ have an upward linear trend. The non-similarity of the highest load range can be partially attributed to the fact that during fatigue loading, the $\lambda = 80\%$ is too high, and the fatigue life is much shorter than the lowest two. Additionally, to that, the test setup is rather sensitive to the increasing load range. Therefore, the determined average value can be different on a larger side in each test case, leading to premature failure of the specimens.

5.5.4 Global slip

Finally, the effect of the textile materials, the load range and the bond length on the measured displacement is examined in this Section. The displacement (average between LVDT 1 and LVDT 2) is plotted against the number of cycles by bond lengths in Figs. 5.37 -5.42 where the Y-axis corresponds to the displacement in mm and the X-axis to the number of cycles up to the failure between two textile materials and three bond lengths (150, 200 and 250 mm). The plots include all tested specimens, i.e., a, b, and c for each bond length.

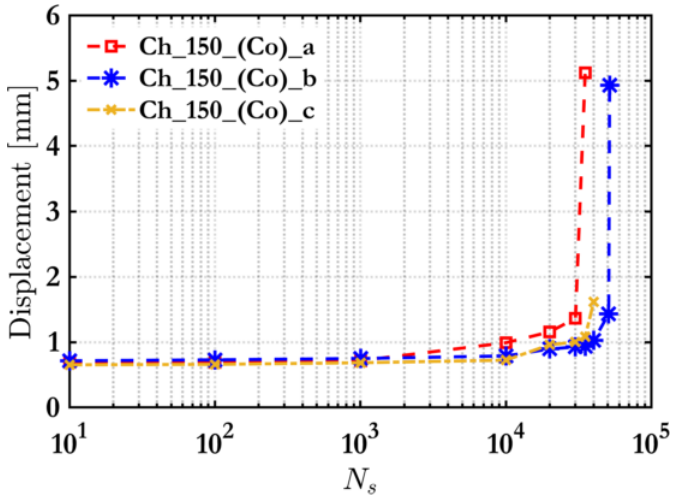

(a) L_b=150mm

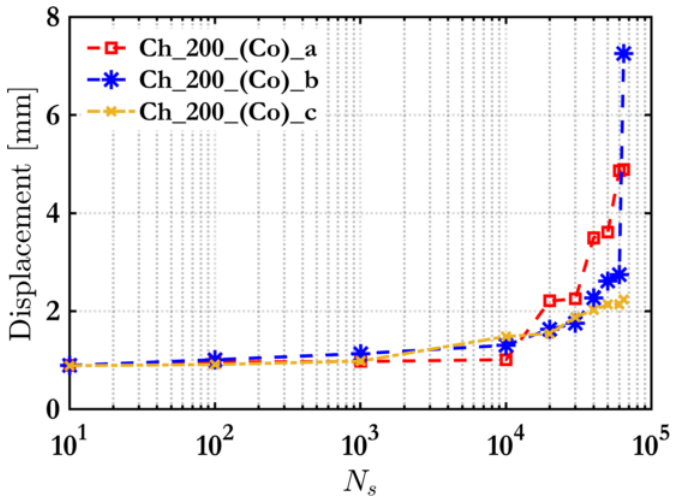

(b) L_b=200mm

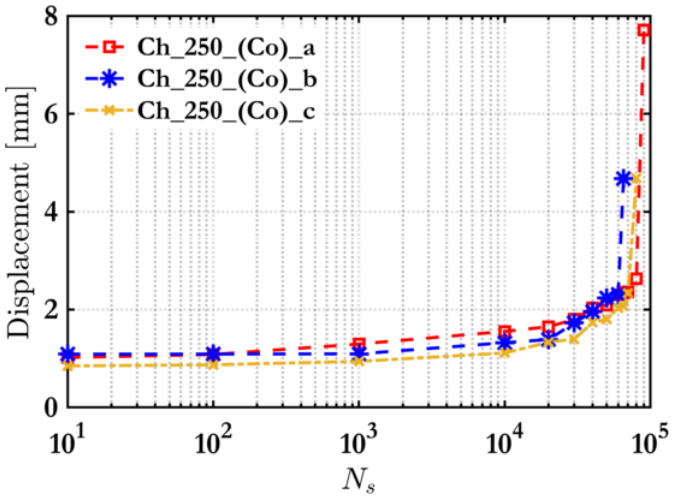

(c) L_b=250mm

Figure 5.37: Fatigue test displacement of cycles N_s for $P_{max} = 0.6P_{max}$: (a) 150mm, (b) 200mm, and (c) 250mm bond length in case of coated carbon

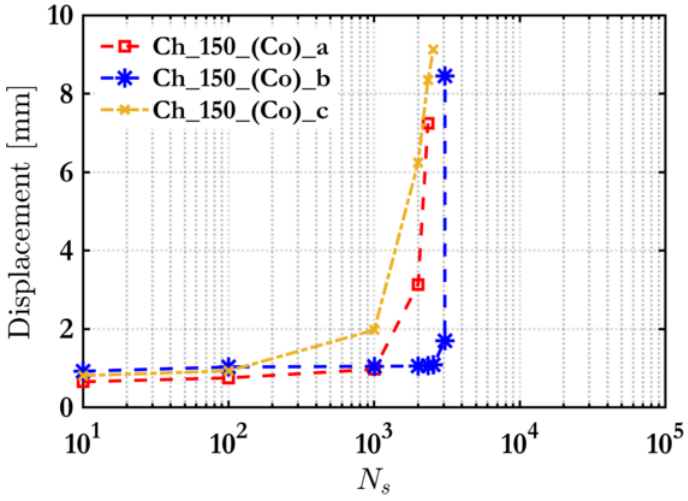

(a) L_b=150mm

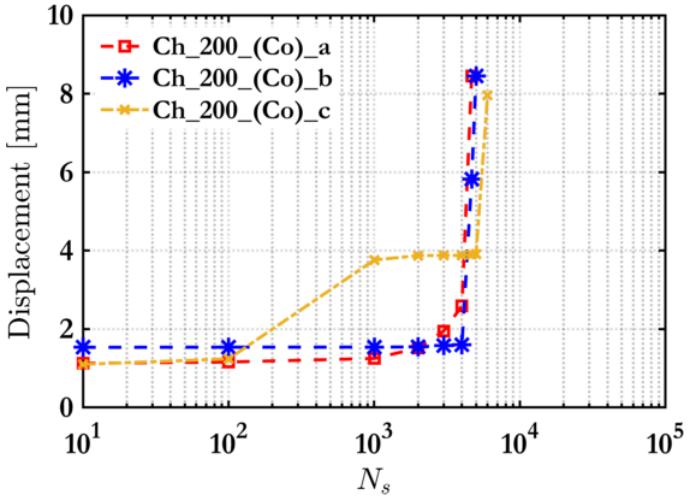

(b) L_b=200mm

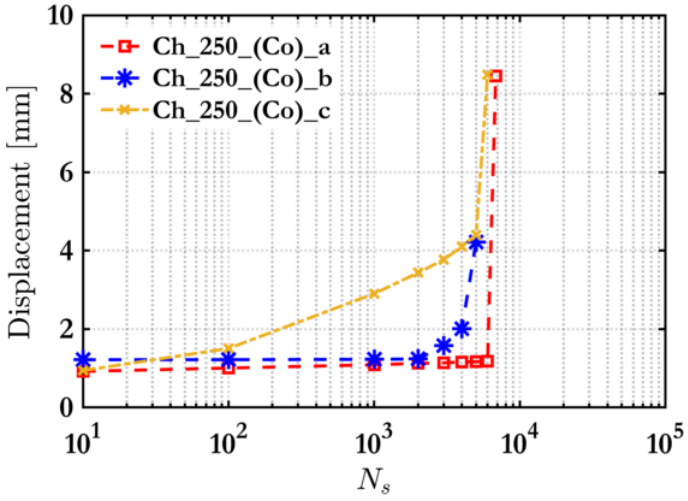

(c) L_b=250mm

Figure 5.38: Fatigue test displacement of cycles N_s for $P_{max} = 0.7P_{max}$: (a) 150mm, (b) 200mm, and (c) 250mm bond length in case of coated carbon

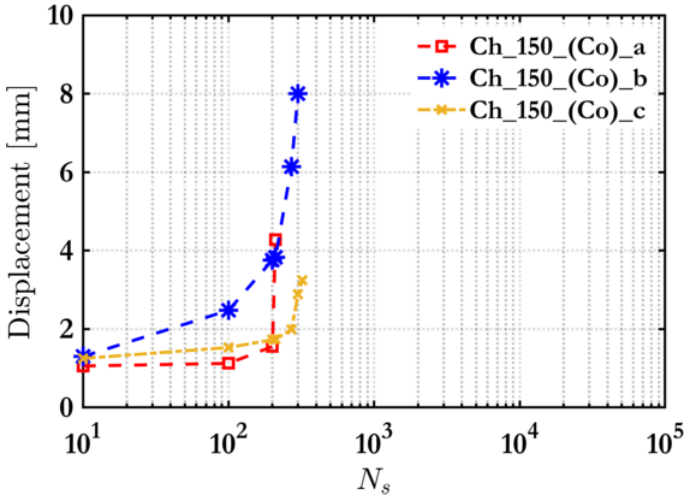

(a) L_b=150mm

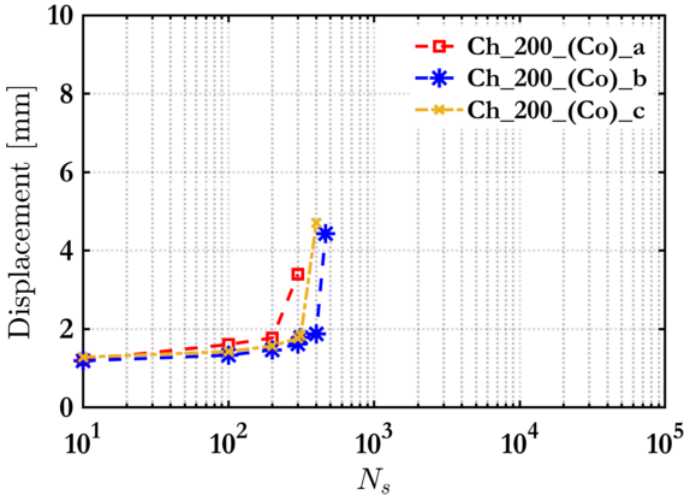

(b) L_b=200mm

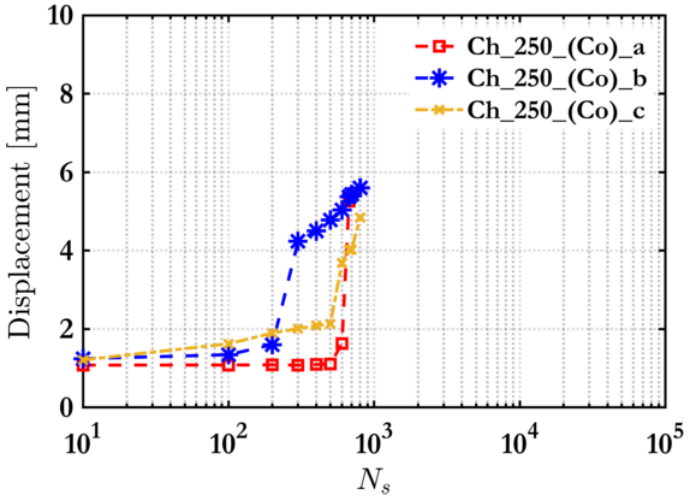

(c) L_b=250mm

Figure 5.39: Fatigue test displacement of cycles N_s for $P_{max} = 0.8P_{max}$: (a) 150mm, (b) 200mm, and (c) 250mm bond length in case of coated carbon

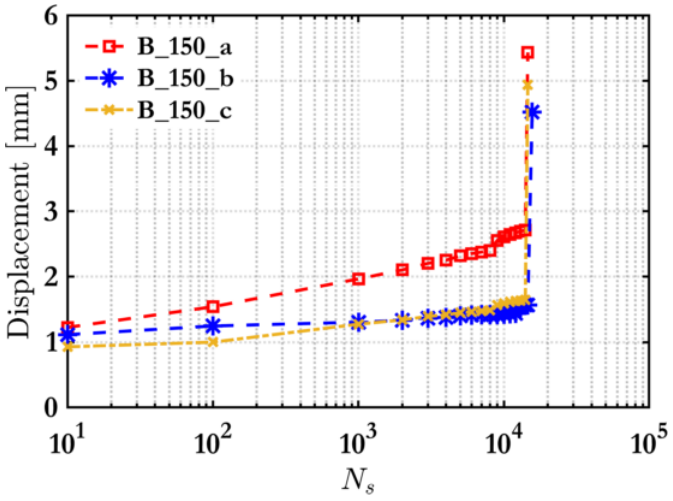

(a) L_b=150mm

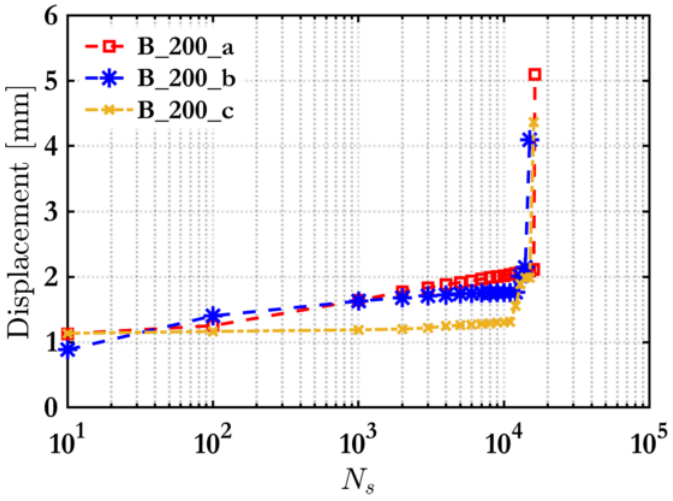

(b) L_b=200mm

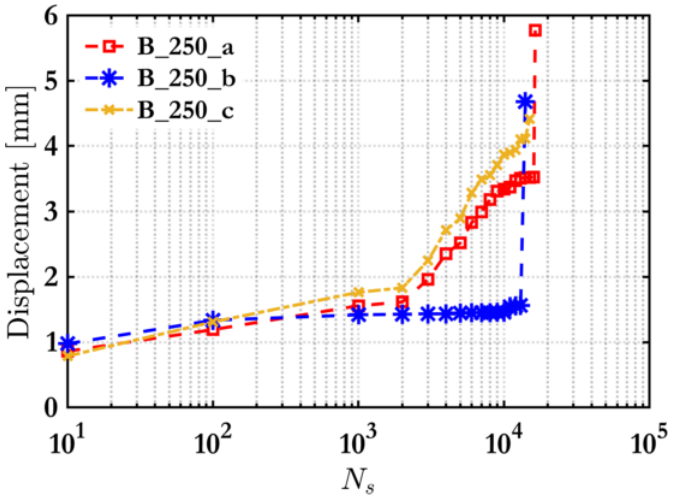

(c) L_b=250mm

Figure 5.40: Fatigue test displacement of cycles N_s for $P_{max} = 0.6P_{max}$: (a) 150mm, (b) 200mm, and (c) 250mm bond length in case of basalt

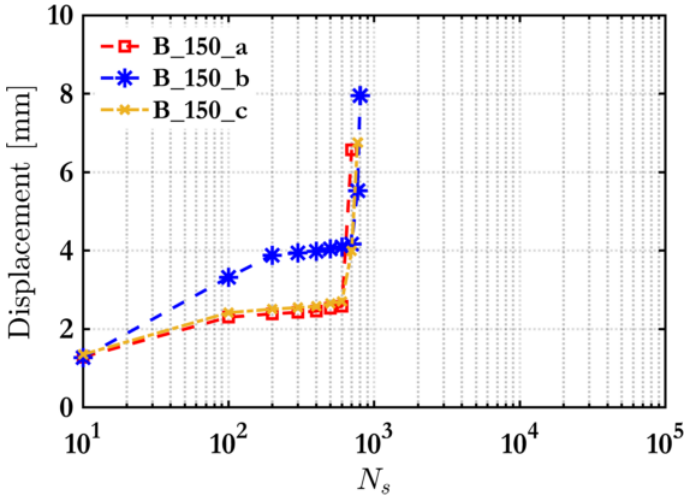

(a) L_b=150mm

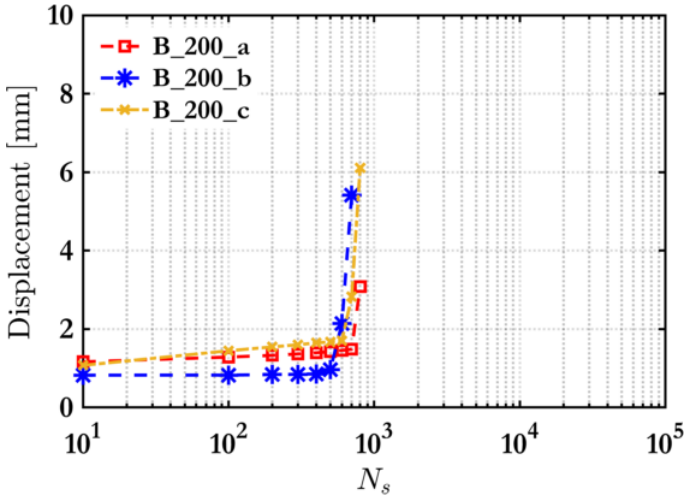

(b) L_b=200mm

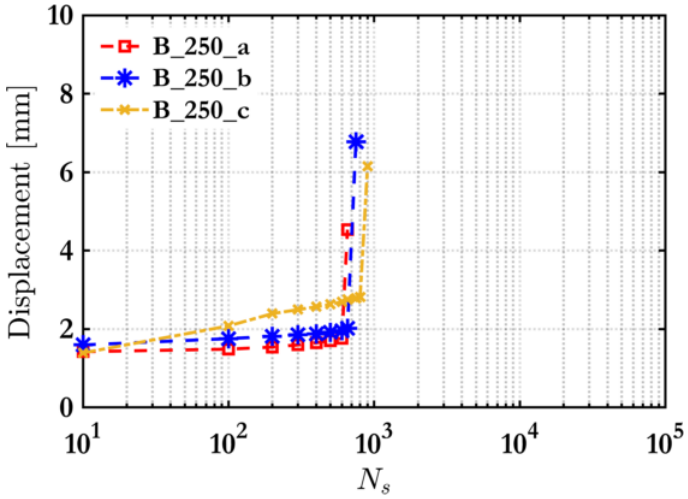

(c) L_b=250mm

Figure 5.41: Fatigue test displacement of cycles N_s for $P_{max} = 0.7P_{max}$: (a) 150mm, (b) 200mm, and (c) 250mm bond length in case of basalt

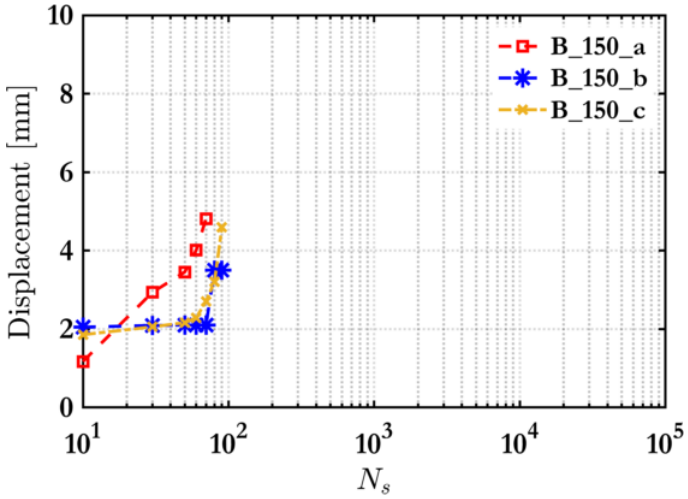

(a) L_b=150mm

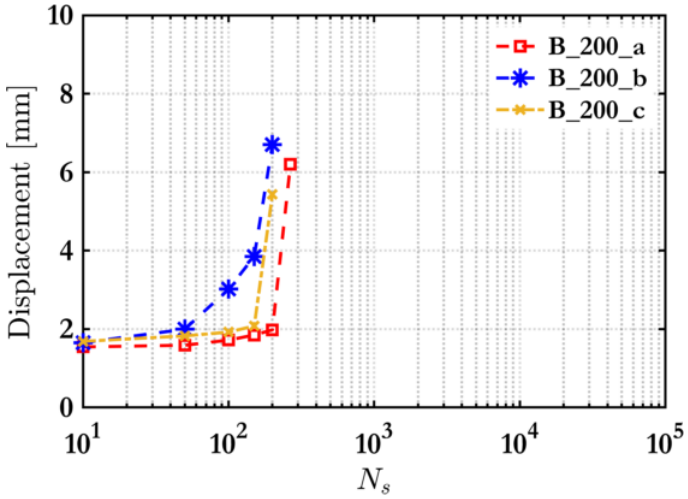

(b) L_b=200mm

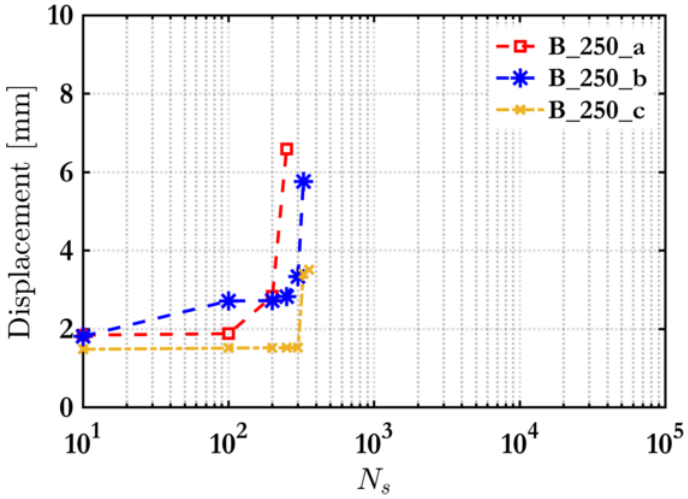

(c) L_b=250mm

Figure 5.42: Fatigue test displacement of cycles N_s for $P_{max} = 0.8P_{max}$: (a) 150mm, (b) 200mm, and (c) 250mm bond length in case of basalt

As the loading factor increases, the global slip increases accordingly. It can be seen that significant slip is grown even in the first ten cycles and increasing gradually up to failure. It observed that in the case of $\lambda = 60\%$ the displacement increases progressively; the slip practically doubles just before the sudden failure (coated carbon) Fig. 5.37. The same trend seen in terms of the rest percentage of the maximum applied load. In common, the slip response depending on the upper load of fatigue tests in good agreement with the quasi-static tests slip results of both textile materials.

5.6 Concluding Remarks

This chapter presents and discusses the results obtained from an experimental campaign investigating the TRM to masonry bond under one-sided cyclic loading conditions. The effect of various load ranges (60%, 70% and 80% of P_{max}), bond lengths (150 mm, 200 mm, 250 mm), and textile materials (carbon, basalt) was investigated. The key observations derived from experimental analysis are:

(i). In case of basalt textile specimens under the cyclic loading conditions considered in this study, a shift in the failure mode observed. For all bond lengths examined, textile slippage observed. Slippage manifests itself with a constant decrease in the TRM stiffness, as shown in the corresponding load-deflection plots. No variation of the maximum number of cycles was observed for larger bond lengths. Although the failure mechanism initiates with the textile slipping through the matrix, slippage arrests, and the textile eventually breaks. This, however seems to be pertinent to the fact that after initial slippage, it is difficult to maintain a uniform stress distribution on the textile under load control

(ii). In the case of coated carbon textile, the fatigue life under fatigue load cycling of lower load amplitude ($\lambda = 60\%$ and $\lambda = 70\%$) is dominated by crack initiation, crack propagation and matrix detachment and finally failure, while on lowering the load amplitude ($\lambda = 80\%$): cracks initiations, cracks propagation and then sudden failure.

(iii). Fatigue failure of Ch_(Co) specimens under fatigue loading condition is caused by textile slippage within the bonded area. This failure mode was different

from the specimens tested under quasi-static monotonic loading, where textile detachment was observed.

(iv). Both textile materials tested demonstrated a similar response under either fatigue or static loading for increasing bond lengths. For the basalt textile, increasing the bond length had no effect on the peak load and N_s up to failure (with the exception of the $\lambda = 80\%$ case). In the case of coated carbon specimens, increasing bond lengths led to an increase in the maximum applied load (static loading) and an increase in the number of cycles up to failure (fatigue loading).

(v). According to the test results, the failure mechanism has developed and provided the main steps of the failure under fatigue life for both textile materials tested.

6 Finite element modelling

6.1 Introduction

The overarching aim of this chapter is to provide a robust procedure for simulating masonry constituent materials and components, consistently backup up by experimental results. To achieve this, appropriate values for the textile to mortar interface properties were identified based on the experimental results discussed in Chapter 3. Next, these values were used to simulate the response of TRM coupons and the results obtained were compared to experimental results obtained from Raoof & Bournas (2017) and Tetta et al. (2018). Furthermore, the same cohesive properties were used to simulate the experiments conducted in Kariou et al. (2018).

In the following, the fundamental constitutive models to account for the nonlinear response of the materials involved and the corresponding interfaces are presented. Next, the simulation procedure proposed for bond tests, textiles, TRM coupon tests, and masonry wallettes in out of plane bending is presented.

6.2 Bond test modelling

The aim this simulation procedure was to identify the appropriate cohesive properties at the fibre to TRM interface based on the experimental results presented in Chapter 3. To this end, the quasi-static bond tests conducted in this research as described in Chapter 4 were simulated in Abaqus. In total, 28 models were made considering all seven textile materials (glass, glass coated, carbon heavy, carbon heavy coated, carbon

light, carbon light coated and coated basalt) and four bond lengths each (100 mm, 150 mm, 200 mm, and 250 mm). All masonry wallettes had dimensions of 365 x 215 x 102.5 mm and were constructed from five clay bricks with a nominal dimension of 215 x 102.5 x 65 mm. The material properties of the clay bricks, join mortar, the strengthening mortar and the textile fibre materials are also provided in Chapter 3.

6.2.1 Geometry and type of elements

In this research, a 3D geometrical representation for the specimens was opted for. This was to allow for a generic representation that can, in future research, account for possible heterogeneities in the material distribution across the volume of the specimen and hence enable for a robust uncertainty quantification procedure as in e.g., the effect of various defects. To simulate the bond at the mortar to brick and textile to mortar interfaces, a cohesive surface approach was implemented.

The bricks and the joint mortar was modelled with solid homogeneous elements. The maximum compressive strength, and the Young's modulus of the bricks are presented in Table 3.1. All masonry wallettes had dimensions of 365 x 215 x 102.5 mm and constructed with the stacked together of five clay bricks with a nominal dimension of 215 x 102.5 x 65 mm. The bricks and the joint mortar were meshed with hexahedral 20-noded elements with reduced integration; reduced integration was opted for to reduce computational costs and alleviate issues pertinent to shear locking (Bathe 2006). A standard convergence analysis was conducted to ensure accuracy and determine an optimum mesh. A 25mm mesh size was chosen for the bricks and a 10mm size for the mortar. Reduced integration shell elements were used to model the TRM matrix. The bond between the matrix and the bricks was realised via a cohesive surface functionality. Details on these cohesive properties are provided in Section 6.2.2.

The textile fabric was modelled with 2-node linear beam elements (B31) Fig. 6.1. The bond between the textile fabric and the matrix was modelled via the definition of a corresponding cohesive surface property. Beam instead of truss elements were chosen so that the contact properties between the textile and the TRM mortar could be established. The mesh size for the textile was equal to 25 mm. A displacement control analysis was contacted as in the actual experiment. Hence, a monotonically

increasing displacement was applied at the top edge of the free textile end (Fig. 6.2). The model geometry and the interaction properties defined are shown in Fig. 6.3.

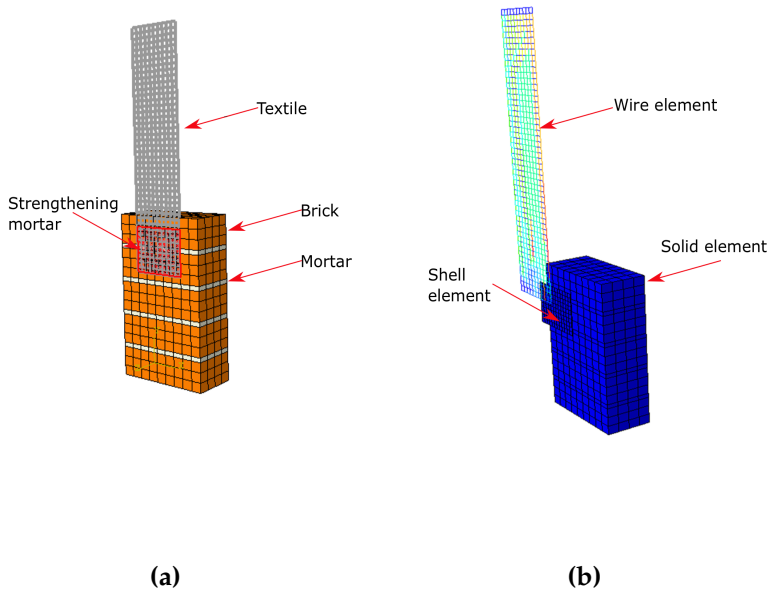

Figure 6.1: Model view glass 100 bond length (a) general view with parts component (b) parts definition

6.2.2 Application of the cohesive modelling approach on the masonry to TRM bond behaviour

The cohesive surface approach described in Section 2.8.1 was implemented to resolve the interface properties at i) the mortar to brick interface and ii) the textile to mortar interface. In this approach, the cohesive textile behaviour models the bond behaviour between the strengthening mortar and individual textile fibre yarn. Hence, the definitions of damage initiation and evolution accounted for a mode-II failure. The same holds for the mortar to brick interface. It is of interest to note that no detachments at the matrix to brick interface was observed in the experiments. Hence, nominal values were chosen for these cohesive properties to ensure the stability of the solution. The values used are provided in Table 6.1.

The interaction properties used for the two interfaces are shown in Table 6.1 (masonry wall to strengthening mortar) and Table 6.2 (strengthening mortar and textile). It is important to note that in this test, the only pertinent properties (and hence identifiable from the experimental results) are the tangential cohesive stiffness K_{tt} and

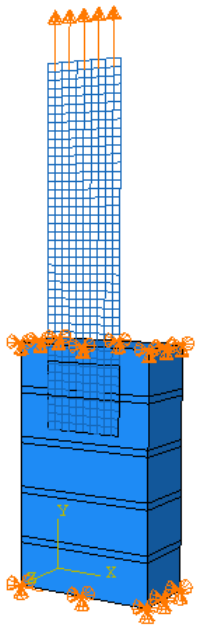

Figure 6.2: Loading of specimen

Table 6.1: Interaction property masonry wall to strengthening mortar

	Tangential behaviour	
Friction formulation	Friction coefficient	
penalty	0.4	
	Normal behaviour	
Pressure-Overclouse	Constraint enforcement method	Contact stiffness
Linear	Default	100000
	Cohesive behaviour	
Knn	Kss	Ktt
10000000	100000	10000
	Damage	
Normal Only	Shear-1	Shear-2
100	100	1000

the mode 2 shear strength. Hence, a set of default values was chosen for all other, non-activated properties.

6.2.3 Finite element analysis results and discussion

In this Section, the simulation results are presented and discussed. In all cases, a fracture energy was chosen equal to 0.067 (Kn/m) according to the literature. Furthermore, a friction coefficient of 0.4 was used in this study to capture the post-damage response although suggested values range between 0.6-0.8 Nazir & Dhanasekar (2013), Bolhassani et al. (2015).

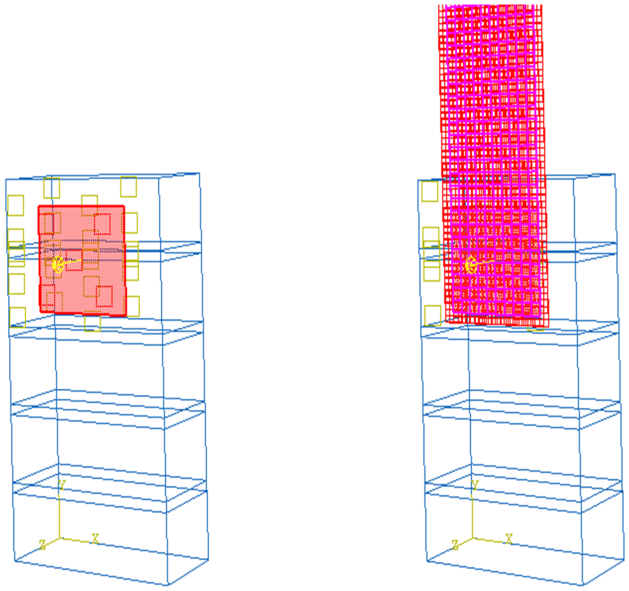

(a) (b)

Figure 6.3: Geometry of assemblages and surface-based interaction of units (a) strengthening mortar to wall (a) textile to strengthening mortar

The resulting load - slip plots are shown in Figs. 6.4-6.10 for the glass light carbon, heavy carbon and basalt and principal stress in Figs 6.11-6.24 . The Table 6.3 shows the peak stress, failure mode and relative deviations of real tests and FEM modelling results. In all cases, a good agreement is retrieved between the simulations and the experimental results in case of P_{max} and displacement to P_{max}. It is important to note that for each material, the same cohesive properties are used across all bond lengths. It is also important to note that in all cases both the peak load and the corresponding deflection are accurately captured.

With the exception of the coated textile specimens. Specimens Ch_(Co) and Cl_(Co) failed due to textile detachment (see Table 6.3) a minimal difference was observed between the stress of the test and model with except Ch_(Co)_200, and Ch_(Co)_250 where the stress is relatively low (in the model). The textile in the model was about to detach, which led to convergence issues in the solution procedure when the peak load was attained, which agrees with the experimental results.

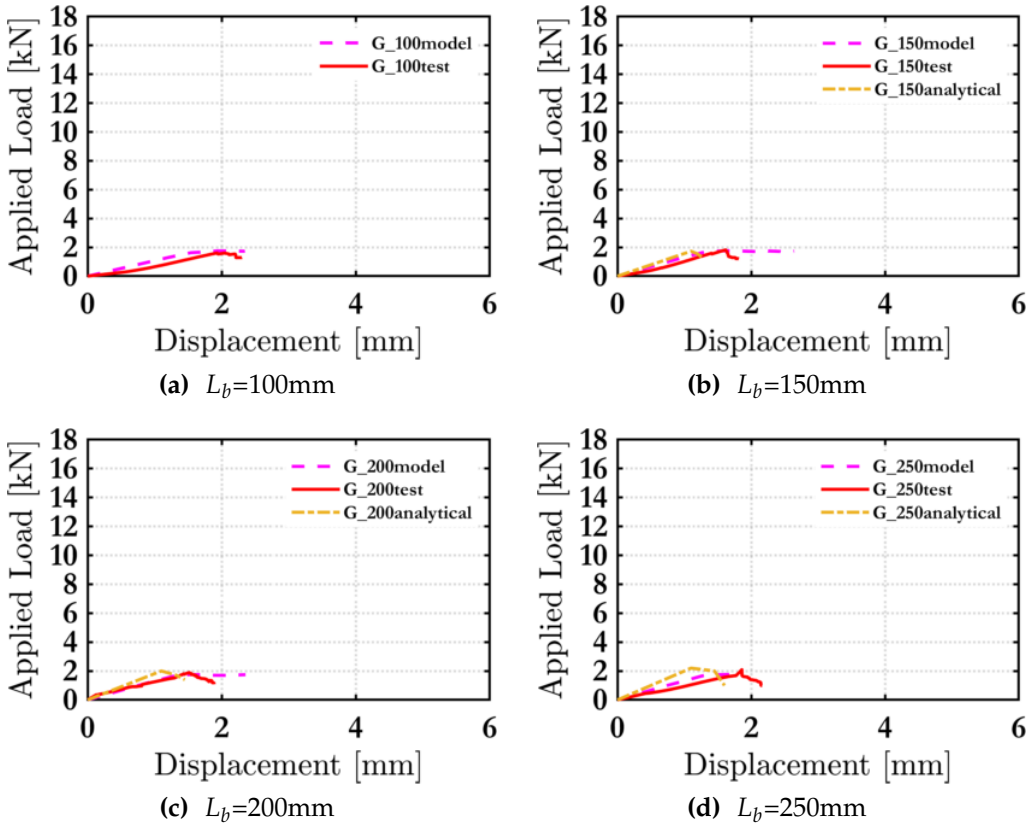

(a) L_b=100mm **(b)** L_b=150mm

(c) L_b=200mm **(d)** L_b=250mm

Figure 6.4: Load-displacement curves of glass specimens

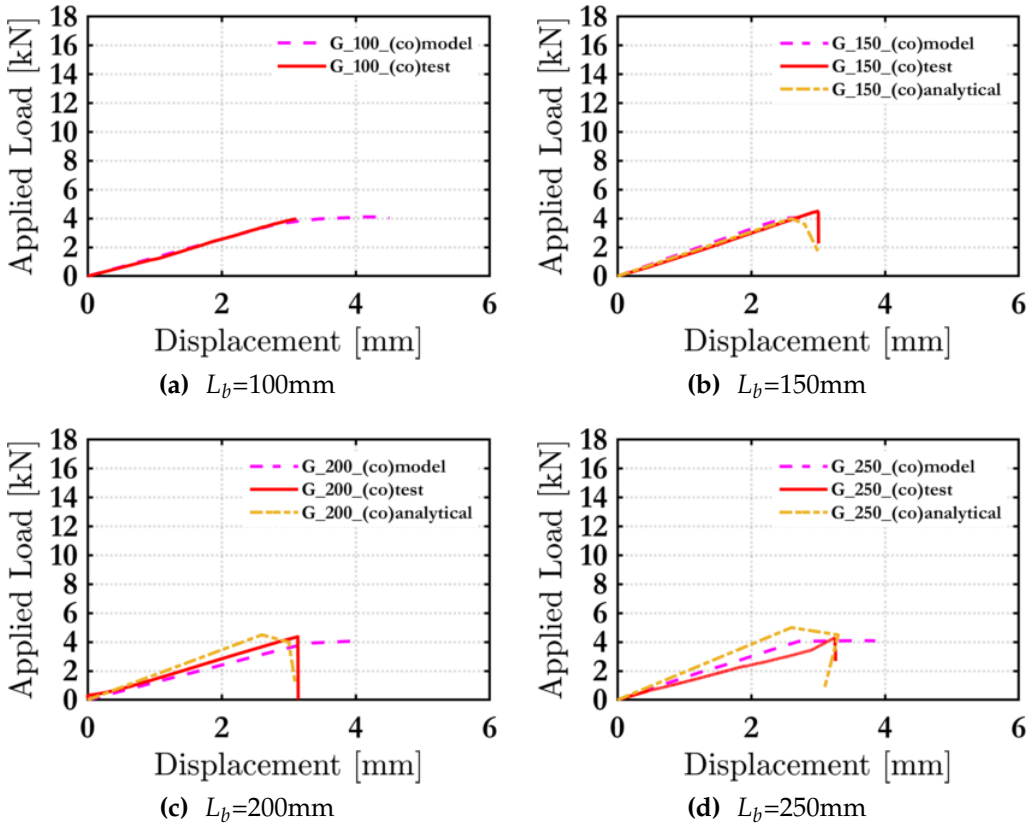

(a) L_b=100mm **(b)** L_b=150mm

(c) L_b=200mm **(d)** L_b=250mm

Figure 6.5: Load-displacement curves of glass coated specimens

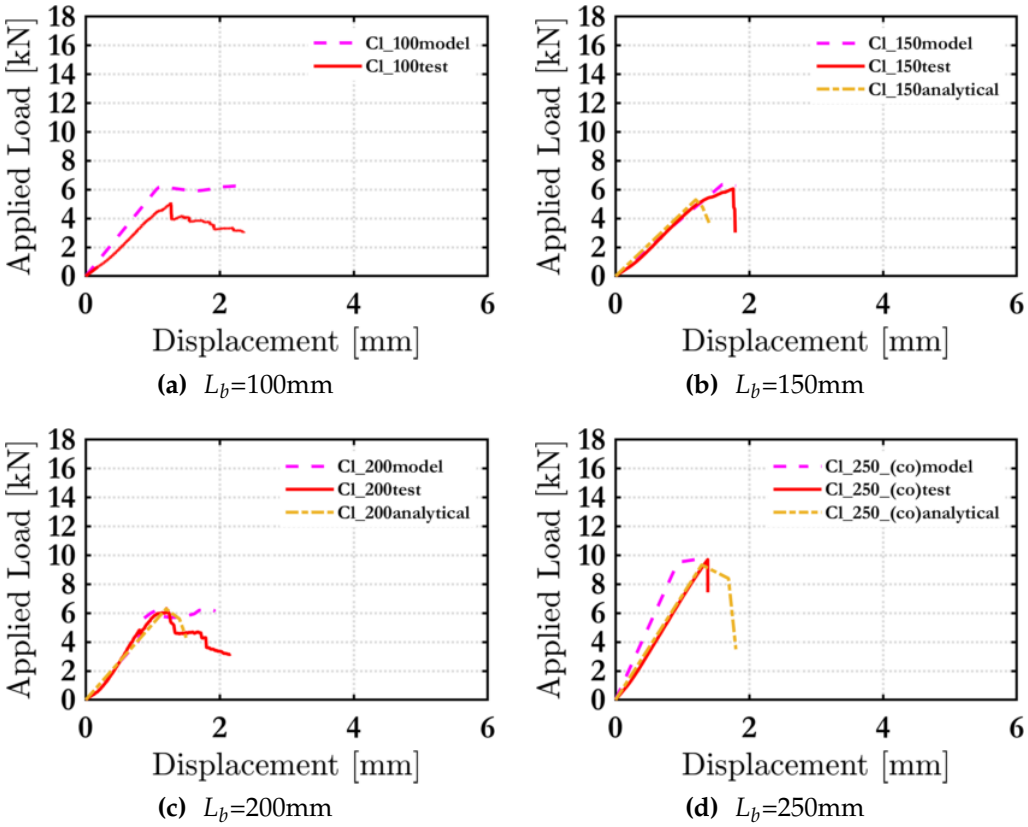

(a) L_b=100mm **(b)** L_b=150mm

(c) L_b=200mm **(d)** L_b=250mm

Figure 6.6: Load-displacement curves of carbon light specimens

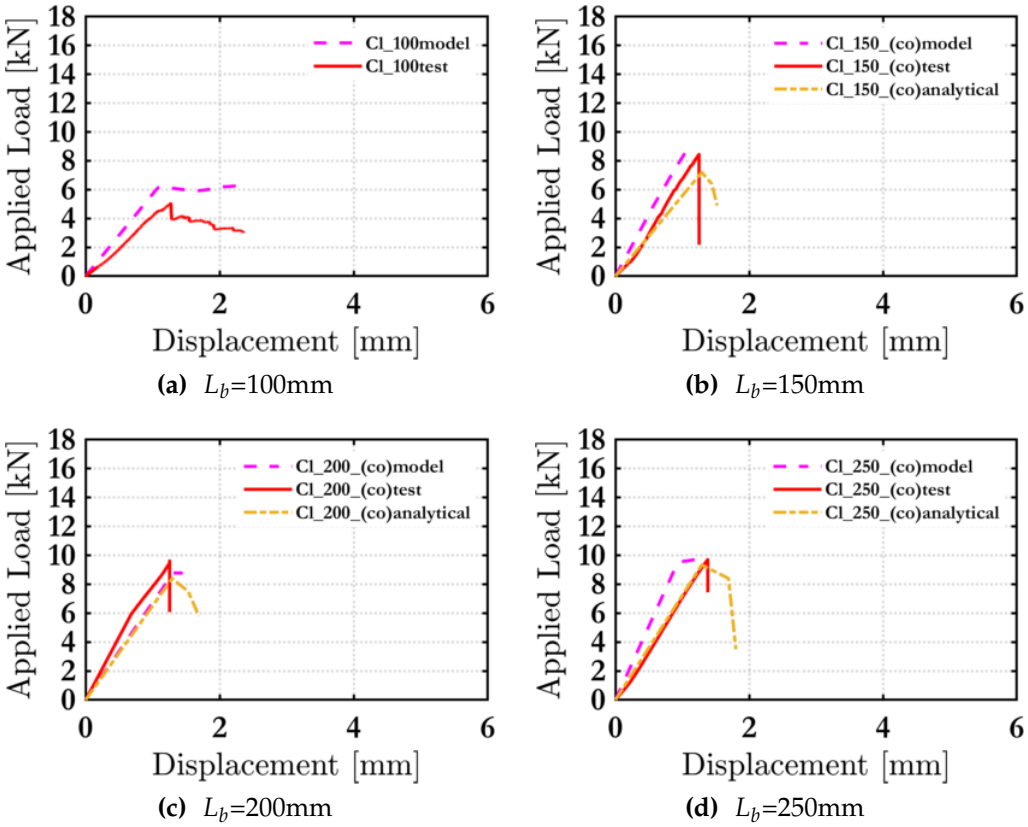

(a) L_b=100mm **(b)** L_b=150mm

(c) L_b=200mm **(d)** L_b=250mm

Figure 6.7: Load-displacement curves of carbon light coated specimens

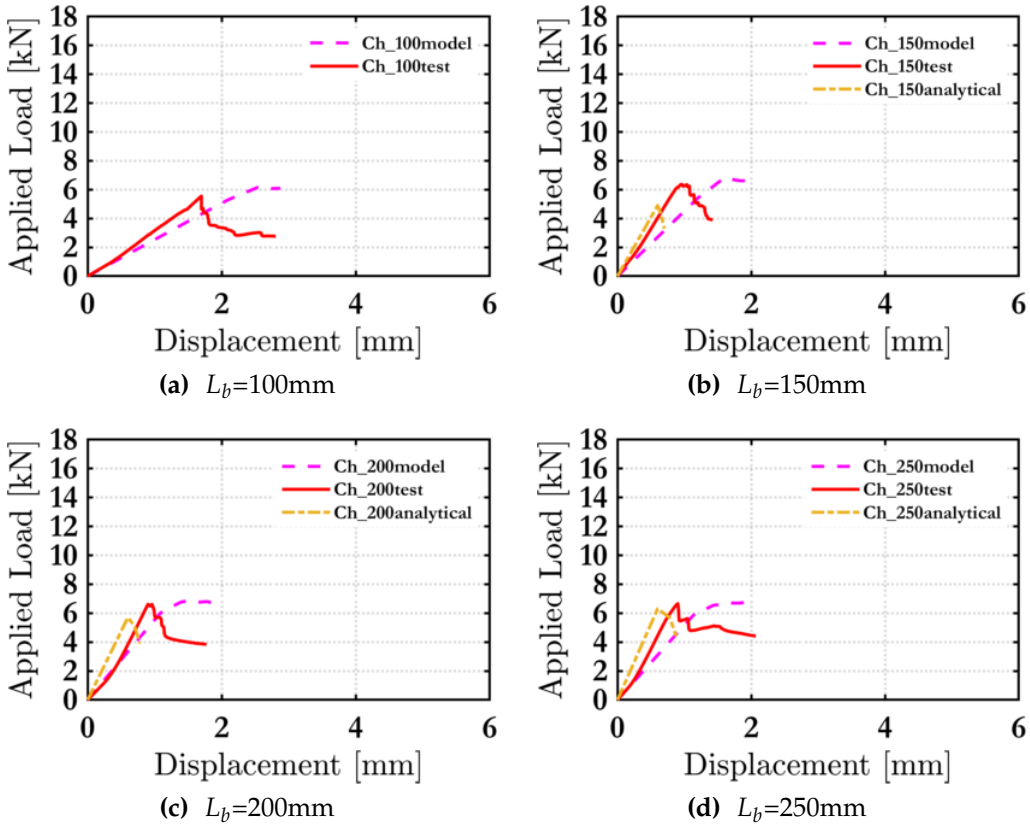

(a) L_b=100mm **(b)** L_b=150mm

(c) L_b=200mm **(d)** L_b=250mm

Figure 6.8: Load-displacement curves of carbon heavy specimens

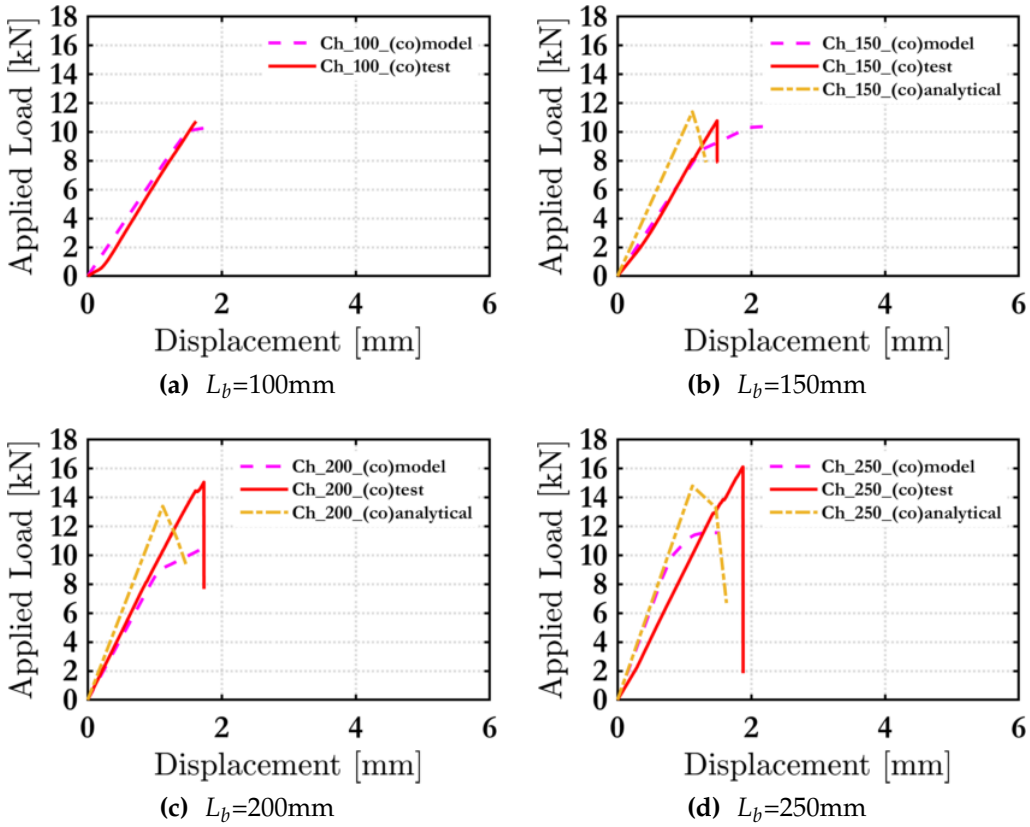

(a) L_b=100mm **(b)** L_b=150mm

(c) L_b=200mm **(d)** L_b=250mm

Figure 6.9: Load-displacement curves of carbon heavy coated specimens

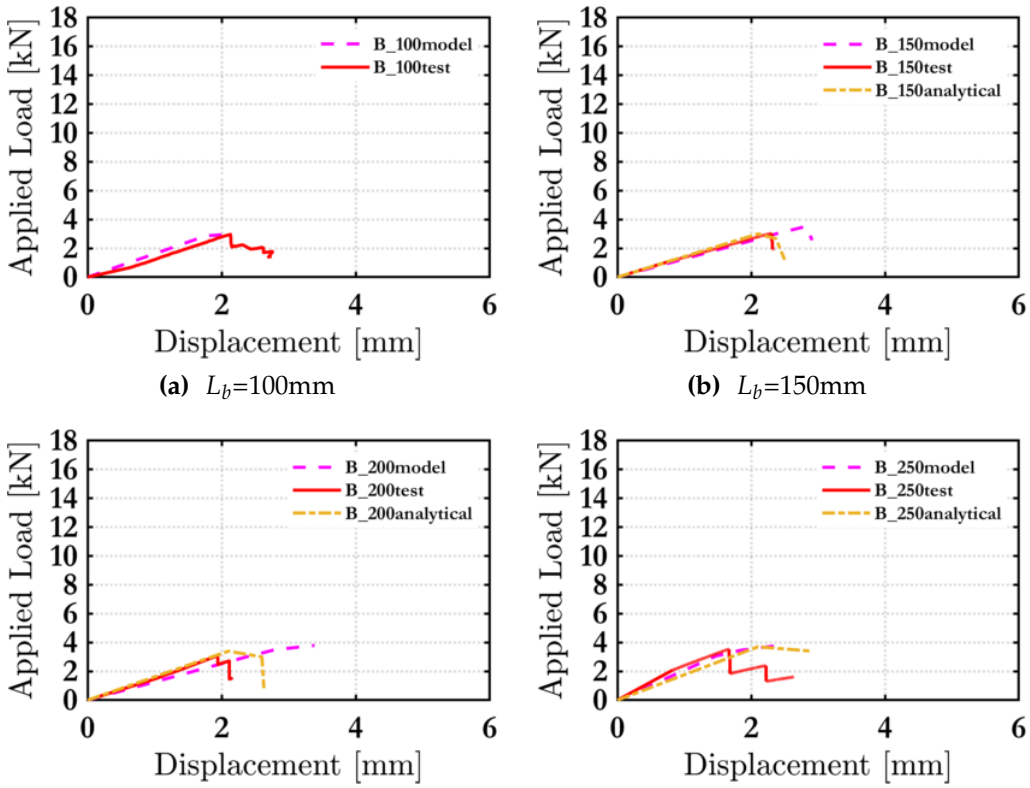

(a) L_b=100mm **(b)** L_b=150mm

(c) L_b=200mm **(d)** L_b=250mm

Figure 6.10: Load-displacement curves of basalt specimens

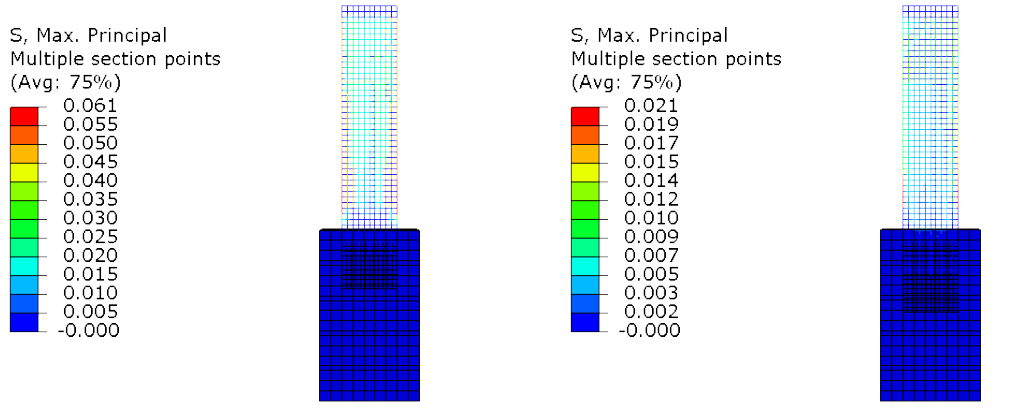

(a) L_b=100mm **(b)** L_b=150mm

Figure 6.11
Principal stress of glass specimens

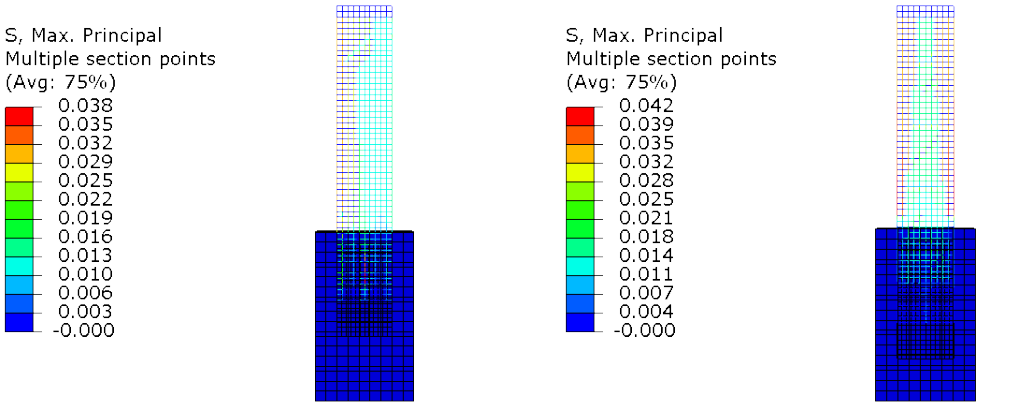

(a) L_b=200mm **(b)** L_b=250mm

Figure 6.12: Principal stress of glass specimens

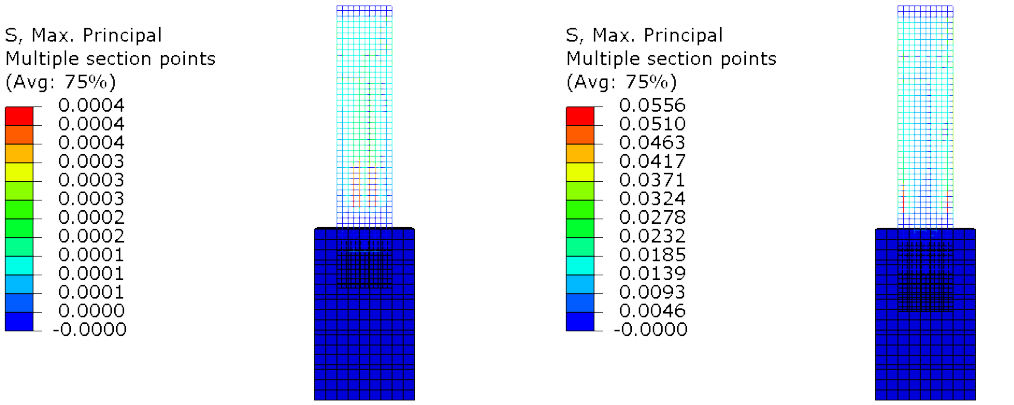

(a) L_b=100mm **(b)** L_b=150mm

Figure 6.13: Principal stress of coated glass specimens

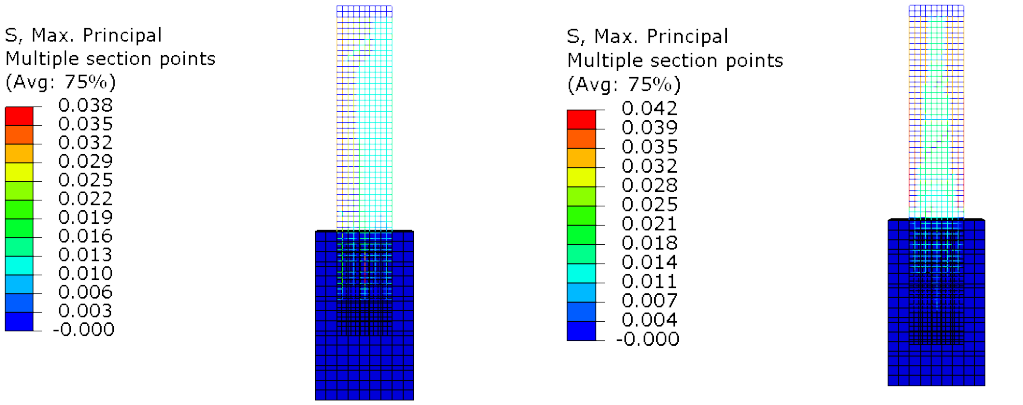

(a) L_b=200mm **(b)** L_b=250mm

Figure 6.14: Principal stress of coated glass specimens

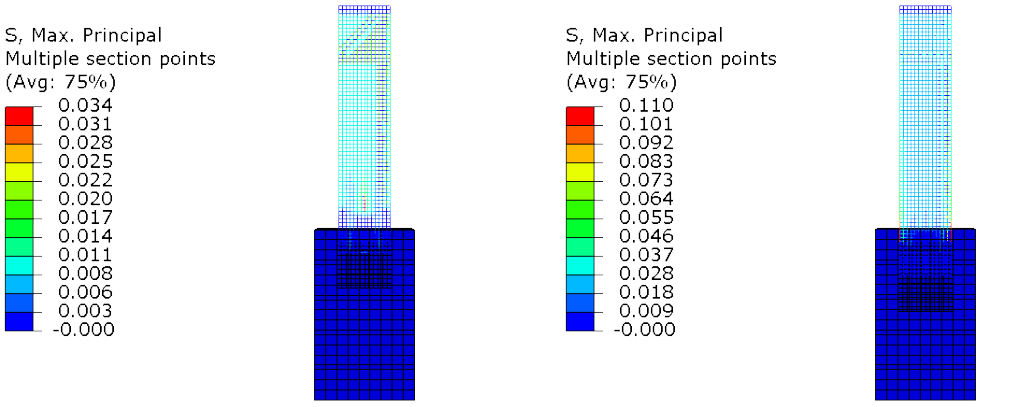

(a) L_b=100mm **(b)** L_b=150mm

Figure 6.15: Principal stress of light carbon specimens

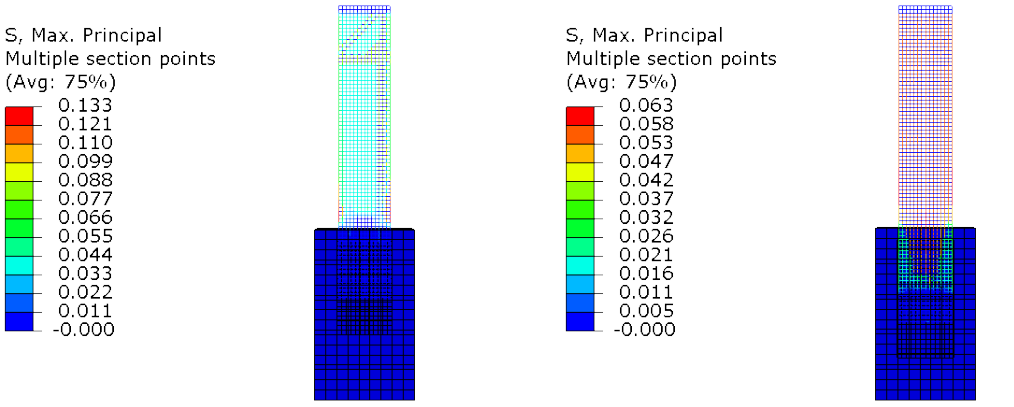

(a) L_b=200mm **(b)** L_b=250mm

Figure 6.16: Principal stress of light carbon specimens

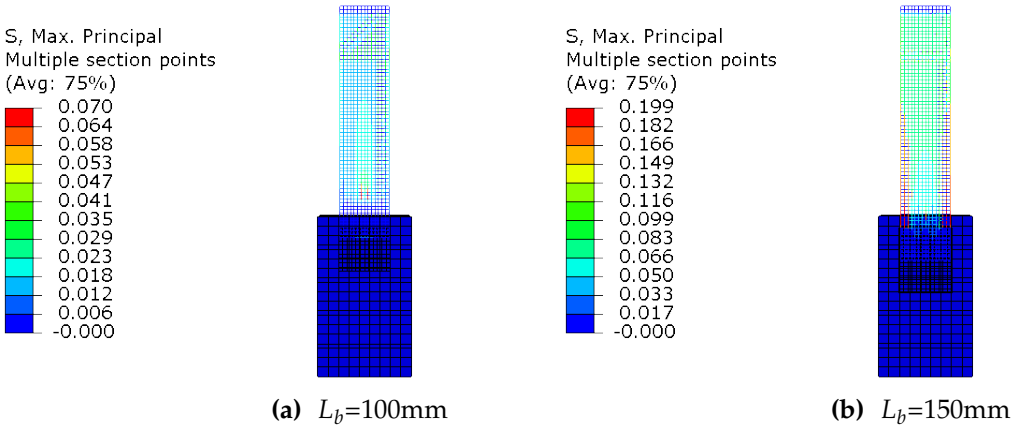

(a) L_b=100mm **(b)** L_b=150mm

Figure 6.17: Principal stress of light carbon coated specimens

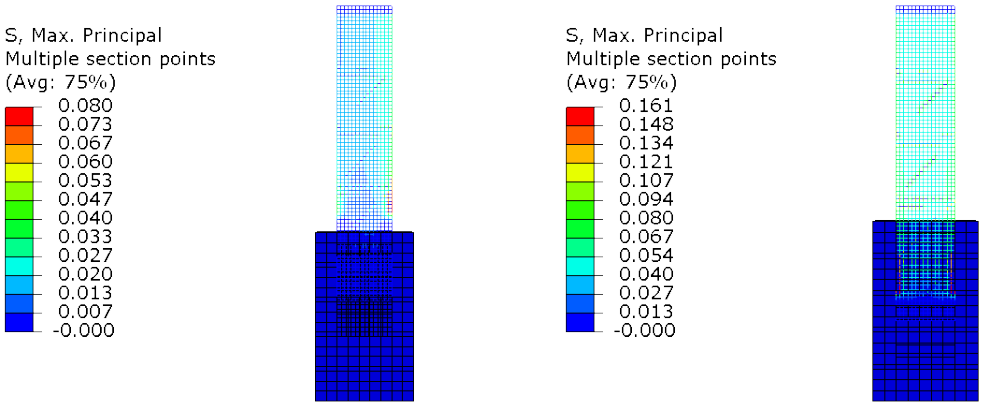

(a) L_b=200mm **(b)** L_b=250mm

Figure 6.18: Principal stress of light carbon coated specimens

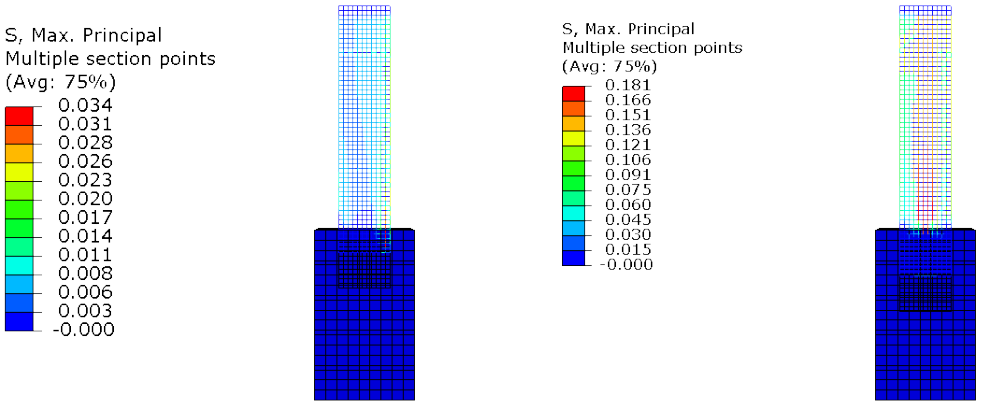

(a) L_b=100mm **(b)** L_b=150mm

Figure 6.19: Principal stress of heavy carbon specimens

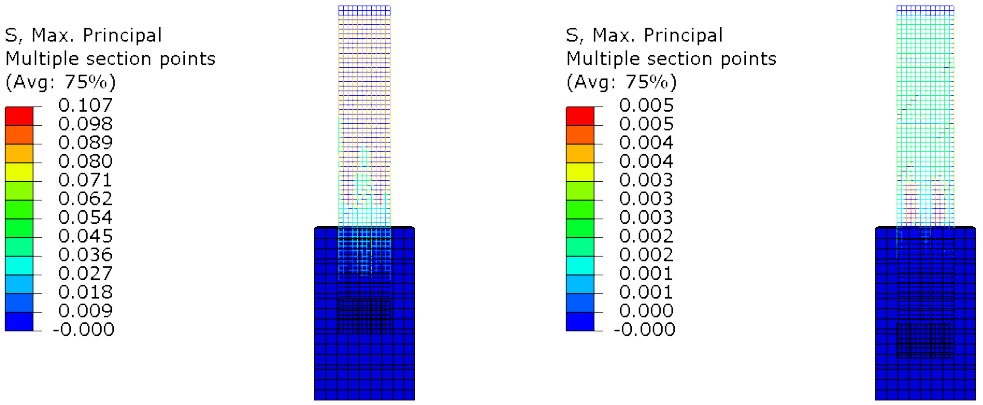

(a) L_b=200mm **(b)** L_b=250mm

Figure 6.20: Principal stress of heavy carbon specimens

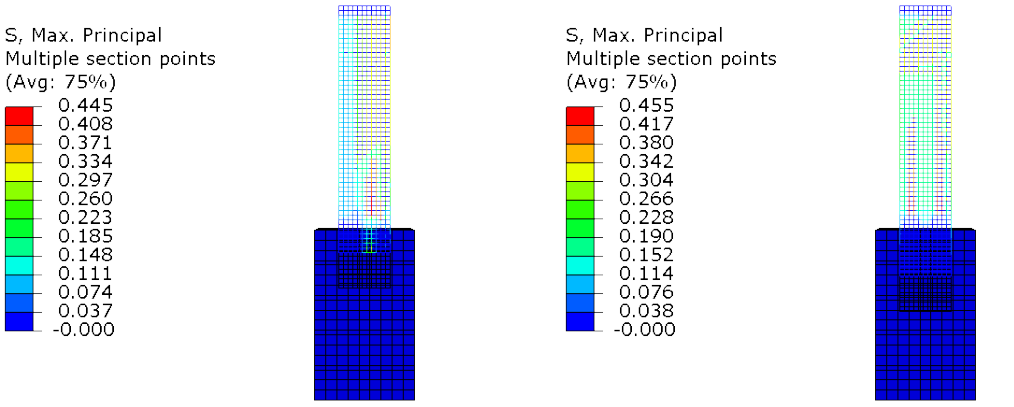

(a) L_b=100mm **(b)** L_b=150mm

Figure 6.21: Principal stress of heavy coated carbon specimens

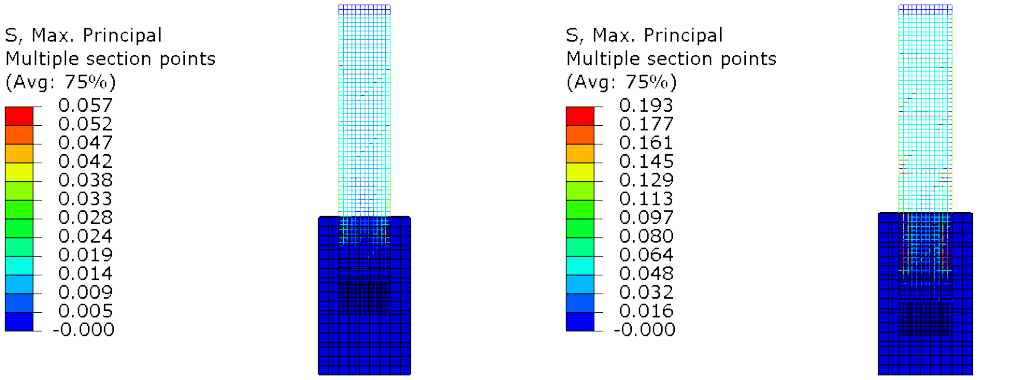

(a) L_b=200mm **(b)** L_b=250mm

Figure 6.22: Principal stress of heavy coated carbon specimens

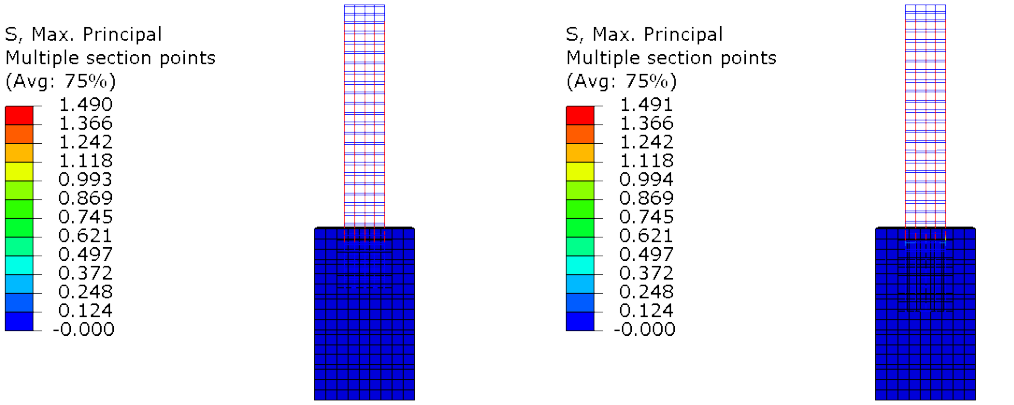

(a) L_b=100mm **(b)** L_b=150mm

Figure 6.23: Principal stress of basalt specimens

Table 6.2: The variation on the interaction property between strengthening mortar and textile

Materials	Interaction property						
	Cohesive Behaviour			Damage			Young's modulus (GPa)
	Knn	Kss	Ktt	Normal	Shear-1	Shear-2	
Glass	1.00E+07	60000	1000	100	15	65	47
Glass coated	1.00E+07	60000	3000	100	15	180	
Carbon (light)	1.00E+07	60000	6000	100	15	350	140
Carbon (light) coated	1.00E+07	60000	4000	100	15	400	170
Carbon (heavy)	1.00E+07	60000	6000	100	15	370	160
Carbon (heavy) coated	1.00E+07	60000	4200	100	15	480	196
Basalt	1.00E+07	60000	2500	100	15	130	59

6.2.4 The effect of the bond length: numerical vs experimental results

Increasing the bond length leads to increasing the value of the maximum applied load. The Fig. 6.25 shows the peak load against bond length between test and modelling result with regards to glass textile coated and not. Specimens G_100, G_150, G_200, and G_250, failed due to slippage. The coated glass specimens G_100_(Co), G_150_(Co), G_200_(Co), and G_250_(Co) failed due to textile rupture, a minimal difference was observed between the stress of the test and model. The interaction property used in the models is shown Table 6.2 and the E_t used from the textile coupon test.

Both uncoated carbons failed due to the slippage of the textile. Except for the coated carbons textile fibre specimens (light and heavy), the effective bond length is in the range of 150-200 mm for all remaining specimens. The simulated result represents the same failure patterns as the test result and the effective bond length lied in the same range as in the experiment. Both coated carbons failed due to the detachment of textiles from the matrix in all bond lengths. This is attributed to either poor mortar matrix tensile property or not enough TRM thicknesses. However, specimens Ch_200_(Co) and Ch_200_(Co) demonstrated the increasing bond performance up almost 50% compared to 150 mm. Is noteworthy that the FEM of coated heavy

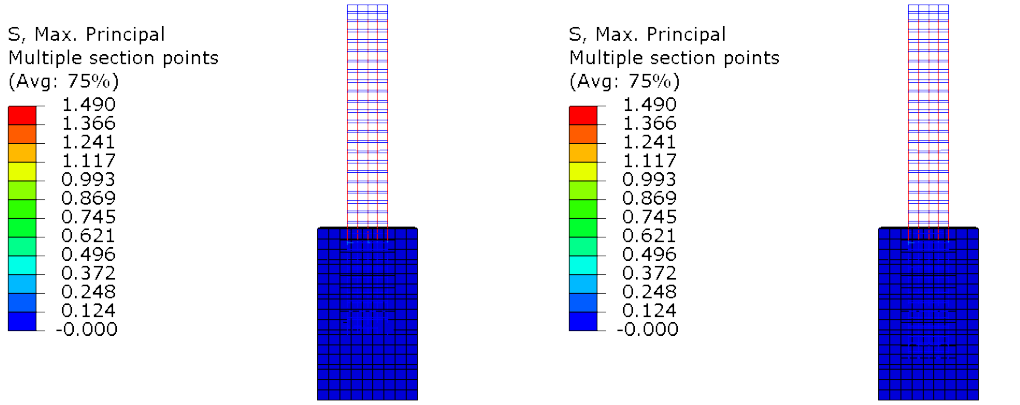

(a) L_b=200mm **(b)** L_b=250mm

Figure 6.24: Principal stress of basalt specimens

carbon represents the same increase of the maximum load after 200 mm bond length. This shows the reliability of the FE results concerning the experimental results. The interaction property of the simulated tests of both coated and not coated carbons are shown in Table 6.2 the. The Young's modulus in FEM specimens was similar to the textile coupons.

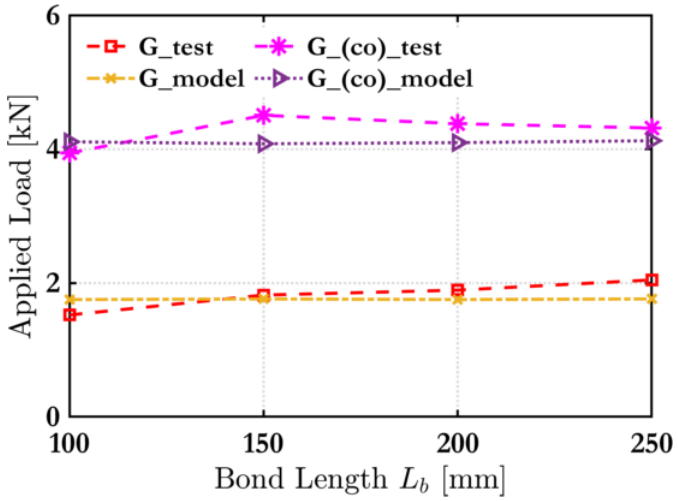

Figure 6.25: Maximum applied load against bond length test result versus model glass coated and uncoated

The observed failure mode in all basalt specimens namely B_100, B_150, B_200 and _250mm was a textile rupture, the recorded P_{max} for L_b =250 mm was increased by 12% with respect to the L_b =200 mm. The textile modulus of elasticity in all basalt bond lengths of FEM had the same values as in the coupon test of bare textile.

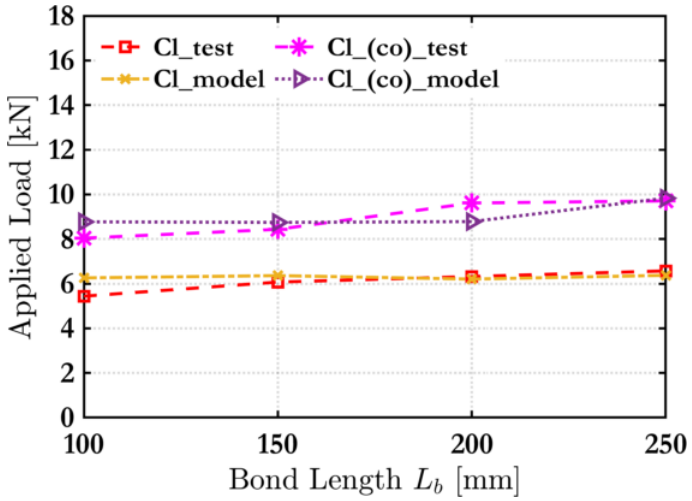

Figure 6.26: Maximum applied load against bond length test result versus model Carbon light coated and uncoated

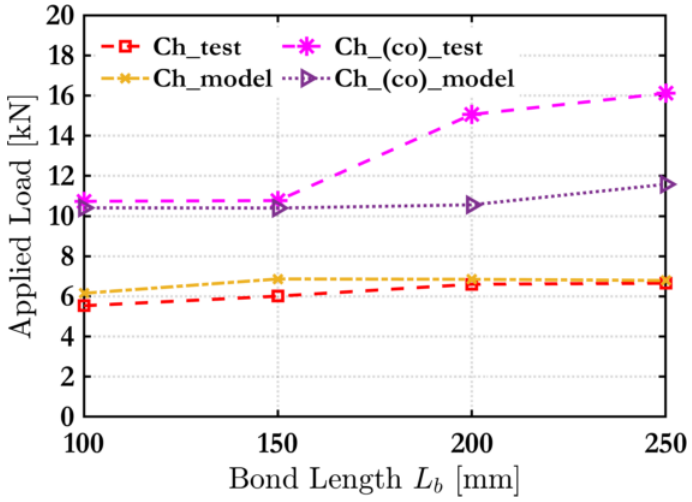

Figure 6.27: Maximum applied load against bond length test result versus model Carbon heavy coated and uncoated

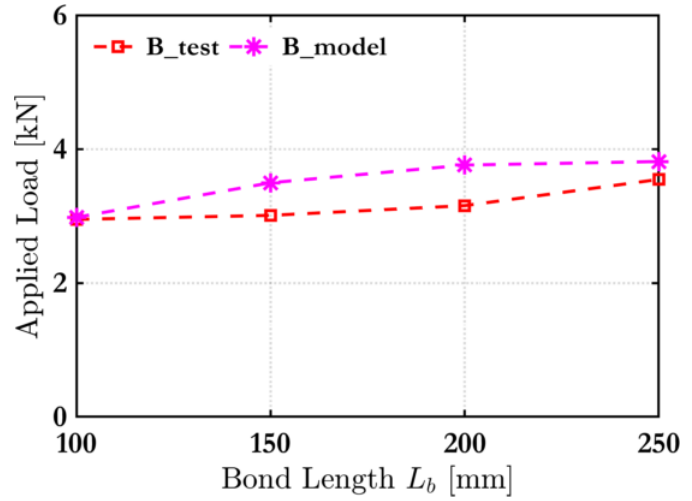

Figure 6.28: Maximum applied load against bond length test result versus model coated basalt

Table 6.3: Experimental and simulated result compare bond test

Specimen	Bond test Peak Stress [MPa]	Failure mode	FEM Peak Stress [MPa]	Failure mode	Rd*
G_100	262	D	301	D	0.0221
G_150	313	D	303	D	0.0011
G_ 200	325	D	301	D	0.0054
G_250	352	D	303	D	0.0191
G_100_(Co)	678	E1	707	D	0.0015
G_150_(Co)	775	E1	702	D	0.0084
G_200_(Co)	754	E1	705	D	0.0045
G_250_(Co)	742	E1	710	D	0.0012
Cl_100	731	D	841	D	0.0224
Cl_150	815	D	854	D	0.0024
Cl_200	849	D	833	D	0.0003
Cl_250	883	D	856	D	0.0009
Cl_100_(Co)	1080	C	1178	D	0.0084
Cl_150_(Co)	1133	C	1175	D	0.0013
Cl_200_(Co)	1292	C	1180	D	0.0075
Cl_250_(Co)	1304	C	1321	D	0.0001
Ch_100	475	D	528	D	0.0124
Ch_150	548	D	589	D	0.0052
Ch_200	567	D	588	D	0.0014
Ch_250	571	D	583	D	0.0004
Ch_100_(Co)	922	C	994	D	0.0062
Ch_150_(Co)	925	C	893	D	0.0011
Ch_200_(Co)	1293	C	906	D	0.0893
Ch_250_(Co)	1384	C	994	D	0.0791
B_100	637	E1	644	E1	0.0001
B_150	650	E1	756	E1	0.0261
B_200	682	E1	813	E1	0.0368
B_250	766	E1	824	E1	0.0056

*Relative deviations$(Stress_FEM - Stress_Experiment)^2 / (Stress_Experiment)^2$)

6.2.5 Effect of the textile material

The textile fibre materials are a significant effect on the test result. According to the experimental data, the lowest result of P_{max} was recorded in specimens strengthening with glass textile, whereas the highest values of P_{max} demonstrate specimens with coated heavy carbons. The distribution of P_{max} for each material considered of 250 mm bond length shown in Fig. 6.29, which is in good agreement with an experimental result where the same range of materials observed. In this simplified model, the differences between the textile materials were the mesh size and the textile materials property.

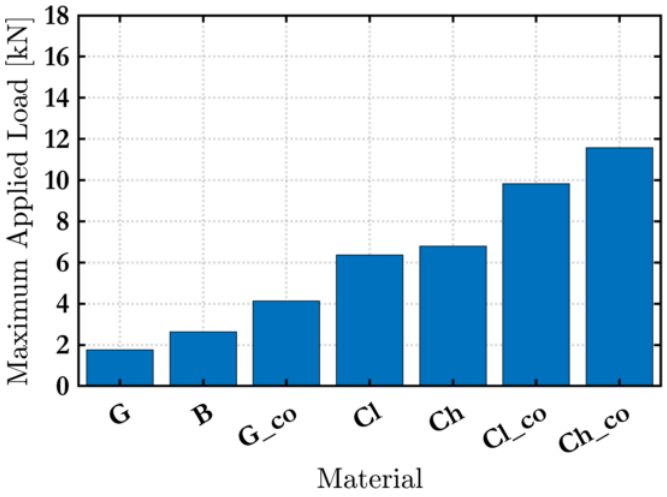

Figure 6.29: Maximum load P_{max} FEM per material. The case of L_b=250mm is considered

6.2.6 Effect of mesh size of strengthening mortar

The mesh size of all specimens' mortar was 10 mm to determine the mesh size influence on the bond behaviour. The parametric analysis performed to compare the results using 5 mm, 10 mm, and 20 mm Fig. 6.30 of strengthening mortar mesh size in all the FE models of the bond test . The load-displacement curves presented in Figs 6.31 - 6.37.

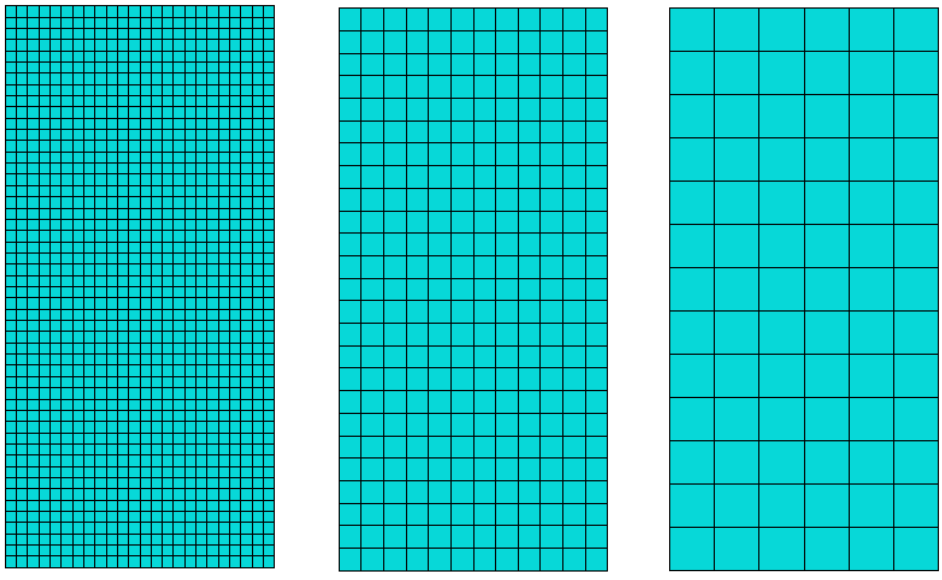

(a) 5mm **(b)** 10mm **(c)** 20mm

Figure 6.30: Mesh size of strengthening mortar

In the different mesh size, a not substantial difference observed in the strengthened specimens' curves.

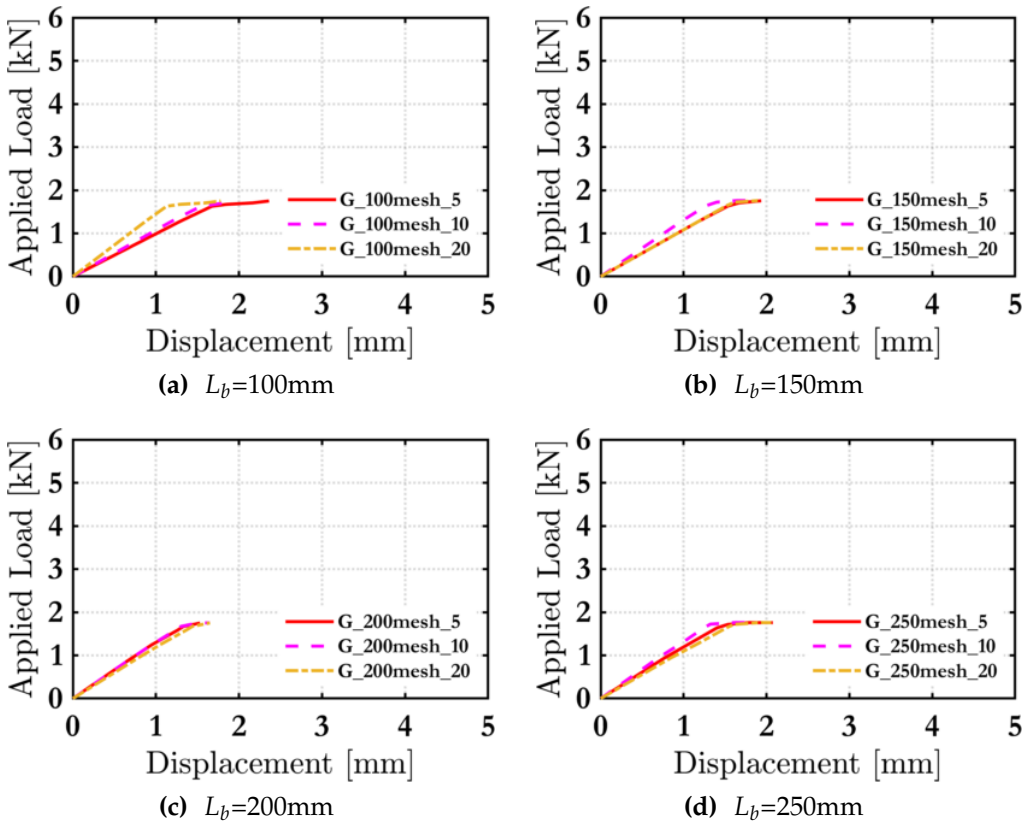

(a) L_b=100mm **(b)** L_b=150mm

(c) L_b=200mm **(d)** L_b=250mm

Figure 6.31: Load-displacement curves of glass specimens variation on mesh size

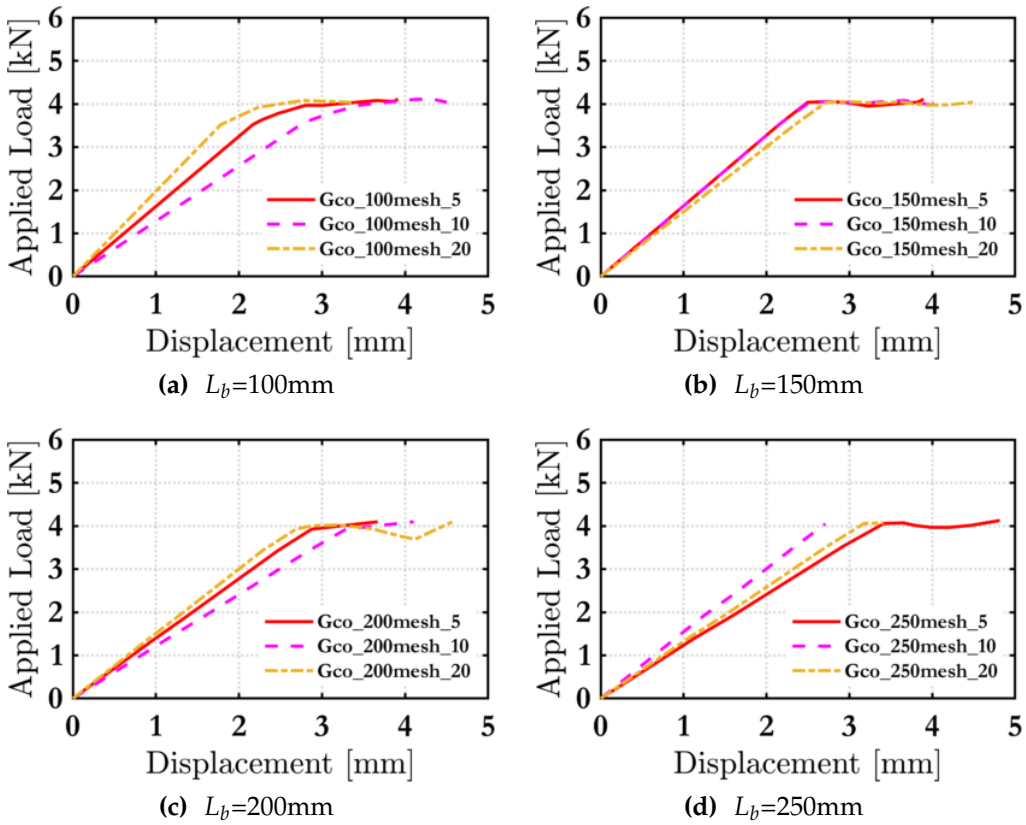

(a) L_b=100mm **(b)** L_b=150mm

(c) L_b=200mm **(d)** L_b=250mm

Figure 6.32: Load-displacement curves of glass coated specimens variation on mesh size

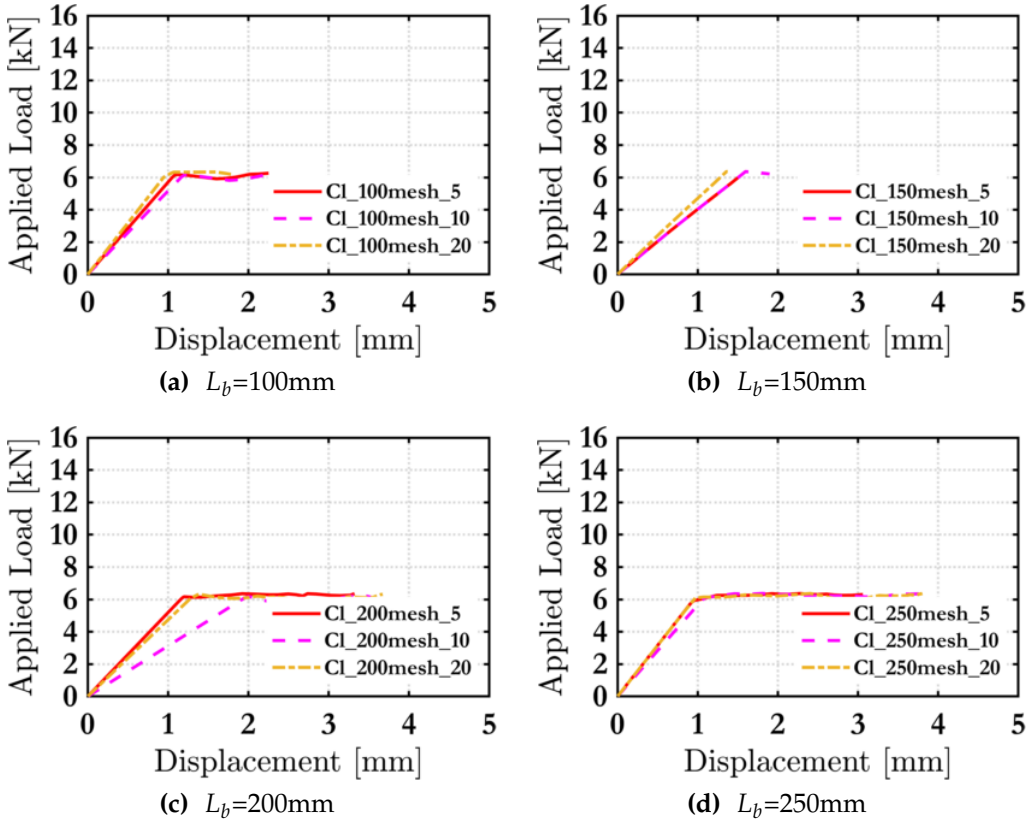

(a) L_b=100mm **(b)** L_b=150mm

(c) L_b=200mm **(d)** L_b=250mm

Figure 6.33: Load-displacement curves of carbon light specimens variation on mesh size

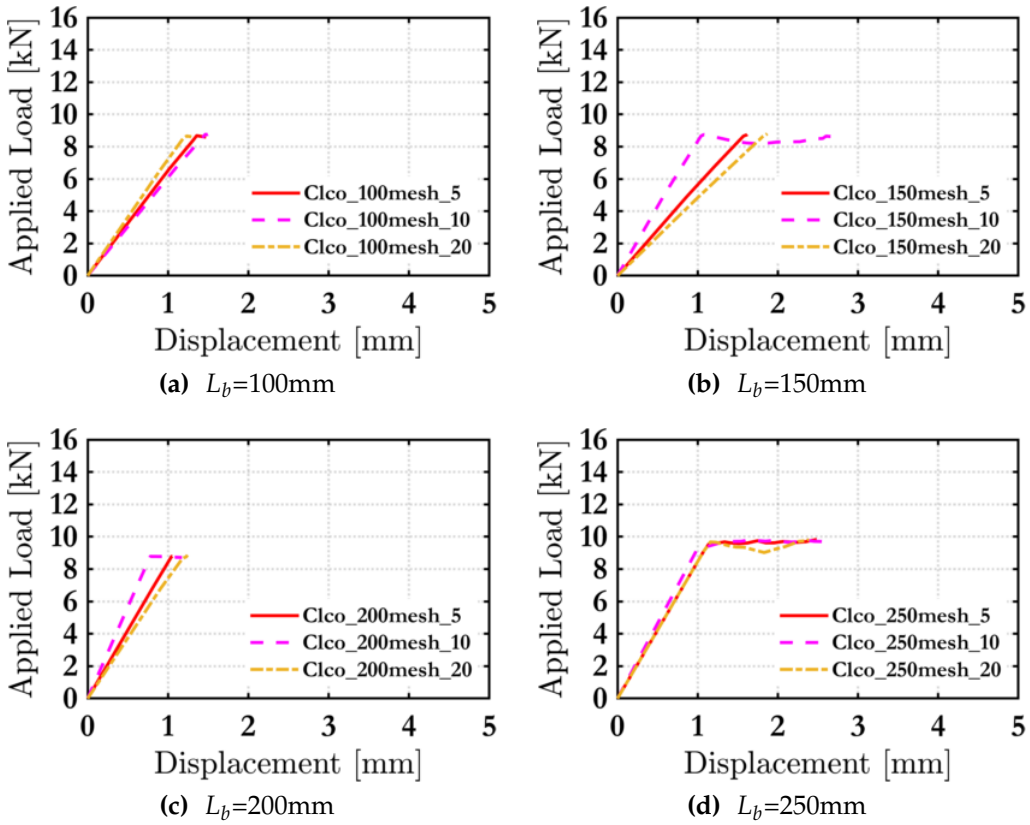

(a) L_b=100mm **(b)** L_b=150mm

(c) L_b=200mm **(d)** L_b=250mm

Figure 6.34: Load-displacement curves of carbon light coated specimens variation on mesh size

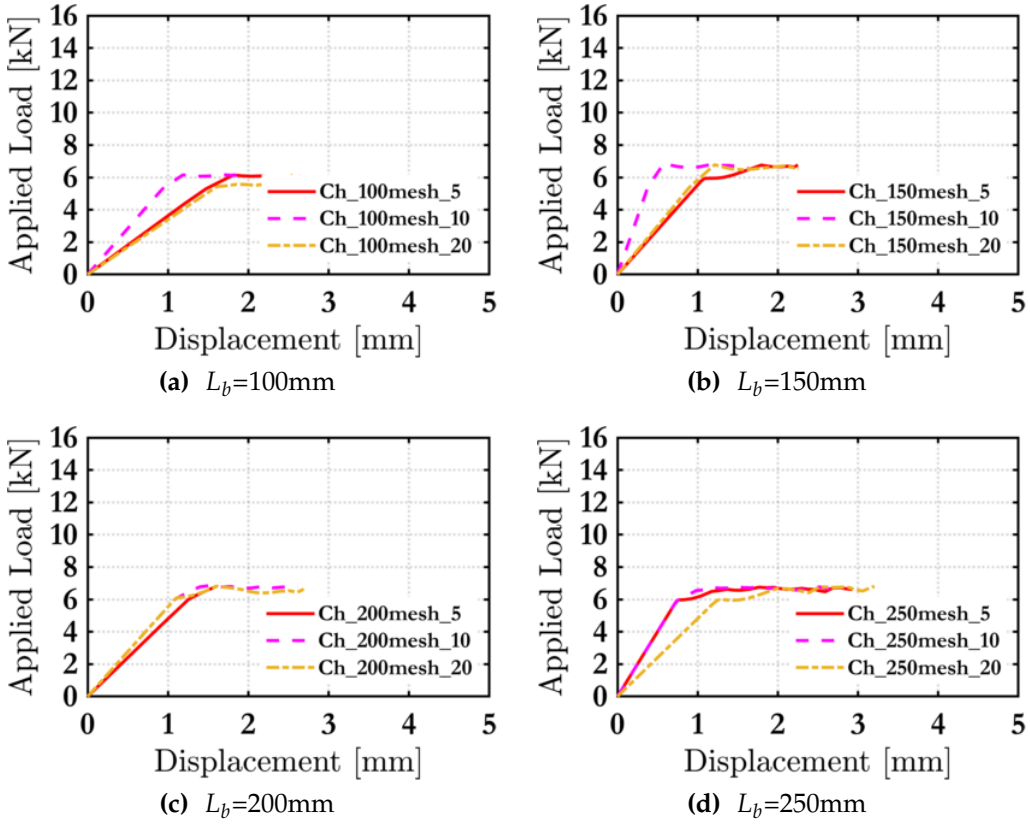

(a) L_b=100mm **(b)** L_b=150mm

(c) L_b=200mm **(d)** L_b=250mm

Figure 6.35: Load-displacement curves of carbon heavy specimens variation on mesh size

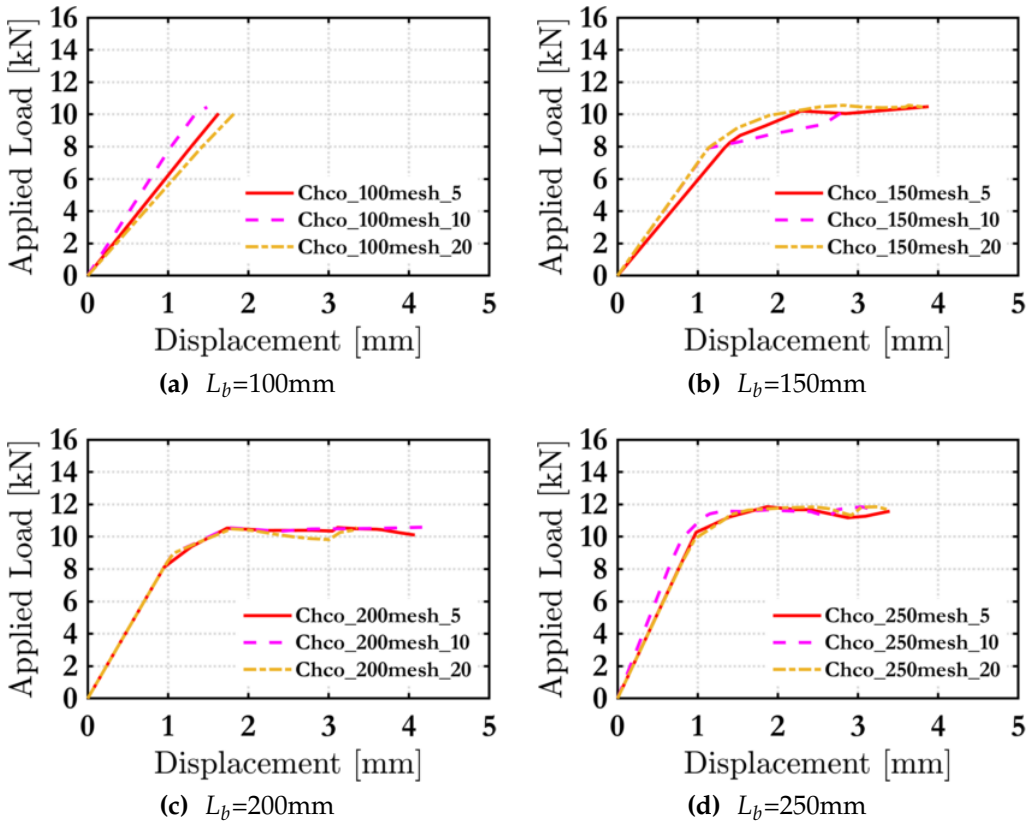

(a) L_b=100mm **(b)** L_b=150mm

(c) L_b=200mm **(d)** L_b=250mm

Figure 6.36: Load-displacement curves of carbon heavy coated specimens variation on mesh size

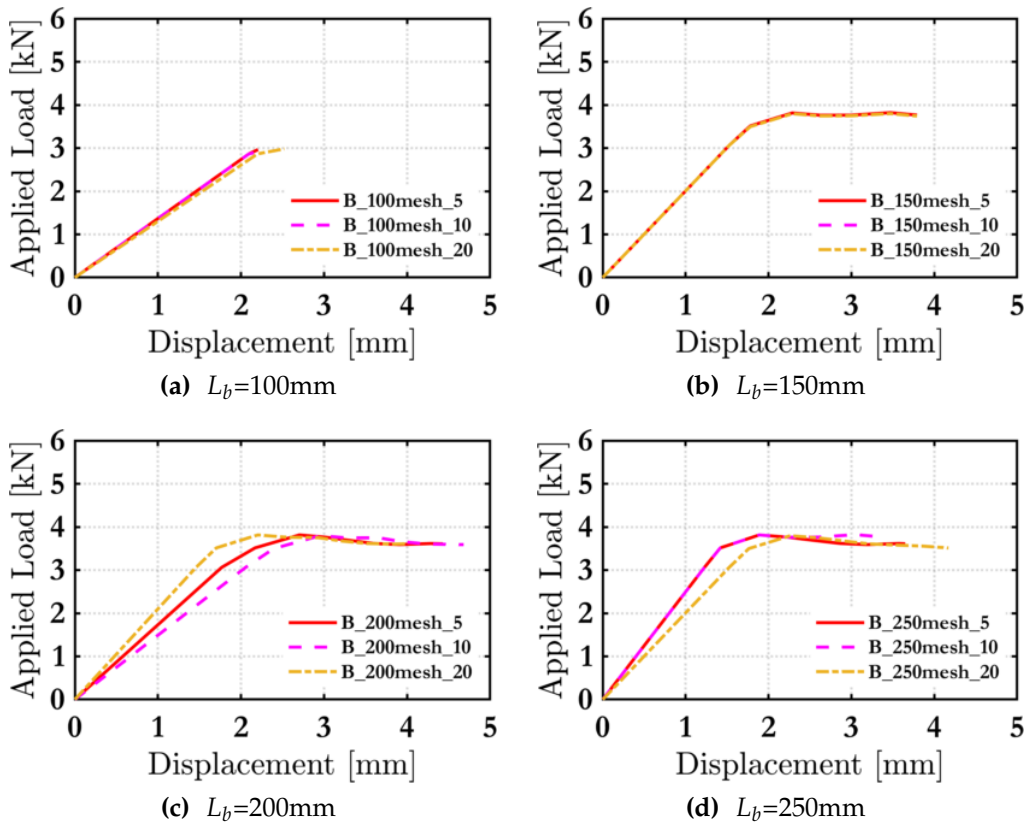

(a) L_b=100mm **(b)** L_b=150mm

(c) L_b=200mm **(d)** L_b=250mm

Figure 6.37: Load-displacement curves of basalt specimens variation on mesh size

The main idea of this modelling was to assemble a universal model which could predict accurately the peak load and the slip related to the peak load. Whereas the post-peak behaviour is not accurately represented. This is mainly due to the simplicity of the model used. According to the plots where the test result plotted against FE and analytical models shows that both models can accurately predict the peak load. The slip to the peak load is more accurately predicted in FE models compare to analytical where it around 10% lower this is mainly due to the s_1 value is appointed value this led to small reductions. To accurately simulate the post-peak response, since the interfaces are the only inelastic elements involved in the simulations, their properties in terms of post-peak behaviour should be accurately nominated.

6.3 TRM coupon test modelling

The mechanical parameters of TRM composite material determined by a tensile test on TRM coupons, which comprised the mortar matrix contribution in the reaction of composite material. In this work, the FEM simulation was carried out based on

the TRM coupon tensile test data Raoof & Bournas (2017), Tetta et al. (2018). The geometry of the test specimens and test setup represent an Fig. 6.38. The Failure mode observed was textile rupture at a central part of TRM coupons. According to the authors, the failure patterns consist of three main stages:

(i). linear elastic behaviour where the TRM mortar remains uncracked,

(ii). non-linear response where mortar cracking occurs and

(iii). increase of the load until the maximum load is attained and fibres rupture occurs

The result of the TRM coupon test of Raoof et al. (2017) are presented in Table 6.4.

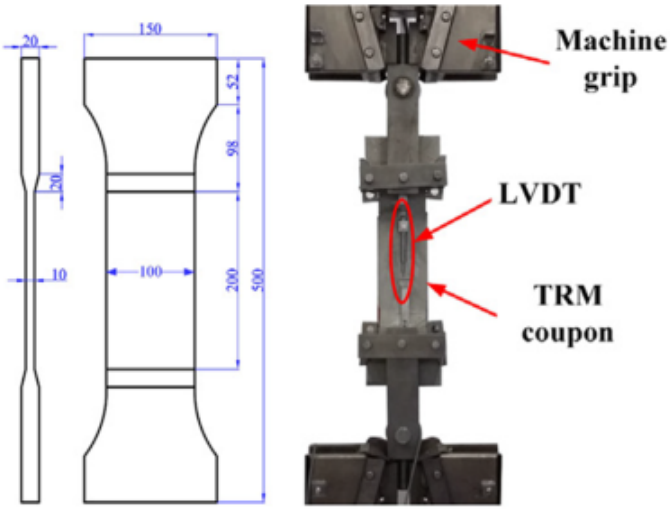

Figure 6.38: Experimental setup and geometry of the TRM coupon Raoof & Bournas (2017)

Table 6.4: Tensile test result on fibre-textile materials

Textile materials	Coupon test		FEM		Rd**
	Peak Stress [MPa]	Failure mode	Peak Stress [MPa]	Failure mode	
Glass	794	H*	684.6234	H*	0.025
Basalt	1190	H*	1232.322	H*	0.001
Carbon coated	2843	H*	3419.113	H*	0.028
Carbon	1518	H*	1624.072	H*	0.004

*Textile rupture at a central part of TRM coupon

**Relative deviations$(Stress_FEM - Stress_Experiment)^2 / (Stress_Experiment)^2$)

The geometry of the test specimen is dog bone-shaped with a length of 500 mm and a width of 10 mm. For the sake of replacing the real tensile test, the boundary

and loading condition was applied directly as in a real test. The lowest grip fixed in all directions, the upper grip loaded with displacement rotation load Fig. 6.39.

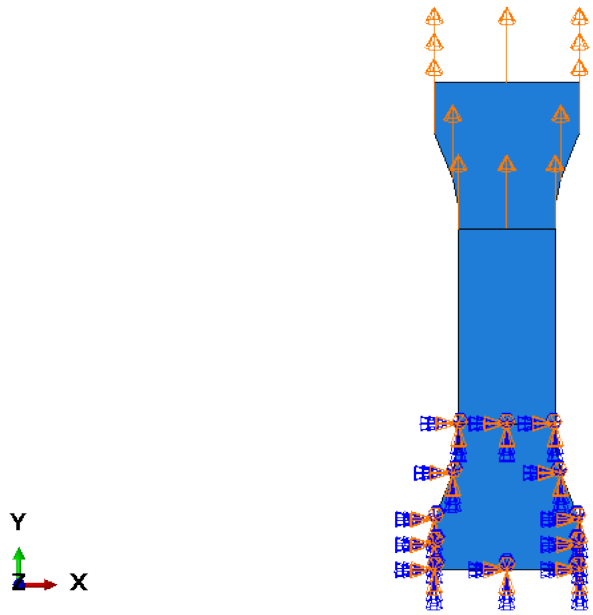

Figure 6.39: FE model- Loading of the coupon sample

To achieve an accurate result of the stress distribution and the acceptable computation time, the meshing technique used to mesh the coupon model with S4R (A 4-node doubly curved thin or thick shell, reduced integration, hourglass control, finite membrane strains). The textile fibres were considered as an embedded reinforcement of the mortar layer. The roving distance was set equal to the textile actual mesh size.

The Fig. 6.40 shown the meshing of the model.A 10 mm mesh size was chosen for the coupon. The mechanical properties of the mortar were adopted by the TRM coupon test results presented in Raoof & Bournas (2017).

6.3.1 Materials definition

The Drucker-Prager yield criterion was adopted to model the constitutive behaviour of the TRM coupons. The materials for the TRM coupon was defined as two primary materials, namely textile materials basalt, glass, heavy carbon, heavy carbon-coated, and mortar matrix. The main property of the textile taken used in the models was as in TRM coupon Table 6.4.

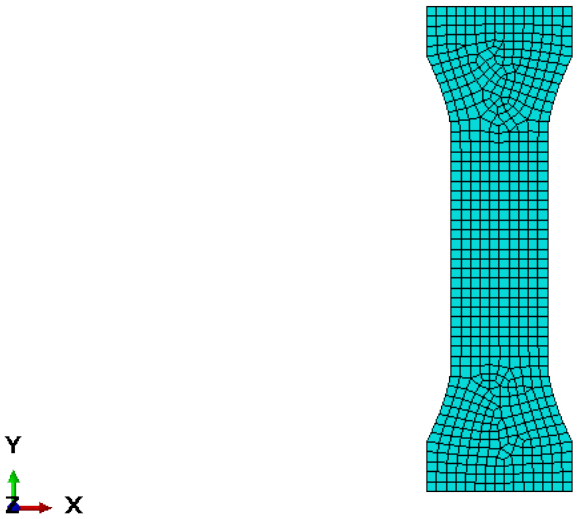

Figure 6.40: FE model mesh of the coupon sample

6.3.2 Finite element analysis results

The Figs 6.41 -6.44 shows the comparison between tests conducted by Raoof & Bournas (2017), and numerical results where a good fit is shown to be achieved.

All specimens failed due to rupture of the fibres at the central region of the gauge length resulted in good agreement between experimental and analytical results.They provide an accurate estimate of the actual maximum stress and strain of the TRM coupon up to the peak stress is accurately accounted for in all cases. In addition, the estimate on the strain corresponding to the maximum and ultimate stress also agrees well with the experimental results (see Figs 6.41 -6.44). Table 6.4 The Table 6.3 shows the relative deviations(Rd) of actual tests and FEM modelling results.

6.4 Modelling of masonry wall specimens

6.4.1 Description of the model

The objective of this Section is to examine the validity of the identified textile properties when used to simulate the response of TRM strengthened masonry at the component level. For this purpose, a finite element model was constructed to simulate

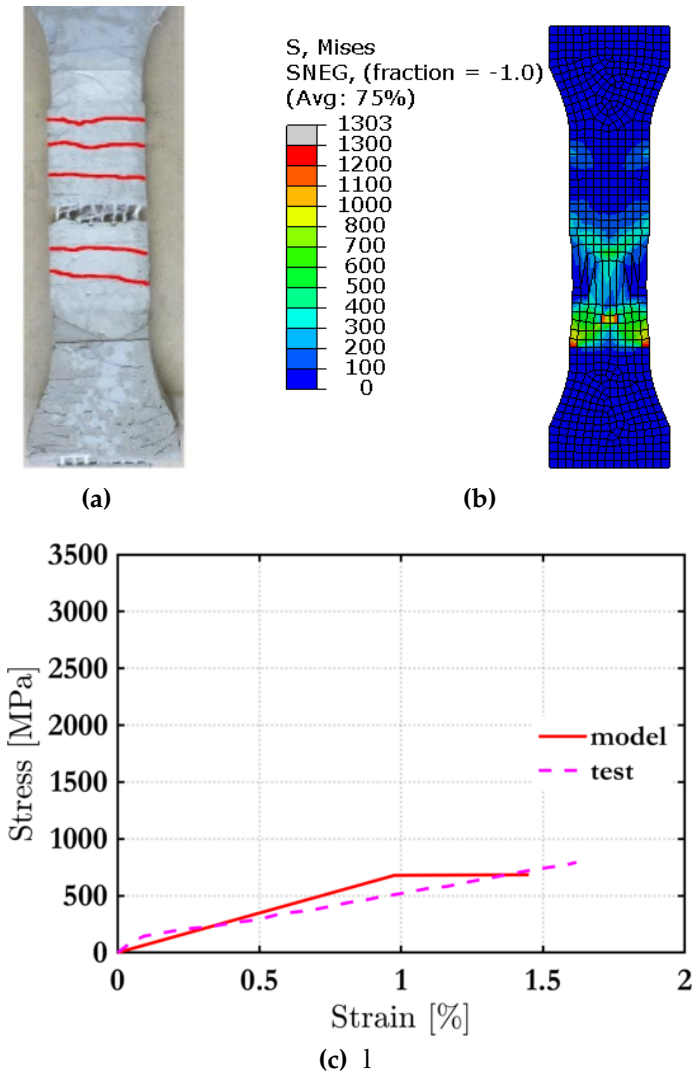

Figure 6.41: TRM glass textile coupon (a) Failure mode (Raoof et al. 2017), (b) Mises stress (c) Stress strain compare test versus mode.

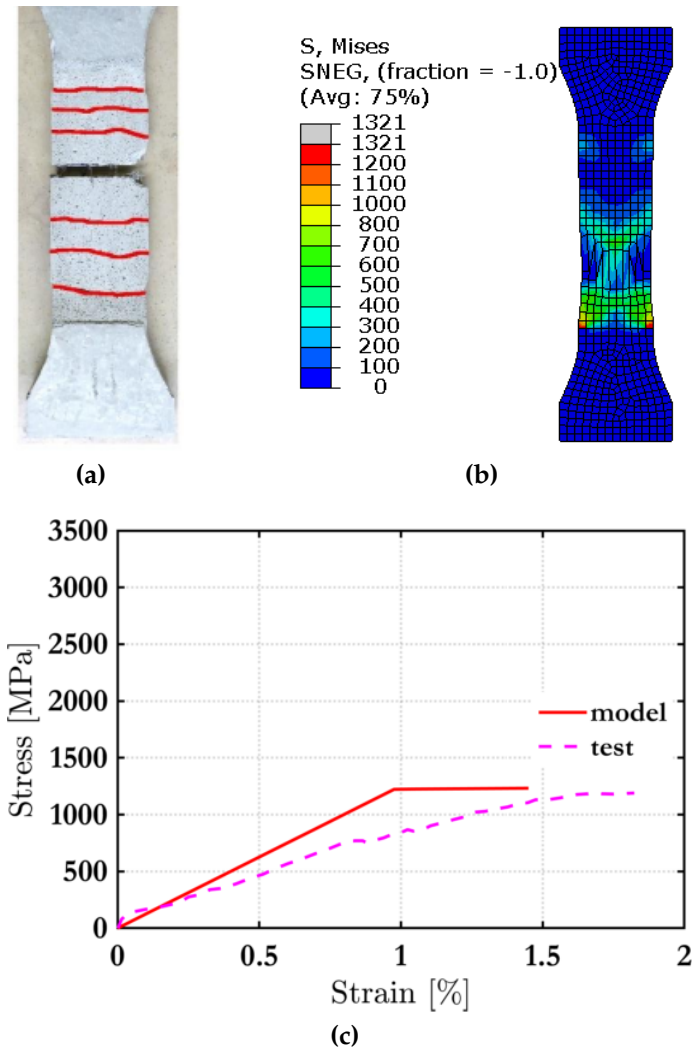

Figure 6.42: TRM basalt textile coupon (a) Failure mode (Raoof et al. 2017), (b) Mises stress (c) Stress strain compare test versus mode

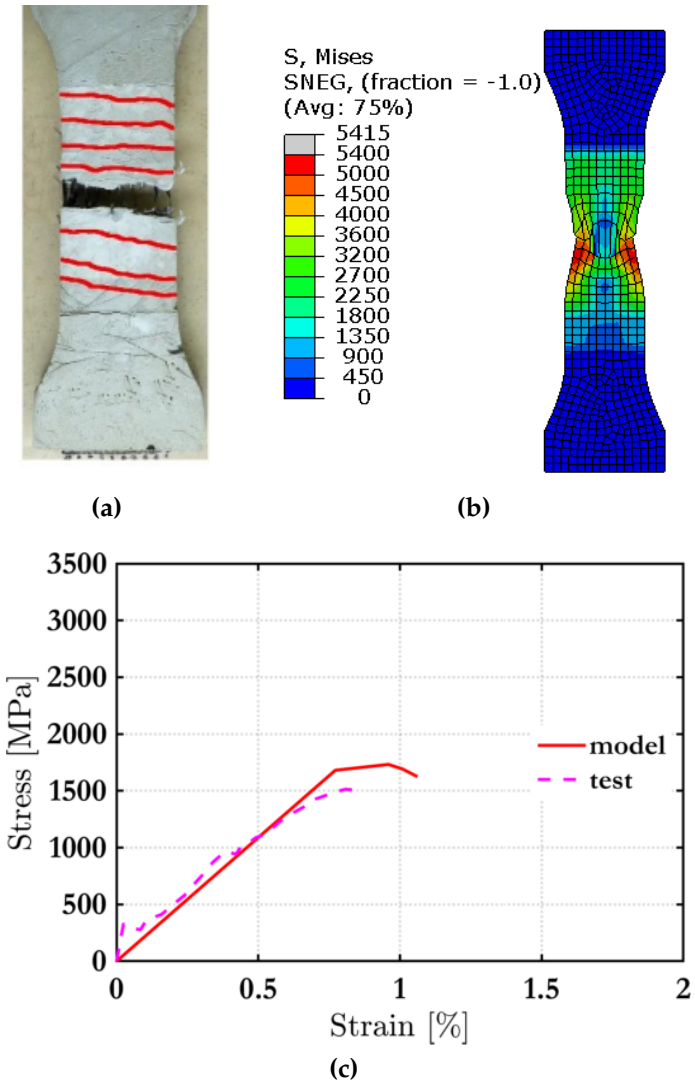

Figure 6.43: TRM carbon textile coupon (a) Failure mode (Raoof et al. 2017), (b) Mises stress (c) Stress strain compare test versus mode

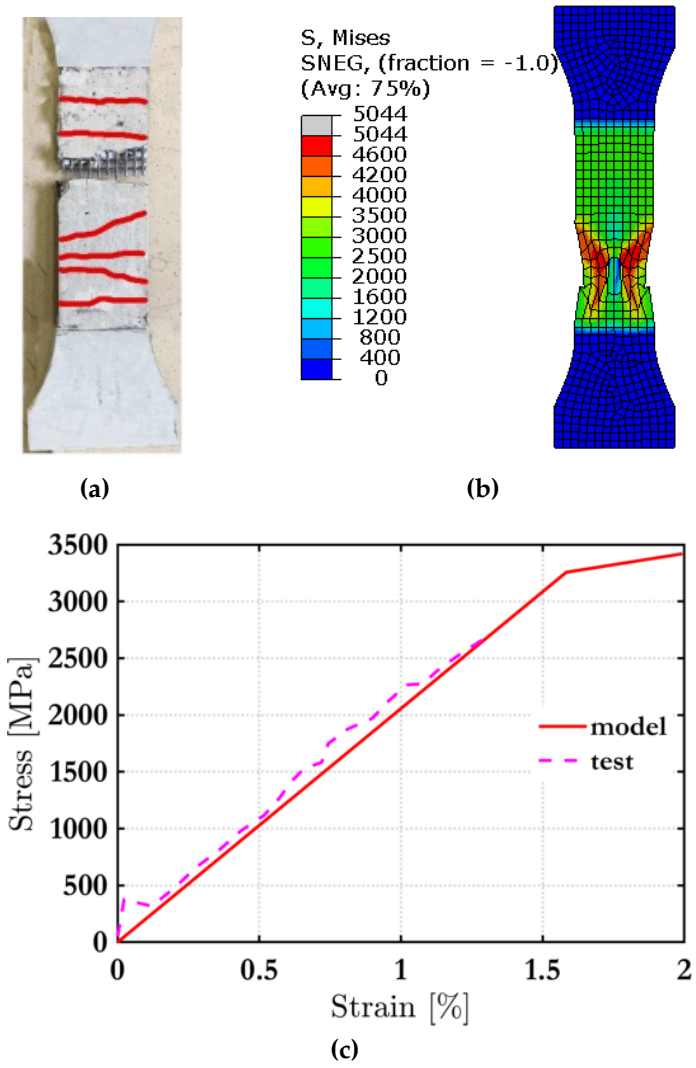

Figure 6.44: TRM carbon heavy coated textile coupon (a) Failure mode (Raoof et al. 2017), (b) Mises stress (c) Stress strain compare test versus mode

the results of the out-of-plane bending experiments conducted in Kariou et al. (2018) where the same type of textile fibre materials were used.

In this model, the simplified micro-model method was adopted as discribed in Section 2.7. Hence, the brick units were extended to the half of both the bed and head mortar joints and cohesive surfaces were used to represent the interface mortar joints. The bricks were modelled by full integration 20-node hex-elements whereas the TRM layer was modelled with reduced integration quadrilateral shell elements. The concrete damage plasticity model (CDP) was used to account for the inelastic constitutive behaviour of the brick masonry units. The experimental brick compressive strength is equal to 21.2 MPa (Kariou et al. 2018), and the corresponding strain is equal 0.0022 as used in Tao et al. (2012).

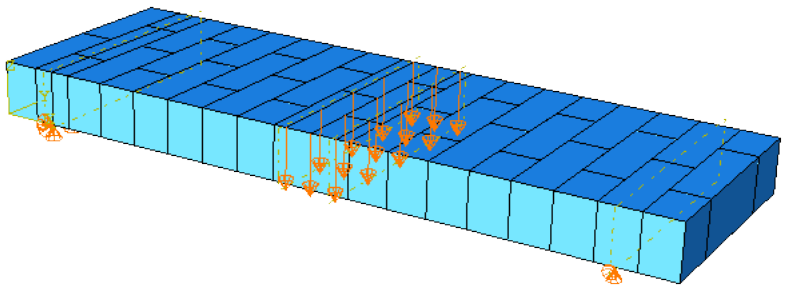

Figure 6.45: Wall specimen: Boundary conditions

The Drucker-Prager yield criterion was adopted to model the nonlinear constitutive behaviour of the TRM strengthening mortar. The textile fibres were considered as an internal reinforcement of the strengthening mortar layer. The roving distance was set equal to the textile actual mesh size. The strengthening mortar thickness was defined as equal to 2.5 mm, 5 mm, and 7 mm, representing the 1, 3, and 7 layers of textiles considered in the experiment. The mesh size was determined equal to 0.04 m along the mortar layer and the masonry wall height.

A displacement control analysis was conducted with a monotonically increasing displacement being applied at the midline of the specimen, similar to the actual ex-

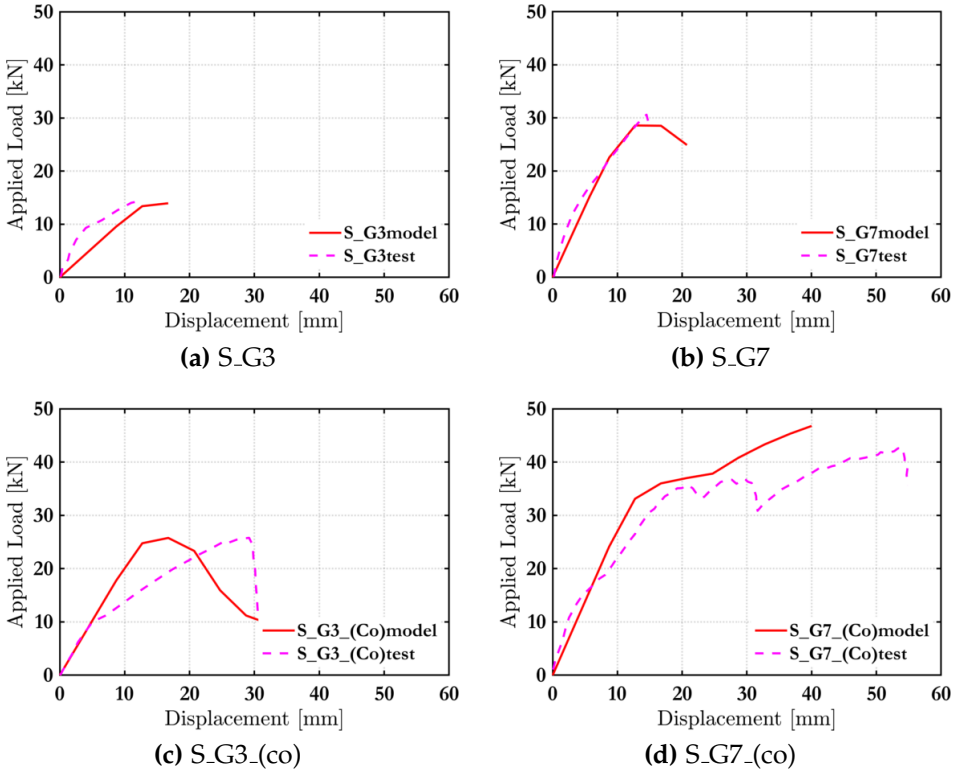

(a) S_G3 **(b)** S_G7

(c) S_G3_(co) **(d)** S_G7_(co)

Figure 6.46: Load-displacement curves

periment. The loading area was 100 mm x 440 mm. The supports were placed at 107.5 mm from the ends of the masonry wall, similar to the actual experiment (Fig. 6.45).

6.4.2 Finite element analysis results and discussion

The graphs Fig. 6.46 and Fig. 6.47 represents the comparison between experimental and numerical data,where a good agreement is achieved.

Notably, it results in a good agreement between numerical and experimental results in specimens that failed due to textile rapture such as S_C1_(Co), S_G3, S_G7, S_G3_(Co), S_B3. The result provides reliable data of the actual maximum load and provides both the elastic and post-elastic stiffness of the masonry walls up to the peak load achieved. Furthermore, the displacement at a peak load also has a good agreement with the experimental result.

According to the experimental result, the S_C1 specimens failed due to the slippage of textile within the mortar, similar to a bond test. Both FEM and real test specimens represent the localised failure of the textile at the mid-span of the wall. The FEM S_C1_(Co) represents approximately the same peak load and lower displacement

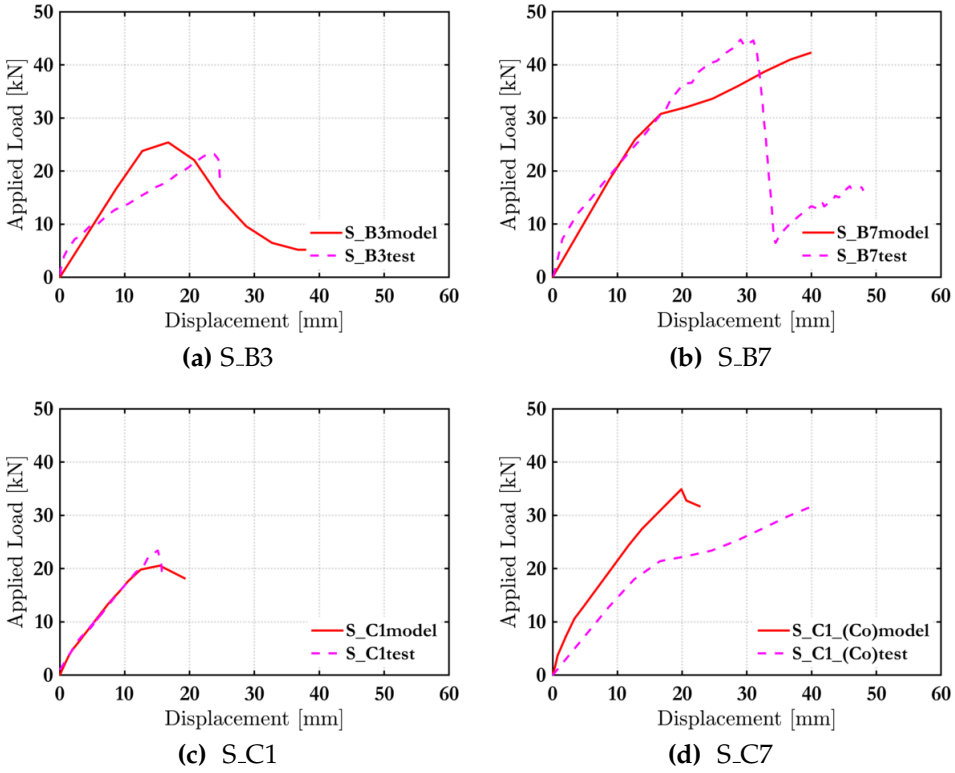

(a) S_B3 **(b)** S_B7

(c) S_C1 **(d)** S_C7

Figure 6.47: Load-displacement curves

value corresponding to maximum load. The E_f in the models S_C1 and S_C1_(Co) decreased by 22% and 9% compared to the TRM coupon Table 6.6. In this case, the higher decrease detected in S_C1 FEM due to the slippage of the fibres within the mortar.

Table 6.5: Wall specimens: Comparison between experimental and simulated failure modes

Specimen	Simulation failure mode	Experimental failure mode
S_C1	Textile rupture	Slippage between mortar-fibres
S_C1_(co)	Textile rupture	Textile rupture
S_G3	Textile rupture	Textile rupture
S_G7	Textile rupture	Textile rupture
S_G3_(co)	Textile rupture	Textile rupture
S_G7_(co)	Shear brick damage	Shear failure
S_B3	Textile rupture	Textile rupture
S_B7	Shear brick damage	Shear failure

The Fig. 6.46 shows the load-displacement relationship of the specimens S_G3 and S_G7. The numerical result shows a good agreement with the experimental result. The specimens S_G3 and S_G7, the textile rupture occurred see Table 6.5. The final maximum principal stress in specimens S_G3 and S_G7 presented in Fig. 6.48 and Fig. 6.49. As can be seen, the maximum stress in the specimens occurred at the

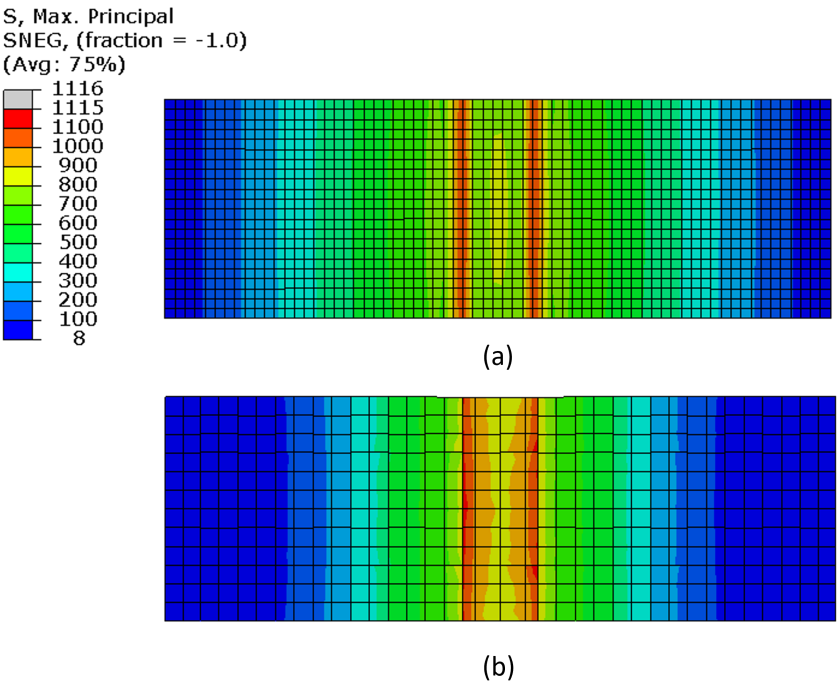

Figure 6.48: Maximum principal stress S_G3 a) TRM b) Masonry wall

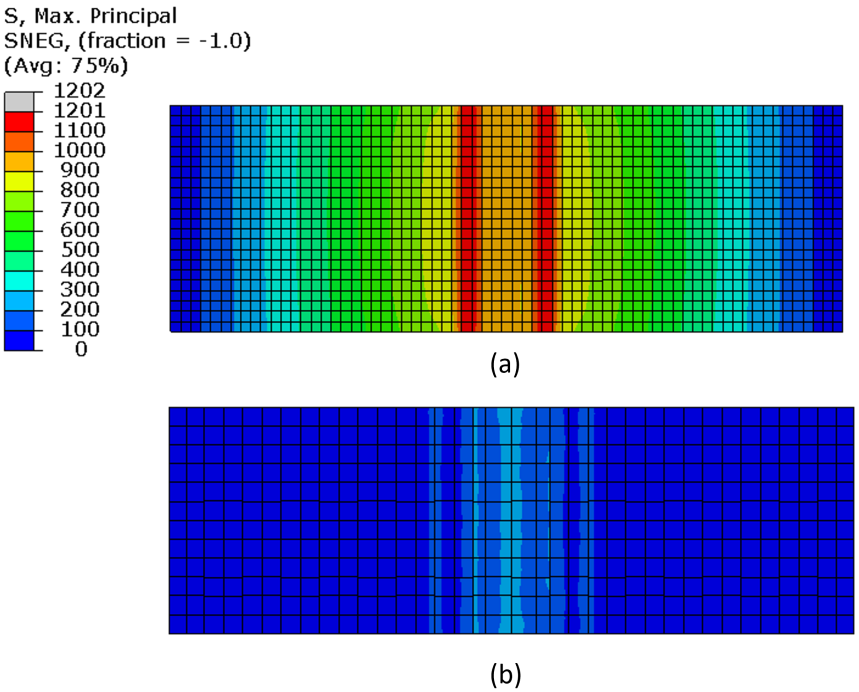

Figure 6.49: Maximum principal stress S_G7 a) TRM b) Masonry wall

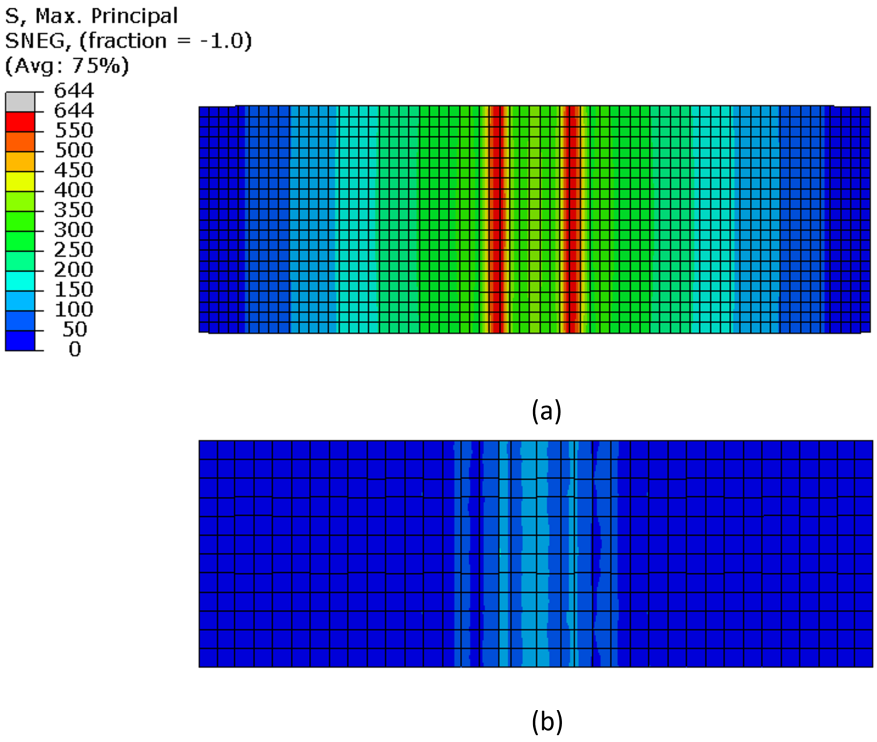

Figure 6.50: Maximum principal stress S_B3 a) TRM b) Masonry wall

Table 6.6: Textile properties of the FE models

Model	FEM results			Coupon results			Rd*
	f_f^uFEM [MPa]	E_fFEM [GPa]	ε_f^uFEM [%]	f_f^u [MPa]	E_f [GPa]	ε_f^u [%]	
S_G3	440	42	1.56	372	47	0.75	0.002
S_G7	462	43	1.62	372	47	0.75	0.001
S_G7_(co)	759	65	3.51	935	70	1.26	0.003
S_G3_(co)	975	63	1.56	935	70	1.26	0.014
S_B3	1144	62	1.58	1082	59	2.22	0.008
S_B7	952	63	3.9	1082	59	2.22	0.003
S_C1	1059	124	1.5	1258	160	0.73	0.003
S_C1_(co)	1799	179	1.85	2541	196	1.2	0.002

*Relative deviations$(Stress_FEM - Stress_Experiment)^2 / (Stress_Experiment)^2$)

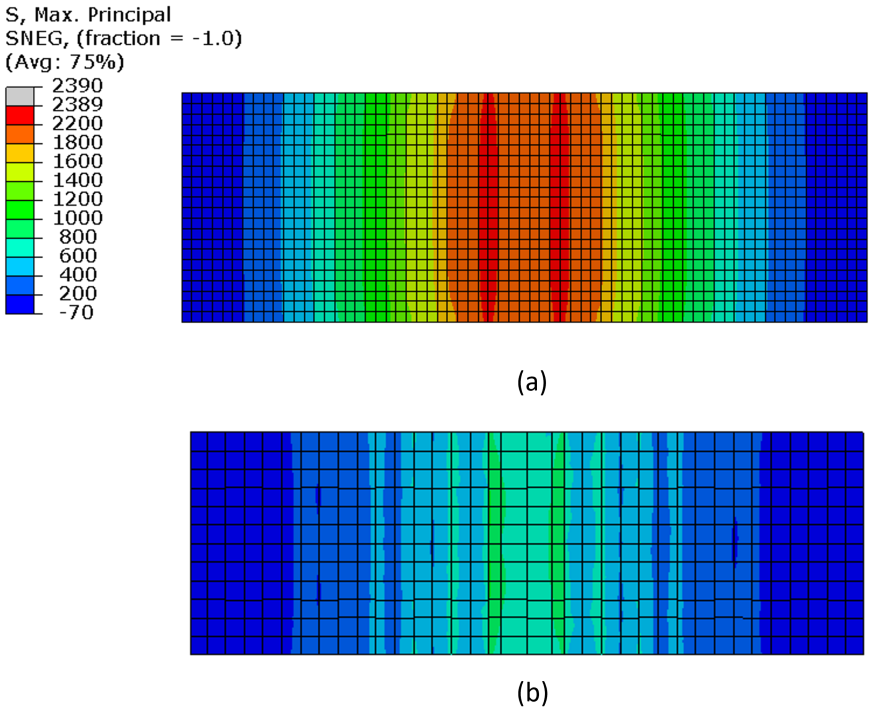

Figure 6.51: Maximum principal stress S_B7 a) TRM b) Masonry wall

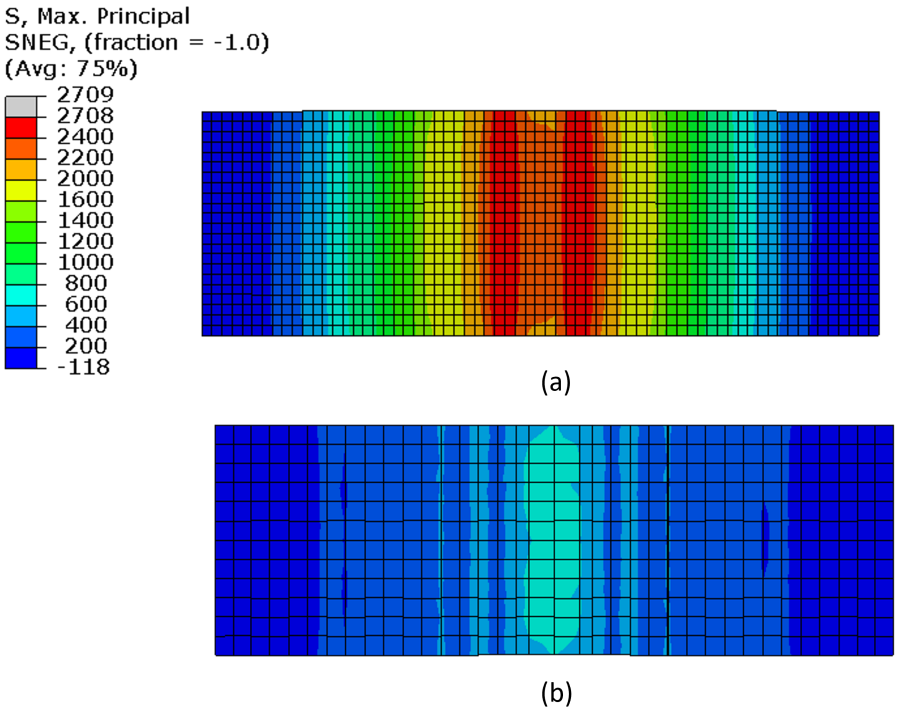

Figure 6.52: Maximum principal stress S_G3_(co) a) TRM b) Masonry wall

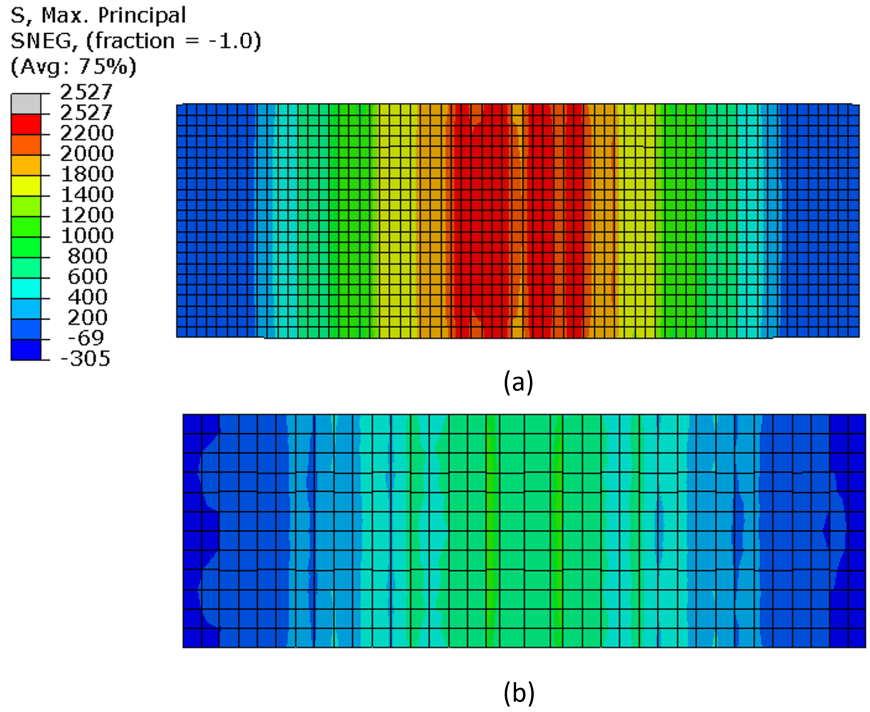

Figure 6.53: Maximum principal stress S_G7_(co) a) TRM b) Masonry wall

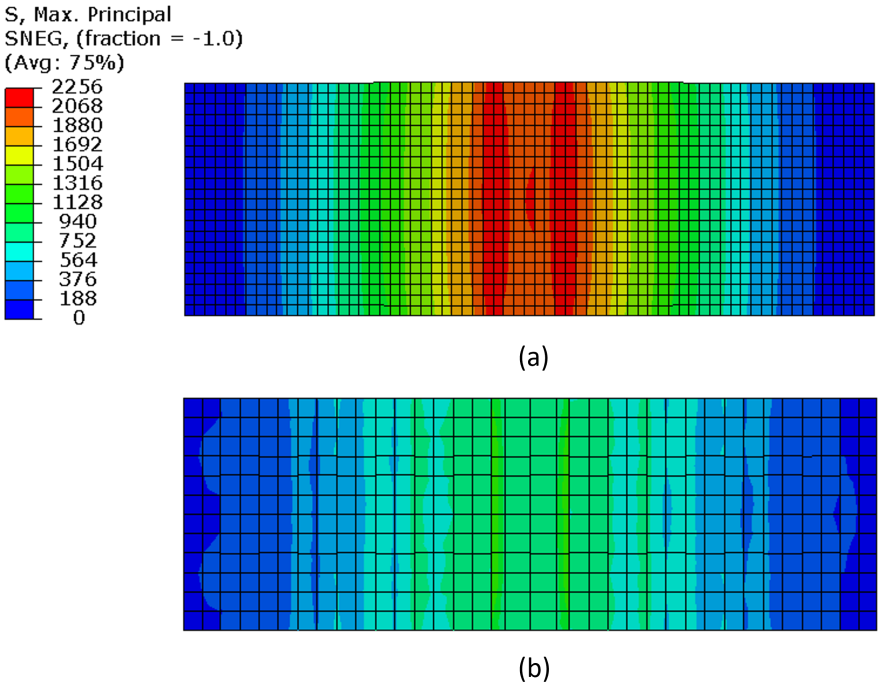

Figure 6.54: Maximum principal stress S_C1 a) TRM b) Masonry wall

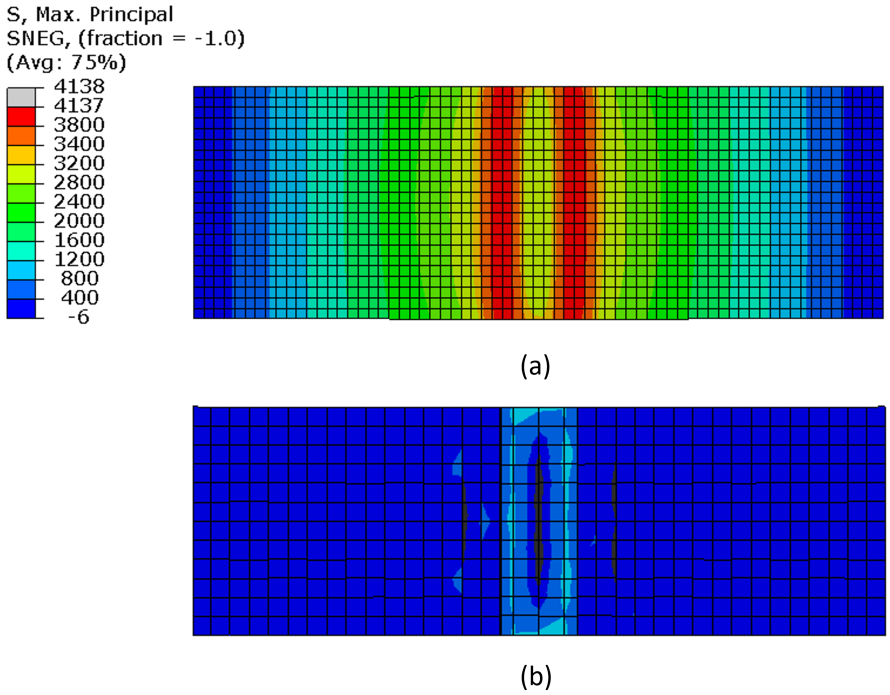

Figure 6.55: Maximum principal stress S_C1_(co) a) TRM b) Masonry wall

middle of the wall, which coincides with the experimental results. The textile Young's modulus in model S_G3 was almost like the TRM coupon, whereas in S_G7 higher value was obtained. This occurred due to better interlocking mechanisms among the increasing numbers of textile layers compared to a single TRM layer, which was also the case in masonry walls experimental work.

According to the test result, the S_G3_(Co) and S_B3 specimens failed due to textile rupture. A similar failure mode was observed in the numerical model is which shows that the textile in the model was about to break Fig. 6.52, Fig. 6.50. The failure mode is similar to the bond test.

According to the test result, S_G7_(Co) and S_B7 specimens failed due to shear. The load vs displacement curves are presented in Fig. 6.53 Fig. 6.51. The Table 6.6 represent the f_f^uFEM of 759 in S_G7_(Co) and 952 for the S_B7. This is lower than the coupon test, and it cannot capture the actual response up to the maximum load, where interlocking mechanism developed between the masonry bricks after the shear failure of the wall. Besides, further increase of the textile strength did not occur,

resulting in decreased exploitation of the textile strength. Moreover, the modulus of elasticity in both specimens decreased compare to the coupon test Table 6.6 due to the shear failure observed in both specimens.

6.5 Concluding Remarks

(i). Cohesive interactions modelled bond between textile and the strengthening mortar. The textile and a mortar modelled as separate surface. This approach provides a good agreement between FEM and test result.

(ii). The numerically derived load vs displacement curves of the specimens of the bond test specimens demonstrated good agreement concerning the experimental results, up to the peak load, and the displacement at the maximum and ultimate load

(iii). Mesh size of the strengthening mortar does not play any valuable role in maximum applied load and displacement.

(iv). Good agreement was observed between the simulated and experimental failure modes in single wall

(v). The bond results obtained in this chapter can be used to simulate the component response accurately. This was observed between the simulated and experimental results in all the single walls modelling. Where FEM bond test result used to simulate bond response of wall model.

7

Conclusions and Future Outlook

7.1 Main Contributions

The constantly increasing demands in transportation activities over an ageing transportation infrastructure pose risks with the integrity of existing structures, e.g., bridges. In many cases, over a century old, bridges comprising masonry arches or vaults must sustain loads beyond their anticipated operational thresholds. Hence, structural strengthening interventions become necessary to extend their operational life and preserve their structural integrity. The Textile Reinforced Mortar (TRM) has emerged as a reliable and efficient technique for strengthening existing structures.

In this project, two main experimental campaigns have been conducted to investigate the bond behaviour between TRM and masonry bond. Initially, uniaxialtensile tests were conducted on the fibre-textiles used to determine their mechanical properties. First is the bond test were performed to investigate the bond behaviour between TRM and masonry in static condition. The investigated parameters were the bond length, the textile-fibre material and the epoxy resin coating.

Next was a series of single-lap shear tests have been conducted on basalt and coated carbon textile fibre TRM bonded to masonry, considering various bond lengths(fatigue loading condition). The objective of this study was to examine the effect of the textile fibres coating, the bond lengths of TRM, failure mode compare to static case and the type of textile fibre material utilised.

To further investigate the underlying mechanics of the TRM to masonry bond

strength , a finite element analysis on the bond behaviour between masonry and TRM was performed using the Abaqus commercial software.

7.2 Conclusions on the experimental work conducted

(i). The highest textile features such as ultimate tensile stress (f_f^t) 2541 MPa and modulus of elasticity (E_f) 196 GPa was observed in the carbon fibre-textile. In opposite the lowest mechanical properties were determined in glass fibre textile f_f^t 669 MPa and E_f 47 MPa. The tests showed that the coated glass and coated basalt fibre textiles had similar mechanical property.

(ii). The beneficial effect of the application of epoxy resin when compared to the bare textile was demonstrated by (i) the uniaxial tensile tests, (ii) the bond test results between the TRM and masonry substrate.

(iii). The epoxy resin applications on both carbons and glass textile improve the tensile strength and modulus of elasticity.

(iv). According to the test results under quasi-static conditions, the failure mode shifted from slippage in both carbons and glass textile to the detachment (coated carbons) to the textile failure out of the matrix (glass coated).

(v). In a single lap bond test, the epoxy-resin coating specimens resulted in increased maximum load capacity when compared their uncoated counterparts. This occurred due to (i) the enhanced bonding between the textile fibre and the mortar matrix and the increased stiffness of the rovings, and (ii) the improved friction among the fibres within a roving resulting in higher tensile strength.

(vi). By increasing the bond lengths from 100 mm to 250 mm, the maximum load gradually increased in most cases both carbons (coated and uncoated), uncoated glass textile.

(vii). By increasing the bond length, the bond capacity increased in a bilinear fashion for all materials examined. After a certain bond length, i.e., the effective bond length L_{eff}, the bond capacity increased marginally. Except for the coated heavy carbon textile fibre materials, the bond length found to be L_{eff} =150-200 mm.

(viii). Increasing values of P_{max} are associated with the increasing axial stiffness of the textile only in the case of the coated specimens. This indicates that coating improves the stress distribution at the textile hence allowing it to develop higher stresses.

(ix). In case of basalt textile shift in the failure mode was observed under the cyclic loading conditions. For all bond lengths examined, textile slippage was observed. Slippage manifests itself with a constant decrease in the TRM stiffness, as shown in the corresponding load-deflection plots. No variation of the maximum number of cycles was observed for more considerable bond lengths basalt textile and increased number of cycles up to failure with increased bond lengths observed in coated carbon textile.

(x). In case of coated carbon textile the failure mode shifted from textile detachment (static case) to slippage (fatigue loading conditions) of $\lambda = 60\%$ and $\lambda = 70\%$. In case of $\lambda = 80\%$ two failure modes were observed: textile detachment and slippage.

(xi). Although the failure mechanism initiates with the textile slipping through the matrix, slippage arrests, and the textile eventually breaks. This, however, seems to be pertinent to the fact that after initial slippage, it is difficult to maintain a uniform stress distribution on the textile under load control.

(xii). According to the test result, the failure mechanism has developed and provided the main steps of the failure under fatigue life.

(xiii). In the case of coated carbon textile, the fatigue life under fatigue load cycling of lower load amplitude ($\lambda = 60\%$ and $\lambda = 70\%$) is dominated by crack initiation, cracks propagation and matrix detachment and finally failure, while on lowering the load amplitude ($\lambda = 80\%$): cracks initiations, cracks propagation and then sudden failure.

(xiv). Both textile materials tested represent similar responses between fatigue and static loading in increasing bond lengths. Increasing bond lengths in the case of basalt textile practically were not affected on the results by static and fatigue loading cases(with exception $\lambda = 80\%$ case). Contrary to basalt, in coated car-

bon bond lengths increasing led to improving maximum applied load (static loading) and increasing numbers of cycles up to failure (fatigue loading).

(xv). The Bond between textile and the strengthening mortar modelled by cohesive interactions. The textile and a mortar modelled as separate surfaces. This approach provides a good agreement between FEM and test result.

(xvi). The numerically derived load vs displacement curves of the specimens of the bond test specimens demonstrated good agreement concerning the experimental results, up to the peak load, and the displacement at the maximum and ultimate load.

(xvii). Mesh size of the strengthening mortar does not play any valuable role in maximum applied load and displacement.

(xviii). Good agreement was observed between the simulated and experimental failure modes in single wall.

(xix). The bond results obtained in this chapter can be used to simulate the component response accurately. This was observed between the simulated and experimental results in all the single walls modelling. Where FEM bond test result used to simulate bond response of wall model.

7.3 Limitations and Suggestions for Further Improvements

As in every externally bonded strengthening technique/material, one of the key parameters controlling the effectiveness of the TRM is the bond strength of the TRM to the masonry interface. Over the past fifteen years, the mechanics of TRM to masonry bond have been investigated experimentally, analytically, and numerically for the case of quasi-static loading. Future research can be focused on the following aspects:

(i). The in-house epoxy-resin coating applied in has been shown to increase significantly the effectiveness of the TRM to masonry bond. Therefore further research can be done to investigate the TRM effectiveness using different amount and different types of coating.

(ii). Additional bond test can be performed using a modified High-performance concrete with different mix proportions and compare the results against the current experimental study.

(iii). The TRM to masonry bond performance can be investigated using a double-lap test setup with double-wall prisms to include multiple layers of TRM and compare the results against the current experimental study.

(iv). A further investigation on the masonry to TRM bond can be performed using different temperature and humidity.

(v). A further investigation on the TRM mortar can be performed using different TRM mortars (cement, lime, earthen). Can determine which mortar is more compatible with each different textile utilised in this project.

(vi). Additional investigation on the TRM to masonry bond under fatigue loading is needed to include different textile compare the results against the current experimental study.

(vii). The numerical models developed to capture the TRM to masonry bond behaviour resulted in good agreement with the experimental results. Thus, a similar modelling approach can be applied to investigate further parameters such as different loading conditions (e.g. fatigue loading). However, the future work also need to pay attentions to the post peak response of the specimens (where relevant).

Bibliography

Ahmad, S., Khan, R. A. & Gupta, H. (2014), 'Seismic performance of a masonry heritage structure', *International Journal of Engineering and Advanced Technology* **3**(4).

Ahsan, R. (2014), Fatigue in concrete structures, *in* 'BSRM Seminar on Fatigue Properties of Constructional Steel'.

Al-Salloum, Y. A., Elsanadedy, H. M., Alsayed, S. H. & Iqbal, R. A. (2012), 'Experimental and numerical study for the shear strengthening of reinforced concrete beams using textile-reinforced mortar', *Journal of Composites for Construction* **16**(1), 74–90.

Alecci, V., De Stefano, M., Luciano, R., Rovero, L. & Stipo, G. (2016), 'Experimental investigation on bond behavior of cement-matrix–based composites for strengthening of masonry structures', *Journal of Composites for Construction* **20**(1), 04015041.

Aljazaeri, Z. R. & Myers, J. J. (2017), 'Fatigue and flexural behavior of reinforced-concrete beams strengthened with fiber-reinforced cementitious matrix', *Journal of Composites for Construction* **21**(1), 04016075.

Ascione, L., de Felice, G. & De Santis, S. (2015), 'A qualification method for externally bonded fibre reinforced cementitious matrix (FRCM) strengthening systems', *Composites Part B: Engineering* **78**, 497–506.

Askouni, P. D. & Papanicolaou, C. G. (2017), 'Experimental investigation of bond between glass textile reinforced mortar overlays and masonry: the effect of bond length', *Materials and Structures* **50**(2), 164.

ASTM, D.-. (2011), 'Standard test method for breaking strength and elongation of textile fabrics', *Annual Book of ASTM* pp. 5034–5095.

Augenti, N. & Parisi, F. (2010), 'Learning from construction failures due to the 2009 L'Aquila, Italy, earthquake', *Journal of Performance of Constructed Facilities* **24**(6), 536–555.

Barducci, S., Alecci, V., De Stefano, M., Misseri, G., Rovero, L. & Stipo, G. (2020), 'Experimental and analytical investigations on bond behavior of Basalt-FRCM systems', *Journal of Composites for Construction* **24**(1), 04019055.

Bathe, K.-J. (2006), *Finite element procedures*, Klaus-Jurgen Bathe.

Bell, B. (2004), European railway bridge demography—Deliverable D1.2, Technical report, EC FP6, Sixth Framework Programs.

Bernat, E., Gil, L., Roca, P. & Escrig, C. (2013), 'Experimental and analytical study of TRM strengthened brickwork walls under eccentric compressive loading', *Construction and Building Materials* **44**, 35–47.

Berto, L., Saetta, A., Scotta, R. & Vitaliani, R. (2004), 'Shear behaviour of masonry panel: parametric FE analyses', *International journal of solids and structures* **41**(16-17), 4383–4405.

Bertolesi, E., Buitrago, M., Giordano, E., Calderon, P. A., Moragues, J. J., Clementi, F. & Adam, J. M. (2020), 'Effectiveness of textile reinforced mortar (TRM) materials in preventing seismic-induced damage in a u-shaped masonry structure submitted to pseudo-dynamic excitations', *Construction and Building Materials* **248**, 118532.

Bertolesi, E., Carozzi, F. G., Milani, G. & Poggi, C. (2014), 'Numerical modeling of fabric reinforce cementitious matrix composites (FRCM) in tension', *Construction and Building Materials* **70**, 531–548.

Bertolesi, E., Milani, G. & Lourenço, P. B. (2016), 'Implementation and validation of a total displacement non-linear homogenization approach for in-plane loaded masonry', *Computers & Structures* **176**, 13–33.

Bertolesi, E., Milani, G. & Poggi, C. (2016), 'Simple holonomic homogenization model for the non-linear static analysis of in-plane loaded masonry walls strengthened with FRCM composites', *Composite Structures* **158**, 291–307.

Bhosale, S. D. & Desai, A. K. (2019), 'Simulation of masonry wall using concrete damage plasticity model', *International Journal of Innovative Technology and Exploring Engineering* **8**(9S3), 1241–1244.

Bolhassani, M., Hamid, A. A., Lau, A. C. & Moon, F. (2015), 'Simplified micro modeling of partially grouted masonry assemblages', *Construction and Building Materials* **83**, 159–173.

Calabrese, A. S., D'Antino, T., Colombi, P., Carloni, C. & Poggi, C. (2020), 'Fatigue behavior of PBO FRCM composite applied to concrete substrate', *Materials* **13**(10), 2368.

Campbell, J. (2015), *Complete casting handbook: metal casting processes, metallurgy, techniques and design*, Butterworth-Heinemann.

Carloni, C., Subramaniam, K. V., Savoia, M. & Mazzotti, C. (2012), 'Experimental determination of FRP-concrete cohesive interface properties under fatigue loading', *Composite Structures* **94**(4), 1288–1296.

Carozzi, F. G., Bellini, A., D'Antino, T., de Felice, G., Focacci, F., Hojdys, Ł., Laghi, L., Lanoye, E., Micelli, F., Panizza, M. et al. (2017), 'Experimental investigation of tensile and bond properties of carbon-FRCM composites for strengthening masonry elements', *Composites Part B: Engineering* **128**, 100–119.

Carozzi, F. G., Colombi, P., Fava, G. & Poggi, C. (2016), 'A cohesive interface crack model for the matrix–textile debonding in FRCM composites', *Composite Structures* **143**, 230–241.

Carozzi, F. G., Milani, G. & Poggi, C. (2014), 'Mechanical properties and numerical modeling of fabric reinforced cementitious matrix (FRCM) systems for strengthening of masonry structures', *Composite structures* **107**, 711–725.

Carozzi, F. G. & Poggi, C. (2015), 'Mechanical properties and debonding strength of fabric reinforced cementitious matrix (FRCM) systems for masonry strengthening', *Composites Part B: Engineering* **70**, 215–230.

Coburn, A. W., Spence, R. J. & Pomonis, A. (1992), Factors determining human casualty levels in earthquakes: mortality prediction in building collapse, *in* 'Proceedings of the 10th world conference on earthquake engineering', Balkema, Rotterdam, the Netherlands, pp. 5989–5994.

Dalalbashi, A., Ghiassi, B., Oliveira, D. V. & Freitas, A. (2018), 'Fiber-to-mortar bond behavior in TRM composites: Effect of embedded length and fiber configuration', *Composites Part B: Engineering* **152**, 43–57.

D'Altri, A. M., Messali, F., Rots, J., Castellazzi, G. & de Miranda, S. (2019), 'A damaging block-based model for the analysis of the cyclic behaviour of full-scale masonry structures', *Engineering Fracture Mechanics* **209**, 423–448.

de Felice, G., Aiello, M. A., Bellini, A., Ceroni, F., De Santis, S., Garbin, E., Leone, M., Lignola, G. P., Malena, M., Mazzotti, C. et al. (2016), 'Experimental characterization of composite-to-brick masonry shear bond', *Materials and Structures* **49**(7), 2581–2596.

De Felice, G., Aiello, M. A., Caggegi, C., Ceroni, F., De Santis, S., Garbin, E., Gattesco, N., Hojdys, Ł., Krajewski, P., Kwiecień, A. et al. (2018), 'Recommendation of RILEM technical committee 250-CSM: Test method for textile reinforced mortar to substrate bond characterization', *Materials and Structures* **51**(4), 95.

de Felice, G., D'Antino, T., De Santis, S., Meriggi, P. & Roscini, F. (2020), 'Lessons learned on the tensile and bond behavior of fabric reinforced cementitious matrix (FRCM) composites', *Frontiers in Built Environment* **6**, 5.

De Felice, G., De Santis, S., Garmendia, L., Ghiassi, B., Larrinaga, P., Lourenço, P. B., Oliveira, D. V., Paolacci, F. & Papanicolaou, C. G. (2014), 'Mortar-based systems for externally bonded strengthening of masonry', *Materials and structures* **47**(12), 2021–2037.

De Santis, S. & de Felice, G. (2015), 'Steel reinforced grout systems for the strengthening of masonry structures', *Composite Structures* **134**, 533–548.

De Santis, S., Hadad, H. A., De Caso y Basalo, F., De Felice, G. & Nanni, A. (2018), 'Acceptance criteria for tensile characterization of fabric-reinforced cementitious matrix systems for concrete and masonry repair', *Journal of Composites for Construction* **22**(6), 04018048.

DeHoff, P. H., Anusavice, K. J. & Wang, Z. (1995), 'Three-dimensional finite element analysis of the shear bond test', *Dental Materials* **11**(2), 126–131.

Department for Transport Statistics UK (2016), Licensed vehicles at the end of the year 1 by tax class, Great Britain from 1909a, Technical report, GOV.UK.

Department for Transport UK (2016), Road traffic (vehicle miles) by vehicle type in Great Britain, annual from 1949, Technical report, GOV.UK.

DIANA FEA (2017), *Diana User's Manual, Release 10.2*, DIANA FEA BV, The Netherlands.

Donnini, J., Corinaldesi, V. & Nanni, A. (2016), 'Mechanical properties of FRCM using carbon fabrics with different coating treatments', *Composites Part B: Engineering* **88**, 220–228.

Drucker, D. C. & Prager, W. (1952), 'Soil mechanics and plastic analysis or limit design', *Quarterly of applied mathematics* **10**(2), 157–165.

D'Ambrisi, A., Feo, L. & Focacci, F. (2013), 'Experimental and analytical investigation on bond between carbon-FRCM materials and masonry', *Composites Part B: Engineering* **46**, 15–20.

D'Antino, T., Carloni, C., Sneed, L. & Pellegrino, C. (2014), 'Matrix–fiber bond behavior in PBO FRCM composites: A fracture mechanics approach', *Engineering Fracture Mechanics* **117**, 94–111.

D'Antino, T., Carloni, C., Sneed, L. & Pellegrino, C. (2015), 'Fatigue and post-fatigue behavior of PBO FRCM-concrete joints', *International Journal of Fatigue* **81**, 91–104.

Elsanadedy, H. M., Almusallam, T. H., Alsayed, S. H. & Al-Salloum, Y. A. (2013), 'Flexural strengthening of RC beams using textile reinforced mortar–experimental and numerical study', *Composite Structures* **97**, 40–55.

EN, B. (1999), '1015-11: Methods of test for mortar for masonry–part 11: Determination of flexural and compressive strength of hardened mortar', *European Committee for Standardization, Brussels* .

Foraboschi, P. (2004), 'Strengthening of masonry arches with fiber-reinforced polymer strips', *Journal of composites for construction* **8**(3), 191–202.

Furtado, A., Rodrigues, H., Arêde, A. & Varum, H. (2020), Cost-effective analysis of textile-reinforced mortar solutions used to reduce masonry infill walls collapse probability under seismic loads, *in* 'Structures', Vol. 28, Elsevier, pp. 141–157.

Garmendia, L., Marcos, I., Garbin, E. & Valluzzi, M. R. (2014), 'Strengthening of masonry arches with textile-reinforced mortar: experimental behaviour and analytical approaches', *Materials and structures* **47**(12), 2067–2080.

Ghiassi, B., Oliveira, D. V., Marques, V., Soares, E. & Maljaee, H. (2016), 'Multi-level characterization of steel reinforced mortars for strengthening of masonry structures', *Materials & Design* **110**, 903–913.

Giaretton, M., Dizhur, D., Garbin, E., Ingham, J. M. & da Porto, F. (2018), 'In-plane strengthening of clay brick and block masonry walls using textile-reinforced mortar', *Journal of Composites for Construction* **22**(5), 04018028.

Grande, E., Imbimbo, M. & Sacco, E. (2018), 'Numerical investigation on the bond behavior of FRCM strengthening systems', *Composites Part B: Engineering* **145**, 240–251.

Hughes, T. (1996), *The testing, analysis and assessment of masonry arch bridges*, CIMNE, Barcelona.

Ismail, N. & Ingham, J. M. (2016), 'In-plane and out-of-plane testing of unreinforced masonry walls strengthened using polymer textile reinforced mortar', *Engineering Structures* **118**, 167–177.

Jendele, L. & Cervenka, J. (2006), 'Finite element modelling of reinforcement with bond', *Computers & structures* **84**(28), 1780–1791.

Kariou, F., Triantafyllou, S. P., Bournas, D. & Koutas, L. (2018), 'Out-of-plane response of masonry walls strengthened using textile-mortar system', *Construction and Building Materials* **165**, 769–781.

Kim, Y. J. & Heffernan, P. J. (2008), 'Fatigue behavior of externally strengthened concrete beams with fiber-reinforced polymers: State of the art', *Journal of Composites for Construction* **12**(3), 246–256.

Kong, K., Mesticou, Z., Michel, M., Larbi, A. S. & Junes, A. (2017), 'Comparative characterization of the durability behaviour of textile-reinforced concrete (TRC) under tension and bending', *Composite Structures* **179**, 107–123.

Kouris, L. A. S. & Triantafillou, T. C. (2018), 'State-of-the-art on strengthening of masonry structures with textile reinforced mortar (TRM)', *Construction and Building Materials* **188**, 1221–1233.

Krevaikas, T. D. & Triantafillou, T. C. (2005), 'Masonry confinement with fiber-reinforced polymers', *Journal of composites for construction* **9**(2), 128–135.

Ku, H., Wang, H., Pattarachaiyakoop, N. & Trada, M. (2011), 'A review on the tensile properties of natural fiber reinforced polymer composites', *Composites Part B: Engineering* **42**(4), 856–873.

La Mendola, L., Accardi, M., Cucchiara, C. & Licata, V. (2014), 'Nonlinear FE analysis of out-of-plane behaviour of masonry walls with and without CFRP reinforcement', *Construction and Building Materials* **54**, 190–196.

Lee, J. & Fenves, G. L. (1998), 'Plastic-damage model for cyclic loading of concrete structures', *Journal of engineering mechanics* **124**(8), 892–900.

Leone, M., Aiello, M. A., Balsamo, A., Carozzi, F. G., Ceroni, F., Corradi, M., Gams, M., Garbin, E., Gattesco, N., Krajewski, P. et al. (2017), 'Glass fabric reinforced cementitious matrix: Tensile properties and bond performance on masonry substrate', *Composites Part B: Engineering* **127**, 196–214.

Li, X., Chen, J.-F., Lu, Y. & Yang, Z. (2015), 'Modelling static and dynamic FRP-concrete bond behaviour using a local concrete damage model', *Advances in Structural Engineering* **18**(1), 45–58.

Lignola, G. P., Caggegi, C., Ceroni, F., De Santis, S., Krajewski, P., Lourenço, P. B., Morganti, M., Papanicolaou, C. C., Pellegrino, C., Prota, A. et al. (2017), 'Performance assessment of basalt FRCM for retrofit applications on masonry', *Composites Part B: Engineering* **128**, 1–18.

Lourénço, P. B., De Borst, R. & Rots, J. G. (1997), 'A plane stress softening plasticity model for orthotropic materials', *International Journal for Numerical Methods in Engineering* **40**(21), 4033–4057.

Lourenço, P. B. & Rots, J. G. (1997), 'Multisurface interface model for analysis of masonry structures', *Journal of engineering mechanics* **123**(7), 660–668.

Lourenço, P. J. B. B. (1997), Computational strategies for masonry structures., Technical report, Delft University.

Lu, X., Ye, L., Teng, J. & Jiang, J. (2005), 'Meso-scale finite element model for FRP sheets/plates bonded to concrete', *Engineering structures* **27**(4), 564–575.

Lubliner, J., Oliver, J., Oller, S. & Oate, E. (1989), 'A plastic-damage model for concrete', *International Journal of solids and structures* **25**(3), 299–326.

Maroudas, S. R. & Papanicolaou, C. C. G. (2017), Effect of high temperatures on the TRM-to-masonry bond, *in* 'Key Engineering Materials', Vol. 747, Trans Tech Publ, pp. 533–541.

Mazzoni, S., Castori, G., Galasso, C., Calvi, P., Dreyer, R., Fischer, E., Fulco, A., Sorrentino, L., Wilson, J., Penna, A. et al. (2018), '2016–2017 Central Italy earthquake sequence: Seismic retrofit policy and effectiveness', *Earthquake Spectra* **34**(4), 1671–1691.

Mesticou, Z., Bui, L., Junes, A. & Larbi, A. S. (2017), 'Experimental investigation of tensile fatigue behaviour of textile-reinforced concrete (TRC): Effect of fatigue load and strain rate', *Composite Structures* **160**, 1136–1146.

Milani, G. (2008), '3D upper bound limit analysis of multi-leaf masonry walls', *International Journal of Mechanical Sciences* **50**(4), 817–836.

Milani, G., Fagone, M., Rotunno, T., Grande, E. & Bertolesi, E. (2020), 'Development of an interface numerical model for C-FRPs applied on flat and curved masonry pillars', *Composite Structures* **241**, 112074.

Milani, G., Grande, E., Bertolesi, E., Rotunno, T. & Fagone, M. (2021), 'Debonding mechanism of FRP strengthened flat surfaces: Analytical approach and closed form solution', *Construction and Building Materials* **302**, 124144.

Milani, G., Lourenço, P. & Tralli, A. (2006), 'Homogenization approach for the limit analysis of out-of-plane loaded masonry walls', *Journal of Structural Engineering* **132**(10), 1650–1663.

Minga, E., Macorini, L. & Izzuddin, B. A. (2018), 'A 3D mesoscale damage-plasticity approach for masonry structures under cyclic loading', *Meccanica* **53**(7), 1591–1611.

Naik, T. R., Singh, S. & Ye, C. (1993), 'Fatigue behavior of plain concrete made with or without fly ash', *A Progress Report Submitted to EPRI* .

Nazir, S. & Dhanasekar, M. (2013), 'Modelling the failure of thin layered mortar joints in masonry', *Engineering structures* **49**, 615–627.

Nuhoğlu, A., Erener, M. F., Hızal, Ç., Kıncal, C., Erdoğan, D. Ş., Özdağ, Ö. C., Akgün, M., Ercan, E., Kalfa, E., Köksal, D. et al. (2021), 'A reconnaissance study in Izmir (Bornova Plain) affected by October 30, 2020 samos earthquake', *International Journal of Disaster Risk Reduction* p. 102465.

Ombres, L., Mancuso, N., Mazzuca, S. & Verre, S. (2018), 'Bond between carbon fabric-reinforced cementitious matrix and masonry substrate', *Journal of Materials in Civil Engineering* **31**(1), 04018356.

Padalu, P., Singh, Y. & Das, S. (2018), 'Efficacy of basalt fibre reinforced cement mortar composite for out-of-plane strengthening of unreinforced masonry', *Construction and Building Materials* **191**, 1172–1190.

Page, J. (1994), *Masonry Arch Bridges-State of the Art. 1st ed*, TSO Stationery, London.

Papanicolaou, C. G., Triantafillou, T. C., Papathanasiou, M. & Karlos, K. (2008), 'Textile reinforced mortar (TRM) versus FRP as strengthening material of URM walls: out-of-plane cyclic loading', *Materials and structures* **41**(1), 143–157.

Papanicolaou, C., Triantafillou, T. & Lekka, M. (2011), 'Externally bonded grids as strengthening and seismic retrofitting materials of masonry panels', *Construction and Building Materials* **25**(2), 504–514.

Pino, V., Akbari Hadad, H., De Caso y Basalo, F., Nanni, A., Ali Ebead, U. & El Refai, A. (2017), 'Performance of FRCM-strengthened RC beams subject to fatigue', *Journal of Bridge Engineering* **22**(10), 04017079.

Raoof, S. M. & Bournas, D. A. (2017), 'TRM versus FRP in flexural strengthening of RC beams: Behaviour at high temperatures', *Construction and Building Materials* **154**, 424–437.

Raoof, S. M., Koutas, L. N. & Bournas, D. A. (2016), 'Bond between textile-reinforced mortar (TRM) and concrete substrates: Experimental investigation', *Composites Part B: Engineering* **98**, 350–361.

Raoof, S. M., Koutas, L. N. & Bournas, D. A. (2017), 'Textile-reinforced mortar (TRM) versus fibre-reinforced polymers (FRP) in flexural strengthening of RC beams', *Construction and Building Materials* **151**, 279–291.

Razavizadeh, A., Ghiassi, B. & Oliveira, D. V. (2014), 'Bond behavior of srg-strengthened masonry units: Testing and numerical modeling', *Construction and Building Materials* **64**, 387–397.

Resta, M., Fiore, A. & Monaco, P. (2013), 'Non-linear finite element analysis of masonry towers by adopting the damage plasticity constitutive model', *Advances in Structural Engineering* **16**(5), 791–803.

Ryall, M. (2008), Loads and load distribution, *in* 'ICE Manual of Bridge Engineering: Second Edition', ICE Publishing, pp. 23–48.

Shabdin, M., Zargaran, M. & Attari, N. K. (2018), 'Experimental diagonal tension (shear) test of un-reinforced masonry (URM) walls strengthened with textile reinforced mortar (TRM)', *Construction and Building Materials* **164**, 704–715.

Shing, P., Lofti, H., Barzegarmehrabi, A. & Bunner, J. (1992), Finite element analysis of shear resistance of masonry wall panels with and without confining frames, *in* 'Proceedings of the 10th World Conference on Earthquake Engineering', AA Balkema Rotterdam, The Netherlands, pp. 2581–2586.

Smith, M. (2012), *ABAQUS/Standard User's Manual, Version 6.11*, Vol. 89, Dassault Systèmes Simulia Corp, United States.

Sneed, L., D'Antino, T., Carloni, C. & Pellegrino, C. (2015), 'A comparison of the bond behavior of PBO-FRCM composites determined by double-lap and single-lap shear tests', *Cement and Concrete Composites* **64**, 37–48.

Solan, B., Nowroozpour, A., Clopper, P., Watters, C. & Ettema, R. (2019), Scour-induced failure of masonry arch bridges: Causes and countermeasures, *in* 'E-proceedings of the 38th IAHR World Congress'.

Stavridis, A. & Shing, P. (2010), 'Finite-element modeling of nonlinear behavior of masonry-infilled RC frames', *Journal of structural engineering* **136**(3), 285–296.

Stratford, T., Pascale, G., Manfroni, O. & Bonfiglioli, B. (2004), 'Shear strengthening masonry panels with sheet glass-fiber reinforced polymer', *Journal of Composites for Construction* **8**(5), 434–443.

Tan, K. H. & Patoary, M. (2004), 'Strengthening of masonry walls against out-of-plane loads using fiber-reinforced polymer reinforcement', *Journal of Composites for Construction* **8**(1), 79–87.

Tao, Y., Chen, J.-F., Stratford, T. & Ooi, J. (2012), Numerical modelling of a large scale model masonry arch bridge, *in* 'Structural Faults and Repair 2012'.

Tetta, Z. C. & Bournas, D. A. (2016), 'TRM vs FRP jacketing in shear strengthening of concrete members subjected to high temperatures', *Composites Part B: Engineering* **106**, 190–205.

Tetta, Z. C., Koutas, L. N. & Bournas, D. A. (2015), 'Textile-reinforced mortar (TRM) versus fiber-reinforced polymers (FRP) in shear strengthening of concrete beams', *Composites Part B: Engineering* **77**, 338–348.

Tetta, Z. C., Koutas, L. N. & Bournas, D. A. (2018), 'Shear strengthening of concrete members with TRM jackets: Effect of shear span-to-depth ratio, material and amount of external reinforcement', *Composites Part B: Engineering* **137**, 184–201.

Triantafillou, T. (2016), Strengthening of existing masonry structures: Concepts and structural behavior, *in* 'Textile fibre composites in civil engineering', Elsevier, pp. 361–374.

Triantafillou, T. C. (1998), 'Strengthening of masonry structures using epoxy-bonded FRP laminates', *Journal of composites for construction* **2**(2), 96–104.

Wang, X., Lam, C. C. & Iu, V. P. (2020), 'Bond behaviour of steel-TRM composites for strengthening masonry elements: Experimental testing and numerical modelling', *Construction and Building Materials* **253**, 119157.

Wu, C., Oehlers, D., Rebentrost, M., Leach, J. & Whittaker, A. (2009), 'Blast testing of ultra-high performance fibre and FRP-retrofitted concrete slabs', *Engineering structures* **31**(9), 2060–2069.

Yuan, H., Lu, X., Hui, D. & Feo, L. (2012), 'Studies on FRP-concrete interface with hardening and softening bond-slip law', *Composite Structures* **94**(12), 3781–3792.

Yuan, H., Teng, J., Seracino, R., Wu, Z. & Yao, J. (2004), 'Full-range behavior of FRP-to-concrete bonded joints', *Engineering structures* **26**(5), 553–565.

Zampieri, P., Zanini, M. A., Faleschini, F., Hofer, L. & Pellegrino, C. (2017), 'Failure analysis of masonry arch bridges subject to local pier scour', *Engineering Failure Analysis* **79**, 371–384.

Zheng, X., Huang, P., Chen, G. & Tan, X. (2015), 'Fatigue behavior of FRP–concrete bond under hygrothermal environment', *Construction and Building Materials* **95**, 898–909.

A

Summary of experimental results available in the literature

Table A.1: Tensile tests on bare fibre textiles

Source	Material	Mesh size [mm]	Sample size [mm]	Strength [MPa]	Young's modulus [GPa]	Strain [%]	Nt* [mm]	As** [N/mm]
Al-Salloum et. al (2012)	basalt	25x25	175x50 (aprox)	623	31.94	-	0.064	2.04
Carozzi et. al (2015)	glass	19x15.5	single rovin	1233	55.6	-	-	-
	carbon	10x10	single rovin	1944	203	-	0.047	9.54
Alecci et. al (2016)	carbon	6x6	220Lx45W (aprox)	1350	244	0.65	0.047	11.46
	glass	15.7x10.1	220Lx45W (aprox)	1370	70.8	1.9	0.023	1.62
Raoof et. al (2017)	carbon	10x10	330x50	1518	166.8	0.793	0.095	15.84
	carbon***	10x10		2843	200.5	1.39	0.095	19.04
	basalt	25x25		1190	63.7	1.825	0.037	2.35
	glass	12x12		794	41.1	1.66	0.044	1.8
Giaretton et. al (2018)	glass	-	300L × 25W mm	1,17	-	-	-	
Padalu et. al (2018)	basalt	25x25 (2strands)	135x2 strands	828	66	1.87	-	
		50x50 (4strands)	165x4 strands	1104	88	2.47	-	
Ombres et. al (2019)	carbon	10x10	-	2130	186	1.15	0.047	8.74

*Nominal thickness, **Axial stiffness, ***Coated carbon textile

Table A.2: FRCM to masonry bond tests

Reference	Textile material	Textile mesh size [mm]	Specimen size	Bond lengths [mm]	Type of test	Maximum load [kN]	Maximum stress [MPa]	Failure mode	Width [mm]	E/r
D'Ambrisi et al. (2013)	carbon1	10x10	2 masonry prism	110	DF	8.26	703	D	250	-
	carbon2	10x10	2 masonry prism	230	DF	7.46	635	D	250	-
	carbon3	10x10	2 masonry prism	350	DF	7.64	650	D	250	
Carozzi et al. (2017)	carbon4	30x30	5 bricks	260	SL	3.08	544.6	B,E1	90	0.30
	carbon5	10x10	5 bricks	260	SL	3.55	1259.6	C,AE2	54	0.37
	carbon6	30x30	5 bricks	260	SL	3.97	701.4	D,B	96	0.38
	carbon7	10x10	5 bricks	260	SL	4.27	1015.7	D+E2	100	0.53
	carbon8	17.5x17.5	5 bricks	260	SL	2.52	1079.8	E2	38	0.43
	carbon9	9.4x9.4	5 bricks	260	SL	2.62	753.6	D	100	0.30
	carbon10	20x20	5 bricks	260	SL	4.47	1587.6	E2	60	0.85
Ombres et al. (2019)	carbon11	10x10	5 bricks	150	SL	1.91	762	D	50	0.36
	carbon12	10x10	5 bricks	200	SL	2.03	813	D	50	0.38
	carbon13	10x10	5 bricks	250	SL	1.73	736	D	50	0.35
	carbon14	10x10	5 bricks	300	SL	1.78	757	D	50	0.36
Alecci et al. (2016)	carbon15	6x6	2 masonry prism	150	DF	4.03	769	D	90	0.57
	carbon16	6x6	2 masonry prism	200	DF	4.1	774	D	90	0.57
	carbon17	6x6	2 masonry prism	250	DF	4.11	774	D	90	0.57
Donnini et al. (2016)	carbon18	dry20x20	1 brick	150	DL	2.99	479	D	60	0.21
	carbon19	L20x20	1 brick	150	DL	3.27	524	D	60	0.28
	carbon20	M20x20	1 brick	150	DL	5.28	846	D	60	0.46
	carbon21	H20x20	1 brick	150	DL	5.25	842	D-E1	60	0.46

Table A.2: FRCM to masonry bond tests

Reference	Textile material	Textile mesh size [mm]	Specimen size	Bond lengths [mm]	Type of test	Maximum load [kN]	Maximum stress [MPa]	Failure mode	Width [mm]	E/r
Leone et. al (2017)	carbon22	LS20x20	1 brick	150	DL	4.07	653	D	60	0.35
	carbon23	MS20x20	1 brick	150	DL	4.65	746	D	60	0.40
	carbon24	HS20x20	1 brick	150	DL	6.49	1040	D-E1	60	0.56
	glass1	15x15	5 bricks	265	SL	1.19	299	D-E1-E2	100	0.47
	glass2	33x33	5 bricks	260	SL	4.7	420	A-E2	100	0.27
	glass3	66x66	5 bricks	240	SL	14.7	970	A-D	140	-
	glass4	99x99	5 bricks	120	SL	7.4	980	-	30	-
	glass5	12x12	5 bricks	260	SL	2.8	801	D	60	0.69
	glass6	15x15	5 bricks	260	SL	1.1	351	E1	100	1.08
	glass7	7.6x7.6	5 bricks	260	SL	0.6	420	D	40	0.96
	glass8	n/a	5 bricks	260	SL	2.1	570	E1-D	75	0.41
	glass9	10x12.5	5 bricks	260	SL	1.5	1098	D	40	0.51
	glass10	15.7x10.1	5 bricks	260	SL	3	671	E2-D	100	0.58
	glass11	25x25	5 bricks	260	SL	1.9	456	E1-D	125	0.57
Alecci et. al (2015)	glass12	15.7x10.1	2 masonry prism	150	DF	1.88	-	D	90	
	glass13	15.7x10.1	2 masonry prism	200	DF	2.95	-	D	90	0.96
	glass14	15.7x10.1	2 masonry prism	250	DF	2.94	-	D	90	0.96
Carozzi et. al (2014)	glass15	17x12	1 brick	50	DL	1.06	-	D	50	-
	glass16	17x12	1 brick	100	DL	2.63	-	D, E1	50	-
	glass17	17x12	1 brick	150	DL	4.06	-	E1	50	-
	glass18	17x12	1 brick	100	DL	1.5	-	B	50	-
	glass19	17x12	1 brick	150	DL	1.73	-	C	50	-
Lignola et al (2017)	basalt1	25x25	5 bricks	260	SL	3.1	934	E1	90	0.43
	basalt2	25x25	5 bricks	260	SL	3.51	1413	E1	90	0.65

Table A.2: FRCM to masonry bond tests

Reference	Textile material	Textile mesh size [mm]	Specimen size	Bond lengths [mm]	Type of test	Maximum load [kN]	Maximum stress [MPa]	Failure mode	Width [mm]	E/r
	basalt3	25x25	5 bricks	260	SL	3.94	1583	E1,D	75	0.73
	basalt4	-	5 bricks	260	SL	1.84	742	E1,C	75	0.34
	basalt5	25x25	5 bricks	260	SL	4.79	1102	E1	75	0.91
	basalt6	25x25	5 bricks	260	SL	3.23	1117	E1,D	50	0.93
	basalt7	6x6	5 bricks	260	SL	2.44	833	E1,D	80	1
	basalt8	6x6	5 bricks	260	SL	2.68	691	E1	100	0.83
	basalt9	6x6	5 bricks	260	SL	4.3	1106	E1,D	125	1.33
	basalt10	6x6	5 bricks	260	SL	4.88	1255	E1	125	0.97
Barducci et al (2020)	basalt11	17x17	1 brick	220	SL	2.92	-	E1	95	1.03
	basalt12	17x17	1 brick	220	SL	2.26	-	E1	95	0.8
	basalt13	17x17	1 brick	220	SL	2.56	-	E1	95	0.91
	basalt14	17x17	1 brick	220	SL	1.68	-	E1	95	0.59
	basalt15	17x17	1 brick	220	DL	3.22	-	E1	95	1.14
	basalt16	17x17	1 brick	220	DL	2.42	-	D	95	0.86
	basalt17	17x17	1 brick	220	DL	1.8	-	D	95	0.61
	basalt18	17x17	1 brick	220	DL	1.41	-	D	95	0.5

DF-double-face,SL-single-lap,DL-double-lap test setup; Failure modes corresponding to Fig. 2.5; E/r-exploitation ratio

B
List of Abbreviations

AR	Alkali Resistant
URM	Unreinforced masonry structures
FRP	Fibre reinforced polymer
COV	Coefficient of variation
CDP	Concrete damage Plasticity
TRM	Textile Reinforced Mortar
URM	Unreinforced masonry structures
FRCM	Fabric reinforced cementitious matrix
TRC	Textile reinforced concrete
PP	Polypropylene
PBO	Polyparaphenyle benzobisoxazole
DIC	Digital image correlation
SRG	Steel-reinforced grout
CMCBC	Cement-matrix-based composites
DF	Double-face
SL	Single-lap
CTRM	Carbon textile reinforced mortar
BTRM	Basalt textile reinforced mortar
CFL	Carbon fiber laminate
RH	Relative humidity
RC	Reinforced concrete
LVDT	Linear variable differential transducers